The Hashemite Kingdom of Jordan Scientific Research Support Fund The Hashemite University

JJEES

Jordan Journal of Earth and Environmental Sciences

Volume (16) Number (3)


Cover photo © Prof Eid Tarazi

JJEES is an International Peer-Reviewed Research Journal

ISSN 1995-6681 jjees.hu.edu.jo September 2025

Jordan Journal of Earth and Environmental Sciences (JJEES)

JJEES is an International Peer-Reviewed Research Journal, Issued by Deanship of Scientific Research, The Hashemite University, in corporation with, the Jordanian Scientific Research Support Fund, the Ministry of Higher Education and Scientific Research.

EDITORIAL BOARD:

Editor –in-Chief:

- **Prof. Dr. Mahmoud M. Abu –Allaban**
  The Hashemite University, Jordan

Assistant Editor:

- **Dr. Mohammed A. Salahat**
  The Hashemite University, Jordan

Editorial Board:

- **Prof. Dr. Abdalla M. Abu Hamad**
  Jordan University
- **Prof. Dr. Hani R. Al Amoush**
  Al al-Bayt University
- **Prof. Dr. Ibrahim M. Oroud**
  Mutah University
- **Prof. Dr. Kamel K. Al Zboon**
  Balqa Applied University
- **Prof. Dr. Khaldoon A. Al-Qudah**
  Yarmouk University

ASSOCIATE EDITORIAL BOARD: (ARRANGED ALPHABETICALLY)

- **Professor Ali Al-Juboury**
  Al-Kitab University, Kirkuk, Iraq
- **Dr. Bernhard Lucke**
  Friedrich-Alexander University, Germany
- **Professor Dhirendra Pandey**
  University of Rajasthan, India
- **Professor Eduardo García-Meléndez**
  University of León, Spain
- **Professor Franz Fürsich**
  Universität Erlangen-Nürnberg, Germany
- **Professor Olaf Elicki**
  TU Bergakademie Freiberg, Germany

INTERNATIONAL ADVISORY BOARD: (ARRANGED ALPHABETICALLY)

- **Prof. Dr. Ayman Suleiman**
  University of Jordan, Jordan.
- **Prof. Dr. Chakroun-Khodjet El Khil**
  Campus Universitaire, Tunisienne.
- **Prof. Dr. Christoph Külls**
  Technische Hochschule Lübeck, Germany.
- **Prof. Dr. Eid Al-Tarazi**
  The Hashemite University, Jordan.
- **Prof. Dr. Fayez Abdulla**
  Jordan University of Science and Technology, Jordan.
- **Prof. Dr. Hasan Arman**
  United Arab Emirates University, U.A.E.
- **Prof. Dr. Hassan Baioumy**
  Universiti Teknologi Petronas, Malaysia.
- **Prof. Dr. Khaled Al-Bashaireh**
  Yarmouk University, Jordan.
- **Dr. Madani Ben Youcef**
  University of Mascara, Algeria.
- **Dr. Maria Taboada**
  Universidad De León, Spain.
- **Prof. Dr. Mustafa Al- Obaidi**
  University of Baghdad, Iraq.
- **Dr. Nedal Al Ouran**
  Balqa Applied University, Jordan.
- **Prof. Dr. Rida Shibli**
  The Association of Agricultural Research Institutions in the Near East and North Africa, Jordan.
- **Prof. Dr. Saber Al-Rousan**
  University of Jordan, Jordan.
- **Prof. Dr. Sacit Özer**
  Dokuz Eylul University, Turkey.
- **Dr. Sahar Dalahmeh**
  Swedish University of Agricultural Sciences, Sweden.
- **Prof. Dr. Shaif Saleh**
  University of Aden, Yemen.
- **Prof. Dr. Sherif Farouk**
  Egyptian Petroleum Institute, Egypt.
- **Prof. Dr. Sobhi Nasir**
  Sultan Qaboos University, Oman.
- **Prof. Dr. Sofian Kanan**
  American University of Sharjah, U.A.E.
- **Prof. Dr. Stefano Gandolfi**
  University of Bologna, Italy.
- **Prof. Dr. Zakaria Hamimi**
  Banha University, Egypt.

EDITORIAL BOARD SUPPORT TEAM:

Language Editor
- **Dr. Abdullah F. Al-Badarneh**

Publishing Layout
- **Obada M. Al-Smadi**

SUBMISSION ADDRESS:

Manuscripts should be submitted electronically to the following e-mail:

jjees@hu.edu.jo

For more information and previous issues:

www.jjees.hu.edu.jo

Hashemite Kingdom of Jordan

Scientific Research Support Fund

Hashemite University

Jordan Journal of
Earth and Environmental Sciences

JJEES

An International Peer-Reviewed Scientific Journal

Financed by the Scientific Research Support Fund

Volume 16 Number (3)

http:// jjees.hu.edu.jo/

ISSN 1995-6681

Taba Sabkha at central Wadi Araba, Jordan. Basement out crops, alluvial fans and mud cracks. By Prof Eid Tarazi

JJEES

Jordan Journal of Earth and Environmental Sciences

JJEES (2025) 16 (3): 220-226
ISSN 1995-6681

Infiltration Capacity and its Relation with Groundwater Potential in West Progo, Indonesia

Listyani, R.A.T. [1*], Nugrahini, R.A. [2], Prabowo, I.A. [2]

[1]*Master of Geological Eng. Dept., Institut Teknologi Nasional Yogyakarta, Indonesia*
[2]*Geological Eng. Dept., Institut Teknologi Nasional Yogyakarta, Indonesia*

Received on January 7, 2025, Accepted o February 12, 2025

Abstract

West Progo area is in Kulon Progo Regency, Yogyakarta Province, Indonesia. This regency has recently developed quite rapidly and requires a lot of research to support regional development. This study aims to conduct a hydrogeological survey to investigate the relationship between infiltration capacity and groundwater potential in the area. The hydrogeological survey collected morphological data, including rock types and geological structures, as well as groundwater levels and measured infiltration rates using a double ring infiltrometer. The study results showed that the infiltration capacity values varied according to the soil cover in the latosol, grumusol, alluvial, and regosol zones, respectively, by 1.2, 12, 68.4, and 84 cm/hour. The average groundwater level in the zone showed a position of 7.94, 5.24, 2.18, and 3.52 m below the surface. There is a powerful correlation between infiltration rate and groundwater level. Infiltration capacity is in line with groundwater potential, where the greater the infiltration capacity, the shallower the groundwater level.

Keywords: *Infiltration, Groundwater, Groundwater Table, Soil Type, Hydrogeology*

1. Introduction

Kulon Progo Regency is a rapidly developing area in the Special Region of Yogyakarta Province, which aligns with constructing a new international airport in the Temon area, Kulon Progo. The development of regional areas requires the availability of natural resources, especially groundwater. Groundwater is a basic substance in life, especially fresh water. In fact, freshwater scarcity is one of the biggest threats facing people in recent years (Mohammed et al, 2024). Therefore, research on groundwater potential needs to be encouraged.

In general, groundwater potential is supported by the large amount of rainfall that enters the subsurface through infiltration. The issue of infiltration becomes critical when we encounter various types of soil cover or rock composition in an area. Water resources in a region are also significantly influenced by water infiltration into the subsurface (Freeze & Cherry, 1979; Listyani, 2022). This process is driven by the amount of rain in the area. Meanwhile, Yang et al. (2016) pointed out that the presence of water in soft rocks is significant when facing geological problems.

Infiltration is the process by which water enters the soil. This process plays a vital role in the hydrogeological cycle as it is the fundamental step for the existence of groundwater in the aquifer. Water that infiltrates and travels through the aeration zone contributes to the groundwater in the aquifer and is referred to as a groundwater recharge component. Besides originating from local groundwater recharge due to rainwater percolation, groundwater is also recharged by regional groundwater flow within the aquifer (Sophocleus, 2004). If the infiltration capacity is low during heavy rainfall, it can lead to surface water runoff, which may result in soil erosion, flooding, or even landslides.

Various hydrological/hydrogeological parameters, such as soil type, temperature, vegetation, and rainfall, are factors that influence the occurrence of infiltration. Of these various parameters, soil hydraulic conductivity is one of the most important factors that controls the infiltration process and then, determines groundwater potential (Sakellariou-Makrantonaki 2016; Sharief et al., 2023).

One of the main factors that affect infiltration is the type of land cover. This factor then determines the physical properties of the soil, such as soil texture, which strongly influences the behavior of water absorption into the soil. The rainfall factor influences where the infiltration capacity will be reached; if the rain exceeds this capacity, while in cases of rain that is less than the infiltration capacity, the average infiltration equals the rainfall (Seyhan, 1990). These changes then affect the behavior of groundwater absorption through infiltration, which also plays a role in local groundwater recharge in the area.

This study was conducted using the Horton model, which aims to determine the value of infiltration capacity in Kulon Progo and its relationship with groundwater potential. Therefore, a study of infiltration capacity needs to be conducted to understand the potential of water resources and support the development of this area.

---

* Corresponding author e-mail: lis@itny.ac.id

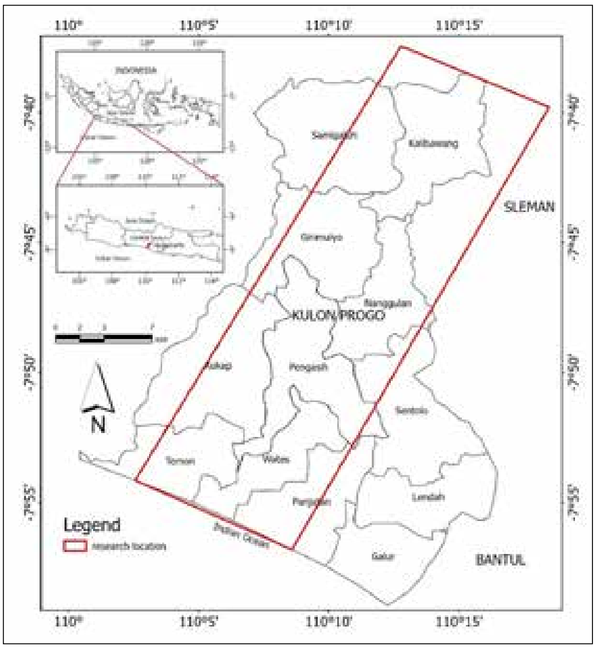

Figure 1. The research area is located in Kulon Progo Regency, Java.

2. Research Materials and Methods

This research was conducted in an area with the physiography of the Kulon Progo dome, the central depression zone to the South Coastal Plain of Java (Van Bemmelen, 1949). In the northern part, the research area has hilly morphology composed of Tertiary sedimentary rocks, including Nanggulan, Old Andesite, and Sentolo Formations (Rahardjo et al., 1995). Meanwhile, the central part of the research area is composed of fluvial-volcanic alluvial deposits resulting from the activities of Mt. Merapi and the Progo River. The southern part of the research area borders the Indian Ocean, consisting of coastal sandy plains and dunes.

The research area is in Kulon Progo, the northern part of the non-Groundwater Basin area or non-potential Groundwater Basin (Geological Agency, 2011). According to the DPWHEMR & CV. CPK (2016), this area is included in the Menoreh Basin. In addition, the Wates Groundwater Basin includes the southern part of the research area (Geological Agency, 2011).

The research area is located in Kulon Progo Regency, part of the Pekalongan regional hydrogeological map area on the southeast side. According to the regional hydrogeological map (Effendi, 1985), the research area comprises varying hydrogeological units, from highly productive to low. Some places even show the local area to rare groundwater potential. Under this condition, the groundwater level and aquifer potential also vary.

Field hydrogeological surveys have been conducted, starting with determining location points in several places, each representing a different soil cover, namely latosol, grumusol, alluvial, and regosol soils. Furthermore, geological descriptions and groundwater level mapping were conducted at several points in each soil zone.

Infiltration speed is measured, using two interrelated parameters: infiltration rate and infiltration capacity. The infiltration rate is the amount of water that enters the soil through the soil surface at a specific time (Maghfiroh, 2020). It is usually expressed in m/s or cm/hour. Meanwhile, infiltration capacity is the maximum infiltration rate in a specific soil type (Harimi, 2018).

Infiltration rate measurements were carried out using a double ring infiltrometer measuring 20 cm high, 15 cm inner ring diameter, and 30 cm outer ring (Figure 2). David et al. (2016) stated that both rings have different functions; the outer ring functions to reduce the possibility of water not moving horizontally and the inner ring functions to measure the diameter. Infiltration measurements were carried out at one selected location representing each soil zone (Figure 3).

Infiltration capacity analysis was carried out using the Horton model. In the Horton method analysis (1940), the infiltration rate can be expressed mathematically using the following equation:

$$f = fc + (f0 - f_c) . e^{-kt} \quad (1)$$

Where:

f: infiltration rate (cm/hr)

f_c: infiltration rate after constant

f_0: initial infiltration capacity

k: rate constant of infiltration capacity reduction

e: exponential number (2.718)

t: time (minutes)

The groundwater level measurements were conducted throughout the research area in each soil zone. For example, the groundwater level measurements in shallow wells are given in Figure 4. Furthermore, a statistical analysis of correlation regression was conducted to determine the relationship between infiltration capacity and the local groundwater level. This groundwater level position assessed the groundwater potential in the research area.

Figure 2. Double ring infiltrometer and geological hammer.

Figure 3. Example of infiltration rate measurement activity in the regosol soil zone.

Figure 4. Example of a shallow well where groundwater level measurements were taken.

3. Results

3.1 Hydrogeological Conditions

DPWHEMR & CV. CPK (2016) stated that the research area in the northern part has an aquifer that can be classified into a group of colluvium aquifers, which are Quaternary deposits. This aquifer group is formed from weathered material or Tertiary formation debris, so its thickness depends on the local weathering level (reaching 30 m in some places). The transmissivity value of this aquifer group ranges from 1 - 100 m^2 / day. This colluvium aquifer group is an unconfined aquifer.

In the southern part, the Wates and Yogyakarta Formations are young rocks that form alluvial. The Wates Formation in the research area is loose material, resulting from the current activity of the Progo River. At the same time, the Yogyakarta Formation is formed by loose material, resulting from the activity of Old and Young Merapi. In the eastern part, the Young Merapi deposits are scattered along the Progo River, which are fluvial-volcanic deposits. These deposits develop as moderate to good aquifers, with a transmissive value of 550 m^2/day (DPWHEMR & CV. CPK, 2016).

The southernmost part of the research area contains a coastal aquifer system, with a coastal alluvial aquifer subsystem formed by the Wates, Merapi, and Sentolo Formations and a dune subsystem.

From the hydrogeological survey and secondary data (KPRRDPA, 2024), it is known that the research area is composed of four soil zones on the surface, namely latosol, grumusol, alluvial, and regosol soils. Latosol soils are formed by the weathering of OAF andesite breccia or Nanggulan sandstone; grumusol soils come from limestone or tuff of the Sentolo Formation; while alluvial soils come from young fluvial-volcanic activities (Figure 5).

3.2 Infiltration Test

In each of these soil zones, one location was taken for infiltration rate testing. Recording water decline was carried out every 5 minutes. The recording was stopped when the water decline was considered stable, which was a minimum of four measurements with the same decline rate.

Table 1 presents the infiltration rate test data. Furthermore, the measurement results in the field are processed using the Horton model, one of the well-known infiltration models in hydrology. The calculation of the infiltration rate (f), f_c (constant infiltration rate), and f_0 (initial infiltration rate) at selected locations is given as an example in (Table 2).

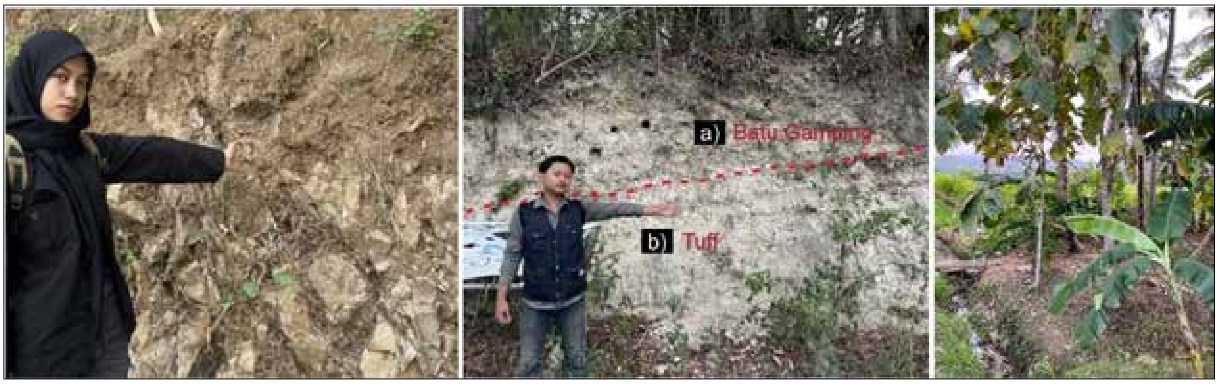

Figure 5. Sandstone outcrops (left), limestone, and tuff (center) in the northern part of the study area, and alluvial deposits scattered in the central part of the study area (right).

Table 1. Summary of water reduction in infiltration tests.

No	Time (t) (minutes)	*Water level drawdown*(cm)			
		Latosol	Grumusol	Alluvial	Regosol
		Loc. 77	Loc. 78	Loc. 79	Loc. 80
1	5	10	10	8	8.4
2	10	10	8	7.5	7.3
3	15	10	5.2	7	7.1
4	20	7.7	2.5	6.8	7
5	25	7.2	2.5	6.5	7
6	30	6	2.5	6	7
7	35	2.7	2.3	6.1	7
8	40	2.8	2.2	6	7
9	45	1.9	1.4	5.7	
10	50	1.3	1	5.7	
11	55	1	1	5.7	
12	60	1	1	5.7	
13	65	0.7	1		
14	70	0.3			
15	75	0.1			
16	80	0.1			
17	85	0.1			
18	90	0.1			

Juliastuti and Suhendra (2011) stated that the f_c value is a constant infiltration capacity that depends on the soil type. The f_0 and f_c values are functions of soil type and cover. Meanwhile, Juwita and Santoso (2019) asserted that fc is the maximum infiltration rate in a situation where the soil's ability to absorb water has reached its maximum. The f value is the maximum infiltration rate, obtained from a particular soil type.

The value of k in the Horton equation is an empirical constant. Applying the Horton equation requires determining the parameters f0, fc, and k. The value of f0 is set as the initial infiltration rate data. Meanwhile, fc and k are established by trial and error or through any optimization procedure to ensure that the Horton curve best fits the data using the fitting method. The Horton equation is an exponential function that shows the soil infiltration rate decreases over time (Duhita et al., 2021). Each soil has an asymptotic value that represents the final infiltration rate, defined as the infiltration capacity.

Horton (1933,1940) observed that infiltration starts from a standard value of f_0 and exponentially decreases to a constant condition of f_c (Andayono, 2018). The f value is the maximum infiltration rate, obtained from a particular soil type. Furthermore, the reference, used to determine the infiltration rate, is the Kohnke classification (1968) based on the f value (Table 3)

Table 2. Example of infiltration calculation in the regosol soil zone.

No	Time (t) (minutes)	Decrease (cm)	Infiltration Rate (f) (cm/min)	fc (cm/min)	$f\text{-}f_c$ (cm/min)	Log $(f\text{-}f_c)$
	0		1.8	1.4	0.4	-0.40
1	5	8.4	1.68	1.4	0.28	-0.55
2	10	7.3	1.46	1.4	0.06	-1.22
3	15	7.1	1.42	1.4	0.02	-1.70
4	20	7	1.4	1.4	0	
5	25	7	1.4	1.4	0	
6	30	7	1.4	1.4	0	
7	35	7	1.4	1.4	0	
8	40	7	1.4	1.4	0	

Table 3. Classification of infiltration rate (Kohnke, 1968).

Class	Infiltration Rate (f) (mm/hr)
Very fast	> 254
Fast	> 127 - 254
Rather fast	> 63 - 127
Medium	> 20 - 63
Rather slow	> 5 - 20
Slow	1 - 5

Figure 6 shows the graph of the relationship between time (t) and log $(f\text{-}f_c)$. Each graph shows the gradient of the regression line. The relationship between the gradient of the regression line and the value of k is shown in the following formula:

$$m = \frac{-1}{k \log e} \tag{2}$$

The formula above can be used to determine the value of k, which is the constant decrease in infiltration rate. For example, in Figure 6, the relationship between water decline time (t) and log (FC) is shown by the equation log $(f\text{-}f_c)$ = -0.0247 t + 0.06269, where the gradient of the regression line from the relationship between the two is -0.0247.

Figure 7 is made to show the graph of the relationship between test time (t) and the infiltration rate value (f). The initial infiltration value (f_0) can be determined from this graph. Duhita et al. (2021) illustrate this relationship (Figure 8).

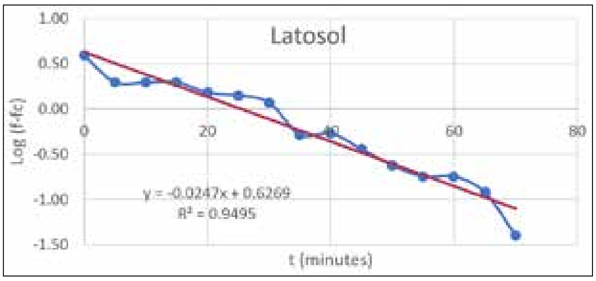

Figure 6. Graph the relationship between time (t) and log (f-fc) in the latosol soil zone.

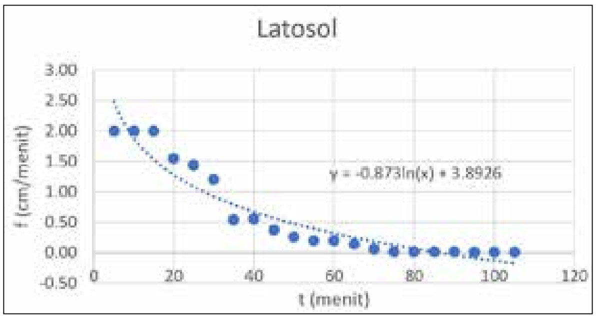

Figure 7. The example of a graph of the relationship between time (t) and f in the latosol soil zone.

The calculation results, based on the Horton formula (1933), obtained the infiltration capacity value in the research area, as listed in Table 4. According to the Kohnke classification (1968; Table 3), the infiltration capacity is in the slow until rather slow category (Table 5). Figure 9 compares f_0, f_c and f values at the four observation locations.

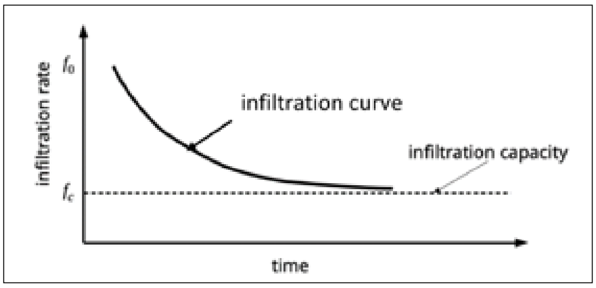

Figure 8. The graph shows the relationship between time (t) and infiltration rate (f) (Duhita et al., 2021).

Table 4. The initial infiltration rate (f_0), constant infiltration rate (f_c), and infiltration capacity (f) are based on the Horton model at the research location.

No	Loc.	f_0 (cm/min)	f_c (cm/min)	Gradient (m)	k	f (cm/min)
1	77	3.89	0.02	-0.0247	93.23174	0.020
2	78	3.03	0.20	-0.0304	75,75078	0.200
3	79	1.95	1.14	-0.041	56,16644	1.140
4	80	1.80	1.40	-0.0914	25,19501	1.400

Table 5. The infiltration capacity of the research area is based on Kohnke's classification (1968).

LP	Soil Type	f (cm/min)	f (mm/hr)	Class
77	Latosol	0.020	1.2	Slow
78	Grumusol	0.200	12	Rather slow
79	Alluvial	1.140	68.4	Rather fast
80	Regosol	1.400	84	Rather fast

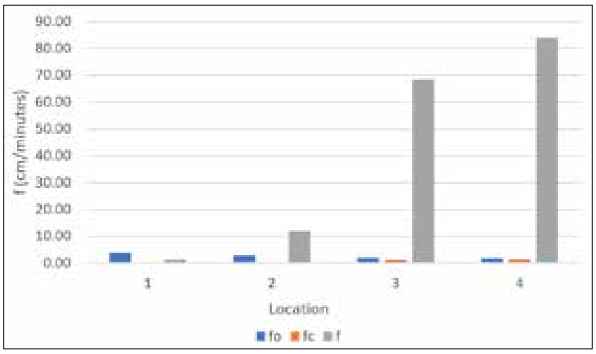

Figure 9. Graph showing the values of f0, fc, and f at locations 1 (latosol), 2 (grumusol), 3 (alluvial), and 4 (regosol).

3.3. Groundwater Level Measurement

Seventy-six dug wells, spread throughout the research area, have had their groundwater levels measured. Examples of dug wells are found in Figure 10. In all observation locations, residents' wells appear to have groundwater, and no dry wells were found. Groundwater levels were also measured at several points around the test location. In this area, the groundwater level is 1.4-12.3 m above sea level or 3.48-123.5 m above sea level, with a measured saturated zone thickness of 0.84-4.5 m. The average groundwater level in the latosol, grumusol, alluvial, and regosol zones is 7.94, 5.24, 2.18, and 3.52 m from the local ground surface, respectively.

Figure 10. Example of the appearance of dug wells, found in the research area.

In the research area, dug wells appear to have groundwater everywhere, as evidenced by data collection. For reference, the survey was conducted in July, which is usually the peak of the dry season. The CSA of Kulon Progo Regency (2022) noted that in that month, the Kulon Progo area generally had the lowest rainfall, with just 2.8 mm and had one rainy day. Although all dug pond wells had water when visited, some of these wells also have the potential to dry up if there is a long dry season.

Generally, the groundwater flow pattern tends towards the south, with variations to the east/southeast (Figure 11). The westward flow pattern is only found a little, on coastal plains or dunes, where it develops locally. The direction of the groundwater flow pattern is in line with the theory of shallow flow patterns, which states that the direction of shallow groundwater flow is generally determined by surface topography (Freeze & Cherry, 1979; Listyani & Budiadi, 2018; Listyani, 2019).

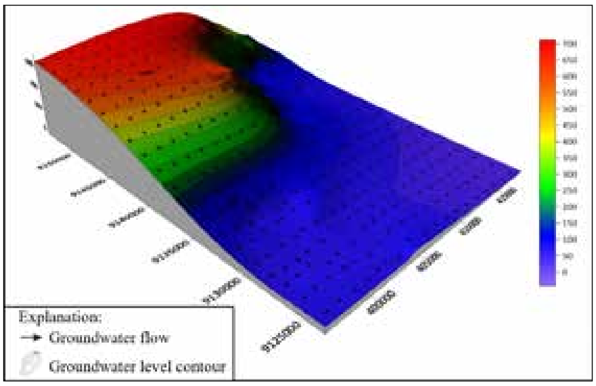

Figure 11. The 3D map of groundwater level in the Kulon Progo area.

4. Discussion

Soil cover (soil type) determines the infiltration capacity (Juwita & Santoso, 2019). The infiltration rate is generally used to evaluate soil quality and health (Saltiel et al., 2022). Therefore, this study conducted an analysis of infiltration capacity on different types of soil. CALRRD (2018) pointed out that several soil types in the study area were latosol, grumusol, alluvial, and regosol. The soil cover's physical properties are essential for studying water resources in certain regions (Listyani et al., 2022).

Infiltration analysis, at selected points representing varying soil cover, yields different values. This analysis means that the infiltration rate is determined by the type of soil cover (soil type). Furthermore, the infiltration rate will be linked to local recharge, by looking at the position of the groundwater table (Table 6; Figure 12).

The position of the shallow groundwater table can be a reference for assessing the potential of groundwater in an area. Areas with a lot of groundwater certainly tend to have relatively shallow groundwater tables. This groundwater table fluctuates. When the quantity of groundwater decreases, the groundwater table tends to become deeper. Therefore, in this study, the position of the groundwater table, measured from the local land surface, is used as one of the parameters to calculate the amount of groundwater recharge in the research area.

Table 6. Infiltration rate (f), saturated zone thickness, and groundwater level in the research area.

LP	Soil Type	f_o (cm/min)	f_c (cm/min)	f (cm/hr)	Groundwater Table (m below surface)
77	Latosol	3.89	0.02	1.2	7.94
78	Grumusol	3.03	0.2	12	5.24
79	Alluvial	2.45	0.2	68.4	2.18
80	Regosol	1.57	0.02	84	3.52

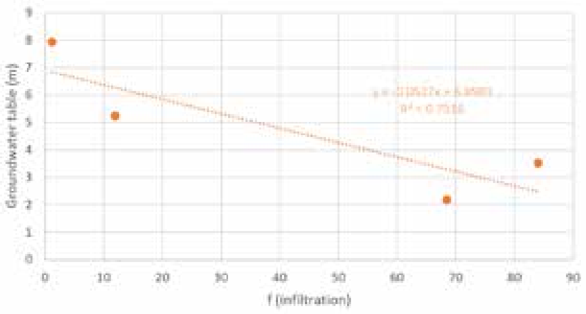

Figure 12. Relationship between infiltration capacity and groundwater table.

Figure 8 shows the relationship between the infiltration rate and local recharge represented by the groundwater level. The correlation between the two is 86.7%, which, according to Sugiyono (2022), shows a very strong correlation between the two variables.

Thus, the rate of rainwater infiltration into the soil in the study area shows powerful results about groundwater recharge, which is represented by the position of the groundwater table. A negative gradient indicates an inverse relationship between the two variables studied.

The higher the infiltration rate in an area is, the shallower the groundwater level will be. The shallowness of the groundwater level indicates that groundwater fluctuations are in good condition, which means that the groundwater potential is good.

Groundwater infiltration in shallow zones can carry materials that can pollute groundwater, such as bottom ashes. Many bottom ashes can percolate into groundwater by precipitation (Park et al., 2022). Therefore, it is necessary to manage materials that have the potential to pollute shallow groundwater. The potential of shallow groundwater in the research area, especially in the alluvial and regosol zones with large infiltration capacities, must be supported by various managements to avoid environmental pollution.

The infiltration process is important in water resource studies, especially in areas with less potential. Some areas that have few water resources can be categorized as an absolute water scarcity (Kharabshah and Alzboon, 2021). This scarcity is largely determined by low rainfall as the main parameter in the water budget (Al-Zboon, 2024). Apart from that, low rainfall can be exacerbated by low infiltration processes. Moreover, water resources also often face significant pressure due to climate change and increasing demand caused by increasing human activity (Abbas et al., 2024). Therefore, maintaining the quantity of water resources needs to be done by maintaining an optimal infiltration process. The potential of groundwater resources, of course, depends on rainfall which can infiltrate the land surface.

5. Conclusion

The infiltration rate values in several areas of Kulon Progo Regency vary according to their land cover in the latosol, grumusol, alluvial, and regosol zones, respectively, by 1.2, 12, 68.4, and 84 cm/hour. The average groundwater level in these zones is 7.94, 5.24, 2.18, and 3.52 m. below ground level. From the analysis results, it is known that there is a powerful correlation between the infiltration rate and the groundwater level. However, the two relationships are inversely proportional. Infiltration capacity is in line with groundwater potential, where the greater the infiltration rate is, the shallower the groundwater level will be.

Acknowledgments

The author would like to thank the Yogyakarta National Institute of Technology for funding internal research with contract number 41/ITNY/LPPMI/Pen.Int./PD/VI/ 2024 so that this paper can be written. The author would also like to thank the assistants who helped collect data in the field, especially Aditya, Triawan, Dhea, and Hezron.

References

Abbas, F.A., Nehme, N., Koubaissy, B., Ibrahim, Z., Khalife, R., Zahran, R., Karameh, J., Tarawneh, K. (2024) Assessment of Water Consumption in Water Scarce Regions by Using Statistical Analysis: A Case Study of El-Maten Region, Lebanon, JJEES (2024) 15 (4): 298-306, ISSN 1995-6681, https://jjees.hu.edu.jo/files/Vol15/No4/JJEES_Vol_15_No_4_P9.pdf

Al-Zboon, K.K., Mansi, O.A. and Ammary, B.Y. (2024) Assessment of Rainwater Harvesting Management in Jordan, JJEES (2024) 15 (3): 156-161, ISSN 1995-6681, https://jjees.hu.edu.jo/files/Vol15/No3/JJEES_Vol_15_No_3_P2.pdf

Andayono, T. (2018) The Effect of Soil Density on Infiltration Rate in The Urban Development Area of Padang, Journal of Civil Engineering & Planning 20 (1), 1-5, http://journal.unnes.ac.id/nju/index.php/jtsp/index

CALRRD (Center for Agricultural Land Resources Research and Development) (2018) Soil Type Map of Galur District and Lendah District, Kulon Progo Regency, Special Region of Yogyakarta, Scale 1: 50,000, BBSDLP, Ministry of Agriculture of the Republic of Indonesia.

CSA (Central Statistics Agency) of Kulon Progo Regency (2022) Kulon Progo Regency in Figures 2022

David, Fauzi, and Sandhyavitri (2016) Analysis of Infiltration Rate on Plantation Land Cover and Industrial Plantation Forest (HTI) in the Siak River Basin (DAS), J. FTEKNIK 3 (2), October 2016.

DPWHEMR (Department of Public Works, Housing and Energy, Mineral Resources) & CV. CPK (CV. Cita Prima Konsultan) (2016) Preparation of Groundwater Basin Geometry Map and Groundwater Conservation Zone Map in Kulon Progo Regency, Final Report.

Duhita, A.D.P., Rahardjo, A.P., Hairani, A. (2021) The Effect of Slope on the Infiltration Capacity and Erosion of Mount Merapi Slope Materials, Journal of the Civil Engineering Forum 7 (1), 71-84, January 2021, DOI 10.22146/jcef.58350.

Effendi, A.T. (1985) Hydrogeological Map of Indonesia, Sheet VI: Pekalongan, Scale 1: 250,000, Directorate of Geological Environmental Management, Bandung.

Freeze, RA and Cherry, JA (1979) Groundwater, Prentice-Hall, Inc., Englewood Cliffs, New Jersey, 604 p.

Geological Agency (2011) Atlas of Indonesian Groundwater Basins, Ministry of Energy and Mineral Resources, Bandung, ISSN 987-602-9105-09-4.

Harimi (2018) The Effect of Vegetation Type on Infiltration Rate in the Geothermal Suum Area, Mesjid Raya District, Aceh Besar Regency as a Reference for Plant Ecology Course, Doctoral Dissertation, UIN Ar-Raniry Banda Aceh.

Horton, R.E. (1933) The Role of Infiltration in The Hydrologic Cycle, Trans. Amer. Geophys. Union, 14, pp. 446 – 460.

Horton, R.E. (1940) An Approach toward A Physical Interpretation of Infiltration Capacity, Soil Sci. Soc. Am. J., 5, 399–417.

Juliastuti and Suhendra, A. (2011) Study of Infiltration Capacity of Horton Method for Use of Biopores on Bina Nusantara University Campus based on Surface Runoff Discharge, ComTech 2 (2), 1343-1349, December 2011, Binus, Jakarta.

Juwita, R. and Santoso, I.B. (2019) Assessment of Soil Infiltration Capability in Balikpapan City, IPTEK Journal of Proc. Series, No. 5, ISSN 2354-6026, IConBMT ITS, Surabaya.

Kohnke, H. (1968) Soil Physics, McGraw-Hill Inc., New York.

KPRRDPA (Kulon Progo Regency Regional Development Planning Agency), 2024, DIY Soil Type Map.

Listyani, R.A.T. (2019) Groundwater Flow Model based on Geology, Hydrochemical and Stable Isotope at Central West Progo Dome, Dissertation, Padjadjaran University, Bandung.

Listyani, R.A.T. (2022) Introduction to Hydrogeology, Deepublish Publisher, 115 p., ISBN 978-623-02-4250-2, Yogyakarta.

Listyani, R.A.T. & Budiadi, Ev. (2018) Groundwater Occurrence Prediction using Regressions on Morphometric Variables in Upstream Progo Watershed, Yogyakarta, Indonesian Journal on Geoscience 5 (3), 265 - 276, DOI:https://doi.org/10.17014/ijog.5.3.265-276,http://ijog.geologi.esdm.go.id.

Listyani, RAT, Prabowo, IA, Suparta, W. (2023) Determination of groundwater recharge–discharge zone to support water resources in Galur–Lendah area, Indonesia, Journal of Water and Land Development 56 (I–III), 203–214, DOI: 10.24425/jwld.2023.143761, https://journals.pan.pl/dlibra/publication/143761/edition/126460/content

Maghfiroh (2020) Analysis of Community Forest Infiltration Rate in Ragang Village, Bajurm Tampojung Teggina, Waru District, Pamekasan Regency, East Java, Doctoral Dissertation, University of Muhammadiyah Malang.

Mohammed A.A., Falih, A.A., AL-Paruany, K., Maliki, A.A., Jasim, A.A. (2024) Study of the Water Quality in the Tigris River using Isotopic and Hydrochemical Techniques in South-Eastern Iraq, Jordan Journal of Earth and Environmental Sciences 15 (4): 250-256, https://jjees.hu.edu.jo/files/Vol15/No4/JJEES_Vol_15_No_4_P4.pdf

Noor, K. and Alzboon, K. (2021) WW treatment and reuse in Jordan, 10 years of development, Desalination and Water Reuse, 2021(238): 15–27.

Park, B.H., Joun, W.T., Ha, S.W., Kim, Y., Choi, H. (2022) A Study on Infiltration Process and Physicochemical Influence in the Unsaturated and the Saturated Zone of the Bottom Ashes from Thermal Power Plant, Economic and Environmental Geology 55 (1), 97-109, https://doi.org/10.9719/EEG.2022.55.1.97

Rahardjo, W., Sukandarrumidi, & Rosidi, H.M.S. (1977) Geological Map of Yogyakarta Quadrangle, Center for Geological Research and Development, Bandung.

Sakellariou-Makrantonaki, M., Angelaki, A., Evangelides, C., Bota, V., Tsianou, E. and Floros, N. (2016) Experimental determination of hydraulic conductivity unsaturated soil column, Procedia Engineering 162, 83–90.

Saltiel, T.M., Heitman, J.L. and Amoozegar, A. (2022) Comparison of infiltration test methods for soil health assessment, Journal of Soil and Water Conservation, 77 (6) 623-629, November 2022; DOI: https://doi.org/10.2489/jswc.2022.00178

Seyhan, E. (1990) Basics of Hydrology, Gadjah Mada University Press, Yogyakarta.

Sharief, S.M.V., Zakwan M. and Farhana S. N. (2023) Estimation of Infiltration Rate using a Nonlinear Regression Model, Journal of Water Management Modeling (JWMM) 31:C509, DOI: https://doi.org/10.14796/JWMM.C509

Sophocleus (2004) Groundwater Recharge, University of Kansas, United States.

Sugiyono (2022) Qualitative Research Methods, CV. Alfabeta, Bandung.

Van Bemmelen, R.W. (1949) The Geology of Indonesia, vol.1A, Martinus Nijhoff, The Hague, Netherland.

Yang, Y., Zhou, J., Xu, F., Xing, H. (2016) An Experimental Study on the Water-Induced Strength Reduction in Zigong Argillaceous Siltstone with Different Degree of Weathering, Advances in Materials Science and Engineering, Vol. 2016, Article ID 4956986, 12 pages, Hindawi Publishing Corporation, http://dx.doi.org/10.1155/2016/4956986

JJEES

JJEES (2025) 16 (3): 227-236
ISSN 1995-6681

Jordan Journal of Earth and Environmental Sciences

Sediments Transport Mitigation and Management in Wadi Shu’eib Dam

Radwan A. Al-Weshah [1, 2*], Khaled Smadi [3], Rakad Ta’any[4]

[1] *Department of Civil Engineering, The University of Jordan, Amman 11942, Jordan.*
[2] *Department of Civil Engineering, Faculty of Engineering and Technology, Al-Zaytoonah University of Jordan, Amman 11733, Jordan.*
[3] *Department of Civil Engineering, The University of Jordan, Amman 11942, Jordan.*
[4] *Faculty of Agricultural Technology, Al Balqa Applied University, Al-Salt 19117 Jordan.*

Received on September 30, 2024, Accepted on February 16, 2025

Abstract

Accumulation of sediments in dams is a significant problem that impacts the storage function of the dam. In Jordan, over 20% of the capacities of major dams are filled with sediment. This study aims to mitigate and manage sediment yield, as well as predict it based on peak flow at the Wadi Shu’eib Dam (WSD) catchment. The WSD has a capacity of 1.4 MCM in the Wadi Shu’eib catchment area in the Al-Balqa governorate. The Watershed Modeling System (WMS) and Soil and Water Assessment Tool (SWAT) models were employed to predict the runoff flood hydrograph and sediment yield of the catchment from 1985 to 2018. The rainfall stations at Wadi Shu’eib, Salt, South Shuna, and Hummar were utilized in the hydrologic modeling. The results indicated that the dominant land use is agricultural, characterized by loamy soil and steep slopes. The average annual precipitation over Wadi Shu’eib is 325 mm, with 60% evapotranspiration and 57 mm of surface runoff. The peak flow values for design storms with return periods of 25, 50, and 100 years were 158, 213, and 277 m3/s, respectively. The average annual sediment yield at the outlet of this dam is approximately 7.6 tons/ha. Four sediment mitigation measures are proposed to decrease the sediment deposited behind the dam. The results of the SWAT model indicated that reforesting 20 ha (about 1.5% of the catchment) would reduce sediment by 21%. Similarly, installing a hydraulic slurry dredge near the dam crest will decrease sediment by 38%. Furthermore, dry excavation of sediment during dry periods will lower the sediment by 40%. Moreover, if all proposed measures are implemented together, sediment removal could increase to 53%.

Keywords: Hydrology, Sediment Mitigation, WMS, SWAT, Wadi Shu’eib

1. Introduction

Jordan is one of the most water-scarce countries in the world, with estimated renewable water resources of less than 61 m^3 per capita annually, and 85% of the country receives less than 200 mm of rainfall per year (MWI, 2023). Given this acute water scarcity, artificial surface water bodies, including dams, are essential for securing residential and agricultural water supplies. Currently, Jordan operates 14 major dams with a combined capacity of approximately 280 million cubic meters (MCM) (JVA, 2021). In rural areas, where household incomes are generally lower, rainwater reservoirs have long served as a critical water supply system, supported by donor agencies and nongovernmental organizations promoting rainwater harvesting systems (FAO, 2011). This infrastructure plays a crucial role in enhancing the country’s resilience to fluctuating and often limited rainfall patterns.

Among the key challenges +- Jordan’s dam infrastructure faces is sedimentation, which refers to accumulating suspended particles that settle out of water due to gravity. This process, driven by erosion caused by rainfall and runoff, leads to sediment transport and deposition in dam reservoirs. The issue of sedimentation is particularly critical in Jordan, where more than 20% of the storage capacities of major dams are filled with sediments, significantly undermining their efficiency and operational longevity (Oroud, 2015; Al-Shibli et.al., 2017; MWI, 2023).

The accumulation of sediments in dam reservoirs reduces both storage capacity and operational efficiency, directly impacting water availability and management strategies. For example, the Wadi Shu’eib Dam (WSD), an earth-fill dam constructed in 1969, was initially designed with a storage capacity of 2.4 MCM. However, due to sedimentation and seepage, its current operational capacity stands at only 1.43 MCM—a reduction of over 40% (MWI, 2020). This significant loss underscores the urgency of adopting effective sedimentation management strategies, especially given the limited opportunities to construct new dams due to geographic and financial constraints.

Understanding and mitigating sedimentation in existing dams require a comprehensive examination of hydrological and sediment transport processes. Surface runoff, the primary driver of sediment yield in catchments, must be thoroughly studied to develop appropriate mitigation strategies. This entails hydrological modelling and analysing flood hydrographs for various design storms (Bani Baker et al., 2022).

Hydrological modelling tools, such as the Watershed Modelling System (WMS), have been widely used to

---

* Corresponding author e-mail: r.weshah@ju.edu.jo

simulate hydrological processes and provide essential tools for watershed delineation, calculations, and modelling (Daniel, 2011; Srinivas et al., 2018; AQUAVEO, 2021). For instance, Al-Weshah and El-Khoury (1999) applied the Hydrologic Engineering Centre (HEC-1) model to analyse and mitigate flood risks in Petra's catchment area. Their study demonstrated the effectiveness of flood mitigation measures, which reduced peak flow by up to 70% for storm events with return periods ranging from 2 to 200 years. Similarly, Aziz (2020) employed the WMS model to estimate annual runoff and peak flow at the Nazanin watershed in Iraq, achieving a mean annual runoff volume of approximately 8 MCM using the SCS method.

In addition to hydrological modelling, sedimentation studies often utilize the Soil and Water Assessment Tool (SWAT) to simulate and predict sediment yields. Developed by the USDA Agricultural Research Service and Texas A&M AgriLife Research, SWAT is a conceptual, physically-based model designed for long-term simulations of watershed processes. The model incorporates the Universal Soil Loss Equation (ULSE) to estimate soil erosion as a function of rainfall energy and other factors (Zeiger et al., 2021; Wischmeier and Smith, 1978). In Jordan, Shaheen (2017) conducted a study on sediment accumulation at King Talal Dam, using SWAT, estimating an annual sediment yield of 0.35 MCM. Similarly, Abu-Zreig and Bani Hani (2021) validated the SWAT model for simulating runoff in the arid Yarmouk River catchment.

This study aims to build upon these research findings by leveraging advanced hydrological and sediment modelling tools to address the sedimentation challenges at Wadi Shu'eib Dam. Given its strategic importance within Jordan's water management system, ensuring the dam's operational sustainability is essential for addressing the country's ongoing water resource challenges. By understanding sediment dynamics and proposing effective mitigation measures, this research seeks to enhance the dam's storage capacity, optimize its operations, and contribute to the broader goal of sustainable water resource management in Jordan.

1.1 Research Context and Objectives

The Wadi Shu'eib Dam catchment, located in the Lower Jordan River basin, encompasses approximately 176 km² in the Al-Balqa governorate, west of Amman, as shown in Figure 1. The catchment features steep slopes and predominantly agricultural land, with loamy soils contributing to sedimentation risks. Limited studies have addressed sediment yields and their management in this area.

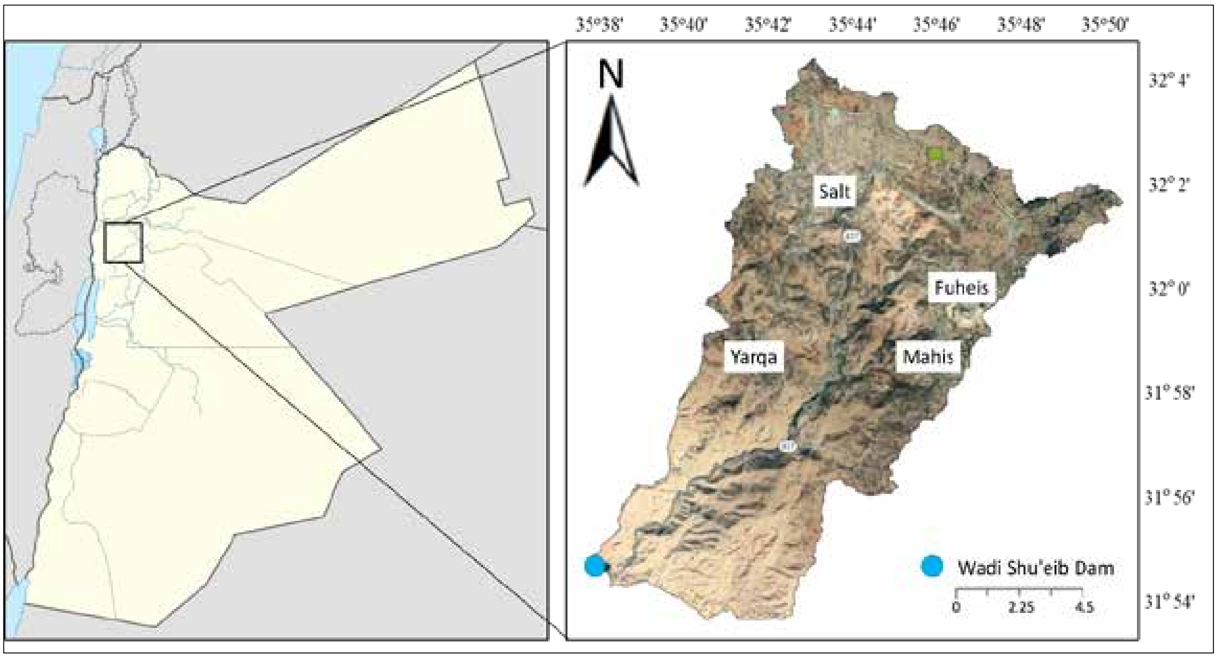

Figure 1. Wadi Shu'eib catchment area and dam location

This research aims to address the sedimentation challenges in WSD by:

- Developing a hydrological model, using WMS to estimate surface runoff and flood hydrographs for design storms with return periods of 25, 50, and 100 years.
- Predicting sediment yield inflow to the reservoir, using the SWAT model.
- Proposing effective sediment mitigation techniques to enhance dam performance.

2. Methods and Tools

The methodology employed in this research includes data collection, hydrologic modelling using the Watershed Modelling System (WMS), sediment yield analysis using the Soil and Water Assessment Tool (SWAT), and the development of mitigation strategies for sediment accumulation.

The WMS version (WMS 11.1) was chosen due to its user-friendly interface and robust hydrologic modelling capabilities, particularly its integration with various runoff estimation methods such as the Curve Number method and its ability to handle complex watershed delineation and terrain analysis. However, the specific version of WMS used in this study needs to be clarified.

The SWAT model version (ArcSWAT 2012 for ArcGIS 10.5) was selected for its comprehensive simulation of watershed processes, including surface runoff, sediment yield, and nutrient transport over long time scales. SWAT is well-known for its applicability in diverse catchments, both gauged and ungauged, and its compatibility with GIS for spatial data integration.

2.1 Data Collection

Data for the Wadi Shu'eib catchment were collected to support hydrological and sediment modeling. The data types and sources included:

- Digital Elevation Model (DEM) used for watershed delineation and slope analysis, Figure 2a.
- Land Use and Cover Maps used to classify and map the land cover categories, Figure 2.b.
- Watershed Characteristics, that is, information on the area, slope, and elevation.
- Soil Maps that Provided data on the distribution and properties of soil types, Figure 2.c.
- Rainfall Data that functioned as historical rainfall records from four stations (Salt, Wadi Shu'eib, Hummar, and South Shuna) and were collected for the period 1985 to 2018.

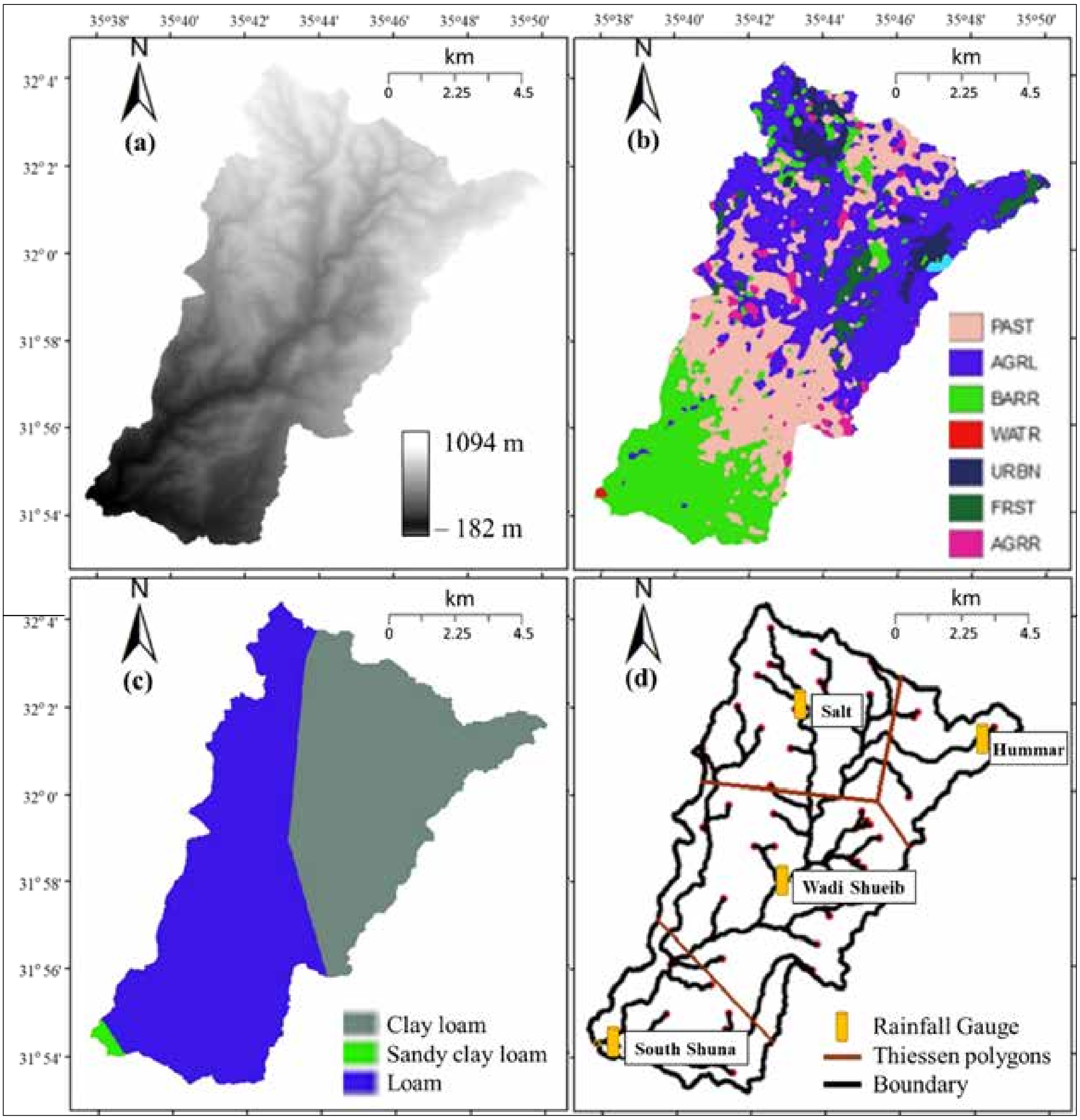

Figure 2. (a) Elevation, **(b)** Land use **(c)** Soil, and **(d)** Thiessen polygons maps of Wadi Shu'eib by WMS 11.1

3. Description of the Study Area

3.1 Location

The Wadi Shu'eib Drainage (WSD) catchment is located at the Lower Jordan River catchment within Al-Balqa Governorate, west of Amman, Jordan. It covers an area of approximately 176 km² at the outlet of WSD. Geographically, it lies between latitudes 31°50' to 32°02' N and longitudes 35°35' to 35°50' E. The catchment has a generally rectangular shape, encompassing Salt City and the towns of Fuheis, Mahis, Yarqa, and Wadi Shu'eib (MWI, 2020), as depicted in Figure 1.

The WSD catchment is characterized by steep terrain, with elevations, ranging from 376 meters below mean sea level in the southwest to 1,100 meters above mean sea level in the northeast. Based on the Digital Elevation Model (DEM), generated using the Watershed Modelling System (WMS), the average elevation is approximately 560 meters, and the average slope is 0.223 m/m. The DEM, with a resolution of 30×30 meters, is presented in Figure 2(a).

3.2.1 Land Use Distribution

A digitized land use map obtained from the Ministry of Water and Irrigation (MWI, 2020) reveals significant variations across the catchment. Figure 2(b) illustrates the land cover distribution. The most dominant land use is Agricultural Land-Generic (AGRL), occupying nearly 46% of the total area, mainly in the upper half of the wadi in the north and east. Row crop land use covers a mere 0.5%.

Pastures (PAST) and barren lands (BARR) dominate the lower section of the wadi. Pastures, the second most common land use, cover more than 30% of the area, while barren lands account for 18%. Residential areas, mixed forests, and water bodies are scattered throughout the watershed, constituting less than 6% of the total area. Each land use type varies in terms of land cover management factors, curve numbers, and Manning's values for overland flow.

3.2.2 Soil Type Distribution

Soil maps from the Ministry of Water and Irrigation (MWI) show that the WSD catchment primarily consists of three soil types: loam, clay loam, and sandy clay loam, as shown in Figure 2(c). Loam is the most prevalent soil type, covering approximately 55.8% of the total area, mainly in the western half of the wadi. Clay loam makes up around 44% and is concentrated in the eastern half. Sandy clay loam, which constitutes less than 0.2% of the area, is primarily found in the southwestern region.

3.2.3 Climate and Rainfall

The climate in the WSD catchment is a combination of Mediterranean and desert climates, characterized by low rainfall and high evaporation rates, with 92.2% of the rainfall evaporating. The average daily minimum temperature in January is around 12°C, while the average daily maximum temperature in July exceeds 40°C. Relative humidity ranges from 38% in June to 68% in January (MWI, 2020).

- Intensity-Duration-Frequency (IDF) curves were used to predict rainfall intensity for different storm durations.
- Thiessen polygon networks were generated for four rainfall stations—Salt, Wadi Shu'eib, Hummar, and South Shuna—using WMS 11.1, as shown in Table 1 and Figure 2(d). Rainfall data from 1985 to 2018 were analysed for 25-, 50-, and 100-year design storms (MWI, 2020).
- The estimation of peak discharge was conducted using the WMS software version 11.1 through the following steps (Figure 3):
- Delineating the catchment area: the catchment area was delineated and subdivided into smaller sub-catchments to enhance the accuracy of the analysis (Table 2).
- Generating synthetic hydrographs: Synthetic hydrographs for 50 and 100-year design storms, utilizing the HEC-1 model integrated within the WMS software.
- Calculating the peak flow rates: The peak flow rates associated with these synthetic hydrographs were calculated to determine the maximum discharge for each return period.

Table 1. Rainfall stations coordination and Thiessen polygons areas with 100-year design storm precipitation

Rainfall station	JTM - N	JTM - E	Elv. (m) (Z)	% of the total area	Design storm precipitation (mm)		
					25 yr	50 yr	100 yr
Wadi Shu'eib	31° 58'	35° 43'	317	42%	87	104	122
Salt	32° 2'	35° 44'	784	28%	112	123	133
South Shuna	31° 54'	35° 38'	-169	17%	35	39	43
Hummar	32° 1'	35° 49'	923	13%	102	113	123
Average precipitation (mm)					87	99	112

Table 2. Sub-catchments characteristics

Sub-catchment	Mean Elevation (m)	Longest path (m)	Area (ha)	No. of HRUs
1	962	5921	867	9
2	949	4909	449	13
3	853	5608	1036	8
4	909	9886	1157	3
5	699	3318	268	8
6	840	6378	590	6
7	749	6741	1185	14
8	591	4330	287	6
9	678	5760	594	8
10	679	5224	728	4
11	571	5323	446	13
12	409	1036	37	7
13	595	4808	449	13
14	415	2311	195	14
15	366	4113	343	8
16	557	7043	987	10
17	592	16035	2252	7
18	275	6784	902	7
19	-109	2234	56	12
20	116	10352	1170	7
21	172	3978	391	4
22	309	10120	1052	6
23	43	8684	1101	4

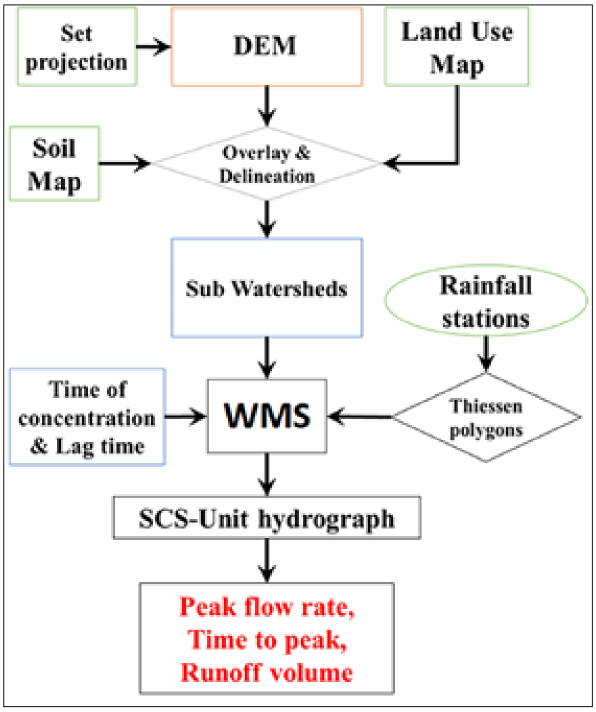

Figure 3. WMS model flowchart

3.4 Estimation of the transported sediments

The sediment yield analysis, using the SWAT model, as summarized in Figure 4, was carried out through the following steps:

1. Watershed Delineation: A DEM grid of the WSD watershed was loaded into the model to define the stream network, flow direction, and accumulation areas. Since the objective of this research is to estimate sediment yield, WSD was selected as the outlet of the catchment. The delineation process involved the following steps:
    a. The projection system used was Jordan Transverse Mercator (JTM), which is commonly applied to geographic maps in Jordan.
    b. The study area boundaries were defined using a catchment shapefile. Flow direction and accumulation areas were then identified to assist the model in creating stream networks and outlets.

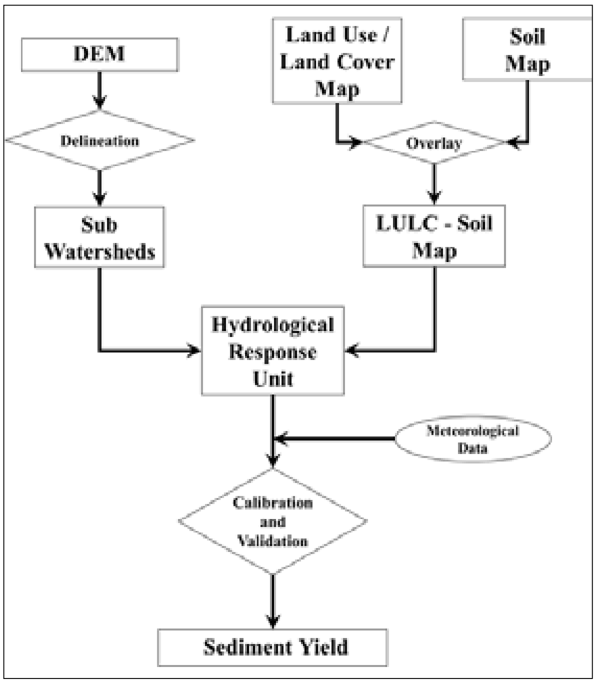

Figure 4. SWAT model flowchart

c. The WSD was identified as the outlet of the catchment, determining the effective sub-catchments, contributing to sediment formation. Parameters such as sub-catchment area, average slope, and stream lengths were generated. The sub-catchment distribution layout is displayed in Figure 5.

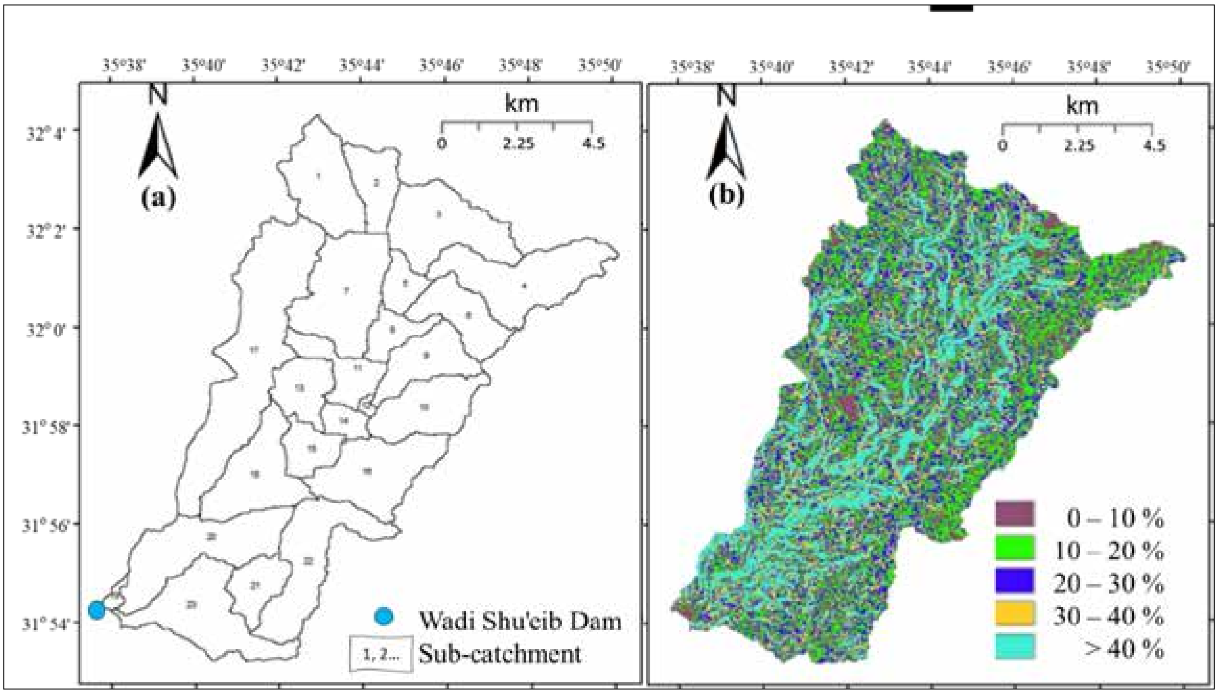

Figure 5. SWAT model **(a)** Sub-catchments and **(b)** Slopes maps of WSD

3. Hydrological Response Units (HRUs) are distinct areas within the sub-catchment that possess unique combinations of land cover, soil types, and slopes (Neitsch et al., 2009). The HRUs for the watershed were defined as follows:
   a. The land use raster map was loaded, and the land use data were reclassified using a text file that specified the properties of the land use categories.
   b. The soil raster map was imported, and a soil text file was inserted to link the map's soil types with those in the SWAT model.
   c. Slopes were categorized into five distinct classes, representing various slope ranges, as illustrated in Figure 3b.
   d. The land use, soil, and slope maps were overlaid using the "overlay" command, and the HRUs were then created by selecting the "define HRU" command.

3.5 Investigation of sediment mitigation and management techniques

An assessment of the technical feasibility of proposed mitigation techniques and the development of ranking criteria for the selection of priority actions were considered to draw the sediment management plan (Yang and WMO, 2003; GIZ, 2021). Sedimentation significantly impacts the efficiency and storage capacity of Wadi Shu'eib Dam. Effective mitigation strategies are crucial to maintain its functionality. This section summarizes the evaluation of mitigation techniques, prioritization criteria, and a comprehensive sediment management plan.

3.5.1 Assessment of Proposed Mitigation Techniques

The evaluation focused on the following factors:

- Technical Feasibility: Suitability based on site-specific conditions (topography, soil type, hydrology).
- Sediment Removal Efficiency: Effectiveness in reducing sediment accumulation.
- Implementation and Operational Requirements: Complexity and technical expertise are needed.
- Economic Viability: Cost analysis for setup and long-term maintenance.
- Environmental Impact: Preference for eco-friendly solutions.

3.5.2 Mitigation Techniques Considered

1. Reforestation: Planting trees on barren land to stabilize soil and reduce sediment yield by 21% (cost: 60,000 JOD).
2. Hydraulic Dredging: Removing underwater sediment near the dam crest, reducing sediment by 38% (cost: 1.4 million JOD).
3. Dry Excavation: Sediment removal during dry periods, reducing 40% of sediment (cost: 1.27 million JOD).
4. Mixed Practices: Integrating all techniques for a 53% reduction (cost: 2.7 million JOD).

3.5.3 Ranking Criteria for Priority Actions

Key criteria for prioritization included:

- Sediment reduction efficiency
- Cost-effectiveness
- Environmental sustainability

- Ease of implementation
- Operational and maintenance requirements

3.5.4 Integration into a Sediment Management Plan

An integrated plan combining multiple techniques was developed to optimize sediment removal and ensure long-term sustainability. This approach balances technical feasibility, economic factors, and environmental preservation to effectively address sedimentation challenges at Wadi Shu'eib Dam.

4. Results and Discussion

4.1 Hydrological Modelling and Analysis

The hydrological analysis conducted using the HEC-1 model within the Watershed Modelling System (WMS 11.1) provides critical insights for flood risk management in the study area. Peak flow rates were computed for design storms with return periods of 25, 50, and 100 years, yielding values of 158, 213, and 277 m³/s, respectively. The SCS hydrographs at the outlet point, as illustrated in Figure 6, demonstrate a consistent time to peak of 16 hours for all three design storms. Runoff volumes for these events were estimated at 4.3, 5.6, and 7.2 million cubic meters (MCM), respectively.

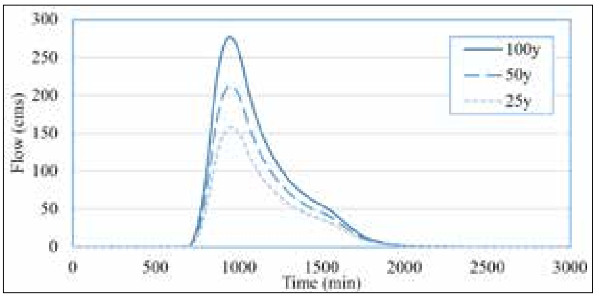

Figure 6. SCS flood hydrographs for 25-, 50- and 100- return years by WMS 11.1

Given the absence of historical flood data due to the ungauged nature of the catchment, these modelled flow rates are vital for establishing baseline flood risk assessments. The computed peak flows suggest a substantial potential for extreme flood events, particularly under the 100-year storm scenario. Climate change is expected to exacerbate such risks by increasing the frequency and intensity of extreme weather events. Consequently, understanding the capacity of existing infrastructure, such as the dam, becomes paramount.

The dam at the outlet was evaluated for its potential to handle runoff from these design storms. Based on the WMS analysis, the dam has a width of approximately 760 meters and a current height of 31 meters, with a possible extension to 40 meters. The dam height cross-section is shown in Figure (7a), while the relationship between dam height and width is depicted in Figure (7b). Given the estimated runoff volume from the 100-year storm (7.2 MCM) and the peak flow rate (277 m³/s), the current dam height of 31 meters may be insufficient to fully mitigate the flood risk from such an extreme event. Raising the dam height to 40 meters could provide a more robust flood control solution, although further detailed hydraulic analyses would be required to confirm its adequacy.

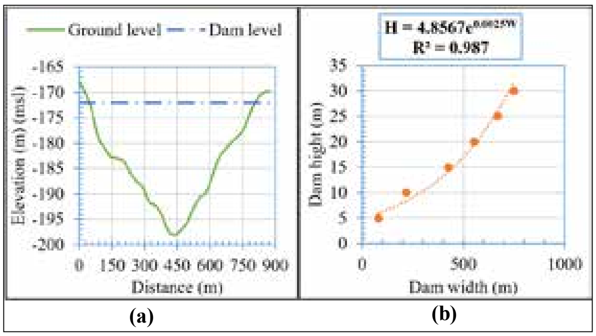

(a) (b)

Figure 7. (a) Dam height cross-section **(b)** The relation between dam's height and width

The study underscores the critical importance of integrating accurate hydrological modelling and infrastructure capacity assessments to enhance flood risk management strategies in ungauged catchments. In the face of potential climate change impacts, proactive measures, such as increasing dam capacity and implementing additional flood mitigation strategies, will be essential for safeguarding the study area.

4.2 Practical Implications for Water Management and Policy Recommendations

- Flood Mitigation:

The computed peak flow rates for 25, 50, and 100-year design storms highlight a growing necessity for comprehensive flood management strategies. Authorities should develop comprehensive flood management strategies, update flood hazard maps, and implement early warning systems to reduce risks from extreme runoff events.

- Dam Capacity Assessment:

The current 31-meter dam may be insufficient for handling the 100-year storm runoff of 7.2 MCM and 277 m³/s. Increasing the height to 40 meters or adding an auxiliary spillway is recommended.

- Climate Change Adaptation:

Despite the absence of historical data, the threat of more intense storms requires climate-resilient infrastructure, including design updates and nature-based solutions.

- Integrated Watershed Management:

Erosion control and upstream retention strategies are essential due to the catchment's steep slope and length. Collaboration between agencies is crucial for effective implementation.

- Data Collection and Monitoring:

Establishing a hydrological monitoring network is imperative to collect real-time data for better calibration of hydrological models and more accurate predictions of flood behavior. The lack of historical data in the study area hinders the development of precise water management plans. Investment in automated monitoring stations would bridge this gap.

4.2 Sediment transport analysis

4.2.1 Sediment yield

The Watershed Study Area (WSD) receives an average annual precipitation of 325 mm, equating to more than

57.2 MCM/year, with 60% (188 mm/year) lost through evapotranspiration. Calibration of the SWAT model was essential to improve accuracy, with the curve number (CN) being the most sensitive parameter, adjusted from 87 to 70 to better match observed conditions.

Following calibration, the model estimated an average annual surface runoff of 57.34 mm (10.7 MCM/year). During the 1985-2018 simulation period, the average sediment yield at the dam outlet was 7.6 tons per hectare. Figure (8) shows the distribution of yearly sediment yields, highlighting significant seasonal variations, with peak sediment yields occurring in winter (January, February, and December).

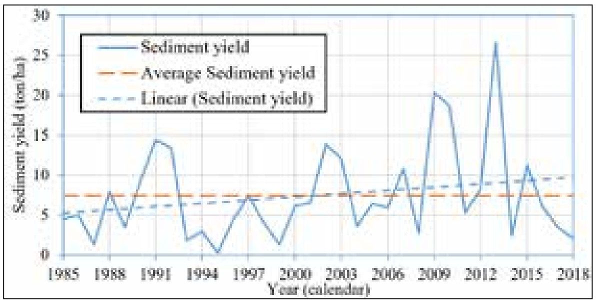

Figure 8. Annual sediment yield fluctuation at WSD (SWAT, 2020)

The results revealed substantial interannual variability in sediment yield, with a maximum of 26.6 tons/ha in 2013 and a minimum of 0.33 tons/ha in 1995. Contributing factors include:

- Climate Patterns: Variations in rainfall intensity and frequency impact runoff and sediment transport.
- Extreme Weather Events: Intense storms, like those in 2013, lead to higher sediment yields.
- Soil Conditions: Changes in soil moisture and saturation influence runoff and sediment mobilization.
- Land Use Changes: Modifications in land cover or agricultural practices contribute to increased erosion.

A linear increase in sediment yields every 10 years suggests progressive land degradation, driven by factors such as deforestation, agricultural expansion, and urbanization. Climate change, including more intense rainfall, likely exacerbates sediment transport.

A strong correlation between surface runoff and sediment yield was found, represented by the following equation Figure (9):

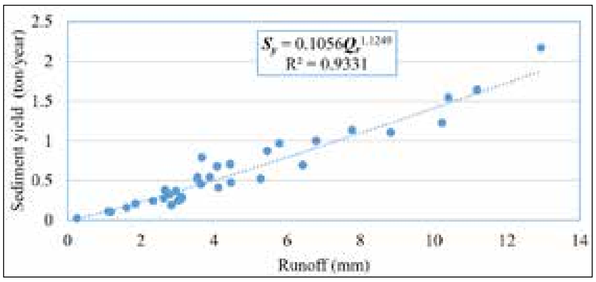

Figure 9. Sediment yield (S_y) and surface runoff (Q_r) correlation

Sy = 0.1056 Qr^1.1249

Where:

Sy = Sediment yield (tons/ha)

Qr = Runoff depth (mm)

$R^2 = 0.9331$

This equation serves as a tool for sediment management strategies, such as:

- Designing Sediment Traps: Estimating sediment volumes based on runoff to guide retention structure design.
- Dam Operation Adjustments: Anticipating sediment inflows for maintenance and flushing schedules.

The Model calibration involved adjusting sensitive parameters, notably the curve number (CN). Performance metrics, including Nash-Sutcliffe Efficiency (NSE), coefficient of determination (R^2), and percent bias (PBIAS), indicated satisfactory performance with NSE values above 0.75 and R^2 above 0.9 for both runoff and sediment yield.

From these findings, several sediment management strategies are recommended:

- Catchment Rehabilitation: Reforestation and soil conservation measures to reduce runoff and sediment yield.
- Structural Controls: Building check dams, silt fences, and vegetative buffers to mitigate sediment transport.
- Monitoring and Adaptive Management: Ongoing monitoring to refine sediment control practices based on observed trends.

In conclusion, the SWAT model provided critical insights into sediment dynamics and their relationship with surface runoff. The results highlight the need for integrated catchment management and effective sediment control to ensure the sustainability of water resources and dam operations.

4.2.2 Sediment Mitigation Measures

This study shows that the west-south areas of the catchment experience the highest surface runoff and sediment yield due to their steep slopes and elevated topography. The sediment management options proposed by GIZ (2021) include:

- Reforestation: Reforestation of approximately 20 ha around the dam could reduce sediment inflow by 21%, lowering the Curve Number (CN) to 65. While it takes years to mature, its long-term impact is positive, but monitoring is needed to address climate and land-use challenges.
- Hydraulic Dredging: Installing a hydraulic dredge near the dam crest would reduce sediment by 38% in about 6 ha. It offers quick results but has high operational costs and could disturb aquatic ecosystems. An environmental impact assessment (EIA) is needed before implementation, along with continuous monitoring downstream.
- Excavation: Excavating 9 ha around the dam would reduce sediment by 40%. This method is effective

but labor-intensive and costly, with potential local environmental impacts, such as soil disturbance. These impacts must be carefully considered during the planning stage.

- Combined Measures: Using all three techniques together could remove up to 53% of sediment. This integrated approach requires careful coordination of resources and time. Details of the mitigation measures are shown in Tables (3) and Figure (10).

Table 3. Proposed sediments removal methods at WSD

Mitigation method	Sediment yield with mitigation (ton/ha)	Sediment reduced (ton/ha)	Area covered (ha)	Removal %
Forestation	6.0	1.6	20	21%
Hydraulic dredging	4.7	2.9	6	38%
Dry excavation	4.6	3.0	9	40%
Mixed	3.6	4.0	35	53%

Figure 10. Dry excavation and hydraulic dredging proposed areas (based on GIZ)

- Feasibility and Environmental Considerations

A cost-benefit analysis is essential to evaluate both financial and environmental costs. Reforestation has lower upfront costs but takes time, while dredging and excavation provide quicker results at a higher cost. Complementary strategies, like check dams, terracing, or upstream erosion control can enhance sediment management and reduce dependence on dredging and excavation.

- Environmental Impacts

Hydraulic dredging may disrupt aquatic ecosystems, so an EIA is necessary. Reforestation could be affected by climate and land-use conflicts, requiring careful planning.

- Maintenance and Monitoring

Sediment management requires ongoing maintenance and monitoring. A program should be established to assess the effectiveness of all measures, ensuring the survival of reforested trees and periodic interventions for dredging and excavation.

In conclusion, combining these techniques with complementary strategies offers the most effective long-term solution for managing sediment yield in the catchment area.

5. Conclusions and recommendations

5.1 Conclusions

A sediment mitigation and management analysis was conducted for the WSD catchment by combining the hydrologic model WMS 11.1 and the sediment SWAT model. The most dominant land use in the WSD catchment is agricultural, characterized by loamy soil and steep slopes. Based on hydrological and sediment modeling, the following conclusions can be drawn:

- Peak flow rates for design storms were computed using the WMS 11.1 model with the SCS hydrographs. The peak flow rates were estimated as 158, 213, and 277 m^3/s, respectively.
- Sediment yield in the WSD catchment was estimated using the SWAT model. The results show that, during the simulation period (1985-2018), the average sediment yield at the outlet of the dam was 7.6 tons, with sediment yield increasing over time.
- The relationship between sediment yield and runoff depth can be modeled using a power equation with a high correlation coefficient.
- Various mitigation techniques were investigated to control sediment transport. Reforestation, dry excavation, hydraulic dredging, and mixed practices were found to reduce sediment by 21%, 40%, 38%, and 53%, respectively.
- However, conservative management practices, such as the construction of check dams, terraces, and contour tillage, should be implemented in the catchment to reduce sediment yield.

5.2 Recommendations

1. A combined approach is recommended for effective sediment management due to the complementary benefits of:

- Reforestation: Stabilizes soil and reduces runoff on steep slopes for long-term erosion control.
- Dry Excavation: Efficient removal of accumulated sediment in dry dam areas.
- Hydraulic Dredging: Immediate sediment removal near the dam crest, restoring storage capacity. This integrated approach balances immediate sediment removal with long-term sustainability and reduces reliance on costly single methods

2. To address the risks posed by climate change, including increased storm intensity and prolonged droughts, we need to:

- Enhance reforestation for slope stability and runoff control.
- Construct check dams and terraces to manage extreme rainfall events.
- Utilize climate-resilient vegetation to maintain stability in drought-prone areas.

3. Implement vegetation restoration, contouring tillage, and construction terraces to minimize erosion across the catchment.

4. Install sediment gauges at WSD for real-time monitoring and conduct comprehensive studies on sedimentation across Jordan's dams to sustain water storage capacities amid changing climate conditions.

Acknowledgement

The authors sincerely thank the Deanship of Scientific Research at the University of Jordan for their partial financial support, making this study possible. They also appreciate the valuable insights and assistance provided throughout the research.

References

Abu-Zreig, M., and Hani, L. B. (2021). Assessment of the SWAT model in simulating watersheds in arid regions: Case study of the Yarmouk River Catchment (Jordan). Open Geosciences, 13(1), 377–389.

Al-Shaer, I. (2018). Surface Water Modeling and Management for Wadi Shu'eib Catchment. Unpublished master's thesis, The University of Jordan, Amman, Jordan.

Al-Shibli, F., William A. Maher, Ross M. Thompson (2017). The Need for a Quantitative Analysis of Risk and Reliability for Formulation of Water Budget in Jordan, JJEES, Volume 8, (Number 2), Jordan.

Al-Weshah, R. A., and El-Khoury, F. (1999). Flood Analysis and Mitigation for Petra Area in Jordan. Journal of Water Resources Planning and Management, 125(3), 170–177.

AQUAVEO. (2021). AQUAVEO – WMS. From: https://www.aquaveo.com, visited on 15 September 2023.

Aziz, Y. (2020). Estimation of annual runoff and peak flow at Nazanin catchment in Erbil, Kurdistan region using different approaches. Iraqi Geological Journal, 53(2E), 96–116.

Bani Baker, M., et al., Stabilization of sandy soils by bentonite clay slurry at laboratory bench and pilot scales. 2022. 12(12): p. 1922.

Chow, V., Maidment, D., and Mays, L. (1988). Applied Hydrology (1st ed.). McGraw-Hill Science/Engineering/Math.

Daniel, E. B. (2011). Watershed Modeling and its Applications: A State-of-the-Art Review. The Open Hydrology Journal, 5(1), 26–50.

FAO. (2000). Soil Erosion by Water, Rome: Food and Agriculture Organization.

FAO. (2011). AquaStat: Jordan Country Fact Sheet.

GIZ. (2021). Integrated sediment management Guidelines and good practices in the context of the Water Framework Directive.

Jain, S. K. and Singh, V. P., (2023). Estimation of Specific Yield Using Laboratory Method and Empirical Approach" published in the Journal of Hydrology.

JVA-Jordan Valley Authority Annual Report (2021).

MWI- Ministry of Water and Irrigation Annual Report (2020).

MWI- Ministry of Water and Irrigation Strategy (2023).

Oroud I. (2015). Water Budget Assessment for a Typical Watershed in the Karak Plateau, Jordan, JJEES, Volume 7, (Number 2), Jordan.

Neitsch, S. L., Arnold, J. G., Kiniry, J. R. and Williams, J. (2009). Soil and Water Assessment Tool Theoretical Documentation. Texas: Texas A and M University.

Shaheen, M. (2017). Accumulation of Sediments at King Talal Dam. Unpublished master thesis, The University of Jordan, Amman, Jordan.

Srinivas, R., Singh, A. P., and Deshmukh, A. (2017). Development of a HEC-HMS-based watershed modeling system for identification, allocation, and optimization of reservoirs in a river catchment. Environmental Monitoring and Assessment, 190(1).

Williams, J. R. (1975). Sediment Routing for Agricultural Watersheds. Journal of the American Water Resources Association, 11(5), 965–974.

Wischmeier, W. and Smith, D. (1978). Predicting Rainfall-Erosion Losses: A Guide to Conservative Planning. Maryland: United States Department of Agriculture.

Yang, X. and World Meteorological Organization (2003). Manual on Sediment Management and Measurement. Secretariat of the World Meteorological Organization.

Zeiger, S. J., Owen, M. R., and Pavlovsky, R. T. (2021). Simulating nonpoint source pollutant loading in a karst catchment: A SWAT modeling application. Science of The Total Environment, 785, 147295.

JJEES

Jordan Journal of Earth and Environmental Sciences

JJEES (2025) 16 (3): 237-246
ISSN 1995-6681

Characterization and Evaluation of Clay Samples Against Bacterial Pathogens

Mirvat Abo Zainab[1], Mariam Shaheen[1], Hoda Yusef [2], Jamilah Borjac[1*]

[1]*Department of Biological Sciences, Faculty of Science, Beirut Arab University, Beirut, Lebanon.*
[2]*Department of Botany and Microbiology, Faculty of Science, Alexandria University, Egypt.*

Received on March 14, 2024, Accepted on February 19, 2025

Abstract

The rise of antimicrobial resistance (AMR) necessitates the development of new antimicrobial agents. This study explores the antibacterial properties of thirteen clay samples (S1-S13) from diverse geological locations against S. aureus, S. epidermidis, E. coli, K. pneumoniae, and P. aeruginosa using the disc diffusion method. Bulk and mineral suspensions of the most active clay leachate samples were then tested for their growth-inhibiting activities against the tested pathogens. Chemical analysis, conductivity, pH measurements, and quantification of iron, aluminium, silver, and copper in selected samples with strong antibacterial effects were performed. They were evaluated and correlated with their antibacterial activities. Inhibition ranges were 60-90% for bulk minerals and 15-65% for mineral suspensions. S2, S6, and S8 clay leachates exhibited significant bactericidal effects, with S8 being the most active. Their activity decreased after three months. Elemental analysis revealed silicon, iron, and aluminium as crucial components. Modified clay samples with hemoglobin (Hb) and sodium borohydride (NaBH4) increased antibacterial activity. Notably, direct contact between clay mineral solutions and bacterial cells was just as successful as dialysis tube separation. These results suggest the potential of clay minerals as alternative agents against AMR pathogens, emphasizing the need for further research into their mechanisms and clinical applications.

Keywords: *Antibacterial Activity, Elemental Analysis Clay, and Clay Leachates*

1. Introduction

The surge of human illnesses that are antibiotic-resistant spurred the investigation into alternative antibacterial agents (Friedlander et al., 2015; Lemire et al., 2013). Conventional antibiotics that affect DNA replication, protein synthesis, and cell wall production induce antimicrobial resistance (AMR) (Walsh, 2000). Diverse bacteria have derived resistance to numerous first-line and last-resort antimicrobials as a result of the selective pressure of antibiotic exposure in medicine and animal husbandry (Bartlett et al., 2013; Gross, 2013; Michael et al., 2014; Spellberg & Gilbert, 2014). The group of microorganisms known as "ESKAPE" (Enterococcus faecalis, Methicillin-resistant Staphylococcus aureus, Klebsiella pneumoniae, Acinetobacter baumannii, Pseudomonas aeruginosa, and Escherichia coli) is generally correlated with the development of multi-drug resistance and virulence (Kirsner, 2016). The O'Neill study predicted that by 2050, AMR might cause 10 million annual deaths globally (O'Neill, 2014). This suggests significant worries about the paucity of innovative antimicrobial medicines under development for different regulatory and economic reasons (Piddock, 2012).

Clays have been applied for curative purposes for decades; however, their practices and reported health advantages are limited (Carretero, 2002; Ferrell, 2008). "Clay" is attributed to minerals of any sort that are less than 2 µm in size. They include smectite, illite, and kaolinite, which, once hydrated, give a massive surface area (100′s m^2/g), allowing for cation exchange. Only a few clays have been noted to possess potent antibacterial activity against a collection of human ailments (Azmi et al., 2021; B. Williams et al., 2008; Morrison et al., 2014; Williams et al., 2011). The French green clay was used in the treatment of Buruli ulcer, a necrotizing cutaneous infection caused by Mycobacterium ulcerans (Williams et al., 2014). Antibacterial potency of clay leachates was also shown against Escherichia coli and methicillin-resistant Staphylococcus aureus (MRSA). The clay deposits can come from hydrothermally changed volcaniclastic settings, either altered pyroclastic material or bentonite, i.e., volcanic ash. However, each deposit is mineralogically unique. Some clays were also used to treat cancer (Cervini-Silva et al., 2016), dermatitis (Fowler, 2001; Sandri et al., 2014), irritable bowel syndrome (Ducrotte et al., 2005), kidney diseases (Zhang et al., 2009), detoxification (Williams et al., 2009), and even many other purposes (Moosavi, 2017).

Clays display a collection of distinctively desirable qualities that could work in their favor for AMR applications. They are widespread and are considered to operate through mechanisms in bacteria that have not yet developed resistance (Williams et al., 2014). Uncertainty surrounds the methods through which some clays appear to be antibacterial. These antibacterial actions may be related to direct contact between the charged surfaces of the clay grains and the bacterial cell surface, resulting in cell lysis. The bacterial cell membrane may also become more permeable when exposed to reactive cations, such as aluminium ion ($Al^{3+)}$ and iron ion (Fe^{2+}), in an aqueous solution, leading to the production of production of reactive oxygen species (ROS) (Londono et al., 2017;

---

* Corresponding author e-mail: j.borjac@bau.edu.lb

Morrison et al., 2016; Otto & Haydel, 2013; Zhao et al., 2005).

Many of the antimicrobial clays that have already been characterized evolved in volcaniclastic settings that have undergone hydrothermal alteration (Williams et al., 2011) such as the Eifel region of West Germany (Zarate-Reyes et al., 2018), the Amazon Rainforest (Londono & Williams, 2016), and the Cascade Mountain range in Douglas County, Oregon (Morrison et al., 2016). Even though the origin of the green clay, known as Argiletz (also known as Illite or Sea Clay) and/or associated clay combinations, is a trade secret, it is most likely from the Massif Central area of France, close to the Chaîne des Puys or the Cantal stratovolcano (Incledion et al., 2021).

Studies on the antibacterial properties of clays shows that the Arab region is scarce, However, Jordanian soils demonstrated significant potential to inhibit certain pathogenic bacteria (Ibbini et al., 2018). In this study, we attempted to bridge this knowledge gap by characterizing the geological and biological properties of 13 soil samples, obtained from Arabic regions including Saudi Arabia, Egypt, Palestine, Syria, Jordan, and Lebanon, and we assessed their antibacterial activity. Given their historical usage as traditional "healing clays," these soil samples may have distinct antibacterial characteristics that need further examination. By assessing their antibacterial activity against MDR organisms, this study adds to the rising interest in natural clay-based medicines as a viable solution to worldwide AMR epidemic.

2. Materials and Methods

2.1 Clay Samples and Their Processing

Table 1 summarizes the sources of the clay samples. Samples were collected at 0–20 cm depth using a 1.45 cm diameter soil core. Samples were packaged in airtight plastic bags, labelled as S1-S13. After that, the samples were air-dried at room temperature and gently disaggregated, using a sterile mortar and pestle to achieve a smooth consistency, allowing them to pass through a 250 mm sieve (Haydel et al., 2007). Fine bulk mineral particles were collected and, then, stored in plastic bags at 4ºC. Before use, all bulk clay mineral samples were sterilized in an autoclave (121°C, 15 psi (pounds per square) inch for 1 hr) to remove any microbial contamination.

Table 1. Clay sample locations and coordinates

Sample reference number	Region and Location of sampling	Coordinates (Decimal Degrees)
S1	Makka (Saudi Arabia). Sample collected from the entrance of Mecca, near the main road at the boundary of the Haram area.	21.3639278, 39.6705242
S2	Madina East area (Saudi Arabia)	24.4687291, 39.6426387
S3	Madina West area (Saudi Arabia)	24.4635445, 39.5647931
S4	Madina Seven Mosques (Saudi Arabia)	24.4768649, 39.5962940
S5	Madina Ohod Mountain (Saudi Arabia)	24.5231679, 39.6268699
S6	Madina Awaly area (Saudi Arabia)	24.7368447, 39.4605876
S7	Alkodus (Palestine)	31.7705626, 35.2227902
S8	Egypt (Helwan)	29.8415394, 31.3341513
S9	Coastline of Sidon (Saida-Lebanon)	33.5582651, 35.3687324
S10	Al-Wastani area of Sidon (Saida-Lebanon) (Red Clay)	33.5529660, 35.3903445
S11	Jordanian side of the Dead Sea (Jordan)	31.5061133, 35.5597424
S12	White clay from Kashta'ar Village in northern Aleppo (Syria)	36.1956659, 37.1095367
S13	Red clay from Kashta'ar Village in northern Aleppo (Syria)	36.1956659, 37.1095367

2.2 Preparation of Clay Leachates, Mineral Suspension, and Modified Clay

The samples, prepared for antibacterial susceptibility testing, included the bulk minerals, aqueous mineral leachates, mineral suspensions, and modified clay samples as follows.

2.2.1 Clay Leachate Preparation: Bulk clay samples were ultrasonically treated with deionized water (100 mg/mL) for 2 minutes, followed by 24 hrs. of shaking, to produce clay mineral aqueous leachates. The mixture was, then, centrifuged for 30 minutes at 15,000 revolutions per minute (rpm). The supernatant, i.e., leachate, was filtered using a 0.22 µm membrane filter (Williams & Hillier, 2014).

2.2.2 Clay Mineral Suspension: Sterilized bulk mineral samples were mixed in sterile deionized water, resulting in a 10% solution.

2.2.3 Sample Modification with Hemoglobin: Sample modifications were performed on S2 from Madina and S8 from Egypt (Helwan) as they showed the most promising antibacterial action. To 4g of each clay sample S2 and S8, 50 mg of oxidized hemoglobin was added, and samples were named S2+ and S8+, respectively. The mixtures were pounded for 15 minutes in a mortar and pestle.

2.2.4 Reduction: S2+ and S8+ (2 grams) were reduced with sodium borohydride ($NaBH_4$, 100 mg) through a 15 minutes mechanochemical grinding. Distilled water (10 ml) was then gradually added until the evolution of hydrogen gas ended. The pastes were then dried at 100°C. These samples were designed as S2++ and S8++ and used to assess their antimicrobial activities.

2.3 Elemental Analysis of Selected Bulk Minerals

X-ray fluorescence (XRF) was performed for quantitative and qualitative determination of the elemental composition of selected bulk minerals. Experiments were performed on samples S2, S6, and S8 at the chemistry laboratory, the Lebanese American University (LAU), using XRF portable Niton (XL3t Thermo). Observing their broad-spectrum antimicrobial activity, they demonstrated efficacy against all tested bacterial pathogens. This targeted approach ensures that the most promising samples are further analyzed to better understand their composition and potential mechanisms of action.

2.4 Conductivity and pH Measurement of Selected Clay Samples

Measurements of pH and electrical conductivity were made for selected clay samples (S2, S6, and S8). Samples were suspended at a ratio of 1 g of clay to 20 mL in distilled water, and measurements were done at 25ºC. The mixtures were first ultrasonicated and shaken for 24 hrs. The pH was measured using a Mi 151 Bench meter, and the electrical conductivity (EC) was measured using a Mi 170 conductivity meter from Martini.

2.5 Antimicrobial Susceptibility Test

The antimicrobial susceptibility of the clay samples was assessed using the agar diffusion method and counting the Colony Forming Unit (CFU). Kirby-Bauer Disk Diffusion Method was used to evaluate the antimicrobial activity of the aqueous clay leachates (Biemer, 1973). Bacterial inoculum (100 µL, 1.5 x 10^8 CFU/ml) was streaked on Mueller Hinton (MH) Agar plates. Sterile filter paper discs of 5 mm diameter, containing 50 µL of the clay leachate solution, were positioned on the surface of the agar. The plates were placed at 4 °C for 2 hours to allow the diffusion of leachates onto the medium, then they were incubated at 35 °C ± 2 °C for 24 hours. Each sample was analyzed in triplicate. In this study, an initial screening of 13 leachate samples was conducted to assess their antibacterial efficacy against three specific bacteria strains: S. aureus, S. epidermidis, and E. coli. From these screenings, the top three samples exhibiting the most promising outcomes were selected for further analysis (S2, S6, and S8). These chosen samples were meticulously preserved for a period of three months in sterile tubes and maintained at a temperature of 4ºC to prevent any alteration in their antibacterial properties. Following the preservation period, the antibacterial activities of these selected samples were systematically re-evaluated, using the disk diffusion method against S. aureus, S. epidermidis, and E. coli. Additionally, the modified samples S2+, S2++, S8+, and S8++ were subjected to rigorous testing against a broader spectrum of bacteria, including P. aeruginosa and K. pneumoniae.

All microbial strains used were clinical isolates, kindly provided by the Microbiology Laboratory at Beirut Arab University. These isolates were previously identified, using 16S rRNA sequencing. To ensure consistency and reliability in the evaluation process, the results obtained from these modified samples were meticulously compared with those from the unaltered clay leachates, specifically S2 and S8, as well as negative controls, utilizing the same disk diffusion method.

2.6. Screening Antibacterial Activity

2.6.1 Screening Antibacterial Activity of Selected Bulk Minerals and Mineral Suspension Against Bacterial Pathogens Using the Plate Counting Method

The quantitative antimicrobial activities of selected bulk minerals and mineral suspensions (S2, S6, and S8) were determined on the tested bacterial pathogens. Determining bacterial growth inhibition vs. bactericidal activity of samples was achieved by plating serial dilutions of bulk minerals/mineral suspensions with pathogens alongside negative controls. CFU/ml was determined for S. aureus, S. epidermidis, and E. coli according to Hedge (Hedges, 2002). 10% clay mineral suspensions in sterile dH_2O were prepared for S2, S6, and S8. Bacterial cells were suspended in 10% mineral suspension, or sterile dH2O (as control), at an initial concentration equivalent to 0.5 McFarland (1.5 x 10^8 CFU/ml). The suspensions were incubated at 37˚C for 24 hrs in a shaker at 150 rpm. Serial dilutions of the mixtures (10 dilutions) were plated onto MH Agar plates and incubated at 37°C for 24 hrs. Colony-forming units (CFU/ml) were determined. All antimicrobial assays were performed in triplicate.

2.6.2 Comparing the Antibacterial Activity of Clay Samples Against E. Coli Directly Mixed with Mineral Suspension and Separated Using a Dialysis Tube

Standard inoculum from E. coli (1.5 × 10^8 CFU/ml) was divided into two parts. The first part was mixed with 10% mineral suspension of S2, S6, and S8 in a ratio of 1:1. The second part was placed in a sterile dialysis tube suspended in 10% mineral suspension of S2, S6, and S8. The two sets, along with negative controls, were incubated at 37 ºC for 24 hrs. E. coli survival was determined post-CFU enumeration.

2.7 Statistical Analysis

The obtained data were presented as mean ± standard deviation. The difference between the groups was statistically determined by t-test and ANOVA, where relevant. Significance set at $P < 0.05$. All statistical analyses were performed using GraphPad Prism 9.0 (GraphPad Software, San Diego, CA).

3. Results

3.1 Antibacterial Effects of Clay Leachates

Leachates of clay samples were assayed against S. aureus, S. epidermidis, E. coli, K. pneumoniae, and P. aeruginosa to evaluate their antimicrobial activities. As shown in Figure 1, clay leachate samples S2, S6, and S8 showed effects against all tested bacteria. The other samples show activity against at least one pathogen. The highest activity was achieved by the sample S8, obtained from Helwan, Egypt, with zone of inhibition (ZOI) of 17.33 ± 1.53, 11.67 ± 0.58, and 11.00 ± 1.00 against S. epidermidis, S. aureus, and E. coli, respectively. Clay leachate samples S2 and S6 from Madina, KSA, showed also antibacterial capabilities against all bacterial pathogens with ZOI of 5.67 ± 0.58, 8.00 ± 0.00, and 6.00 ± 0.00 for S2 against S. aureus, S. epidermidis, and E. coli, respectively and where S2 showed the highest inhibition among tested leachates against K. pneumoniae, and P. aeruginosa with ZOI of 7.33 ± 1.15, and 7.67 ± 0.58, respectively. As for S6, ZOI were 7.00 ± 0.58, 5.67 ± 0.58, 7.67 ± 0.58, 6.67 ± 0.58, and 6.67 ± 0.58 were determined for S. aureus, S. epidermidis, E. coli, K. pneumoniae, and P. aeruginosa, respectively. Clay leachate of sample S11 from the Dead Sea in Jordan gave a ZOI of 11.67± 0.58 against S. epidermidis, lower values were recorded for S. aureus and E. coli with no effect seen against the other 2 pathogens. Almost all clay leachate samples showed an inhibition activity against E. coli, except for S12 and S13 which showed inhibitory activity only against S. aureus and S. epidermidis. S2, S6, and S8 clay leachates were the most active against the tested pathogens, therefore they were selected for further studies.

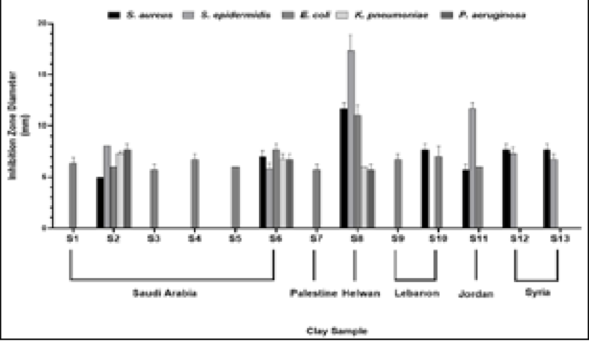

Figure 1. Comparison of antibacterial activities of clay leachates. Results are represented as the mean of triplicate ± SD.

Clay leachate samples S2, S6, and S8 were then preserved at 4 ºC and were tested again after 3 months to determine their stability with time. They were tested against the most susceptible pathogens S. aureus, S. epidermidis, and E. coli. As shown in Table 2, the three clay leachate samples exhibited decreased activity against the tested pathogens. S2 seemed to lose all its activity (98%, 97.5%, and 98.3% against S. aureus, S. epidermidis, and E. coli, respectively while S6 and S8 showed a significant reduction in activity.

Table 2. Effects of selected clay leachates against S. aureus, S. epidermidis, and E. coli following three months of preservations. Results are recorded as the mean of triplicate ± SD.

	Sample number	Inhibition zone (mm)	Reduction in activity (%)
S. aureus	S2	5.67±0.58	98
	S6	7.00±0.58	14
	S8	11.67±0.58	42
S. epidermidis	S2	8.00 ± 0.00	98
	S6	5.67 ± 0.58	96
	S8	17.33 ± 1.53	62
E. coli	S2	6.00 ± 0.00	98
	S6	7.67 ± 0.58	22
	S8	11.00 ± 1.00	27

3.2 Determining pH and Conductivity Measurements of Selected Clay Samples

The pH and conductivity of the 5% sample leachates of S2, S6, and S8 were determined at 25 ºC (Table 3). The pH values ranged from 8.05 to 8.45, while the conductivities of the leachates ranged from 695 ± 4.24 µS/cm to 1458.5 ± 94 µS/cm. The pH of the most active leachate S8 was 8.05 ± 0.49 with a mean conductivity of 1458.5 ± 94 µS/cm.

Table 3. Conductivity and pH measurements of selected clay leachates (S2, S6, and S8)

Sample number	pH	EC (µS/cm)
S2	8.35 ± 0.21	695 ± 4.24
S6	8.45 ± 0.07	6745 ± 134
S8	8.05 ± 0.49	1458.5 ± 94

3.3 Elemental Analysis of Most Effective Clay Samples

The results of the elemental analysis are shown in Table 4. Silicon (Si), Fe, and Al were found in higher percentages compared to the others. The highest percentages of Si, Fe, and Al were found in S2 with values of 63.725, 25.022, and 10.600 %, respectively. S8 showed the highest Silver (Ag) content with 3.460 %, as well as the highest amount of Zinc (Zn) and Copper (Cu) with 0.888 and 0.759 %, respectively. The highest amount of Zirconium (Zr) was detected in S6 with 1.215%.

Table 4. Elemental analysis of selected clay samples using X-ray Fluorescence

Element	S2 (%)	S6 (%)	S8 (%)
Mo	0.022	0.014	0.024
Zr	0.430	1.215	0.624
Sr	0.012	0.008	0.050
W	0.013	0.013	0.023
Zn	0.003	0.003	0.888
Cu	0.002	0.002	0.759
Ni	0.004	0.004	0.025
Co	0.009	0.009	0.010
Fe	25.022	23.683	8.194
Mn	0.037	0.032	0.026
Cr	0.013	0.028	0.039
V	0.028	0.028	0.122
Ti	0.166	0.165	0.113
Al	10.600	8.407	9.290
Si	63.725	28.348	47.887
Sb	0.005	0.004	4.085
Ag	0.009	0.005	3.460

3.4 Antibacterial Effect of Modified Clay Samples

Modified Clay leachate samples $S2^{+}$, S2++, S8+, and S8++ were prepared for testing their antibacterial activities against all five tested pathogens. The results were compared with those of unmodified clay leachates (S2 and S8), using the Kirby Bauer method. Figure 2 shows the results. The addition of Hb to S2 significantly increased the inhibition of S. aureus and E. coli by 44%, and 25%, respectively. A slighter increase in the inhibition of P. aeruginosa and K. pneumoniae by 12% and 10%, respectively was obtained. The addition of Hb + NaBH4 to S2 led to a significant increase in inhibition of S. aureus, K. pneumoniae, P. aeruginosa, and E. coli by 59 %, 41 %, 38 %, and 22 %, respectively.

Concerning S8 (Figure 3), the addition of Hb significantly increased the inhibition of P. aeruginosa and K. pneumoniae by 53% and 41%, respectively. Also, the addition of Hb + NaBH4 to S8 led to a significant increase in inhibition of P. aeruginosa and K. pneumoniae by 52%, and 51%, respectively. For S. aureus and E. coli, the increase in inhibition was by 17% and 15%, respectively when compared with the addition of Hb alone. It should be noted that the addition of Hb or Hb + NaBH4 to S2 did not increase the growth inhibition of S. epidermidis and the same modification of S8 significantly decreased the inhibition of S. epidermidis by approximately half.

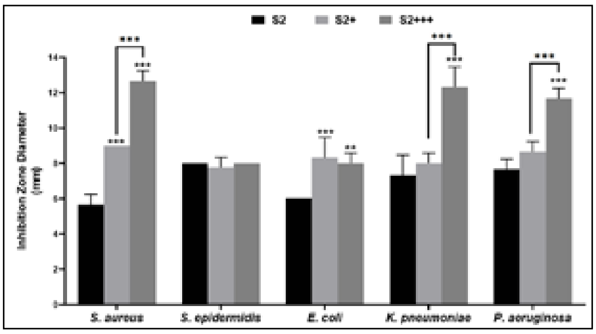

Figure 2. Effect of S2 modifications on bacterial growth. Results are recorded as the mean of triplicate ± SD. The difference in the inhibition zone was analyzed using two-way ANOVA. Results were compared against S2 unless indicated on the graph. **P<0.01, *** P<0.001. +: Hb, ++: Hb + NaBH4

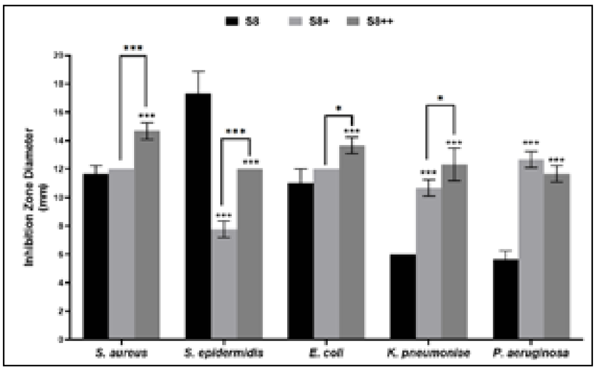

Figure 3. Effect of S8 modifications on bacterial growth. Results are recorded as the mean of triplicate ± SD. The difference in the inhibition zone was analyzed using two-way ANOVA. Results were compared against S2 unless indicated on the graph. *P<0.05, ***P<0.001. +denotes Hb only, ++ denotes Hb and NaBH4.

3.5 Growth Inhibition of Bacterial Pathogens Treated with Mineral Suspensions and Bulk Minerals

The effects of the clay samples S2, S6, and S8 as mineral suspensions (10%) and bulk minerals on the growth of S. aureus, S. epidermidis, and E. coli are shown in Figure 4. The bulk minerals of the tested samples (S2, S6, and S8) showed a significant reduction in CFU for S. aureus, S. epidermidis, and E. coli when compared to the effect of mineral suspensions of the tested samples. The mean increase in percent reduction was 50.75% ±5, except for S8 which was tested against S. epidermidis, where bulk minerals showed a decrease in reduction in CFU by 5% compared to the effect of mineral suspension. S2 bulk minerals showed the highest reduction in E. coli CFU with a mean percent reduction of 90%, followed by S. epidermidis with a mean percentage reduction of 85% ± 5, then S. aureus with a mean percentage reduction of 83.33% ± 5.77.

3.6 Antibacterial Activity of Mineral Suspensions Separated from Bacteria by Dialysis

The activity of the clay samples S2, S6, and S8 on E. coli, suspended in solution, was determined directly when mixed with mineral suspensions and after separating them from the mineral suspensions, using sterile dialysis tubes. The results were compared with those obtained with non-treated bacteria. The results are shown in Figure 5 where inhibitory activities were still recorded on E. coli bacterial suspension even when separated from mineral suspensions by dialysis. No difference was obtained when the % reduction in CFU of E. coli mixed with S2 mineral suspension or separated by dialysis tube was compared. However, a reduction in CFU by 10 and 6% was observed when E. coli was treated with S6 and S8, respectively, and separated by dialysis tubes. No significant statistical difference in % reduction in CFU of E. coli subjected directly to mineral suspensions or separated by dialysis tubes (p>0.05) was also noted.

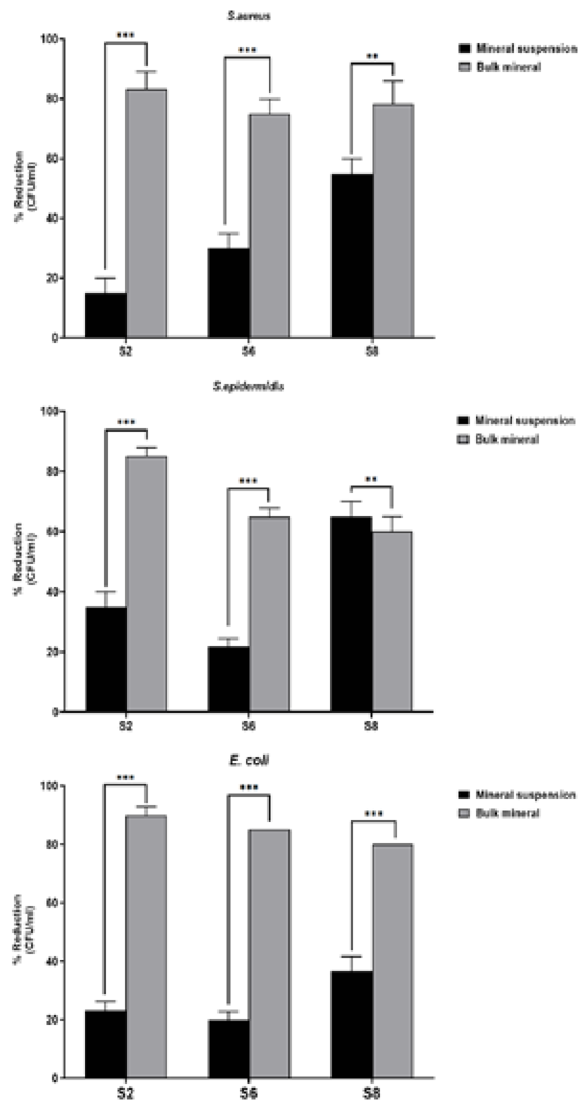

Figure 4. Percent reduction in bacterial pathogens counts (CFU/ml) using mineral suspensions and bulk minerals. Comparison of the effect of selected clay samples (Mineral suspensions) and (Bulk minerals) against bacterial pathogens. Results are mean of triplicates ± SD. The difference between Clay Mineral Suspensions and Bulk Minerals was assessed using a paired sample t-test. ** P<0.01, ***P<0.001.

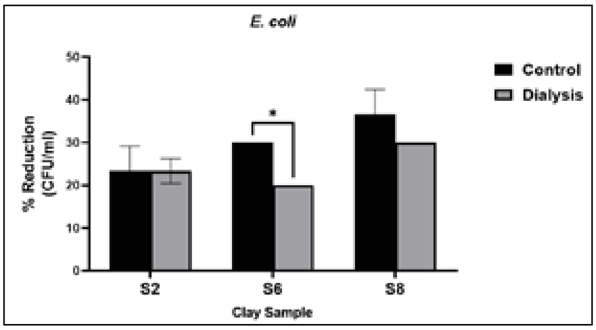

Figure 5. Percent reduction in E. coli CFU/ml using mineral suspensions with and without dialysis. Results are mean of triplicate ± SD. The difference was assessed using a paired sample t-test. * p<0.05

4. Discussion

In 2021, AMR was expected to cause 4.71 million deaths worldwide, with 1.14 million fatalities directly attributed to AMR (Naghavi et al., 2024). According to projections, by 2050, AMR would cause 1.91 million attributable deaths and 8.22 million related fatalities globally, with South Asia and Latin America anticipated to have the greatest rates (Naghavi et al., 2024). These alarming results underline the critical need for new antibiotic treatments to tackle resistant diseases. In this context, our research looks at the potential of clay-based materials as a new antibacterial method, including their efficiency against resistant microorganisms and their potential function as an alternative or supplement to traditional antibiotics. In the present investigation, antibacterial susceptibility testing was performed on aqueous mineral leachates, modified mineral leachates, bulk mineral, and mineral suspension samples. Leachates of all collected clay samples have been tested against two Gram-positive bacteria (S. aureus & S. epidermidis) and three Gram-negative (E. coli, K. pneumoniae & P. aeruginosa) as they belong to the "ESKAPE" group. These bacteria showed various levels of tolerance to metal ions leached, and this tolerance could be attributed to the difference in the cell wall structure (Kirsner, 2016). Initially, the primary focus of this research was on evaluating the leachates' effectiveness against the well-known and prevalent pathogens, S. aureus, S. epidermidis, and E. coli. Encouraged by the promising results obtained in this phase, the study's scope was broadened to encompass additional bacterial strains, namely P. aeruginosa and K. pneumoniae. This expansion aimed to comprehensively assess the leachates' antibacterial potential across a wider range of pathogens, enhancing the study's overall significance and applicability.

Clay leachates S2, S6, and S8 were observed to possess broad-spectrum antimicrobial capabilities, displaying activities against all tested bacterial pathogens. The highest activity resulted from S8 (Egypt - Helwan) against S. epidermidis followed by S. aureus, and finally E. coli. Both clay leachate S2 (Madina - Saudi Arabia) and S6 (Madina-Saudi Arabia) showed broad-spectrum antimicrobial capabilities against all bacterial pathogens. The results were consistent with the study done on two types of French green clays sold as "healing clays" (Williams et al., 2008b). Clay leachate labeled S11 (Dead Sea- Jordan) showed an effect against S. epidermidis, with a lower effect against S. aureus and E. coli; whereas clay leachate S9 (Saida-Lebanon) showed no activity against any of the pathogens tested in the current study except against E. coli. Many of the tests of the leachates inhibited the E. coli strain, as well as other pathogenic strains of S. aureus, S. epidermidis, K. pneumoniae, and P. aeruginosa but in different degrees of activity. The present study revealed no significant difference in the tolerance of metal ions between Gram-positive and Gram-negative bacteria; however, E. coli exhibited greater susceptibility to clay leachates compared to S. aureus. Consequently, each microbial strain may possess a distinct inhibitory control that interacts with its antimicrobial mechanism (Ibbini et al., 2018).

The highest activity recorded was attained against S. epidermidis which was inhibited using S8. Clay mineral surfaces are naturally negatively charged thus allowing free exchange of positively charged species, such as metal cations. In a hydrated suspension, these cations can be released from the surface of the minerals into the surrounding medium (Cunningham et al., 2010; Otto & Haydel, 2013; Williams & Haydel, 2010). It can also be suggested that the clay leachates inhibit the activity of cells due to the soluble species that react with bacteria (Londono & Williams, 2016; Morrison et al., 2014). The activity of metals in solution may be influenced by the surface chemistry of the clays that alter their potential energy or reactivity

Williams and et al. found that the antibacterial French green clay leachates lose their bactericidal effect after sitting in a test tube for 6 months (Williams et al., 2008b). Whether this is due to a change in oxidation state or another chemical effect regulated by the clay surface should be further evaluated. To verify this hypothesis, the activity of clay leachates preserved for 3 months was tested on the bacterial pathogens. The results showed that almost all leachates exhibited decreased activity against the tested pathogens. S2 seemed to lose almost all its activity.

The selection of samples S2, S6, and S8 for elemental analysis and chemical modifications was based on their broad-spectrum antimicrobial activity, as they demonstrated efficacy against all tested bacterial pathogens. The quantitative and qualitative XRF analyses of mineral mixtures of selected clay samples (S2, S6, and S8) revealed the presence of Si, Fe, Al, Ag, Cu, and Zn. The highest percentage of elements was obtained for Si > Fe > Al. The highest percentages of Si, Fe, and Al were present in S2. S8 and showed the highest Ag content as well as the highest amount of Zn and Cu. Ag primarily exert their antimicrobial action by binding to thiol (sulfhydryl) groups in bacterial proteins and enzymes, disrupting their function (Bragg & Rainnie, 1974; Fuhrmann & Rothstein, 1968; Furr et al., 1994). This interaction impairs essential cellular processes and leads to bacterial death. Other sulfur-containing compounds do not neutralize silver's activity, highlighting the significance of thiol group binding. Additionally, silver ions can disrupt bacterial membranes by causing the release of potassium ions (K^+), further contributing to its bactericidal effect (Fuhrmann & Rothstein, 1968; Rayman et al., 1972; Schreurs & Rosenberg, 1982). As for Cu, it can initiate cell damage through several mechanisms. The first involves oxidative damage, where copper ions produce reactive oxygen species (ROS) that disrupt membrane integrity and lead to cell death. This death occurs via non-enzymatic oxidative damage to membrane phospholipids (Santo et al., 2012). Additionally, copper ions penetrate the bacterial cell, causing oxidative stress and DNA degradation through redox cycling, which results in the destruction of genetic material (Dalecki et al., 2017; Santo et al., 2011). However, the exact sequence of events in "contact killing" is debated, with some studies suggesting that copper's antibacterial effect could also involve inhibition of cellular respiration and DNA damage rather than direct membrane degradation (Weaver et al., 2010).

The highest amount of Zn was detected in S6. Other elements such as Sb, Mo, Sr, Ni, Ti, and V, were present in small quantities. It is well known that the antibacterial properties vary with the metal toxicity and the type of bacteria (Yasuyuki et al., 2010). Some metals display specific effects on bacteria due to their chemical or physical properties (Morrison et al., 2016; Williams & Haydel, 2010).

The crystalline structure of metal elements disrupts bacterial cell envelopes, and/or impairs the efflux of bacterial metabolites (Ghadiri et al., 2015). Morrison and et al. showed that a clay derived from volcanogenic hydrothermal alteration destroys bacteria through the synergistic actions of Fe and Al (Morrison et al., 2016). Metals can interact synergistically to produce a toxicity level greater than that predicted by adding their toxicities (Preston et al., 2000). For example, lower concentrations of Fe can be toxic to E. coli in the presence of Al (Fatima Camoes Amador, 1999), also Zn and Cu have been shown to act synergistically against E. coli (Preston et al., 2000).

pH enhances the solubility of metals in leachate, thus elevating their concentration and possibly their toxicity to organisms within their scope of influence (Antoniadis et al., 2006). pH and conductivity measurements for clay leachate samples S2, S6, and S8 were conducted in the present study to determine their influence on antibacterial activities. The most active leachate S8 recorded a mean pH measurement of 8.05 ± 0.49, which was slightly alkaline similar to pH values recorded for S2 and S6 (8.35, and 8.45, respectively). The mean conductivity determined for S8 was 1458.5 ± 94 µS/cm. Conductivities of the other leachate samples ranged from 695 ± 4.24 µS/cm for S2 to 6747 ± 134 µS/cm for S6. Many bacteria can adapt to varying external pH conditions; however, pH impacts the rate of chemical reactions that affect the flow of nutrients through the membrane. A study done by Borquaye et al. measured both the pH and conductivities of aqueous clay leachates collected from Ghana to examine if they played any role in the observed antimicrobial activities (Borquaye et al., 2016) and found the most active antibacterial clay leachate had a pH of 2.81 and a conductivity of 54.2 µS/cm.

Sorokina and et al. demonstrated that in bacterial cells, iron is known to be present as Fe^{2+} and Fe^{3+}, which may be converted to one another (Sorokina et al., 2013). However, iron is important for biological systems; its concentration in the cells should be maintained at a definite low level. At high concentrations, iron has a toxic effect. The ferrous iron cations generate ROS, which cause peroxidation of the cell membrane lipids, as well as protein and DNA damage (Storz & Imlayt, 1999). As the chemical composition of the tested clay samples in the current study indicated the presence of Fe in the most potent antibacterial samples from Madina (S2) and Helwan (S8), therefore, modifications of these clays via solid-state mechanochemical addition of hemoglobin, the most abundant hemeprotein in biological systems, was done. The expected results must answer the following questions: a) Does hemoglobin with iron in the bound state act as an inhibitor of bacterial pathogens? b) In what oxidation state is the inhibition more effective? c) What is the effect of structure on the magnitude of inhibition? and d) How do other metals, e.g., silver, influence the magnitude of inhibition? Modified Clay leachate samples $S2^{+}$, $S2^{++}$, $S8^{+}$, and $S8^{++}$, were examined for their antibacterial activities against all bacterial pathogens using the disk diffusion method. The addition of hemoglobin (Hb) was referred to as oxidized hemoglobin samples (OHB) and the addition of Hb and NaBH4 was referred to as reduced hemoglobin samples (RHB). Zones of inhibitions detected for bacterial pathogens treated with (S2 and S8) and modified samples (S2+, S2++, S8+, and S8++) were compared. The addition of Hb to clay samples (S2 and S8) resulted in varying degrees of increased inhibition against bacterial pathogens, ranging from 10% to 53%, while further addition of $NaBH_4$ to these samples led to even higher inhibition percentages, ranging from 22% to 59%. OHB showed an increase in antibacterial effect compared to the unmodified clay against selected pathogens. Reduced modified clay RHB showed appreciable bioactivity enhancement compared to OHB, as well as to that of the unmodified clay against the same selected pathogens. The ferric ion in oxidized hemoglobin (in its high spin state [$3d^5$, S=5/2]) is displaced from the heme plane as compared to that in the reduced low spin state [$3d^6$, S=0], where the ferrous ion lies in the heme plane. The topology/morphology of the tested pathogens can be thought to exist in a 2D dimensional state, making it easy to interact more with the iron in the plane of the heme ring than when it is displaced. It can be concluded that Hb with Fe in the bound state showed increased activity as an inhibitor of selected pathogens, and the low spin state enhanced the interaction between the reducing agent and selected pathogens in a way that increased its inhibition. Haydel and et al. added that the combination of elevated levels of reduced iron in French green clay samples and excessive free radical production in the presence of oxygen could cause oxidative stress and damage to bacterial cells, resulting in cell death (Haydel et al., 2007). As a result, the chemical structure and stereochemistry of the active clay-modified materials seem to play a major role in the bioactivity process. In the current study, chemical analysis of the clay sample of Helwan (S8) revealed the presence of Ag, and the highest antibacterial activity was achieved by this clay leachate sample against S. epidermidis, S. aureus, and E. coli. Miyoshi et al. prepared Ag nanoparticles on a type of clay mineral in n-hexanol by chemical reduction with $NaBH_4$ and they studied the antibacterial effect of samples against E. coli incubated in light and the dark. Results showed that action in the light was higher probably due to the formation of ·OH radicals. Antibacterial action was observed even after several years (Miyoshi et al., 2010). The effect of reduction on other metals, such as Ag, can be related to nanoparticle silver and light plasmonic antipathogenic effect, leading to the rupture of the double-helical DNA structure. The results showed that the antibacterial properties varied significantly with different metals.

The bulk mineral of the tested samples (S2, S6, and S8) showed a significant reduction in CFU for S. aureus, S. epidermidis, and E. coli. The mean increase in percent reduction was 50.75% compared to the effect of mineral suspensions of the same tested samples. S2 bulk minerals showed the highest reduction in E. coli CFU followed by a reduction in S. epidermidis CFU and finally S. aureus. Results were consistent with the conclusion presented by Morrison et al.; who showed that the freely exchangeable metal ions bound to the surface of the pathogens might be responsible for the antibacterial activity of clay mixtures (Morrison et al., 2016). Williams and et al. declared that when antibacterial clays are hydrated, a series of spontaneous reactions occur emphasizing the importance of bacterial-clay contact for efficient contact killing (Williams et al., 2008b).

A study done by Cohn and et al. to test for the physical effect of clay on bacteria showed that the bacteria were killed without physically contacting the clay mineral surfaces (Cohn et al., 2006). In the present study determination of clay samples activities (S2, S6, and S8) against E. coli was evaluated by plate counting of the bacterial culture directly mixed with mineral suspensions and separated by dialysis. Inhibitory activities were still recorded on the bacterial suspension of E. coli, even when suspended in the dialysis tube. Comparing the % reduction of CFU of E. coli mixed with mineral suspensions and separated from mineral suspensions by dialysis tubes showed no significant difference. Results verified that physical contact as well as chemical transfer of chemicals between the clay and bacteria were required for antibacterial activity.

Clay's future medicinal uses offer significant potential, especially as an alternative to antibiotics in certain situations. Given its broad-spectrum antibacterial action, clay could be applied in topical therapies for skin conditions such as wound healing or dermatitis, providing a safer, non-toxic alternative to conventional antibiotics (Incledion et al., 2021). Clay could also be incorporated into medicinal formulations like ointments, lotions, or wound dressings, where it may act as a carrier for other therapeutic substances or promote healing by reducing bacterial loads and inflammation (Viseras et al., 2019). Additionally, clay-based formulations could be utilized as mouthwashes or toothpastes to address oral infections, even those resistant to conventional antibiotics (Borges de Macedo et al., 2022).

However, different limitations must be overcome before these prospective uses may be realised. One major problem is the chemical stability of clay formulations, since the antibacterial activity of clay leachates might diminish with time, as shown in this work. The long-term stability of these compounds in medicinal formulations must be extensively examined, including any possible changes in chemical composition and activity while kept or exposed to environmental conditions. Furthermore, environmental conditions such as pH, temperature, and humidity may have a major impact on the activity of clay-based formulations, necessitating the establishment of standardised techniques for clay preparation and preservation. Furthermore, although clays have shown promising results in vitro, their clinical use would demand extensive safety and toxicity testing, as well as investigations to identify their biocompatibility and possible negative effects in humans. Despite these obstacles, continuous research and development may someday allow clays to be employed in medical therapies, providing a unique method to fighting infections, especially in light of rising worries about antimicrobial resistance.

5. Conclusion

The study highlights the complexity of natural clay's antibacterial process and urges more investigation to find new clay deposits with potent antibacterial properties. Furthermore, emphasis is placed on the necessity of doing additional research on active chemical substances and their mechanisms of action. Although the antibacterial activity of clay leachates has been shown in vitro, more investigation—including animal models and clinical trials—is required to confirm the potential medicinal applications of this material.

Acknowledgment

The authors acknowledge Dr. Ahmad Kabbani from the Lebanese American University for his guidance throughout the clay reduction and elemental analysis experiments, May his soul rest in peace. His generosity in sharing the experimental protocol and providing essential reagents has significantly contributed to the successful execution of this research.

Declaration

The authors declare that no similar work has been published by another journal, and the paper is the original work of the author(s) and not copied (in whole or in part) from any other works.

Data Availability

The datasets utilized or analyzed in the present study can be obtained from the corresponding author upon reasonable request.

Funding

This research did not receive any specific grant from funding agencies in the public, commercial, or not-for-profit sectors.

References

Antoniadis, V., Tsadilas, C., Samaras, V., & Sgouras, J. (2006). Availability of heavy metals applied to soil through sewage sludge. Taylor & Francis.

Azmi, N. N., Mahyudin, N. A., Wan Omar, W. H., Mahmud Ab Rashid, N.-K., Ishak, C. F., Abdullah, A. H., & Sharples, G. J. (2021). Antibacterial Activity of Clay Soils against Food-Borne Salmonella typhimurium and Staphylococcus aureus. Molecules, 27(1), 170. https://doi.org/10.3390/molecules27010170

B. Williams, L., E. Haydel, S., F. Giese, Jr. , R., & D. Eberl, D. (2008). Chemical and Mineralogical Characteristics of French Green Clays Used for Healing. Clays and Clay Minerals, 56(4), 437–452. https://doi.org/10.1346/CCMN.2008.0560405

Bartlett, J. G., Gilbert, D. N., & Spellberg, B. (2013). Seven Ways to Preserve the Miracle of Antibiotics. Clinical Infectious Diseases, 56(10), 1445–1450. https://doi.org/10.1093/cid/cit070

Biemer, JJ. (1973). Antimicrobial susceptibility testing by the Kirby-Bauer disc diffusion method. . Ann Clin Lab Sci. , 3, 135–140.

Borges de Macedo, J., Bonametti Olivato, J., Marini, J., Aenishanslin, J., Pianaro, S. A., & Colerato Ferrari, P. (2022). Halloysite/cellulose derivatives-based bionanocomposites for controlled naproxen delivery. Journal of Applied Polymer Science, 139(14). https://doi.org/10.1002/app.51889

Borquaye, L. S., Ocansey, E., & Semenya, J. (2016). Inhibitory effect of selected ghanaian clay leachates on some pathogenic microbes. American Journal of Microbiology and Immunology, 1, 1–5.

Bragg, P. D., & Rainnie, D. J. (1974). The effect of silver ions on the respiratory chain of Escherichia coli. Canadian Journal of Microbiology, 20(6), 883–889. https://doi.org/10.1139/m74-135

Carretero, M. I. (2002). Clay minerals and their beneficial effects upon human health. A review. Applied Clay Science, 21(3–4), 155–163. https://doi.org/10.1016/S0169-1317(01)00085-0

Cervini-Silva, J., Ramírez-Apan, M. T., Kaufhold, S., Ufer, K., Palacios, E., & Montoya, A. (2016). Role of bentonite clays on cell growth. Chemosphere, 149, 57–61. https://doi.org/10.1016/j.chemosphere.2016.01.077

Cohn, C. A., Laffers, R., Simon, S. R., O'Riordan, T., & Schoonen, M. A. (2006). Role of pyrite in formation of hydroxyl radicals in coal: possible implications for human health. Particle and Fibre Toxicology, 3(1), 16. https://doi.org/10.1186/1743-8977-3-16

Cunningham, T. M., Koehl, J. L., Summers, J. S., & Haydel, S. E. (2010). pH-Dependent Metal Ion Toxicity Influences the Antibacterial Activity of Two Natural Mineral Mixtures. PLoS ONE, 5(3), e9456. https://doi.org/10.1371/journal.pone.0009456

Dalecki, A. G., Crawford, C. L., & Wolschendorf, F. (2017). Copper and Antibiotics (pp. 193–260). https://doi.org/10.1016/bs.ampbs.2017.01.007

Ducrotte, P., Dapoigny, M., Bonaz, B., & Siproudhis, L. (2005). Symptomatic efficacy of beidellitic montmorillonite in irritable bowel syndrome: a randomized, controlled trial. Alimentary Pharmacology and Therapeutics, 21(4), 435–444. https://doi.org/10.1111/j.1365-2036.2005.02330.x

Fatima Camoes Amador, M. S. (1999). Lipid Peroxidation Facilitates Aluminum Accumulation in Rat Brain Synaptosomes. Journal of Toxicology and Environmental Health, Part A, 58(7), 427–435. https://doi.org/10.1080/009841099157151

Ferrell, R. E. (2008). Medicinal clay and spiritual healing. Clays and Clay Minerals, 56(6), 751–760. https://doi.org/10.1346/CCMN.2008.0560613

Fowler, J. F. (2001). A Skin Moisturizing Cream Containing Quaternium-18-Bentonite Effectively Improves Chronic Hand Dermatitis. Journal of Cutaneous Medicine and Surgery: Incorporating Medical and Surgical Dermatology, 5(3), 201–205. https://doi.org/10.1007/s102270000020

Friedlander, L. R., Puri, N., Schoonen, M. A. A., & Wali Karzai, A. (2015). The effect of pyrite on Escherichia coli in water: proof-of-concept for the elimination of waterborne bacteria by reactive minerals. Journal of Water and Health, 13(1), 42–53. https://doi.org/10.2166/wh.2014.013

Fuhrmann, G.-F., & Rothstein, A. (1968). The mechanism of the partial inhibition of fermentation in yeast by nickel ions. Biochimica et Biophysica Acta (BBA) - Biomembranes, 163(3), 331–338. https://doi.org/10.1016/0005-2736(68)90118-1

Furr, J. R., Russell, A. D., Turner, T. D., & Andrews, A. (1994). Antibacterial activity of Actisorb Plus, Actisorb and silver nitrate. Journal of Hospital Infection, 27(3), 201–208. https://doi.org/10.1016/0195-6701(94)90128-7

Ghadiri, M., Chrzanowski, W., & Rohanizadeh, R. (2015). Biomedical applications of cationic clay minerals. RSC Advances, 5(37), 29467–29481. https://doi.org/10.1039/C4RA16945J

Gross, M. (2013). Antibiotics in crisis. Current Biology, 23(24), R1063–R1065. https://doi.org/10.1016/j.cub.2013.11.057

Haydel, S. E., Remenih, C. M., & Williams, L. B. (2007). Broad-spectrum in vitro antibacterial activities of clay minerals against antibiotic-susceptible and antibiotic-resistant bacterial pathogens. Journal of Antimicrobial Chemotherapy, 61(2), 353–361. https://doi.org/10.1093/jac/dkm468

Hedges, A. J. (2002). Estimating the precision of serial dilutions and viable bacterial counts. International Journal of Food Microbiology, 76(3), 207–214. https://doi.org/10.1016/S0168-1605(02)00022-3

Ibbini, J., Al-Qinna, M., Mashal, K., Abuidhail, J., & Alzoubi, H. (2018). Are Clay Minerals in Jordanian Soils Antibacterial? Jordan Journal of Earth and Environmental Sciences, 9(2), 108–115.

Incledion, A., Boseley, M., Moses, R. L., Moseley, R., Hill, K. E., Thomas, D. W., Adams, R. A., Jones, T. P., & BéruBé, K. A. (2021). A New Look at the Purported Health Benefits of Commercial and Natural Clays. Biomolecules, 11(1), 58. https://doi.org/10.3390/biom11010058

Kirsner, R. S. (2016). The wound healing society chronic wound ulcer healing guidelines update of the 2006 guidelines-blending old with new. Wound Repair and Regeneration, 24(1), 110–111. https://doi.org/10.1111/wrr.12393

Lemire, J. A., Harrison, J. J., & Turner, R. J. (2013). Antimicrobial activity of metals: mechanisms, molecular targets and applications. Nature Reviews Microbiology, 11(6), 371–384. https://doi.org/10.1038/nrmicro3028

Londono, S. C., Hartnett, H. E., & Williams, L. B. (2017). Antibacterial Activity of Aluminum in Clay from the Colombian Amazon. Environmental Science & Technology, 51(4), 2401–2408. https://doi.org/10.1021/acs.est.6b04670

Londono, S. C., & Williams, L. B. (2016). Unraveling the antibacterial mode of action of a clay from the Colombian Amazon. Environmental Geochemistry and Health, 38(2), 363–379. https://doi.org/10.1007/s10653-015-9723-y

Michael, C. A., Dominey-Howes, D., & Labbate, M. (2014). The Antimicrobial Resistance Crisis: Causes, Consequences, and Management. Frontiers in Public Health, 2. https://doi.org/10.3389/fpubh.2014.00145

Miyoshi, H., Ohno, H., Sakai, K., Okamura, N., & Kourai, H. (2010). Characterization and photochemical and antibacterial properties of highly stable silver nanoparticles prepared on montmorillonite clay in n-hexanol. Journal of Colloid and Interface Science, 345(2), 433–441. https://doi.org/10.1016/j.jcis.2010.01.034

Moosavi, M. (2017). Bentonite Clay as a Natural Remedy: A Brief Review. Iranian Journal of Public Health, 46(9), 1176–1183.

Morrison, K. D., Misra, R., & Williams, L. B. (2016). Unearthing the Antibacterial Mechanism of Medicinal Clay: A Geochemical Approach to Combating Antibiotic Resistance. Scientific Reports, 6(1), 19043. https://doi.org/10.1038/srep19043

Morrison, K. D., Underwood, J. C., Metge, D. W., Eberl, D. D., & Williams, L. B. (2014). Mineralogical variables that control the antibacterial effectiveness of a natural clay deposit. Environmental Geochemistry and Health, 36(4), 613–631. https://doi.org/10.1007/s10653-013-9585-0

Naghavi, M., Vollset, S. E., Ikuta, K. S., Swetschinski, L. R., Gray, A. P., Wool, E. E., Robles Aguilar, G., Mestrovic, T., Smith, G., Han, C., Hsu, R. L., Chalek, J., Araki, D. T., Chung, E., Raggi, C., Gershberg Hayoon, A., Davis Weaver, N., Lindstedt, P. A., Smith, A. E., … Murray, C. J. L. (2024). Global burden of bacterial antimicrobial resistance 1990–2021: a systematic analysis with forecasts to 2050. The Lancet, 404(10459), 1199–1226. https://doi.org/10.1016/S0140-6736(24)01867-1

O'Neill, J. (2014). Antimicrobial Resistance: Tackling a Crisis for the Health and Wealth of Nations. (Grande-Bretagne, Ed.). Review on Antimicrobial Resistance.

Otto, C. C., & Haydel, S. E. (2013). Exchangeable Ions Are Responsible for the In Vitro Antibacterial Properties of Natural Clay Mixtures. PLoS ONE, 8(5), e64068. https://doi.org/10.1371/journal.pone.0064068

Piddock, L. J. (2012). The crisis of no new antibiotics—what is the way forward? The Lancet Infectious Diseases, 12(3), 249–253. https://doi.org/10.1016/S1473-3099(11)70316-4

Preston, S., Coad, N., Townend, J., Killham, K., & Paton, G. I. (2000). Biosensing the acute toxicity of metal interactions: Are they additive, synergistic, or antagonistic? Environmental Toxicology and Chemistry, 19(3), 775–780. https://doi.org/10.1002/etc.5620190332

Rayman, M. K., Lo, T. C., & Sanwal, B. D. (1972). Transport of succinate in Escherichia coli. II. Characteristics of uptake and energy coupling with transport in membrane preparations. The Journal of Biological Chemistry, 247(19), 6332–6339.

Sandri, G., Bonferoni, M. C., Ferrari, F., Rossi, S., Aguzzi, C., Mori, M., Grisoli, P., Cerezo, P., Tenci, M., Viseras, C., & Caramella, C. (2014). Montmorillonite–chitosan–silver sulfadiazine nanocomposites for topical treatment of chronic skin lesions: In vitro biocompatibility, antibacterial efficacy and gap closure cell motility properties. Carbohydrate Polymers, 102, 970–977. https://doi.org/10.1016/j.carbpol.2013.10.029

Santo, C. E., Lam, E. W., Elowsky, C. G., Quaranta, D., Domaille, D. W., Chang, C. J., & Grass, G. (2011). Bacterial Killing by Dry Metallic Copper Surfaces. Applied and Environmental Microbiology, 77(3), 794–802. https://doi.org/10.1128/AEM.01599-10

Santo, C. E., Quaranta, D., & Grass, G. (2012). Antimicrobial metallic copper surfaces kill Staphylococcus haemolyticus via membrane damage. MicrobiologyOpen, 1(1), 46–52. https://doi.org/10.1002/mbo3.2

Schreurs, W. J., & Rosenberg, H. (1982). Effect of silver ions on transport and retention of phosphate by Escherichia coli. Journal of Bacteriology, 152(1), 7–13. https://doi.org/10.1128/jb.152.1.7-13.1982

Sorokina, E. V., Yudina, T. P., Bubnov, I. A., & Danilov, V. S. (2013). Assessment of iron toxicity using a luminescent bacterial test with an Escherichia coli recombinant strain. Microbiology, 82(4), 439–444. https://doi.org/10.1134/S0026261713040115

Spellberg, B., & Gilbert, D. N. (2014). The Future of Antibiotics and Resistance: A Tribute to a Career of Leadership by John Bartlett. Clinical Infectious Diseases, 59(suppl 2), S71–S75. https://doi.org/10.1093/cid/ciu392

Storz, G., & Imlayt, J. A. (1999). Oxidative stress. Current Opinion in Microbiology, 2(2), 188–194. https://doi.org/10.1016/S1369-5274(99)80033-2

Viseras, C., Carazo, E., Borrego-Sánchez, A., García-Villén, F., Sánchez-Espejo, R., Cerezo, P., & Aguzzi, C. (2019). Clay Minerals in Skin Drug Delivery. Clays and Clay Minerals, 67(1), 59–71. https://doi.org/10.1007/s42860-018-0003-7

Walsh, C. (2000). Molecular mechanisms that confer antibacterial drug resistance. Nature, 406(6797), 775–781. https://doi.org/10.1038/35021219

Weaver, L., Noyce, J. O., Michels, H. T., & Keevil, C. W. (2010). Potential action of copper surfaces on meticillin-resistant Staphylococcus aureus. Journal of Applied Microbiology, 109(6), 2200–2205. https://doi.org/10.1111/j.1365-2672.2010.04852.x

Williams, L. B., & Haydel, S. E. (2010). Evaluation of the medicinal use of clay minerals as antibacterial agents. International Geology Review, 52(7–8), 745–770. https://doi.org/10.1080/00206811003679737

Williams, L. B., Haydel, S. E., & Ferrell, R. E. (2009). Bentonite, Bandaids, and Borborygmi. Elements, 5(2), 99–104. https://doi.org/10.2113/gselements.5.2.99

Williams, L. B., & Hillier, S. (2014). Kaolins and Health: From First Grade to First Aid. Elements, 10(3), 207–211. https://doi.org/10.2113/gselements.10.3.207

Williams, L. B., Holland, M., Eberl, D. D., Brunet, T., & Brunet de Courrsou, L. (2014). Killer Clays! Natural antibacterial clay mineral. Mineralogical Society Bulletin, 139, 3–8.

Williams, L. B., Metge, D. W., Eberl, D. D., Harvey, R. W., Turner, A. G., Prapaipong, P., & Poret-Peterson, A. T. (2011). What Makes a Natural Clay Antibacterial? Environmental Science & Technology, 45(8), 3768–3773. https://doi.org/10.1021/es1040688

Yasuyuki, M., Kunihiro, K., Kurissery, S., Kanavillil, N., Sato, Y., & Kikuchi, Y. (2010). Antibacterial properties of nine pure metals: a laboratory study using Staphylococcus aureus and Escherichia coli. Biofouling, 26(7), 851–858. https://doi.org/10.1080/08927014.2010.527000

Zarate-Reyes, L., Lopez-Pacheco, C., Nieto-Camacho, A., Palacios, E., Gómez-Vidales, V., Kaufhold, S., Ufer, K., García Zepeda, E., & Cervini-Silva, J. (2018). Antibacterial clay against gram-negative antibiotic resistant bacteria. Journal of Hazardous Materials, 342, 625–632. https://doi.org/10.1016/j.jhazmat.2017.08.078

Zhang, Y., Wang, X., Long, L., Liu, T., & Cao, Y. (2009). Montmorillonite adsorbs creatinine and accelerates creatinine excretion from the intestine. Journal of Pharmacy and Pharmacology, 61(4), 459–464. https://doi.org/10.1211/jpp/61.04.0007

Zhao, Y., Lei, J., Lai, B. Y. C., & Tan, H. S. (2005). What Makes the Difference? A Practical Analysis of Research on the Effectiveness of Distance Education. Teachers College Record: The Voice of Scholarship in Education, 107(8), 1836–1884. https://doi.org/10.1111/j.1467-9620.2005.00544.x

JJEES

Jordan Journal of Earth and Environmental Sciences

JJEES (2025) 16 (3): 247-252
ISSN 1995-6681

Efficiency of Chemically Activated Carbon Derived from Palmyra Palm Shell for Water Hardness Removal

Tinnapan Netpae

Department of Applied Science, Nakhon Sawan Rajabhat University, Nakhon Sawan, Thailand.

Received on December 21, 2024, Accepted on February 19, 2025

Abstract

The primary goal of this study was to examine the efficiency of Palmyra palm shell activated carbon (PPSAC) generated through chemical activation in eliminating hardness from synthetic water. Locally available palmyra palm shells from Nakhon Sawan province, Thailand, were used as raw materials for activated carbon production. The Palmyra palm shells were heated at 400 °C and 500 °C for varying durations of 1, 2, and 3 hours. The activation processes utilized H_3PO_4, $ZnCl_2$, and KOH as activating agents. The optimal carbonization temperature identified in the research was 500 °C with 2 hours of activation time. The highest iodine adsorption of 884 mg/g was achieved with PPSAC using 30% H_3PO_4 at a ratio of 1:3 (charcoal to H_3PO_4) at 500°C for 1 hour. The removal efficiency of $CaCO_3$ decreased gradually following contact time at 2 hours. SEM analysis revealed the presence of calcium ions on the PPSAC surface became evident. Equilibrium data were analyzed by Langmuir, Freundlich, and Temkin adsorption isotherm models. The graphical representation of adsorption isotherms indicated that the adsorption of $CaCO_3$ on PPSAC through H_3PO_4 activation followed the Freundlich adsorption model, with a highest adsorption capacity (K_F) of 10.50 mg $CaCO_3$/g at equilibrium.

Keywords: *Hardness, Palmyra palm shell, Activated carbon, Adsorption, Isotherm*

1. Introduction

Globally, hardness is a significant concern in water quality management. Primarily attributed to calcium ions (Ca^{2+}) and magnesium ions (Mg^{2+}), it also involves other cations like aluminum (Al^{2+}) and ferrous ions (Fe^{2+}). While hard water doesn't directly jeopardize health, it does impede the efficacy of soaps and detergents. Additionally, its mineral content, including calcium carbonate ($CaCO_3$), calcium sulfate ($CaSO_4$), and magnesium hydroxide ($Mg\ (OH)_2$), can accumulate in pipes and boilers. This buildup reduces water flow and compromises heating efficiency. Carbonate hardness shows heightened sensitivity to high-temperature water. Calcium and magnesium salts also form hard scales in industrial boilers. Addressing water hardness is imperative for industries to avoid economic losses due to equipment failures and maintenance issues, which often result in unplanned shutdowns for repairs and cleanings. Soda ash and lime are highly effective and commonly used to reduce water hardness through chemical reactions, but they can be very expensive when treating large volumes of water (Brandt et al., 2016). In 2022, the global water hardness treatment market was valued at USD 1,728 million (Business Research Insights, 2023).

Activated carbon, known for its high absorption efficiency, is an essential material widely used for filtering harmful chemicals from water and air pollution. It's derived from graphite and processed to generate numerous small pores between carbon atoms. Researchers have explored low-cost activated carbon adsorbents from agricultural by-products, such as coconut shells, cashew nut shells, pineapple peels, and drumstick tree seed husks to remove hardness ions from water (China, 2016; Rolence et al., 2014; Ashtaputrey and Ashtaputrey, 2016; Khati, 2018).

The Palmyra palm (Borassus flabellifer Linn.) is a vital palm species within the sugar palm group, widely found in tropical Asian countries, including Thailand. Its fruits contain sweet, fibrous flesh encased in a hard shell. Despite being a significant economic resource for various communities, the palm's shell is typically discarded as waste after seed extraction. This study examines the viability of utilizing activated carbon derived from Palmyra palm shells (PPSAC) via chemical activation with different agents (H_3PO_4, $ZnCl_2$, and KOH) for the adsorption of calcium hardness in water (expressed as mg $CaCO_3$/L). It delves into the efficiency of PPSAC under varied conditions like contact time and initial concentration. The objective of this study is to evaluate the adsorption capacity of PPSAC and understand potential adsorption mechanisms through analyzing three distinct adsorption isotherms.

2. Materials and methods

2.1 Adsorbate preparation

Synthetic hardness water was produced by dissolving 1.19 g $CaCl_2$ and 1 g $MgSO_4$ into 1 L of deionized water. The solution's pH value was adjusted with 0.1 mol/L of HCl or NaOH until it reached pH 6.8 (Rolence et al., 2014)) and served as the synthetic hardness water stock.

2.2 Adsorbents preparation

Palmyra palm shell samples were collected from a local food processing community enterprise in Chum Saeng

---

* Corresponding author e-mail: tinnapan.n@nsru.ac.th

district in Nakhon Sawan province, located in the lower northern region of Thailand. Chum Saeng district has a tropical savanna climate with average temperatures that range from 26 °C to 32 °C. The region receives 1,475 mm of rainfall annually, with high humidity and heavy rain from June to October.

Initially, the Palmyra palm shells were washed and oven-drying at 50°C for 12 hours. Dried shells were carbonized into charcoal at temperature at 400 °C and 500 °C at the intervals of 1, 2, and 3 hours in the muffle furnace. After that, Palmyra palm shell charcoals were crushed in a mortar and mesh-sieved to obtain particles with a diameter of less than 150 µm. The charcoal was determined for physical properties by methods of American Society for Testing and Materials (ASTM). The percentage of moisture content, volatile matter, and ash content were assessed using ASTM 3173 (2012), ASTM D 3175 (2012), and ASTM D 3174 (2012) methods, respectively.

The percentage of fixed carbon (FC) in charcoal was calculated by subtracting the summation moisture content (Mc), ash content (Ac), and volatile matter (Vm) from 100% (equation 1).

$$\mathrm{FC}\,(\%) = 100\% - \mathrm{Mc}\,(\%) + \mathrm{Ac}\,(\%) + \mathrm{Vm}\,(\%) \qquad (1)$$

Subsequently, a concentration of 30% (w/v) $ZnCl_2$, KOH, and H_3PO_4 solution was used for chemical activation with the ratio of ground charcoal to activating solutions ranging from 1:0 to 1:4 (w/v).

To ensure adequate penetration of the activating agent, the mixtures were agitated for 24 hours at room temperature (28±2°C) and 150 rpm. Afterwards, the samples were washed with deionized water until reaching a pH of 7.0±0.1, followed by drying overnight in an oven at 50 °C. The dried material was activated for an hour at 500 °C in a muffle furnace. After that, the dried material was cooled to room temperature. All activated carbons produced were sieved to a particle less than 150 µm and collected in plastic containers for further analysis (Figure 1).

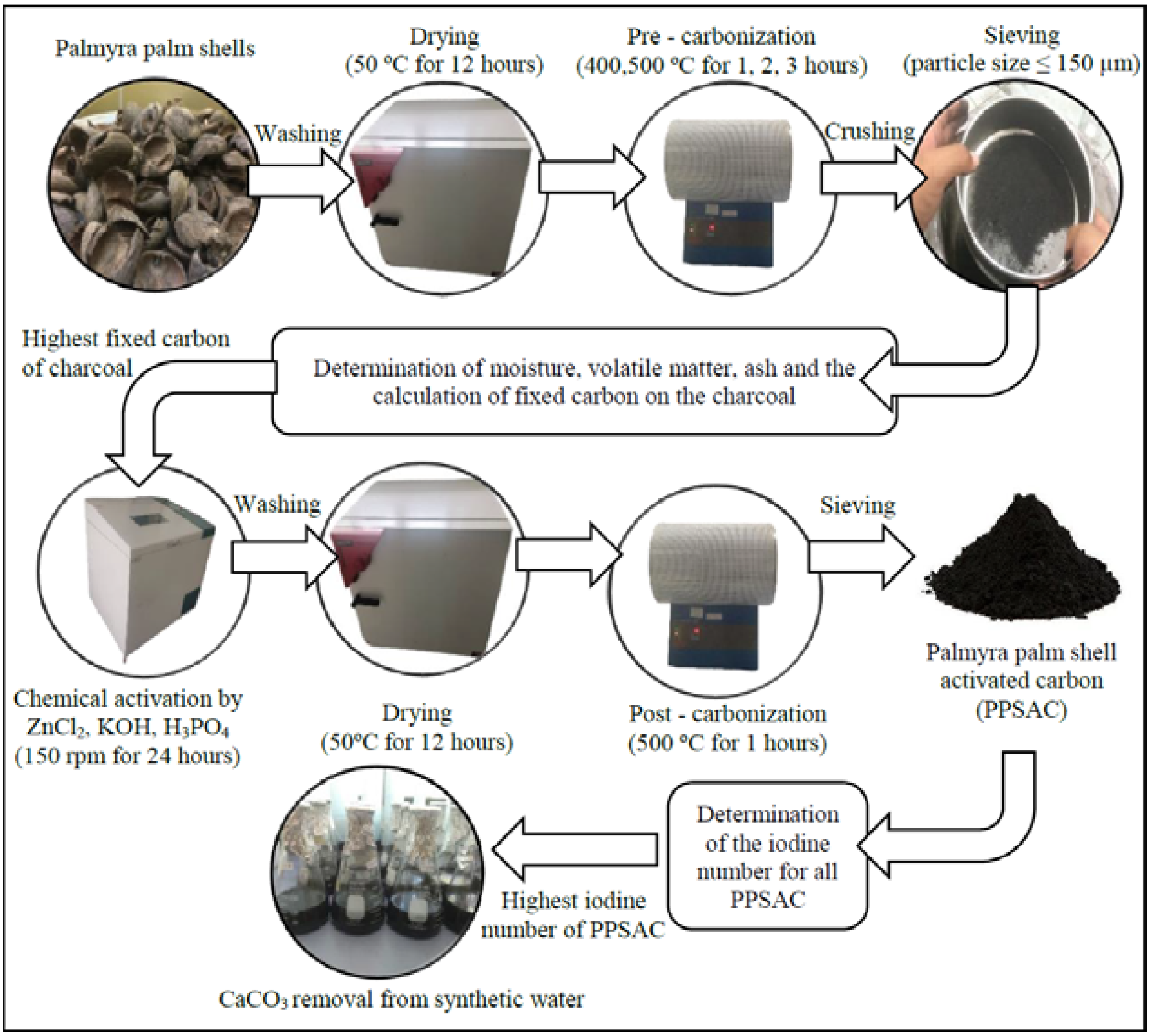

Figure 1. The schematic diagram of PPSAC powder prepared by chemical activation for $CaCO_3$ adsorption from synthetic water.

2.3 Characterization of PPSAC adsorbent

The iodine number was determined for all PPSAC adsorbents based on ASTM D 4607-86 (2006), using the sodium thiosulphate volumetric method. This served as a measure of the activated carbon's activity level or micropore content. The iodine value is a key parameter for evaluating the activity of activated carbon. A higher iodine value indicates more activation. The iodine number (mg/g) represents the amount of iodine (I_2) in milligrams adsorbed per gram of PPSAC from an iodine solution (Ashtaputrey and Ashtaputrey, 2016).

2.4 Effects of concentration and contact time on the efficiency of hardness adsorption by PPSAC

The adsorption efficiency of PPSAC was conducted by contacting 1 g of the PPSAC with 100 mL of synthetic water at different concentrations (100 to 500 mg/L as CaCO3) on a rotary shaker at 150 rpm and room temperature (28±2°C). The contact time on the hardness sorption was determined between 30 minutes to 4 hours. The samples were collected at various intervals and analyzed for hardness concentration using the EDTA titrimetric method (APHA, AWWA, WEF, 2017).

The amount of hardness uptake by the PPSAC is expressed as follows: equation 2.

$$q = Ci - Cf \times V \times W \tag{2}$$

In equation 2, q is the hardness uptake (mg $CaCO_3$/g dry mass), whereas Ci and Cf are the initial and the equilibrium concentrations of $CaCO_3$ in the solution (mg/L), respectively. V is the volume of synthetic water (mL), and W is the weight of activated carbon used (g).

Scanning electron microscopy (SEM- Hitachi S-3500, Japan) was used to examine the microstructure changes of the PPSAC surface before and after hardness adsorption. The PPSAC samples were covered with a thin layer of carbon, and the electron-accelerated voltage of the microscope used for imaging was set at 20 kV.

2.5 Adsorption isotherm models

The linearization analysis has been one of the most applied tools for defining the best-fitting adsorption isotherm models due to its mathematical simplicity (Al-Shaybe and Khalili, 2009; Al-Haj-Ali and Marashdeh, 2014). The isotherm models analyzed in this experimental data were the Langmuir, Freundlich, and Temkin equations.

Equilibrium in the adsorption process is quickly established between the amount of hardness adsorbed onto the activated carbon (qe, mg/g) and the quantity of hardness remaining in the solution (Ce, mg/L).

The Langmuir isotherm model is utilized for monolayer sorption on a homogeneous site on the surface of the sorbent. The Langmuir isotherm model is represented by the following equation 3.

$$1/qe = (1 / qm\,K_L)\,(1 / Ce) + 1 / qm \tag{3}$$

In equation 3, K_L is the Langmuir isotherm constant, while qm is the maximum monolayer adsorption capacity, while 1/qe represents the slope and 1/Ce serves as the intercept on the vertical axis (Langmuir, 1916).

On the other hand, the Freundlich isotherm model is commonly applied to illustrate the adsorption characteristics of heterogeneous surfaces. The equation for the Freundlich isotherm model is represented by the following equation 4:

$$\log q_e = (1 / n) \log C_e + \log K_F \tag{4}$$

The Freundlich constant (K_F) and adsorption intensity (1/n) are obtained directly from the slope and intercept by plotting log q_e versus log C_e. The value of n is generally between 2 to 10. K_F (mg/g) represents the adsorption or distribution coefficient, indicating the amount of dye adsorbed onto the adsorbent at one unit of equilibrium concentration (Freundlich, 1906).

The Temkin isotherm incorporates a factor that explicitly accounts for the interactions between the adsorbent and adsorbate. The linearized form of the Temkin isotherm model is represented by the following equation 5:

$$q_e = B_T \ln A_T + B_T \ln C_e \tag{5}$$

where A_T is the Temkin isotherm equilibrium constant (mg/L), B_T is the constant related to the heat of sorption (J/mol), R is the universal gas constant (8.314 J/mol/K), T is the absolute temperature (298K), and B_T is Temkin isotherm constant or R_T/B_T. A plot of qe versus ln Ce makes possible the determination of the isotherm B and KT constants from the slope and the intercept, respectively (Temkin, 1940).

2.6 Statistical analysis

All laboratory experiments were done three times, and mean values were subjected to one-way ANOVA and Post Hoc Duncan's test ($p < 0.05$) for statistical analysis.

3. Results and discussions

3.1 Physical properties of Palmyra palm shell charcoal

Variations in the physical properties of charcoal were evident across different carbonization temperatures and durations. As the carbonization temperature increased from 400 °C to 500 °C, the moisture and volatile matter percentages decreased, while the ash content increased, especially with prolonged carbonization periods. The highest fixed carbon (72.72%) was achieved at a carbonization temperature of 500 °C for 2 hours, indicating optimal conditions for char formation (Table 1). The significance of fixed carbon content lies in its role in adsorption, where the carbon surface retains adsorbate molecules through weak Van der Waals forces (McDougall, 1991; Sharififard,2018). Consequently, a higher fixed carbon content corresponds to a larger carbon surface area available for adsorption of the adsorbate (Paethanom and Yoshikawa, 2012).

Values with the same superscript letters within each column are not significantly different at $p < 0.05$ based on Duncan's multiple range test.

Furthermore, the percentage of fixed carbon in charcoal derived from Palmyra palm shells at 500 °C for 2 hours (72.72%) closely rivaled that of bamboo charcoal (73.15%), coconut shell charcoal (74.35%), and conventional charcoal (77.20%) (Mahanim et al., 2011; Nukman et al., 2014; Njenga et al., 2016). Notably, it surpassed the fixed carbon content found in silky oak charcoal (56.2 ± 0.63) and mangrove charcoal (68.78%) (Njenga et al., 2016; Rahman et al., 2019).

Table 1. The physical properties of palmyra palm shell charcoal were assessed at varying carbonization durations (1, 2, and 3 hours) and two different temperatures.

Carbonization temperature (°C)	Time (hours)	Moisture content (%)	Volatile matter content (%)	Ash content (%)	Fixed carbon (%)
400	1	8.99±1.06^{d}	13.46±1.93^{e}	10.96±1.08^{a}	66.59
	2	8.84±0.47^{cd}	12.68±2.76^{de}	11.88±0.83^{ab}	66.60
	3	8.60±1.33^{c}	11.13±1.92^{d}	12.77±0.94^{b}	67.50
500	1	7.72±1.05^{b}	7.44±1.70^{c}	14.17±1.08^{c}	70.67
	2	6.42±0.80^{a}	6.51±1.20^{b}	14.35±0.83^{c}	72.72
	3	6.40±1.01^{a}	6.35±0.81^{a}	18.61±1.03^{d}	68.64

3.2 Effect of the impregnation ratio of PPSAC with chemical agents on iodine number

Chemical activation was conducted using Palmyra palm shells, which were charred at a temperature of 500 °C for 2 hours. Figure 2 illustrates the iodine number of the activated carbon alongside the chemical agents employed for activation. The results indicate that all activated carbons exhibited superior adsorption efficiency compared to charcoal. Notably, activated carbon impregnated with H_3PO_4 demonstrated the highest iodine number, while the lowest iodine number was observed for activated carbon impregnated with $ZnCl_2$ and KOH.

Phosphoric acid acts as a catalyst, promotes bond cleavage reactions, and facilitates crosslinking through cyclization, condensation, and combines with organic species to form phosphate and polyphosphate esters. These mechanisms assist in preserving the internal pore structure and prevent excessive burning of the adsorbent during carbon activation (Xu et al., 2014).

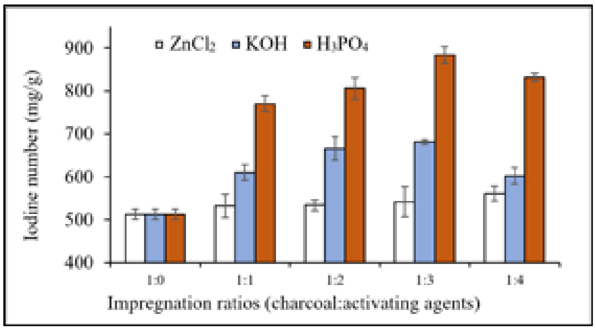

Figure 2. The iodine number was investigated to assess the effect of impregnation ratio of PPSAC with chemical agents ($ZnCl_2$, KOH, and H_3PO_4).

The impregnation ratio between charcoal and H_3PO_4 increased from 1:1 to 1:3, increasing the adsorbed CaCO3 volume. Similarly, the iodine value of the PPSA activated with H_3PO_4 was increased from 770 to 884 mg/g as the ratio increased. The elevated iodine number observed in PPSA confirms its developed micropore structure and indicates a good adsorption capacity.

This increase may result from chemisorption within the pores during activation and leads to variations in reactivity with different activating agents and subsequent enhancement in pore structure (Sahira et al., 2013). Consequently, a charcoal to H_3PO_4 impregnation ratio of 1:3 showed the best adsorption capacity. It was selected to evaluate the effectiveness of $CaCO_3$ adsorption.

3.3 Effect of Initial Concentration and Contact Time on Hardness Removal by PPSAC with H3PO4 Activation

Figure 3 illustrates the impact of $CaCO_3$ concentration (100, 200, 300, 400, and 500 mg/L) and contact time (30 minutes, 1, 2, 3, and 4 hours) on the hardness adsorption by Palmyra palm shell activated carbon (PPSAC), carbonized at 500 °C and prepared with 30% H_3PO_4 at a ratio of 1:3. Initially, the adsorption of $CaCO_3$ increases with rising concentration, plateauing beyond 400 mg/L. The removal efficiency escalates rapidly up to the optimum time (2 hours) due to ample active binding sites. However, as concentration and contact time increase, hardness ion removal diminishes steadily, likely due to decreased availability of adsorption sites (Ugwu et al., 2020). Eventually, the adsorption process becomes less efficient due to surface saturation with calcium ions (China, 2016).

SEM analysis, depicted in Figure 4(a), reveals numerous micron-sized pores on the surface of PPSAC, attributed to carbonization at 500 ºC and H_3PO_4 activation. Subsequently, Figure 4(b) shows SEM images of the adsorbent after $CaCO_3$ adsorption, indicating the presence of calcium ions on the PPSAC surface. The activation process not only preserved the structure but also facilitated homogeneous pore distribution (Stc, 2011).

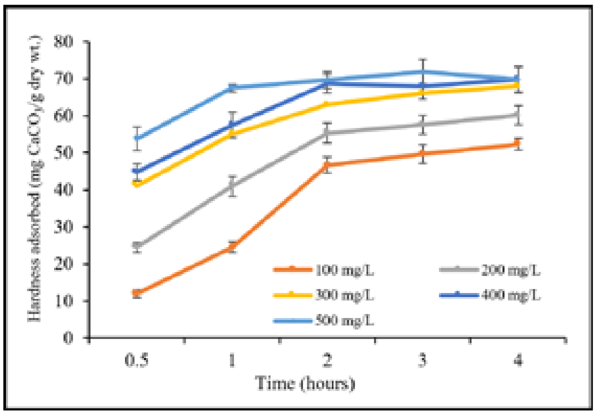

Figure 3. Effect of initial concentration and contact time on hardness removal efficiency by PPSAC with H_3PO_4 activation at 1:3 ratio.

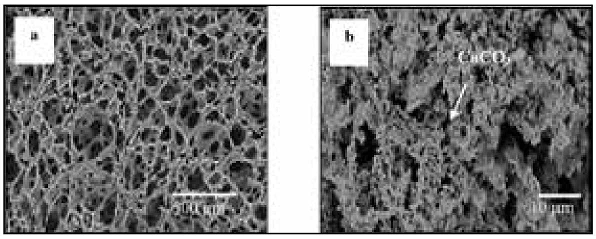

Figure 4. SEM images of PPSAC surface before (a) and after (b) $CaCO_3$ adsorption by H_3PO_4 activation.

3.4 Adsorption isotherms study

The Freundlich isotherm better fits the adsorption of hardness onto PPSAC by H_3PO_4 activation in a 1:3 ratio compared to the Langmuir and Temkin isotherms, as indicated by correlation coefficients exceeding 0.9866 (Figure 5). The adsorption capacity or Freundlich constant (K_F) and intensity (1/n) of the Freundlich isotherm were determined to be 10.50 mg $CaCO_3$/g, and 0.3612, respectively (Table 2). The adsorption capacity of $CaCO_3$ by PPSAC after activation with H_3PO_4 observed in this work was higher than other activated carbons prepared by different sources, such as moringa seed pod husk (Khati, 2018), cashew nut shell (China, 2016), coconut shell (Rolence et al., 2014), but lower than pitombeira seeds, presenting K_F values 19.05 mg $CaCO_3$/g (Mendonça et al., 2022). A value of 1/n between 0 and 1 signifies favorable adsorption, with the Freundlich isotherm showing high adsorbent loadings at higher concentrations (n > 1) (Worch, 2012). This model assumes multi-layer absorption and heterogeneous surface characteristics, making it widely applicable for describing activated carbon adsorption in wastewater treatment (Budhiary and Sumantri, 2020). These findings demonstrate the potential of economically viable PPSAC for efficient water hardness removal.

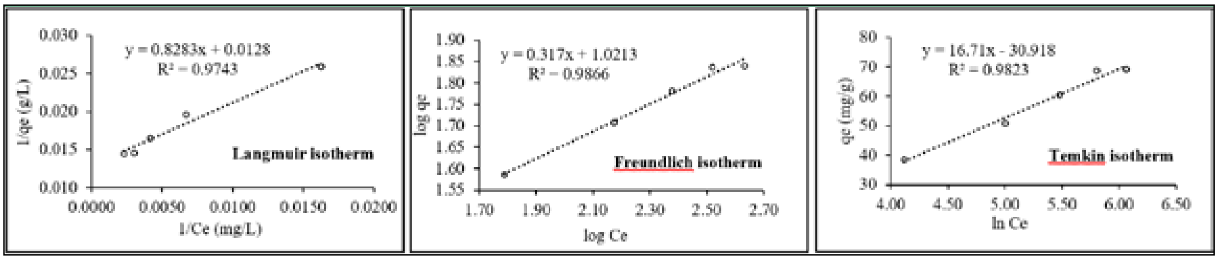

Figure 5 The isotherm curves depict the efficiency of hardness removal by PPSAC through H_3PO_4 activation at a 1:3 ratio, with a contact time of 2 hours.

Table 2. Comparison of the Langmuir, Freundlich, and Temkin constants for the adsorption of hardness onto PPSAC by H_3PO_4 activation at a 1:3 ratio.

Langmuir isotherm			Freundlich isotherm			Temkin isotherm		
q_m (mg/g)	K_L	R^2	1/n	K_F (mg/g)	R^2	B_T	A_T (L/mg)	R^2
82.64	0.0146	0.9743	0.3612	10.50	0.9866	16.71	0.1572	0.9823

4. Conclusions

The findings of this study demonstrate that PPSAC exhibits significant potential for removing hardness from aqueous solutions. Optimal adsorption occurred at a contact time of 2 hours. The process of hardness adsorption by PPSAC through H_3PO_4 activation at a 1:3 ratio adheres well to the Freundlich adsorption isotherm equation, with a correlation coefficient of 0.9866 and the highest adsorption capacity of 10.50 mg $CaCO_3$/g.

Acknowledgment

I am grateful to acknowledge the financial support provided by the Faculty of Science and Technology at Nakhon Sawan Rajabhat University, Thailand.

References

Al-Haj-Ali, A.M., Marashdeh, L.M. (2014). Removal of Aqueous Chromium (III) Ions Using Jordanian Natural Zeolite Tuff in Batch and Fixed Bed Modes. Jordan Journal of Earth and Environmental Sciences, 6 (2): 45-51.

Al-Shaybe, M. and Khalili, F. (2009). Adsorption of Thorium (IV) and Uranium (VI) by Tulul alShabba Zeolitic Tuff, Jordan. Jordan Journal of Earth and Environmental Sciences, 2 (Special Publication 1): 108-119.

APHA, AWWA, WEF. (2017). Standard methods for the examination of water and wastewater. 23rd Edition, American Public Health Association, American Water Works Association, Water Environment Federation, Denver.

Ashtaputrey, S.D., and Ashtaputrey, P.D. (2016). Preparation, characterization and application of pineapple peel activated carbon as an adsorbent for water hardness removal. Journal of Chemical and Pharmaceutical Research, 8: 1030-1034.

ASTM D 3173. (2012). Standard test method for moisture in the analysis sample of coal and coke. Annual book of ASTM standard Vol 05, Philadelphia, D3173-11.

ASTM D 3174. (2012). Standard test method for ash in the analysis sample of coal and coke. Annual book of ASTM standard. Vol 05, Philadelphia, D3174-11.

ASTM D 3175. (2012). Standard test method for volatile in the analysis sample of coal and coke. Annual book of ASTM standard. Vol 05, Philadelphia, D3175-11.

ASTM D 4607. (2006). Standard test method for determination of iodine number of activated carbon, Annual book of ASTM standard. Vol 03, Philadelphia, D 4607-86.

Brandt, M.J., Johnson, K.M., Elphinston, Andrew, Ratnayaka, D.D. (2016). Twort's Water Supply. 7th Ed., Butterworth-Heinemann, Oxford.

Budhiary, K.N.S., and Sumantri, I. (2020). Langmuir and Freundlich isotherm adsorption using activated charcoal from banana peel to reduce total suspended solid (TSS) levels in tofu industry liquid waste. International Conference on Chemical and Material Engineering, 1053, 012113.

Business Research Insights. (2023). Global water hardness removal industry research report 2023, competitive landscape, market size, regional status and prospect. Maia-22374995, 123.

Freundlich, H.M.F. (1906). Over the adsorption in solution. The Journal of Physical Chemistry A, 57: 385-471.

Khati, V.V. (2018). Adsorption studies on water hardness removal by using Moringa oleifera seed pod husk activated carbon as an adsorbent. International Journal of Life Sciences, 12: 1-8.

Langmuir, I. (1916). The constitution and fundamental properties of solids and liquids, Part. I: Solids. Journal of the American Chemical Society, 38: 2221-2295.

Mahanim, S. MA., Ibrahim, W.A., Jalil, R., Elham, P. (2011). Production of activated carbon from industrial bamboo waste.

Journal of Tropical Forest Science, 23: 417-424.

McDougall, G.J. (1991). The physical nature and manufacture of activated carbon. Journal- South African Institute of Mining and Metallurgy, 91: 109-120.

Mendonca, J.C., Cantanhede, L.B., Rojas, M.O.A.I., Rangel, J.H.G., Bezerra, C.W.B. (2022). Preparation of activated charcoal adsorbent from pitombeira seeds (Talisia esculenta) and its application for Ca2+ ions removal. Water Supply, 22 (1): 481–495.

Njenga, M., Mahmoud, Y., Mendum, R., Iiyama, M. Jamnadass R., Roing de Nowina, K., Sundberg, C. (2016). Quality of charcoal produced using micro gasification and how the new cook stove works in rural Kenya. Environmental Research Letters, 12, 095001.

Nukman, Sipahutar, R., Yani, I., Arief, T. (2014). The blending effect of coalite, coconut shell charcoal and gelam wood charcoal on calorific value. American Journal of Applied Sciences, 11: 833-836.

Paethanom, A., and Yoshikawa, K. (2012). Influence of pyrolysis temperature on rice husk char characteristics and its tar adsorption capability. Energies, 5: 4941-4951.

Rahman, R., Widodo, S., Azikin, B., Tahir, D. (2019). Chemical composition and physical characteristics of coal and mangrove wood as alternative fuel. Journal of Physics: Conference Series, 1341: 052008.

China, C.R. (2016). Adsorption studies on water hardness removal by using cashew nut shell activated carbon as an adsorbent. African Journal of Science and Research, 4: 78-81.

Rolence, C., Machunda, R.L., Njau, K.N. (2014). Water hardness removal by coconut shell activated carbon. International Journal of Science, Technology and Society, 2: 97-102.

Sahira, J., Mandira, A., Prasad, B.P., Ram, R.P. (2013). Effect of activating agents on the activated carbons prepared from lapsi seed stone. Research Journal of Chemical Sciences, 3: 19-24.

Sharififard, H., Lashanizadegan, A., Pazira, R., Darvishi, P. (2018). Xylene removal from dilute solution by palm kernel activated charcoal: Kinetics and equilibrium analysis. Advances in Environmental Technology, 4: 107-117.

Stc, H. (2011). Characterization of activated carbons produced from oleaster stones. InTech.

Temkin, M.I., and Pyzhev, V. (1940). Kinetics of ammonia synthesis on promoted iron catalyst. Acta Physicochimica, 12: 217-222.

Ugwu, E.I., Tursunov, O., Kodirov, D., Shaker, L., Al-Amiery, A.A., Yangibaeva, I., Shavkarov, F. (2020). Adsorption mechanisms for heavy metal removal using low cost adsorbents: A review. IOP Conference Series: Earth and Environmental Science, 614, 012166.

Worch, E. (2012). Adsorption technology in water treatment: fundamentals, processes, and modeling, De Gruyter, Boston.

Xu, J., Chen, L., Qu, H., Jiao, Y., Xie, J., Xing, G. (2014). Preparation and characterization of activated carbon from reedy grass leaves by chemical activation with H3PO4. Applied Surface Science, 320: 674-680.

JJEES

Jordan Journal of Earth and Environmental Sciences

JJEES (2025) 16 (3): 253-266
ISSN 1995-6681

When will 100 Global Coastal Cities Be Flooded by the Sea?

Pierre Rostan* and Alexandra Rostan

American University of Iraq - Baghdad (AUIB), Airport Road, Baghdad, Iraq

Received on August 26, 2024, Accepted on February 19, 2025

Abstract

This article estimates the years when 100 coastal cities in 55 countries around the world will be flooded by the sea, home to 438 million people in 2024, or about 5% of the world's population. Estimated flood years are obtained by forecasting global ocean mean sea level anomalies, using wavelet analysis up to 2301. Altimetry data are provided by NOAA Laboratory for Satellite Altimetry. 2100 median projections of regional sea level rise for 100 coastal cities, relative to a 1995 to 2014 baseline, provided by the Intergovernmental Panel on Climate Change's Sixth Assessment Report presented through NASA datasets, allow the authors to evaluate how far the sea level of 100 cities will expand in 2100 from the average sea-level for each city and transform the sea level to the scale of the projected sea-level and to obtain an estimated year of flooding for each city. Assuming that the floods correspond to a 1 meter-rise in sea level, the estimated flood years for the 100 cities will range from 2083 for Manila to 2274 for Stockholm with an average flood year average around 2201 for cities like Amsterdam, Dakar, Dalian, Izmir, Lisbon, London, Perth, Rio de Janeiro, Sydney, Taipei, Valencia and Xiamen, close to the average year.

Keywords: *Sea level rise; Flood; Forecast; Wavelet analysis; Burg model.*

1. Introduction

The objective of the paper is to estimate in what years 100 coastal cities in 55 countries around the world will be flooded by the sea, home to 438 million people in 2024 or about 5% of the world population. Estimated years of flooding are obtained by forecasting mean sea level anomalies of the global ocean with wavelet analysis until 2301. A mean sea level anomaly is the difference from an average or baseline, global sea level. One of the most significant potential impacts of climate change is sea level rise, which may cause inundation of coastal areas and islands, shoreline erosion, and destruction of important ecosystems such as wetlands and mangroves. Coastal cities will not be spared by this phenomenon. By 2023, 2.15 billion people were living in the near-coastal zone and 898 million in the low-elevation coastal zone globally or 26.70% and 11.16% of the global population, respectively. Coastal areas are subject to hazards that can have severe impacts due to the high concentration of people and goods in exposed areas. Although climate-induced sea level rise will exacerbate these risks over the 21st Century, future dynamics of socio-economic development will play an important role in determining impacts – as well as adaptation responses – particularly in countries with rapid population growth in low-lying coastal areas (Reimann et al., 2023). This study will focus on the impact of global warming on sea level rise.

2. Literature Review

2.1. Overview of the literature on the Earth's flood

One of the most significant potential impacts of climate change is sea level rise that may cause inundation of coastal areas and islands, shoreline erosion, and destruction of important ecosystems such as wetlands and mangroves. Rostan and Rostan (2023a) assert this connection as global temperatures increase, sea level rises because of a thermal expansion of upper layers of the ocean and melting of glaciers and ice sheets (NOAA, 2024). The cause of global temperature increase is mainly greenhouse-gas emissions.

In 2016, governments around the world ratified the Paris Agreement on climate change, aiming to keep or move major investors away from fossil fuels to save the planet from global warming. In 2017, the One Planet conference was organized to uphold the Paris Agreement by pressuring governments and the World Bank to end subsidies and public financing of fossil fuels (Harvey, 2017).

The UN COP27 on climate change was held in Egypt in 2022. For the first time, COP participants agreed on a loss and damage fund, but no commitment to phase out fossil fuels was taken, which constitutes a rather pessimistic result. It was because voters and politicians place greater importance on immediate issues, such as inflation and the economy, leaving politicians to ignore global warming (Weisman and Ulloa, 2022). "Après moi, le deluge!" ("After me, the flood!") is a saying attributed to Louis the 15th, King of France in the 18th Century. Due to his mismanagement of the kingdom lacking a long-term vision, France experienced the fall of the monarchy during the French Revolution under the reign of his grandson, Louis the 16th, who succeeded him and was guillotined in 1793.

Today, a league of influential politicians, such as American Republicans, including U.S. President Donald Trump, Senator James Inhofe, and American Democrats, including Senator Joe Manchin III or former World Bank President David Malpass, are accused of climate denial when they refused to acknowledge that fossil fuels are warming the planet (Gelles and Rappeport, 2022). "Après

---

* Corresponding author e-mail: rostan.pierre@gmail.com

moi, le deluge!" is their rallying cry to defend the fossil fuel industry responsible for global warming. They claimed that the scientific consensus on global warming was based on a conspiracy. In this context of lobbying and defamation, where the maximization of shareholder wealth takes precedence over environmental issues, newly re-elected President Trump declared a national energy emergency on his first day in office in January 2025, part of a series of pro-fossil fuel actions and efforts to "unleash" already booming U.S. energy production. He reiterated the 2016 Paris withdrawal plan and rolled back emissions standards (Noor, 2025). To counter this mode of thinking, every year, countries that have joined the United Nations Framework Convention on Climate Change (UNFCCC, United Nations, 2024a) meet to measure progress and negotiate multilateral responses to climate change. 198 Parties have joined the Convention nowadays. The first Conference of the Parties (COP) was held in Berlin, Germany 1995. The 28th COP was held at the end of 2023 in Dubai, United Arab Emirates. It included the first Global Stocktake, where States assessed the progress made towards the goals set in the Paris Agreement and charted a course of action. The role of fossil fuels in Gulf economies has made the issue of phasing out fossil fuels a particularly controversial topic at COP28, as phasing out fossil fuels could be very costly for these Gulf countries. COP29 was held in Baku, Azerbaijan, in November 2024. Environmentalists are not convinced of the outcomes of these conferences. Countries and peoples, hit hardest by climate change, are unable to get their voices heard during these Climate summits (Steffen and Niranjan, 2021). Environmentalists say the COP is overwhelmingly white and rich. For these rich and white people work those influential politicians, supporters of the fossil fuel industry, who accuse the spreaders of fake news of harming the industry with false data. Fake news spreaders may include Ekwurzel et al. (2017), who stated that 90 carbon producers contributed approximately 42-50% of the increase in global average temperature during the period 1880-2010. These 90 carbon producers also massively contributed to the observed rise in atmospheric CO2, whose increase is responsible for global warming and the rise of global sea level, according to the paper. Eighty-three of those companies produce coal, oil, and natural gas, while the remaining seven are cement manufacturers. As mentioned earlier, newly re-elected President Trump reiterated the 2016 Paris withdrawal plan in January 2025 and rolled back emissions standards (Noor, 2025). According to an annual United Nations emissions report, the Paris agreement would provide only a third of the greenhouse gas reductions that environmentalists say are needed to avoid catastrophic warming (The Economist, 2017). If all countries (minus the U.S. now), involved in the Paris agreement, meet their commitments by 2030 – which is doubtful –, temperatures should rise at least another 3 degrees Celsius by 2100. How long will the Earth live under the deadly threat of global warming on its inhabitants?

Supporters of President Trump have claimed that global warming predictions are based on computer models that are unreliable predictors. Furthermore, the UN report acknowledged that the Paris climate agreement was flawed. Government leaders in Paris were just pretending since their timid commitments would not prevent global warming and flooding. So, Trump supporters believed he was right to stop pretending. The study by Willner et al. (2018) is one such computer model predicting the end of the world. The study calculates the amount required to maintain a constant risk of large floods over the next 25 years. Willner et al. estimate that global warming is expected to bring more rain, exposing millions of people to river flooding, particularly in America and parts of Asia, Africa, and central Europe. Based on models 10 times more accurate than commonly used climate computer simulations, if action is not taken, the number of people affected by devastating floods could skyrocket. Asia – the continent with the greatest historical risk of high-level flooding – would be hardest hit, with the number of people affected by river flooding expected to rise from 70 million to 156 million by 2040. In August 2022, episodes of massive flooding took place in Asia. Among them, a report that floods affected nearly 500,000 residents in Odisha, eastern India, and some 60,000 people were displaced from their homes. Parts of Vietnam, northern Thailand, border areas of Myanmar, and northern Laos witnessed heavy rains caused by tropical storm Mulan, which caused flooding and landslides, resulting in 5 dead and 4 missing. In Afghanistan, flash floods kill more than 30 people in Parwan (FloodList, 2022). During summer 2023, at least 16 cities and provinces in northeastern China experienced record rainfall and flooding due to Typhoon Doksuri, the 5th typhoon in the Pacific in 2023. Beijing experienced its heaviest rainfall in 140 years. The rain exceeded 60% of a typical ' 'year's rain in just 83 hours. On Sept. 2, 2023, Typhoon Saola hit southern China, prompting the evacuation of more than 880,000 people, notably in the Hebei Province (Centre for Disaster Philanthropy, 2023). Global warming is also responsible for sea level rise. In 2016, Solomon Islands, an archipelago of six major islands and about 992 small islands, atolls, and reefs located in the Pacific Ocean, lost five of its islands (Albert et al., 2016). In Indonesia, Jakarta, whose metropolitan area is home to about 31 million, representing the second-most populous urban area in the world after Tokyo, is sinking so fast that Jakarta may vanish since the sea level is expected to rise by three feet in the region within the Century (Kimmelman, 2017). In 2024, floods made headlines around the world, with heavy rains causing flooding in the United Arab Emirates, mainly affecting the cities of Dubai and Sharjah, the Northern Emirates, and different areas of the Emirate of Ras Al Khaimah. Dubai flights in the world's second busiest international airport were delayed or cancelled, while people and students were asked to work and study from home (Salem et al., 2024). In Jordan, Irbid governorates has experienced several flash floods in recent years, which have caused extensive damage to infrastructure and 'residents' lives. Al Azzam and Al Kuisi (2023) developed a forecasting model based on the integration of a geographic information system, a watershed modeling system, a hydrological modeling system, and a river analysis system, which shows that in the next thousand years, Irbid governorate will experience persistent floods. People in the low-lying coastal districts of southwestern Bangladesh are particularly exposed to natural disasters such as coastal flooding and sea-level rise, the intensity of which has increased in recent years (Sultana and Hasan, 2024). Texas experienced heavy rainfall in the Houston area and other parts of Southeast Texas, which led to hundreds of rescues, including people, stranded on rooftops (Lozano, 2024). The death toll from the Kenya floods rises to 228 by May 2024. Torrential rains caused widespread flooding and landslides across the country (Miriri et al., 2024). By November 2024, in the Edo State of Nigeria, where crop farming is among the primary sources of income, 42,284 individuals in 7,656 households were affected by the floods (Reliefweb, 2024). Odiana, Mbee, and Akpoghomeh (2023) assessed the flood disaster preparedness and capacity assessment of crop farmers after years of regular flooding. Flood and landslide hit Indonesia's Sulawesi Island, killing 14 (Tarigan, 2024). Weeks of deadly floods triggered by record-smashing rainfall left parts of southern Brazil in disaster (Gilbert, 2024). More than 170 people were killed and nearly 580,000 displaced after storms and floods battered Brazil's southernmost state of Rio Grande do Sul, with local authorities describing it as the worst disaster in the region's history. Climate change has made devastating floods twice as likely (Araujo, 2024). Russia and Kazakhstan suffered the worst flooding in 80 years. Higher-than-usual spring temperatures caused much snow to melt rapidly, inundating parts of both countries (Fedorinova and Gizitdinov, 2024). Flooding hit China's south in June 2024. Heavy rains lashed the southeastern Fujian province and the Guangxi region (Master and Cao, 2024). Flooding, landslides, and damage to infrastructure have been reported following heavy rains affecting Northeastern and Central Switzerland as well as Southern Germany, where floods killed at least four (Swissinfo.ch, 2024). Floods due to intense precipitation are explained by climate change. Warmer oceans due to global warming increase the amount of water that evaporates into the air. When more moisture-laden air moves over land or converges on a storm system, it can produce more intense precipitation, resulting in a flood (EPA, 2024). In addition, as global temperatures increase, sea level rises due to a thermal expansion of the upper layers of the ocean and the melting of glaciers and ice sheets. For example, warmer waters north of Antarctica have melted and weakened the world's largest iceberg, A23a, which broke off the Filchner Ice Shelf in 1986. A23a got stuck on the seabed, then caught in an ocean vortex, but eventually started drifting again, finding itself in January 2025 about 280km from South Georgia island, on a collision course with this island of 3,755km^2, wildlife refuge, where it could run aground and break into pieces, endangering penguins and seals living there (Rannard and Rivault, 2025). Using a wavelet analysis forecasting model applied to global ocean mean sea level anomalies, this paper focuses on the alarming impact of global warming on seas and oceans across the Earth, especially on sea level rise.

Reviewing the literature that presents forecasts of floods in coastal cities, C40 is a global network of nearly 100 mayors of the world's leading cities that are united in action to confront the climate crisis (C40 Cities, 2025). Their article on sea level rise and coastal flooding predicts that by 2050, 800 million people will live in cities where sea levels could rise by more than half a metre. NASA presented a sea level projection tool on https://sealevel.nasa.gov/ipcc-ar6-sea-level-projection-tool based on the U.S. Intergovernmental Panel on Climate Change (IPCC) 6th Assessment Report Sea Level Projections with median projections of global and regional sea level rise, relative to a 1995-2014 baseline. The projections span from 2020 to 2150 presented by decades. Many studies address the consequences of floods on coastal cities and how they should prevent flooding but studies that apply a formal methodology to estimate in what years coastal cities will be flooded by the sea are scarce. For example, Kirezci et al. (2020) showed that in the absence of coastal protection or adaptation, and under a medium RCP8.5 scenario, there would be a 48% increase in global land area, a 52% increase in global population, and a 46% increase in global assets exposed to flood risk by 2100. In total, 68% of global coastal flooding will be caused by tides and storms, including 32% by projected regional sea-level rise. But no specific data on coastal cities was provided. Specifically, the present paper focuses on 100 coastal cities, estimating the years when floods will hit them with a sea level rise of 1 and 1.5 meters. The next section focuses on the literature on wavelet analysis applied to forecasting used in this paper.

2.2. Wavelet analysis applied to forecasting

Wavelet analysis has been primarily applied to physical phenomena such as electrical, audio, or seismic signals, which propagate through space in waveforms. Wavelet analysis has also been applied in finance and economics since interest rates, exchange rates, volatility of asset returns, gross domestic product, levels of employment or consumer spending propagate through time in waveforms. For example, Rostan and Rostan (2018a) illustrated the versatility of wavelet analysis to the forecast of financial time series with distinctive properties. The versatility of wavelet analysis was also demonstrated when applied to forecasting the growing number of European Muslim population (Rostan and Rostan, 2019), to assess the financial sustainability of the Spanish pension system (Rostan et al., 2015) as well as the Saudi pension system (Rostan and Rostan 2018b). Extending the analysis to the complex-behaviour of economic signals, wavelet analysis was applied to economic variables subject to common dynamics such as GDP time series that were used to forecast the Spanish economy (Rostan and Rostan, 2018c), as well as Greek (Rostan and Rostan, 2018d), Saudi (Rostan and Rostan, 2021a, 2024b, Rostan et al., 2024), Austrian (Rostan and Rostan, 2020), Persian Gulf (2022a), Turkish (2022b), UK (2022c) Australian (2024a), South Korea's (2023b), Cyprus' (2023c), Brazil's, Mexico's and Argentina's (2024b), Slovenia's (2024d), China's (2025) and the Eurozone's (Rostan et al., 2023) economies. Interest rates were forecasted with wavelet analysis due to their valuable property of propagating through time in waveforms (Rostan et al., 2017). In addition, fossil fuels price estimates (Rostan and Rostan, 2021b), solid waste of OECD countries (2023d), casualties resulting from state-based conflicts (2024e), and population estimates (Rostan and Rostan, 2017) were forecasted with wavelet analysis as well as global temperatures (Rostan and Rostan, 2023a). The methodology of the present paper involves a wavelet analysis forecasting model that generates forecast estimates of mean sea level anomaly of global ocean (annual signals retained) until 2301.

3. Materials and Methods

The aim of the study is to estimate in what years 100 coastal cities will be flooded by 1 to 1.5 meters by the sea. These 100 coastal cities were home to 438 million people in 2024, or about 5% of the world's population. Estimated years of flooding are obtained by forecasting mean sea level anomalies of global ocean with wavelet analysis until 2301. A mean sea level anomaly is the difference from an average, or 1995-2014 baseline, global sea level. Satellite altimeter radar measurements are combined with precisely known spacecraft orbits to measure sea level on a global basis with unprecedented accuracy. The methodology follows 4 steps illustrated in Figure 1.

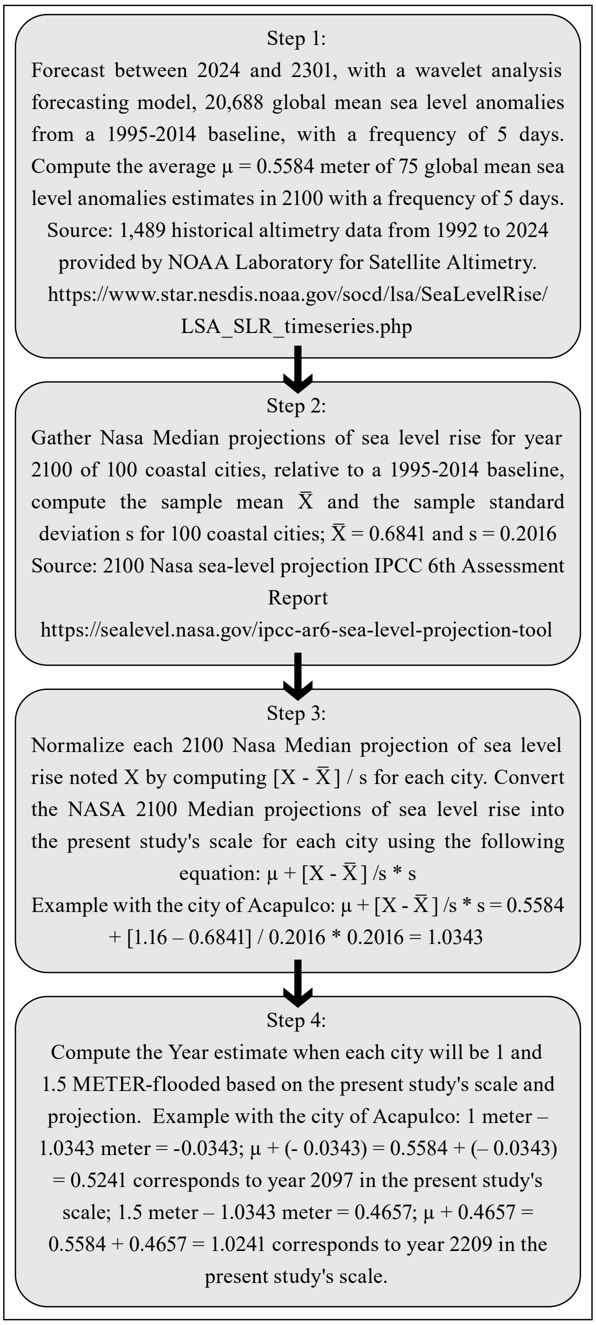

Step 1:
Forecast between 2024 and 2301, with a wavelet analysis forecasting model, 20,688 global mean sea level anomalies from a 1995-2014 baseline, with a frequency of 5 days. Compute the average μ = 0.5584 meter of 75 global mean sea level anomalies estimates in 2100 with a frequency of 5 days.
Source: 1,489 historical altimetry data from 1992 to 2024 provided by NOAA Laboratory for Satellite Altimetry.
https://www.star.nesdis.noaa.gov/socd/lsa/SeaLevelRise/LSA_SLR_timeseries.php

Step 2:
Gather Nasa Median projections of sea level rise for year 2100 of 100 coastal cities, relative to a 1995-2014 baseline, compute the sample mean $\bar{X}$ and the sample standard deviation s for 100 coastal cities; $\bar{X}$ = 0.6841 and s = 0.2016
Source: 2100 Nasa sea-level projection IPCC 6th Assessment Report
https://sealevel.nasa.gov/ipcc-ar6-sea-level-projection-tool

Step 3:
Normalize each 2100 Nasa Median projection of sea level rise noted X by computing $[X - \bar{X}] / s$ for each city. Convert the NASA 2100 Median projections of sea level rise into the present study's scale for each city using the following equation: $\mu + [X - \bar{X}] / s * s$
Example with the city of Acapulco: $\mu + [X - \bar{X}] / s * s = 0.5584 + [1.16 - 0.6841] / 0.2016 * 0.2016 = 1.0343$

Step 4:
Compute the Year estimate when each city will be 1 and 1.5 METER-flooded based on the present study's scale and projection. Example with the city of Acapulco: 1 meter – 1.0343 meter = -0.0343; μ + (- 0.0343) = 0.5584 + (– 0.0343) = 0.5241 corresponds to year 2097 in the present study's scale; 1.5 meter – 1.0343 meter = 0.4657; μ + 0.4657 = 0.5584 + 0.4657 = 1.0241 corresponds to year 2209 in the present study's scale.

Figure 1. Flowchart of the methodology from steps 1 to 4.

3.1. Step 1: Forecasting between 2024 and 2301, with a wavelet analysis forecasting model, mean sea level anomalies from a 1995-2014 baseline

The methodology, improved with a de-noising and compression, presented in a seminal paper of Rostan and Rostan (2018a), requires four levels illustrated with data from 1992 to 2024 (1,489 data) with a frequency of 5 to 10 days with an uncertainty of 3–4 mm representing mean sea level anomaly global ocean (annual signals retained), using a reference series of satellite missions that started with TOPEX/Poseidon (T/P) in 1992 and continued with Jason-1 (2001–2013), Jason-2 (2008–2019), Jason-3 (2016–present), and Sentinel-6MF (2020–present) estimate global mean sea level. For information, Jason-3, launched on January 17 2016, was a joint effort between NOAA, the National Aeronautics and Space Administration, France's Centre National d'Études Spatiales or CNES and the European Organisation for the Exploitation of Meteorological Satellites or EUMETSAT (NOAA, 2024).

Figure 2 illustrates the methodology of step 1. The detailed methodology of step 1, applied to temperature anomalies projections, is documented in Rostan and Rostan (2023a).

Steps 2, 3, and 4 are detailed in Table 1 of the Results section.

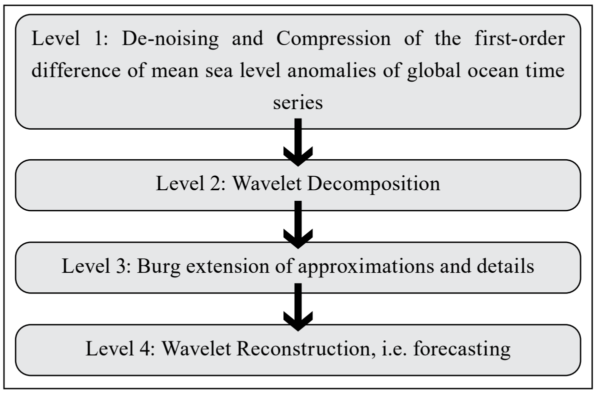

Level 1: De-noising and Compression of the first-order difference of mean sea level anomalies of global ocean time series

Level 2: Wavelet Decomposition

Level 3: Burg extension of approximations and details

Level 4: Wavelet Reconstruction, i.e. forecasting

Figure 2. Flowchart of the methodology of step 1.

Figure 3 illustrates the historical time series from 1992 to 2024 of 1,489 mean sea level anomalies with a frequency of 5 to 10 days (Source: NOAA/Laboratory for Satellite Altimetry). https://www.star.nesdis.noaa.gov/socd/lsa/SeaLevelRise/LSA_SLR_timeseries.php)

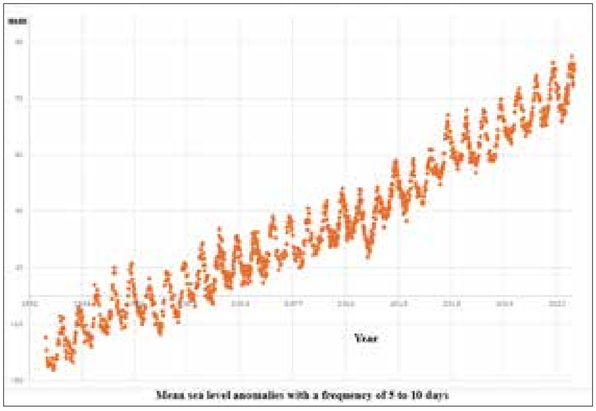

Figure 3. Historical time series from 1992 to 2024 of 1,489 mean sea level anomalies with a frequency of 5 to 10 days (Source: NOAA/Laboratory for Satellite Altimetry https://www.star.nesdis.noaa.gov/socd/lsa/SeaLevelRise/LSA_SLR_timeseries.php)

Figure 4 illustrates the historical time series from 1992 to 2024 of 1,489 mean sea level anomalies with a frequency of 5 to 10 days (Source: NOAA/Laboratory for Satellite Altimetry. https://www.star.nesdis.noaa.gov/socd/lsa/SeaLevelRise/LSA_SLR_timeseries.php) They are combined with the time series of 20,688 estimates of mean sea level anomalies from 2024 to 2301 with a frequency of 5 days obtained with the wavelet analysis forecasting model explained in step 1. The forecasting model, using Matlab, cannot generate 20,688 estimates at once from 1,489 historical data. The forecasting process is divided into 3 steps: 1) estimate 2,200 data from 1,489 historical data, 2) estimate 5,200 data from 3,689 data (2,200 + 1,489), and 3) estimate 13,288 data from 8,889 data (5,200 + 2,200 + 1,489). The total of the estimates is 2,200 + 5,200 + 13,288 = 20,688.

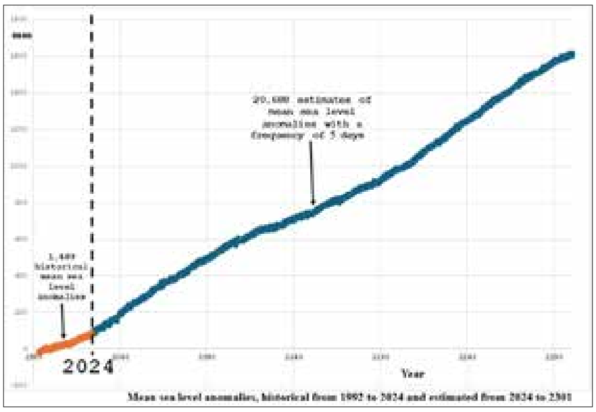

Figure 4. Historical time series from 1992 to 2024 of 1,489 mean sea level anomalies with a frequency of 5 to 10 days (Source: NOAA/Laboratory for Satellite Altimetry https://www.star.nesdis.noaa.gov/socd/lsa/SeaLevelRise/LSA_SLR_timeseries.php) combined with the time series of 20,688 estimates of mean sea level anomalies from 2024 to 2301 with a frequency of 5 days obtained with the wavelet analysis forecasting model explained in step 1.

3.2. Identifying the optimal level of decomposition

This section focuses on the optimal level of decomposition of the wavelet analysis forecasting model (Level 2: Wavelet Decomposition of step 1 presented in Figure 2). For this exercise, the 1,489 historical data are cut into two samples of size two-third and one-third: 997 historical data are used to estimate 497 in-sample data that are compared to the existing set of historical data. 7 models are used with level of decomposition ranging from 1 to 7. Levels 1, 3, 4, 5, 6, 7-decomposition return an error message. Only level 2-decomposition of the wavelet analysis generate estimates. The 2nd level of decomposition is, therefore, used to forecast 20,688 estimates, illustrated in Figure 4.

3.3. Benchmarking the level 2 wavelet analysis forecasting model to Linear and Polynomial extrapolations

20,688 estimates are generated from 1,489 historical data. Two other common methods of forecasting are used: linear and second-order polynomial extrapolations. As illustrated by Figure 5, second-order polynomial extrapolations bracket level 2 wavelet analysis estimates from above and linear extrapolations from below. The wavelet analysis forecasting model can be considered as the average scenario between the other two.

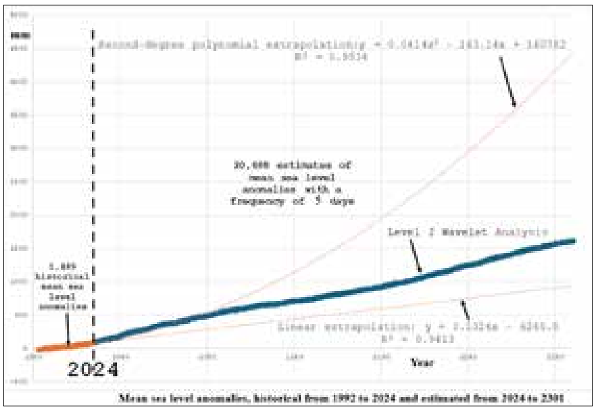

Figure 5. Historical time series from 1992 to 2024 of 1,489 mean sea level anomalies with a frequency of 5 to 10 days (Source: NOAA/Laboratory for Satellite Altimetry https://www.star.nesdis.noaa.gov/socd/lsa/SeaLevelRise/LSA_SLR_timeseries.php) combined with the time series of 20,688 estimates of mean sea level anomalies from 2024 to 2301 with a frequency of 5 to 10 days obtained with the wavelet analysis forecasting model benchmarked to Linear and Second-order polynomial extrapolations.

4. Results

The objective of the paper is to estimate in what years 100 coastal cities in 55 countries around the world will be flooded by the sea, home to 438 million people in 2024, or about 5% of the world's population. These 100 coastal cities can be identified on the map provided by NASA presented as a sea level projection tool on https://sealevel.nasa.gov/ipcc-ar6-sea-level-projection-tool as mentioned earlier. Estimated flood years are obtained by forecasting global ocean mean sea level anomalies with wavelet analysis up to 2301. Altimetry data are provided by NOAA Laboratory for Satellite Altimetry. 2100 median projections of regional sea level rise for 100 coastal cities, relative to a 1995 to 2014 baseline, provided by the Intergovernmental Panel on Climate Change's Sixth Assessment NASA Report, allow the authors to evaluate how far the sea level of 100 cities will expand in 2100 from the average sea-level for each city and transform the sea level to the scale of the projected sea-level relative to a 1995-2014 baseline to obtain an estimated year of flooding for each city. For the decomposition/reconstruction part of wavelet analysis, the 2nd level is used.

Table 1 presents the years in which 100 coastal cities worldwide will be flooded by the sea, using the wavelet analysis model presented in the methodology section, with floods of 1 meter (column 7) and 1.5 meters (column 8) and with information on each city and intermediate results. Used as benchmarks, columns 9 and 10 present the median projections of global and regional sea level rise, for floods of 1 meter and 1.5 meters respectively, provided by the United States Intergovernmental Panel on Climate Change (IPCC, 2025).

Table 1. In what years 100 coastal cities around the world will be flooded by the sea with floods of 1 meter (column 7) and 1.5 meters (column 8) versus IPCC 6th Assessment Report Sea Level Projections of 1 meter (column 9) and 1.5 meters (column 10) with information on each city and intermediate results.

	City	Population in million (1)	Country	Income level (2)	2100 Nasa Median project-tions of sea level rise (3)	Compute $(x - \bar{x})$ / s (4)	2100 average sea-level projected by the present study (5)	Conver-sion of the NASA scale into the present study's scale (6)	Year-estimate the City will be 1 meter-flooded based on the present study (7)	Year-estimate the City will be 1.5 meter-flooded based on the present study (8)	Year-estimate the City will be 1.0 meter-flooded based on IPCC (9)	Year-estimate the City will be 1.5 meter-flooded based on IPCC (10)
1	Acapulco	1.032	Mexico	Upper-middle-income	1.16	2.3605	0.5584	1.0343	2097	2209	2100	2130
2	Aden	1.116	Yemen	Low-income	0.67	-0.0699	0.5584	0.5443	2206	2278	2130	After 2150
3	Alexandria	5.2	Egypt	Lower-middle-income	0.74	0.2773	0.5584	0.6143	2191	2267	2130	After 2150
4	Amsterdam	0.821	Nether-lands	High-income	0.69	0.0293	0.5584	0.5643	2202	2274	2150	After 2150
5	Antalya	1.372	Turkey	Upper-middle-income	0.74	0.2773	0.5584	0.6143	2191	2267	2130	After 2150
6	Athens	3.154	Greece	High-income	0.48	-1.0124	0.5584	0.3543	2232	After 2301	After 2150	After 2150
7	Auckland	1.692	New Zealand	High-income	0.73	0.2277	0.5584	0.6043	2194	2270	2130	After 2150
8	Bandar Abbas*	0.526	Iran	Upper-middle-income	0.61	-0.3675	0.5584	0.4843	2214	2289	2140	After 2150
9	Baltimore	1.462	US	High-income	0.94	1.2693	0.5584	0.8143	2147	2238	2110	2150
10	Bangkok	11.234	Thailand	Upper-middle-income	1.79	5.4854	0.5584	1.6643	Soon	2073	2070	2090
11	Barcelona	5.711	Spain	High-income	0.75	0.3269	0.5584	0.6243	2191	2267	2130	After 2150
12	Batumi	0.152	Georgia	Upper-middle-income	0.6	-0.4171	0.5584	0.4743	2214	2293	2150	After 2150
13	Belem	2.432	Brazil	Upper-middle-income	0.69	0.0293	0.5584	0.5643	2202	2274	2130	After 2150
14	Belfast	0.647	UK	High-income	0.48	-1.0124	0.5584	0.3543	2232	After 2301	After 2150	After 2150
15	Boston	0.629	US	High-income	0.89	1.0213	0.5584	0.7643	2158	2247	2120	After 2150
16	Buenos Aires	15.37	Argentina	High-income	0.65	-0.1691	0.5584	0.5243	2208	2283	2140	After 2150
17	Busan	3.477	South Korea	High-income	0.73	0.2277	0.5584	0.6043	2194	2270	2130	After 2150
18	Brisbane	2.69	Australia	High-income	0.68	-0.0203	0.5584	0.5543	2203	2277	2130	After 2150
19	Cape Town	4.977	South Africa	Upper-middle-income	0.68	-0.0203	0.5584	0.5543	2203	2277	2130	After 2150
20	Cardiff	0.362	UK	High-income	0.64	-0.2187	0.5584	0.5143	2210	2284	2150	After 2150
21	Cartagena	1.096	Colombia	Upper-middle-income	0.94	1.2693	0.5584	0.8143	2147	2238	2110	2150

Continuing from Table 1. In what years 100 coastal cities around the world will be flooded by the sea with floods of 1 meter (column 7) and 1.5 meters (column 8) versus IPCC 6th Assessment Report Sea Level Projections of 1 meter (column 9) and 1.5 meters (column 10) with information on each city and intermediate results.

	City	Population in million (1)	Country	Income level (2)	2100 Nasa Median projections of sea level rise (3)	Compute $(x - \bar{x}) / s$ (4)	2100 average sea-level projected by the present study (5)	Conversion of the NASA scale into the present study's scale (6)	Year-estimate the City will be 1 meter-flooded based on the present study (7)	Year-estimate the City will be 1.5 meter-flooded based on the present study (8)	Year-estimate the City will be 1.0 meter-flooded based on IPCC (9)	Year-estimate the City will be 1.5 meter-flooded based on IPCC (10)
22	Chennai	6.6	India	Lower-middle-income	0.57	-0.5659	0.5584	0.4443	2220	2299	2150	After 2150
23	Copenhagen	1.391	Denmark	High-income	0.61	-0.3675	0.5584	0.4843	2214	2289	2150	After 2150
24	Dakar	3.54	Senegal	Upper-middle-income	0.69	0.0293	0.5584	0.5643	2202	2274	2130	After 2150
25	Dalian	6.217	China	Upper-middle-income	0.7	0.0789	0.5584	0.5743	2198	2273	2130	After 2150
26	Davao	1.991	Philippines	Lower-middle-income	0.71	0.1285	0.5584	0.5843	2197	2272	2130	After 2150
27	Doha*	0.665	Qatar	High-income	0.61	-0.3675	0.5584	0.4843	2214	2289	2140	After 2150
28	Dubai*	3.4	United Arab Emirates	High-income	0.61	-0.3675	0.5584	0.4843	2214	2289	2140	After 2150
29	Dublin	1.284	Ireland	High-income	0.6	-0.4171	0.5584	0.4743	2214	2293	2150	After 2150
30	Durban	3.262	South Africa	Upper-middle-income	0.68	-0.0203	0.5584	0.5543	2203	2277	2130	After 2150
31	Edinburgh	0.105	UK	High-income	0.55	-0.6651	0.5584	0.4243	2223	After 2301	After 2150	After 2150
32	Genoa	0.674	Italy	High-income	0.61	-0.3675	0.5584	0.4843	2214	2289	2150	After 2150
33	Gdansk	0.465	Poland	High-income	0.75	0.3269	0.5584	0.6243	2191	2267	2130	After 2150
34	Goteborg	0.638	Sweden	High-income	0.42	-1.3100	0.5584	0.2943	2242	After 2301	After 2150	After 2150
35	Haiphong	1.463	Vietnam	Lower-middle-income	0.5	-0.9132	0.5584	0.3743	2230	After 2301	2130	After 2150
36	Hamburg	1.841	Germany	High-income	0.73	0.2277	0.5584	0.6043	2194	2270	2130	After 2150
37	Havana	2.152	Cuba	Upper-middle-income	0.83	0.7237	0.5584	0.7043	2173	2254	2120	After 2150
38	Helsinki	1.346	Finland	High-income	0.32	-1.8060	0.5584	0.1943	2255	After 2301	After 2150	After 2150
39	Hiroshima	2.062	Japan	High-income	0.95	1.3189	0.5584	0.8243	2146	2236	2110	2140
40	Ho Chi Minh City	9.568	Vietnam	Lower-middle-income	0.5	-0.9132	0.5584	0.3743	2230	After 2301	2130	After 2150
41	Hong Kong	7.726	Hong Kong	High-income	0.68	-0.0203	0.5584	0.5543	2203	2277	2140	After 2150
42	Istanbul**	15.97	Turkey	Upper-middle-income	0.58	-0.5163	0.5584	0.4543	2220	After 2301	2150	After 2150

Continuing from Table 1. In what years 100 coastal cities around the world will be flooded by the sea with floods of 1 meter (column 7) and 1.5 meters (column 8) versus IPCC 6th Assessment Report Sea Level Projections of 1 meter (column 9) and 1.5 meters (column 10) with information on each city and intermediate results.

	City	Population in million (1)	Country	Income level (2)	2100 Nasa Median projections of sea level rise (3)	Compute $(x - \bar{x}) / s$ (4)	2100 average sea-level projected by the present study (5)	Conversion of the NASA scale into the present study's scale (6)	Year-estimate the City will be 1 meter-flooded based on the present study (7)	Year-estimate the City will be 1.5 meter-flooded based on the present study (8)	Year-estimate the City will be 1.0 meter-flooded based on IPCC (9)	Year-estimate the City will be 1.5 meter-flooded based on IPCC (10)
43	Izmir	3.12	Turkey	Upper-middle-income	0.71	0.1285	0.5584	0.5843	2197	2272	2140	After 2150
44	Jacksonville	0.971	US	High-income	0.84	0.7733	0.5584	0.7143	2171	2254	2120	After 2150
45	Jeddah****	4.18	Saudi Arabia	High-income	0.67	-0.0699	0.5584	0.5443	2206	2278	2130	After 2150
46	Karachi	17.649	Pakistan	Lower-middle-income	0.6	-0.4171	0.5584	0.4743	2214	2293	2150	After 2150
47	Kolkata	15.571	India	Lower-middle-income	0.5	-0.9132	0.5584	0.3743	2230	After 2301	2130	After 2150
48	Kuala Lumpur	8.815	Malaysia	Upper-middle-income	0.65	-0.1691	0.5584	0.5243	2208	2283	2150	After 2150
49	Lisbon	3.014	Portugal	High-income	0.71	0.1285	0.5584	0.5843	2197	2272	2130	After 2150
50	London	8.982	UK	High-income	0.67	-0.0699	0.5584	0.5443	2206	2278	2140	After 2150
51	Los Angeles	3.97	US	High-income	0.54	-0.7147	0.5584	0.4143	2225	After 2301	After 2150	After 2150
52	Manila	14.942	Philippines	Lower-middle-income	1.22	2.6581	0.5584	1.0943	2083	2196	2090	2120
53	Marseille	1.635	France	High-income	0.63	-0.2683	0.5584	0.5043	2211	2287	2140	After 2150
54	Miami	0.449	US	High-income	0.85	0.8229	0.5584	0.7243	2169	2251	2120	After 2150
55	Monaco	0.036	Monaco	High-income	0.56	-0.6155	0.5584	0.4343	2221	After 2301	2150	After 2150
56	Mombasa	1.495	Kenya	Lower-middle-income	0.74	0.2773	0.5584	0.6143	2191	2267	2130	After 2150
57	Mumbai	21.673	India	Lower-middle-income	0.58	-0.5163	0.5584	0.4543	2220	After 2301	2150	After 2150
58	Naples	0.954	Italy	High-income	0.61	-0.3675	0.5584	0.4843	2214	2289	2150	After 2150
59	New Orleans	1.021	US	High-income	1.02	1.6661	0.5584	0.8943	2124	2227	2100	2140
60	New York City	19.034	US	High-income	0.93	1.2197	0.5584	0.8043	2152	2239	2110	2150
61	Osaka	18.967	Japan	High-income	1.05	1.8149	0.5584	0.9243	2115	2222	2100	2130
62	Oslo	0.84	Norway	High-income	0.25	-2.1532	0.5584	0.1243	2267	After 2301	After 2150	After 2150
63	Palermo	0.85	Italy	High-income	0.61	-0.3675	0.5584	0.4843	2214	2289	2150	After 2150
64	Panama City	2.015	Panama	High-income	0.74	0.2773	0.5584	0.6143	2191	2267	2130	After 2150

Continuing from Table 1. In what years 100 coastal cities around the world will be flooded by the sea with floods of 1 meter (column 7) and 1.5 meters (column 8) versus IPCC 6th Assessment Report Sea Level Projections of 1 meter (column 9) and 1.5 meters (column 10) with information on each city and intermediate results.

	City	Population in million (1)	Country	Income level (2)	2100 Nasa Median projections of sea level rise (3)	Compute $(x - \bar{x}) / s$ (4)	2100 average sea-level projected by the present study (5)	Conversion of the NASA scale into the present study's scale (6)	Year-estimate the City will be 1 meter-flooded based on the present study (7)	Year-estimate the City will be 1.5 meter-flooded based on the present study (8)	Year-estimate the City will be 1.0 meter-flooded based on IPCC (9)	Year-estimate the City will be 1.5 meter-flooded based on IPCC (10)
65	Perth	2.143	Australia	High-income	0.69	0.0293	0.5584	0.5643	2202	2274	2130	After 2150
66	Philadelphia	3.677	US	High-income	0.92	1.1701	0.5584	0.7943	2154	2242	2110	2150
67	Port Elizabeth	1.312	South Africa	Upper-middle-income	0.72	0.1781	0.5584	0.5943	2196	2270	2130	After 2150
68	Port Said	0.78	Egypt	Lower-middle-income	0.69	0.0293	0.5584	0.5643	2202	2274	2130	After 2150
69	Rangoon	7.36	Myanmar	Lower-middle-income	0.82	0.6741	0.5584	0.6943	2175	2255	2120	After 2150
70	Recife	4.305	Brazil	Upper-middle-income	0.69	0.0293	0.5584	0.5643	2202	2274	2130	After 2150
71	Reykjavik	0.128	Iceland	High-income	0.26	-2.1036	0.5584	0.1343	2266	After 2301	After 2150	After 2150
72	Riga	0.618	Latvia	High-income	0.63	-0.2683	0.5584	0.5043	2211	2287	2150	After 2150
73	Rio de Janeiro	13.824	Brazil	Upper-middle-income	0.7	0.0789	0.5584	0.5743	2198	2273	2130	After 2150
74	Salvador do Bahia	2.9	Brazil	Upper-middle-income	0.7	0.0789	0.5584	0.5743	2198	2273	2130	After 2150
75	San Diego	2.35	US	High-income	0.65	-0.1691	0.5584	0.5243	2208	2283	2140	After 2150
76	San Francisco	0.9	US	High-income	0.63	-0.2683	0.5584	0.5043	2211	2287	2140	After 2150
77	San Jose	0.645	Philippines	Lower-middle-income	0.96	1.3685	0.5584	0.8343	2141	2235	2100	2140
78	Seattle	0.757	US	High-income	0.61	-0.3675	0.5584	0.4843	2214	2289	2150	After 2150
79	Sevastopol	0.401	Ukraine	Lower-middle-income	0.54	-0.7147	0.5584	0.4143	2225	After 2301	After 2150	After 2150
80	Shenzhen	13.312	China	Upper-middle-income	0.6	-0.4171	0.5584	0.4743	2214	2293	2140	After 2150
81	Singapore	6.052	Singapore	High-income	0.65	-0.1691	0.5584	0.5243	2208	2283	2140	After 2150
82	St. Petersburg ***		Russia	Upper-middle-income	0.52	-0.8140	0.5584	0.3943	2227	After 2301	After 2150	After 2150
83	Stockholm	0.975	Sweden	High-income	0.19	-2.4508	0.5584	0.0643	2274	After 2301	After 2150	After 2150
84	Sydney	5.33	Australia	High-income	0.68	-0.0203	0.5584	0.5543	2203	2277	2130	After 2150
85	Tianjin	14.471	China	Upper-middle-income	0.65	-0.1691	0.5584	0.5243	2208	2283	2140	After 2150

Continuing from Table 1. In what years 100 coastal cities around the world will be flooded by the sea with floods of 1 meter (column 7) and 1.5 meters (column 8) versus IPCC 6th Assessment Report Sea Level Projections of 1 meter (column 9) and 1.5 meters (column 10) with information on each city and intermediate results.

	City	Population in million (1)	Country	Income level (2)	2100 Nasa Median project-tions of sea level rise (3)	Compute ($x - \bar{x}$) / s (4)	2100 average sea-level projected by the present study (5)	Conver-sion of the NASA scale into the present study's scale (6)	Year-estimate the City will be 1 meter-flooded based on the present study (7)	Year-estimate the City will be 1.5 meter-flooded based on the present study (8)	Year-estimate the City will be 1.0 meter-flooded based on IPCC (9)	Year-estimate the City will be 1.5 meter-flooded based on IPCC (10)
86	Taipei	2.766	Taiwan	High-income	0.71	0.1285	0.5584	0.5843	2197	2272	2130	After 2150
87	Thessaloniki	0.815	Greece	High-income	0.75	0.3269	0.5584	0.6243	2191	2267	2130	After 2150
88	Tokyo	37.115	Japan	High-income	0.61	-0.3675	0.5584	0.4843	2214	2289	2140	After 2150
89	Trieste	0.216	Italy	High-income	0.58	-0.5163	0.5584	0.4543	2220	After 2301	2150	After 2150
90	Valencia	0.839	Spain	High-income	0.71	0.1285	0.5584	0.5843	2197	2272	2130	After 2150
91	Valparaiso	1.016	Chile	High-income	0.44	-1.2108	0.5584	0.3143	2238	After 2301	After 2150	After 2150
92	Vancouver	0.678	Canada	High-income	0.41	-1.3596	0.5584	0.2843	2244	After 2301	After 2150	After 2150
93	Varna	0.334	Bulgaria	Upper-middle-income	0.52	-0.8140	0.5584	0.3943	2227	After 2301	After 2150	After 2150
94	Venezia	0.641	Italy	High-income	0.68	-0.0203	0.5584	0.5543	2203	2277	2140	After 2150
95	Visakhapatnam	2.385	India	Lower-middle-income	0.54	-0.7147	0.5584	0.4143	2225	After 2301	2150	After 2150
96	Vung Tao	0.466	Vietnam	Lower-middle-income	0.72	0.1781	0.5584	0.5943	2196	2270	2130	After 2150
97	Washington DC	7.82	US	High-income	0.94	1.2693	0.5584	0.8143	2147	2238	2110	2150
98	Xiamen	4.007	China	Upper-middle-income	0.71	0.1285	0.5584	0.5843	2197	2272	2130	After 2150
99	Yangon	5.71	Myanmar	Lower-middle-income	0.82	0.6741	0.5584	0.6943	2175	2255	2120	After 2150
100	Yantai	2.834	China	Upper-middle-income	0.61	-0.3675	0.5584	0.4843	2214	2289	2150	After 2150
	Total population of 100 cities:	438		Mean of (3):	0.6841			Max:	2274	2299		
				Standard deviation of (3):	0.2016			Min:	2083	2073		
								Mean:	2201	2267		

(1) 2024 population estimate of the city in million.

(2) Income level of the country's economy (2024 World Bank ranking).

(3) 2100 Nasa Median projections of sea level rise, relative to a 1995-2014 baseline.

(4) Compute ($\bar{X}$) / s with X = (3), $\bar{X}$= 3 mean of column (3), s = Standard deviation of column (3).

(5) 2100 average sea-level projected by the present study above the 1995-2014 index average in meter.

(6) Conversion of the NASA scale into the present study's scale for a given City (5)+(4)*s.

(7) Year-estimate the City will be 1 meter-flooded based on the present study's scale and projection.

(8) Year-estimate the City will be 1.5 meter-flooded based on the present study's scale and projection.

(9) Year-estimate the City will be 1 meter-flooded based on the U.S. Intergovernmental Panel on Climate Change (IPCC) 6th Assessment Report Sea Level Projections of Median projections of global and regional sea level rise available on https://sealevel.nasa.gov/ipcc-ar6-sea-level-projection-tool.

(10) Year-estimate the City will be 1.5 meter-flooded based on the U.S. Intergovernmental Panel on Climate Change (IPCC) 6th Assessment Report Sea Level Projections of Median projections of global and regional sea level rise available on https://sealevel.nasa.gov/ipcc-ar6-sea-level-projection-tool.

Sources: https://sealevel.nasa.gov/ipcc-ar6-sea-level-projection-tool
https://www.nestpick.com/2050-climate-change-city-index/
https://www.macrotrends.net/global-metrics/cities/largest-cities-by-population
https://earth.org/data_visualization/sea-level-rise-by-2100-dubai/
https://earth.org/data_visualization/sea-level-rise-by-2100-qatar-and-bahrain/
https://blogs.worldbank.org/en/opendata/world-bank-country-classifications-by-income-level-for-2024-2025
(*) Bandar Abbas, Doha, Dubai estimates based on Masirah (Oman) estimate
(**) Istanbul estimate based on Bourgas (Bulgaria) estimate
(***) St. Petersburg estimate based on Primorsk (Russia) estimate
(****) Jeddah estimate based on Aden (Yemen) estimate

Regarding the results in Table 1, it is essential to mention that in addition to sea level rise, flooding comes from heavy rains. In 2024, floods made headlines around the world, with heavy rains causing flooding in the United Arab Emirates, Texas, Kenya, the Indonesian island of Sulawesi, Brazil, Russia, Kazakhstan, China, Switzerland, and Germany. Flooding, due to intense rainfall, can also be explained by climate change. Warmer oceans, due to global warming, increase the amount of water that evaporates into the air. When more moisture-laden air moves over land or converges into a storm system, it can produce more intense precipitation leading to flooding (EPA, 2024). The combined effect of sea level rise and heavy rains, which may cause the floods, were not considered in this article to obtain an estimate of the flood years of 100 cities, but only from the perspective of sea level rise. The estimates of flood years, provided in Table 1, are therefore very conservative. To illustrate this conservative approach, the year-estimate when the City will be 1 meter-flooded based on the present study's scale and projection (column 7) and the year-estimate the City will be 1.5 meter-flooded based on the present study's scale and projection (column 8) have been benchmarked with the year-estimate when the City will be 1 meter-flooded based on Median projections of global and regional sea level rise provided by the U.S. Intergovernmental Panel on Climate Change (IPCC) 6th Assessment Report Sea Level Projections (column 9) and the year-estimate the City will be 1.5 meter-flooded based on Median projections of global and regional sea level rise provided again by the US IPCC 6th Assessment Report Sea Level Projections (column 10). Where estimates were available (the IPCC did not provide projections beyond 2150), estimates obtained from wavelet analysis (i.e. the model used by the authors) confirm that they are more conservative, while the IPCC authors estimate that flood dates will occur in the nearer future, on average, for the sample of 100 cities, 57 years earlier for the 1-meter flood estimates and 73 years earlier for the 1.5-meter flood estimates.

5. Discussion and conclusion

This article estimates in what years 100 coastal cities in 55 countries around the world will be flooded by the sea, home to 438 million people in 2024, or about 5% of the world's population. Estimated flood years are obtained by forecasting global ocean mean sea level anomalies with wavelet analysis up to 2301. Altimetry data are provided by NOAA Laboratory for Satellite Altimetry. 2100 median projections of regional sea level rise for 100 coastal cities, relative to a 1995 to 2014 baseline, provided by the Intergovernmental Panel on Climate Change's Sixth Assessment NASA Report, allow the authors to evaluate how far the sea level of 100 cities will expand in 2100 from the average sea-level for each city and transform the sea level to the scale of the projected sea-level relative to a 1995-2014 baseline to obtain an estimated year of flooding for each city. If the floods correspond to a 1 meter-rise in sea level, the estimated flood years for the 100 cities will range from 2083 for Manila to 2274 for Stockholm and the floods will average 2201 for cities, like Amsterdam, Dakar, Dalian, Izmir, Lisbon, London, Perth, Rio de Janeiro, Sydney, Taipei, Valencia, and Xiamen, close to the average year. As global temperatures increase, sea level rises because of a thermal expansion of upper layers of the ocean and melting of glaciers and ice sheets (NOAA, 2024). In addition to sea level rise, flooding comes from heavy rains. In 2024, floods made headlines around the world, with heavy rains causing flooding in the United Arab Emirates, Texas, Kenya, the Indonesian island of Sulawesi, Brazil, Russia, Kazakhstan, China, Switzerland, and Germany. Flooding, due to intense rainfall, can also be explained by climate change. Warmer oceans, due to global warming, increase the amount of water that evaporates into the air. When more moisture-laden air moves over land or converges into a storm system, it can produce more intense precipitation leading to flooding (EPA, 2024). The combined effect of sea level rise and heavy rains, which may cause the floods, were not considered in this article to obtain an estimate of the flood years of 100 cities, but only from the perspective of sea level rise. The estimated flood years provided in the results are therefore very conservative. Benchmarking the year-estimates of flood to the median projections of global and regional sea level rise provided by the US IPCC 6th Assessment Report Sea Level Projections shows that the IPCC authors estimate that flood dates will occur in the nearer future, on average, for the sample of 100 cities, 57 years earlier for the 1-metre flood estimates and 73 years earlier for the 1.5-metre flood estimates. Future will tell which methodology is more accurate.

Looking at the impact on coastal cities, flooding can lead to loss of life, damage to property and infrastructure, road closures, erosion and landslide risks, ineffective flood drainage system, contamination of freshwater supplies, rapid shoreline retreat (Bidorn et al., 2021), and groundwater salinization (Lassiter, 2021). Tools to prevent or delay flooding include flood protection structures such as levees, dikes, polder systems, river embankments, waterway improvements, drainage infrastructure upgrades and pumping stations (Coastal Wiki, 2025). They also include adapting households to flooding by raising floors and adding storeys to their homes. Urban planning can be involved to relocate populations and essential infrastructure to higher ground. Flood forecasting (as in this paper) and early warning systems can be put in place to prepare residents and flood management services.

The cause of an increase of global temperature responsible for floods is mainly greenhouse-gas emissions. Fossil fuels – coal, oil and gas – are, by far, the largest contributor to global climate change, accounting for over 75% of global greenhouse gas emissions and nearly 90% of all carbon dioxide emissions. As greenhouse gas emissions blanket the Earth, they trap the sun's heat (United Nations, 2024b). In 2016, world governments ratified the Paris agreement on climate change with the main objective to keep or to move major investors away from fossil fuels in order to save the planet from global warming. The Conferences of the Parties (COP) assess the progress made towards the goals set in the Paris Agreement and charted a course of action. The 28th COP was held at the end of 2023 in Dubai, United Arab Emirates. The role of fossil fuels in Gulf economies has made the issue of phasing out fossil fuels a particularly controversial topic at COP28, as phasing out fossil fuels could be very costly for these Gulf countries. COP29 was held in Baku, Azerbaijan, in November 2024. Environmentalists are not convinced of the outcomes of these conferences. Countries and peoples hit hardest by climate change are unable to get their voices heard during these Climate summits (Steffen and Niranjan, 2021). Environmentalists point out that COP is overwhelmingly white and rich and in no hurry to prevent the devastating effects of global warming. With so much coal, oil, and gas revenue involved and generated by the fossil fuel industry, the main culprit of global warming. "We are close to the tipping point where global warming will become irreversible" warned late physicist and cosmologist Stephen Hawking in 2017. Critical solutions to stopping global warming and its destructive and pervasive effects lie in the hands of responsible Earthlings and their political representatives.

Declarations

Data Availability Statement

The datasets supporting the findings of this study are openly available from the following sources:

- NOAA Laboratory for Satellite Altimetry: Mean sea level anomaly (global ocean, annual signals retained) derived from altimetry data, available at https://www.star.nesdis.noaa.gov/socd/lsa/SeaLevelRise/LSA_SLR_timeseries.php.
- NASA/IPCC Sea Level Projection Tool: Median projections of regional sea level rise by 2100 for 100 coastal cities, relative to a 1995–2014 baseline, based on the Intergovernmental Panel on Climate Change's Sixth Assessment Report, accessible via https://sealevel.nasa.gov/ipcc-ar6-sea-level-projection-tool.
- Macrotrends Database: Population data for the world's largest cities, available at https://www.macrotrends.net/global-metrics/cities/largest-cities-by-population.

Funding

The authors did not receive any funding or financial support from any organization for the submitted work.

Competing Interests

The authors declare that they have no competing financial or non-financial interests relevant to the content of this article.

References

Al Azzam, N., and Al Kuisi, M. (2021). Determination of Flash Floods Hazards and Risks for Irbid Governorates Using Hydrological and Hydraulic Modelling. Jordan Journal of Earth and Environmental Sciences 12 (1): 81-91 https://jjees.hu.edu.jo/files/Vol12No1/JJEES_Vol_12_No_1_P9.pdf (Feb. 19, 2025).

Araujo, G. (2024). Climate change made devastating Brazil floods twice as likely, scientists say. Reuters. https://www.reuters.com/business/environment/climate-change-made-devastating-brazil-floods-twice-likely-scientists-say-2024-06-03/ (Feb. 19, 2025).

Bidorn, B., Sok, K., Bidorn, K., and Burnett, W.C. (2021). An analysis of the factors responsible for the shoreline retreat of the Chao Phraya Delta (Thailand). Science of the Total Environment 769: 145253, https://doi.org/10.1016/j.scitotenv.2021.145253. (Feb. 19, 2025).

Center for Disaster Philanthropy. (2023). 2023 China Floods, https://disasterphilanthropy.org/disasters/2023-china-floods/ (Feb. 19, 2025).

C40 Cities. (2025). Sea Level Rise and Coastal Flooding, https://www.c40.org/what-we-do/scaling-up-climate-action/water-heat-nature/the-future-we-dont-want/sea-level-rise/ (Feb. 19, 2025).

Coastal Wiki. (2025). Coastal cities and sea level rise, https://www.coastalwiki.org/wiki/Coastal_cities_and_sea_level_rise#cite_note-L21-20 (Feb. 19, 2025).

Ekwurzel, B., Boneham, J., Dalton, M.W., Heede, R., Mera, R.J., Allen, M.R. and Frumhoff, P.C. (2017). The rise in global atmospheric CO2, surface temperature, and sea level from emissions traced to major carbon producers. Climatic Change 144(4): 579-590.

EPA, (2024). Climate Change Indicators: Heavy Precipitation, U.S. Environmental Protection Agency, https://www.epa.gov/climate-indicators/climate-change-indicators-heavy-precipitation (Feb. 19, 2025).

Fedorinova, Y., and Gizitdinov, N. (2024). Russia and Kazakhstan Suffer Worst Flooding in 80 Years. Bloomberg, https://www.bloomberg.com/news/articles/2024-04-19/russia-floods-latest-hundreds-of-thousands-evacuated-damage-uncertain (Feb. 19, 2025).

FloodList. (2022). Asia, https://floodlist.com/asia (Feb. 19, 2025).

Gilbert, M. (2024). ' 'Brazil's floods smashed through barriers designed to keep them out, trapping water in for weeks — and exposing social woes. CNN, https://edition.cnn.com/2024/05/19/climate/brazil-floods-social-problems-intl/index.html (Feb. 19, 2025).

Hamadeh, N., Van Rompaey, C., and Metreau, E. (2023). World Bank Group country classifications by income level for FY24 (July 1, 2023- June 30, 2024). World Bank Blogs, https://blogs.worldbank.org/en/opendata/new-world-bank-group-country-classifications-income-level-fy24 (Feb. 19, 2025).

Harvey, F. (2017). Calls for greater fossil fuel divestment at anniversary of Paris climate deal. The Guardian, https://www.theguardian.com/environment/2017/dec/12/calls-for-greater-fossil-fuel-divestment-at-anniversary-of-paris-climate-deal (Feb. 19, 2025).

Hawking, S. (2017). We Are Close to the Tipping Point Where Global Warming Becomes Irreversible. Futurism.com, https://futurism.com/stephen-hawking-we-are-close-to-the-tipping-point-where-global-warming-becomes-irreversible (Feb. 19, 2025).

Kimmelman, M., (2017). Jakarta Is Sinking So Fast, It Could End Up Underwater. New York Times, https://www.nytimes.com/interactive/2017/12/21/world/asia/jakarta-sinking-climate.html (Feb. 19, 2025).

IPCC. (2025). Intergovernmental Panel on Climate ‘ ‘Change’s Sixth Assessment Report 6th Assessment Report Sea Level Projections of median projections of global and regional sea level rise, https://sealevel.nasa.gov/ipcc-ar6-sea-level-projection-tool (Feb. 19, 2025).

Kirezci, E., Young, I.R., Ranasinghe, R., et al. (2020). Projections of global-scale extreme sea levels and resulting episodic coastal flooding over the 21st Century. Sci Rep 10: 11629, https://doi.org/10.1038/s41598-020-67736-6 (Feb. 19, 2025).

Lassiter, A. 2021. Rising seas, changing salt lines, and drinking water salinization. Current Opinion in Environmental Sustainability 50: 208–214.

Lozano, J. A. (2024). Floodwaters start receding around Houston area as recovery begins following rescues and evacuations. AP, https://apnews.com/article/houston-texas-flooding-severe-weather-117b0f63c9bd53be31ee34e11547da21 (Feb. 19, 2025)

Master, F., and Cao, E. (2024). Flooding hits China’s south, temperatures sizzle elsewhere. Reuters, https://www.reuters.com/world/china/flooding-hits-chinas-south-temperatures-sizzle-elsewhere-2024-06-16/ (Feb. 19, 2025).

Miriri, D., Malalo, H., and Biryabarema, E. (2024). Death toll from Kenya floods rises to 228. Reuters, https://www.reuters.com/world/africa/death-toll-kenya-floods-rises-228-2024-05-05/ (Feb. 19, 2025).

NOAA. (2024). Ocean Topography and Cryosphere Branch / Laboratory for Satellite Altimetry / Sea Level Rise, https://ww.star.nesdis.noaa.gov/socd/lsa/SeaLevelRise/ (Feb. 19, 2025).

Noor, D. (2025). Trump vows to ‘”unleash’ oil and gas drilling as he rolls back climate rules. The Guardian, https://www.theguardian.com/us-news/2025/jan/20/trump-executive-order-energy-emergency (Feb. 19, 2025).

Odiana, S., Mbee, D.M, and Akpoghomeh, O.S. (2023). Flood Disaster Preparedness and Capacity Assessment Among Crop Farmers in Edo State, Nigeria. Jordan Journal of Earth and Environmental Sciences 14(2): 83-90. https://jjees.hu.edu.jo/files/Vol14/No.2/JJEES_Vol_14_No_2_P1.pdf (Feb. 19, 2025).

Rannard, G., and Rivault, E. (2025). Giant iceberg on crash course with island, putting penguins and seals in danger. BBC, https://www.bbc.com/news/articles/cd64vvg4z6go (Feb. 19, 2025).

Reimann, L., Vafeidis, A.T., and Honsel, L.E. (2023). Population development as a driver of coastal risk: Current trends and future pathways. Cambridge Prisms: Coastal Futures 1: e14. doi:10.1017/cft.2023.3, https://www.cambridge.org/core/journals/cambridge-prisms-coastal-futures/article/population-development-as-a-driver-of-coastal-risk-current-trends-and-future-pathways/8261D3B34F6114EA0999FAA597D5F2E2 (Feb. 19, 2025).

Reliefweb. (2024). Nigeria: Joint Post-Flood Situation Report - Edo State (30 November 2024), https://reliefweb.int/report/nigeria/nigeria-joint-post-flood-situation-report-edo-state-30-november-2024 (Feb. 19, 2025).

Rostan, P., Belhachemi, R., and Rostan, A. (2015). Appraising the financial sustainability of a pension system with signal processing. Studies of Applied Economics 33(3): 1-16. doi: http://dx.doi.org/10.25115/eea.v33i3.3134 http://ojs.ual.es/ojs/index.php/eea/article/view/3134 (Feb. 19, 2025)

Rostan, P., Belhachemi, R., and Racicot, F.E. (2017). Forecasting the yield curve with the Burg model. Journal of Forecasting 36(1): 91-99. doi: 10.1002/for.2416

Rostan, P., and Rostan, A. (2017). Population Projections and Pension System Sustainability. Lambert Academic Publishing, Saarbrücken. ISBN 978-620-2-06479-8, https://www.morebooks.de/gb/search?utf8=%E2%9C%93andq=978-620-2-06479-8 (Feb. 19, 2025).

Rostan, P., and Rostan, A. (2018a). The versatility of spectrum analysis for forecasting financial time series. The Journal of Forecasting 37(3): 327-339. doi: https://doi.org/10.1002/for.2504

Rostan, P., and Rostan, A. (2018b). Will Saudi Arabia Get Older? Will its pension system be sustainable? Spectral Answers. PSU Research Review 2(3): 189-205. doi: https://doi.org/10.1108/PRR-12-2017-0045, https://www.emeraldinsight.com/doi/full/10.1108/PRR-12-2017-0045 (Feb. 19, 2025).

Rostan, P., and Rostan, A. (2018c). Forecasting Spanish and Euro Area GDPs with Spectral Analysis. Estudios De Economía Aplicada 36(1): 217-234, https://dialnet.unirioja.es/servlet/articulo?codigo=6283924 (Feb. 19, 2025).

Rostan, P. and Rostan, A. (2018d). Where is ‘ ‘Greek’s Economy Heading? International Journal of Management and Applied Science (IJMAS) 4(3): 28-31, http://ijmas.iraj.in/paper_detail.php?paper_id=11490andname=Where_is_Greece%E2%80%99s_Economy_Heading?_A_Spectral_Perspective (Feb. 19, 2025).

Rostan, P., and Rostan, A. (2019). When will European Muslim Population be majority and in which country. PSU Research Review 3(2). doi: https://doi.org/10.1108/PRR-12-2018-0034 https://www.emerald.com/insight/content/doi/10.1108/PRR-12-2018-0034/full/html (Feb. 19, 2025).

Rostan, P., and Rostan, A. (2020). Where is ‘ ‘Austria’s Economy Heading? Economic and Business Review 22(1): 105-130, doi: https://doi.org/10.15458/ebr97. https://www.ebrjournal.net/uploads/ebr/public/document/13-ebr_221_d_rostan_barvni_en.pdf (Feb. 19, 2025).

Rostan, P., and Rostan, A. (2021a). Where is Saudi ‘ ‘Arabia’s Economy Heading? International Journal of Emerging Markets 16(8): 2009-2033. doi: https://doi.org/10.1108/IJOEM-08-2018-0447), https://www.emerald.com/insight/content/doi/10.1108/IJOEM-08-2018-0447/full/html (Feb. 19, 2025).

Rostan, P., and Rostan, A. (2021b). Where are fossil fuels prices heading? International Journal of Energy Sector Management 15(2): 309-327. doi: https://doi.org/10.1108/IJESM-07-2019-0009. https://www.emerald.com/insight/content/doi/10.1108/IJESM-07-2019-0009/full/html (Feb. 19, 2025).

Rostan, P., and Rostan, A. (2022a). 2050 Projections of the Persian Gulf Economies. Iranian Economic Review 26(2): 269-288. doi: 10.22059/ier.2022.88164. https://ier.ut.ac.ir/article_88164.html (Feb. 19, 2025).

Rostan, P., and Rostan, A. (2022b). Assessing the Resilience of ‘ ‘Turkey’s Economy during the Covid-19 Pandemic with its 2050 Projections. Journal of Emerging Economies and Policy 7(2): 38-49, https://dergipark.org.tr/en/download/article-file/2595010 (Feb. 19, 2025).

Rostan, P., and Rostan, A. (2022c). Assessing The Resilience of ‘ ‘UK’s Economy After the Covid-19 Pandemic and Brexit. Online Journal Modelling the New Europe 40: 47-77, doi: 10.24193/OJMNE.2022.40.03. http://neweurope.centre.ubbcluj.ro/wp-content/uploads/2022/12/3.pdf (Feb. 19, 2025).

Rostan, P., and Rostan, A. (2023a). The Benefit of the Covid-19 Pandemic on Global Temperature Projections. Journal of Forecasting 42(8): 2079-2098, doi: https://doi.org/10.1002/for.3011, https://onlinelibrary.wiley.com/doi/10.1002/for.3011 (Feb. 19, 2025).

Rostan, P., and Rostan, A. (2023b). How South ‘ ‘Korea’s economy gained momentum because of Covid-19. Studies of Applied Economics 41(2). doi: 10.25115/sae.v41i2.9096, https://ojs.ual.es/ojs/index.php/eea/article/view/9096 (Feb. 19, 2025).

Rostan, P., and Rostan, A. (2023c). How ‘Cyprus’ Economy Coped with The Covid-19 Pandemic. Online Journal Modelling the New Europe 42: 109-137. doi: 10.24193/OJMNE.2023.42.06, http://neweurope.centre.ubbcluj.ro/wp-content/uploads/2023/09/06-rostan.pdf (Feb. 19, 2025).

Rostan, P., and Rostan, A. (2023d). Assessing the current and future efficiency of OECD countries in managing municipal solid waste. Journal of Recycling Economy and Sustainability Policy 2(2), https://respjournal.com/index.php/pub/article/view/20 (Feb. 19, 2025).

Rostan, P., and Rostan, A. (2024a). How ‘ ‘Australia’s economy gained momentum because of Covid-19. Australian Economic Papers 63(1). doi: https://doi.org/10.1111/1467-8454.12308, https://onlinelibrary.wiley.com/doi/10.1111/1467-8454.12308 (Feb. 19, 2025).

Rostan, P., and Rostan, A. (2024b). How Brazil’s, ‘ ‘Mexico’s and ‘ ‘Argentina’s economies coped with the Covid-19 pandemic. Studies of Applied Economics 42(1), https://ojs.ual.es/ojs/index.php/eea/article/view/9417 (Feb. 19, 2025).

Rostan, P., and Rostan, A. (2024c). Assessing the Saudi Vision plan with its 2030 and 2050 projections. IER Economic Review. doi: 10.22059/ier.2024.369480.1007879, https://ier.ut.ac.ir/article_96120.html. (Feb. 19, 2025).

Rostan, P., and Rostan, A. (2024d). The positive impact of the Covid-19 pandemic on the Slovenian economy. International Journal of Euro-Mediterranean Studies 17(1), https://ijems.emuni.si/index.php/home/article/view/160. (Feb. 19, 2025).

Rostan, P., and Rostan A. (2024e). When and Where Will State-Based Conflicts Occur in the Remaining 21st Century. Journal of the Belarusian State University. International Relations 2: 40-46.

Rostan, P., and Rostan A. (2025). Assessing the sustainability of post-Covid ‘ ‘China’s economy. Studies of Applied Economics 43(1). doi: https://doi.org/10.25115/8qvkyc46. https://ojs.ual.es/ojs/index.php/eea/article/view/9992 (Feb. 19, 2025).

Rostan, P., Rostan, A., and Nurunnabi, M. (2023). Forewarned is forearmed: Forecasting expansions and contractions of the Saudi Economy. Journal of Emerging Economies and Policy 8(1): 178-190, https://dergipark.org.tr/tr/download/article-file/3051860 (Feb. 19, 2025).

Rostan, P., Rostan, A., and Wall, J. (2024). Measuring the resilience to the Covid-19 pandemic of Eurozone Economies with their 2050 forecasts. Computational Economics 63: 1137-1157. doi: 10.1007/s10614-023-10425-z, https://link.springer.com/article/10.1007/s10614-023-10425-z (Feb. 19, 2025).

Salem, M., Al Lawati, A., and Dewan, A. (2024). Dubai flights cancelled, schools and offices shut as rain pelts UAE just weeks after deadly floods. CNN, https://edition.cnn.com/2024/05/02/middleeast/uae-rain-storm-dubai-flights-disruption-climate-intl/index.html (Feb. 19, 2025).

Steffen, S., and Niranjan, A. (2021). Environmentalists say COP26 is overwhelmingly white and rich. DW, https://www.dw.com/en/cop26-climate-conference-glasgow-delegates-representation-global-south/a-59708405 (Feb. 19, 2025).

Sultana, N., and Hasan, M. K. (2024). Identifying Climate Scenarios and an Index-Based Assessment of Household Vulnerability to Climate Change in the South-West Coastal Region of Bangladesh. Jordan Journal of Earth and Environmental Sciences 15 (2): 136-145, https://jjees.hu.edu.jo/files/Vol15/No2/JJEES_Vol_15_No_2_P8.pdf (Feb. 19, 2025).

Swissinfo.ch. (2024). Parts of Switzerland and Germany waterlogged as heavy rains continue, https://www.swissinfo.ch/eng/life-aging/heavy-rains-continue-to-batter-parts-of-switzerland-and-germany/79414923 (Feb. 19, 2025).

Tarigan, E. (2024). Flood and landslide hit ‘ ‘Indonesia’s Sulawesi island, killing 14. AP, https://apnews.com/article/indonesia-sulawesi-luwu-flood-landslide-c19c525d08f17412d0ee0c64b9a78cd7 (Feb. 19, 2025).

The Economist (2017). Summit-mania New life for the Paris climate deal, https://www.economist.com/news/international/21732525-flurry-meetings-should-help-curb-greenhouse-gas-emissions-global-agreement (Feb. 19, 2025).

The White House (2021). President Biden Sets 2030 Greenhouse Gas Pollution Reduction Target Aimed at Creating Good-Paying Union Jobs and Securing U.S. Leadership on Clean Energy Technologies, https://www.whitehouse.gov/briefing-room/statements-releases/2021/04/22/fact-sheet-president-biden-sets-2030-greenhouse-gas-pollution-reduction-target-aimed-at-creating-good-paying-union-jobs-and-securing-u-s-leadership-on-clean-energy-technologies/ (Feb. 19, 2025).

United Nations. (2024a). UN Climate Change Conferences, https://www.un.org/en/climatechange/un-climate-conferences (Feb. 19, 2025).

United Nations. (2024b). Causes and Effects of Climate Change, https://www.un.org/en/climatechange/science/causes-effects-climate-change (Feb. 19, 2025).

Weisman, J., and Ulloa, J. (2022). As the Planet Cooks, Climate Stalls as a Political Issue. The New York Times, https://www.nytimes.com/2022/07/17/us/politics/climate-change-manchin-biden.html (Feb. 19, 2025).

Willner, S.N., Levermann, A., Zhao, F., and Frieler, K. (2018). Adaptation required to preserve future high-end river flood risk at present levels. Science Advances 4, 1-8. doi: 10.1126/sciadv.aao1914 (Feb. 19, 2025).

JJEES

JJEES (2025) 16 (3): 267-275
ISSN 1995-6681

Jordan Journal of Earth and Environmental Sciences

Assessing Land Use/Land Cover and Predicting Future Scenarios in Kano Metropolis, Northern Nigeria

Akus Kingsley Okoduwa[1*], Chika Floyd Amaechi[1] , Alex Ajeh Enuneku[1,2]

[1] *Department of Environmental Management and Toxicology, Faculty of Life Sciences, University of Benin, PMB 1154, Benin City, Nigeria.*
[2] *Laboratory for Ecotoxicology and Environmental Forensics, University of Benin, PMB 1154, Benin City, Nigeria*

Received on August 26, 2024, Accepted on February 22, 2025

Abstract

Uncontrolled urban development has significant implications for sustainable urban progress. Assessing and predicting changes in land use/land cover (LULC) are essential for effective environmental monitoring and management. This study evaluates LULC changes from 1984 - 2023 in the Kano metropolis, Nigeria, while also forecasting future transformations. Landsat-5 Thematic Mapper (1984), Landsat-4 Thematic Mapper (1998), and Landsat-8 Operational Land Imager/Thermal Infrared Sensor (2023) imagery from the United States Geological Survey Earth Explorer were used. LULC classification was conducted using the support vector machine (SVM) supervised approach, categorizing the landscape into built-up areas, vegetation, water bodies, and bare land. The accuracy of the classified LULC maps was computed using ENVI 5.3, ArcGIS, and Google Earth Pro. The CA-Markov model in IDRISI TerrSet Software (2020) was employed to project LULC changes for 2050. The classification accuracies for 1984, 1998, and 2023 were 99.59%, 94%, and 98.96%, respectively, with kappa coefficients of 0.99, 0.92, and 0.98. The results indicate a 41.8% increase (204.63 km²) in built-up areas from 1984 - 2023, while vegetation expanded by 2% (8.55 km²). Water bodies slightly decreased by 0.12 km² (<1%), and bare land declined by 213.35 km² (43%). Projections for 2050 anticipate further expansion of built-up areas (16%) alongside reductions in vegetation (1%), water bodies (<1%), and bare land (16%). These findings suggest continued urban growth at the expense of natural landscapes. To enhance environmental sustainability, this study recommends ecosystem-based adaptation strategies and legal frameworks to mitigate the adverse effects of urban expansion.

Keywords: *LULC, CA-Markov model, Projection, Kano Metropolis, Nigeria*

1. Introduction

According to Bren d'Amour et al. (2016) findings, global urbanization by 2030 will cause arable land losses of 1.8 to 2.5%, with Africa and Asia accounting for 80% of this loss. Given that more than 60% of the world's irrigation fields are near urban areas, there is potential competition for land between agriculture and urbanization (Mohammad, 2020). By 2050, more than 68% of the world's population, approximately 9.8 billion people, will reside in cities, with the majority residing in less-developed countries (Li et al., 2013; United Nations, 2020). This demographic shift will impose considerable pressure on resource consumption, especially in terms of land-use changes (Alqahtany et al., 2013), potentially leading to uncontrolled urban sprawl (Osman et al., 2018) and significant alterations in the urban-regional landscape (Xu et al., 2012).

The rapid urbanization and growth rate in Kano, Nigeria, pose substantial challenges to urban environmental sustainability. Kano's urbanization has made it Nigeria's most populous northern urban state (Okopi, 2021). Urbanization attracts populations, shapes activities, and drives infrastructure development, including road networks, public utilities, and land-use changes (Mohammad, 2020), leading to expanded built-up areas, diminished green spaces, increased urban surface temperatures, urban heat island formation, and climate change (Singh et al., 2017; Wang, 2019; Huang et al., 2019; Rigden and Li, 2017; Li et al., 2018; Liang et al., 2019; Fabolude and Aighewi, 2022; Amaechi et al., 2023, Okoduwa et al., 2024).

Analyzing land-use changes across past, present, and future scenarios allows for assessing resource expansion and degradation, guiding current and prospective land-use decisions (Mohammad, 2020). Furthermore, understanding the impact of urban development informs the adoption of efficient land management policies and strategies (Nourqolipour et al., 2016; Munthali et al., 2019). Addressing urban challenges requires enhancing urban land-use efficiency for sustainable development (Zhu et al., 2019) and analysing the root causes of uncontrolled urban growth for improved future planning (Osman, 2018).

Modelling LULC changes offers an effective way to simulate land-use dynamics and understand interactions between LULC changes and the environment (Lia et al., 2016; Tobore et al., 2021). Various methods exist for modeling LULC changes, including Cellular Automata (CA) (He et al., 2005), Clue-s model (Verburg and Overmars, 2007), Markov model (Guan et al., 2008), and the hybrid CA-Markov model (Khawaldah, 2016). The Markov model is widely used for simulating and predicting LULC changes, indicating change directions and providing a framework for assessing future land-use demands (Jiansheng et al., 2012). However, traditional models often lack spatial analysis capabilities and

---

* Corresponding author e-mail: okoduwaakus@gmail.com

struggle to predict land requirements within geographical space (Han et al., 2015). In contrast, the CA-Markov model offers robust dynamic simulation capabilities, effectively representing spatial and temporal changes by combining the strengths of both the Markov and CA models (Yuan et al., 2015).

By integrating the spatial continuity of the cellular automata (CA) model with the Markov chain's long-term prediction abilities, the CA-Markov hybrid model has proven effective for modeling various LULC classes (Chotchaiwong and Wijitkosum, 2019). This hybrid approach offers a dynamic, reliable, and robust technique for predicting spatiotemporal LULC changes in rapidly developing urban areas. Several studies (Liping et al., 2018; Wang et al., 2018; Sun et al., 2018; Samat et al., 2020; Wang et al., 2022; Fabolude and Aighewi, 2022; and Amaechi et al., 2023) have demonstrated the effectiveness of the CA-Markov model in predicting LULC change. Using this hybrid model as a predictive tool can significantly contribute to effective land use planning, management, and ecological system restoration (Koko et al., 2022).

This study addresses the critical gap in understanding the long-term impact of urbanization on LULC dynamics in Kano Metropolis. While previous research has examined urban growth in Nigeria, limited studies have provided a spatiotemporal assessment covering nearly four decades (1984–2023). Additionally, the lack of predictive models for future urban expansion has hindered proactive urban planning. By employing the CA-Markov model, this study projects LULC changes for 2050, offering a data-driven approach to inform sustainable land management policies. The findings contribute to knowledge by providing evidence of urban expansion trends, their implications for environmental sustainability, and the need for adaptive urban planning strategies in rapidly growing cities like Kano.

2. Materials and methods

2.1. Study area

Kano Metropolis (Figure 1) is located between latitudes 11°51'0'N and 12°01'30'N and longitudes 8°25'0'E to 8°30'0'E. It is located in northern Nigeria's most populous state, and the study area is Nigeria's second most populous metropolis (Koko et al., 2022). The city's urban population was 3.8 million in 2018, and it is predicted to grow to 5.6 million by 2030 (Koko et al., 2022). Kano's urban structure has evolved, with significant transformations driven by industrialization and economic development in the 21st century. The city's urban fabric has gradually been shaped by rapid urban expansion, extending from the central and densely settled zones to the peripheral and surrounding areas of the urban center (Mohammed et al., 2014).

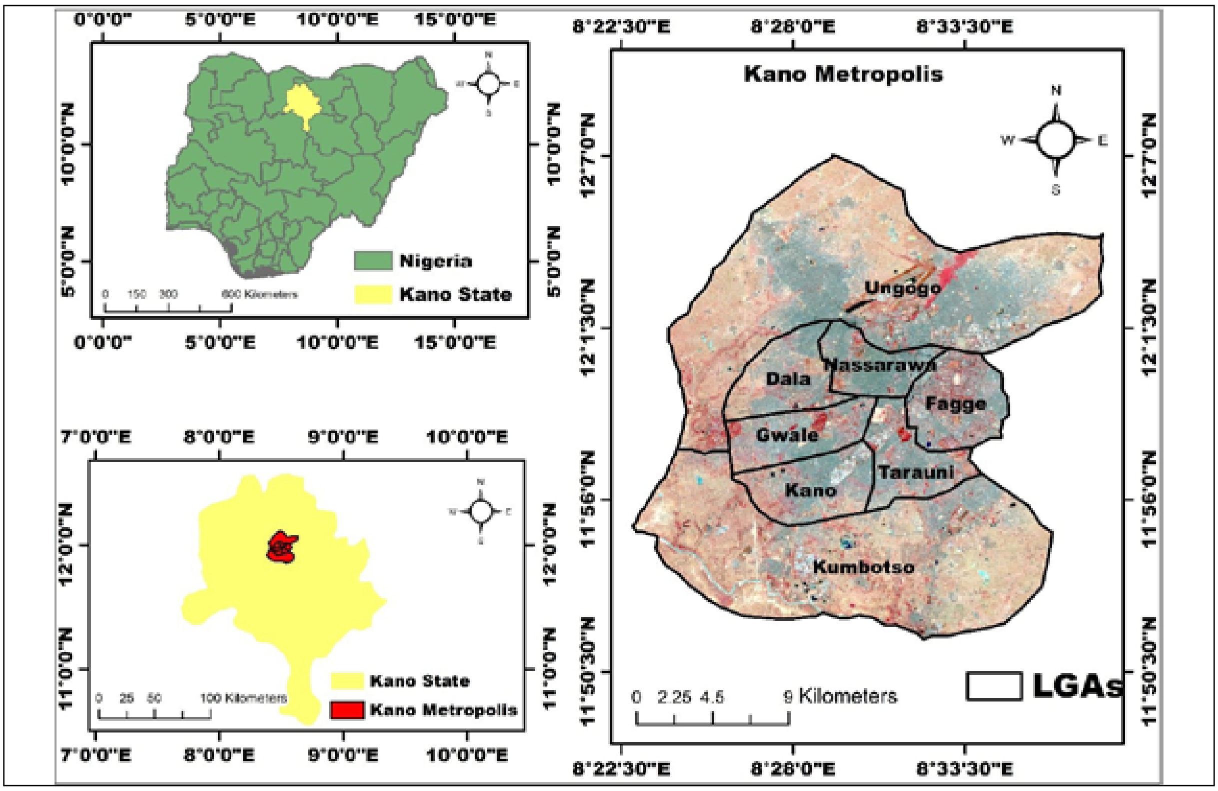

Figure 1. Study area (Kano Metropolis) displayed using a False Color Composite with Landsat 8 bands 5 (Near Infrared), 4 (Red), and 3 (Green) to enhance land cover distinction.

The city has a wet season that lasts from May to October, followed by a dry season from November to April (Dankani, 2013). The annual precipitation in Kano varies between its northern and southern regions, from 800 mm to 1100 mm (Nabegu, 2014). The city's average yearly temperature is approximately 26°C (Nwagbara, 2015). Kano has an abundance of fertile soil that supports a variety of food and cash crops, including millet, rice, sorghum, wheat, cowpeas, groundnuts, and other vegetables (Koko et al., 2022). The metropolis is one of Nigeria's fastest-growing urban areas, and its commercial and agricultural activities have continued to attract new residents (Okopi, 2021).

2.2 Data Acquisition

This study utilized Landsat 5 Thematic Mapper (TM), Landsat 4 Thematic Mapper (TM), and Landsat 8 Operational Land Imager/Thermal Infrared Sensor (OLI/TIRS) data for path and row 188/054 from 1984, 1998, and 2023 (Table 1). These images were obtained from the United States Geological Survey (USGS) website (https://earthexplorer.usgs.gov/). To ensure data quality and enhance the reliability of the analyses, only images with 0.00% cloud cover were selected.

The selection of Landsat 5 for 1984 and Landsat 4 for 1998 was based on image availability with 0.00% cloud cover. While both satellites carried the TM sensor, Landsat 5 was chosen for 1984 because it provided a cloud-free image for that year. For 1998, the cloud-free image available came from Landsat 4, making it the most suitable option for maintaining consistency in data quality. Thus, the choice of data sources was guided by the need to ensure the highest quality cloud-free imagery for analysis.

Table 1. Data type and data sources

Data	Source	Resolution	Land/Scene Cloud Cover	Date
Landsat 5 TM	USGS Earth Explorer	30	0.00	1984-12-29
Landsat 4 TM	USGS Earth Explorer	30	0.00	1998-11-18
Landsat 8 OLI/TIRS	USGS Earth Explorer	30	0.00	2023-12-09

2.3 Image Preprocessing

To ensure the accuracy and reliability of the classification results, preprocessing was performed on the Landsat images before classification. ENVI (Environment for Visualizing Images) software version 5.3 was used for image preprocessing, which included radiometric calibration, atmospheric correction, geometric correction, and clipping of the study area.

Radiometric Calibration: This step converted the digital numbers (DN) of the Landsat images into at-sensor radiance values, correcting for sensor-specific variations and ensuring consistency across different acquisition years.

Atmospheric Correction: Atmospheric correction was performed using the Fast Line-of-Sight Atmospheric Analysis of Spectral Hypercubes (FLAASH) tool in ENVI 5.3. FLAASH removes the effects of atmospheric scattering and absorption, thereby enhancing the spectral fidelity of the images and improving the accuracy of land cover classification.

Geometric Correction: The images were georeferenced to the Universal Transverse Mercator (UTM) coordinate system using the World Geodetic System (WGS) 1984 datum to ensure spatial alignment across different years. This correction minimizes geometric distortions caused by variations in satellite positioning and terrain effects.

Clipping of the Study Area: To focus on the region of interest, each Landsat image was clipped to the boundaries of Kano Metropolis using a shapefile of the study area. This step eliminated unnecessary data outside the study area, reducing processing time and improving classification accuracy. These preprocessing steps were essential for ensuring data consistency, reducing atmospheric and radiometric distortions, and enhancing the accuracy of subsequent classification and analysis.

2.4 Image Classification

ENVI software version 5.3 was utilized for LULC classification of the 1984 and 2023 images, while ArcGIS 10.7.1 was used for the 1998 image. A limitation of the cracked version of ENVI is the lack of support for Landsat 4 data processing. Consequently, ArcGIS was selected to effectively process and classify the 1998 image while maintaining overall methodological consistency. Despite the use of different software, classification consistency was ensured by applying the same supervised classification approach and validation techniques across all datasets. The same algorithm (SVM) was used to classify all land cover classes.

Implementing this technique on Landsat images included utilizing four distinct classes: built-up (impervious surface area including building materials and asphalt), vegetation (areas dominated by trees and grasses), waterbody (area covered by water), and bare land (non-vegetated barren areas) (Okoduwa and Amaechi, 2024). These land cover classes were selected for this study based on the observed land cover classes available within the Landsat images through false and true color composites. The supervised classification process involved the use of meticulously collected training signature samples. The CA-Markov model in TerrSet Geospatial Monitoring and Modelling Software version 2020 was utilized to carry out LULC projections for 2050. ArcGIS 10.7.1 was used to mask the boundaries of the study area, perform post-classification operations, generate statistical data, develop map layouts, and create visualizations. Figure 2 depicts the research methodology flowchart.

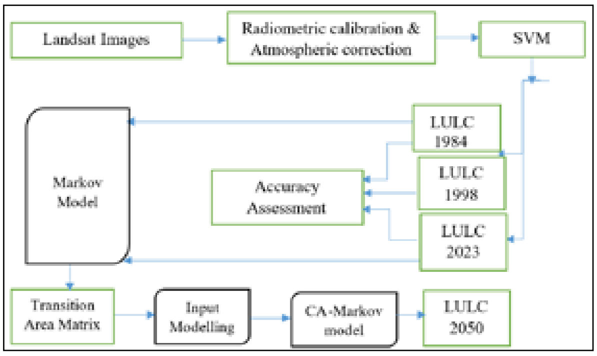

Figure 2. Research methodology flowchart for LULC classification and projection

2.5 Accuracy Assessment

The accuracy assessment of the classified LULC maps was conducted using different methodologies, reflecting the software used for classification. ENVI 5.3 was utilized for the accuracy assessment of the 1984 and 2023 images, while ArcGIS and Google Earth Pro were used for the 1998 image. This approach was necessary to maintain methodological consistency, as ENVI was used for classifying the 1984 and 2023 images, whereas ArcGIS was used for the classification of the 1998 image. Additionally, Google Earth Pro provided access to historical high-resolution imagery, which enhanced the validation process for 1998.

In ENVI 5.3, accuracy assessment was performed through a two-step process. First, various band combinations were used to extract ground truth pixels from high-resolution raster images (unclassified rasters) for 1984 and 2023, representing distinct land cover classes. Next, the polygon tool was employed to extract corresponding ground truth pixels from the classified maps for these years. The Ground Truth ROI function in ENVI 5.3 was then used to generate a confusion matrix, comparing the classified land cover pixels with the reference ground truth data. The results, including the number of correctly and incorrectly classified pixels, are presented in Tables 2 and 4.

For the 1998 image, an accuracy assessment was conducted using ArcGIS and Google Earth Pro. A total of 100 accuracy assessment points were generated in ArcGIS using the Create Accuracy Assessment Points tool, with the equalized stratified random sampling method ensuring balanced distribution across all LULC classes. The generated points were then converted to KML format and imported into Google Earth Pro, where the Show Historical Imagery feature was used to retrieve corresponding 1998 satellite imagery (Figure 3). Each assessment point was visually cross-referenced with the historical imagery to verify classification accuracy.

Following validation, a confusion matrix was computed in ArcGIS to assess classification performance. The overall accuracy, 'user's accuracy (UA), 'producer's accuracy (PA), and Kappa coefficient (KC) were then derived to quantify classification reliability, as presented in Equation 1-4. Table 3 shows the numbers of correct and incorrect ground truth points for 1998.

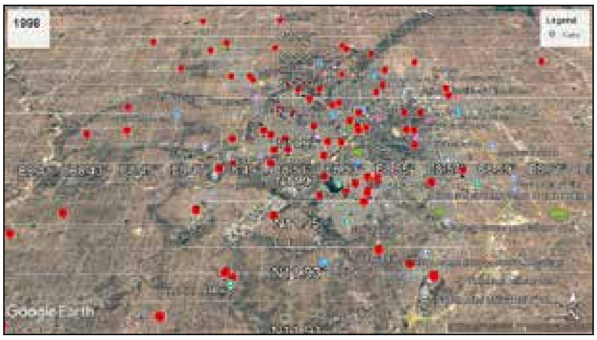

Figure 3. Google Earth Pro showing 1998 image for accuracy assessment.

Table 2. Correct and incorrect numbers of ground truth pixels for 1984

LULC Class	Built-up	Vegetation	Waterbody	Bareland	Total
Built-up	1418	0	12	4	1434
Vegetation	1	286	5	2	294
Water bodies	1	0	97	0	98
Bareland	2	6	4	7105	7117
Total	1422	292	118	7111	8943

Table 3. Correct and incorrect numbers of ground truth points for 1998

LULC Class	Built-up	Vegetation	Water bodies	Bare land	Total
Built-up	1	22	0	2	25
Vegetation	22	0	0	3	25
Water bodies	0	0	25	0	25
Bare land	0	0	0	25	25
Total	23	22	25	30	100

Table 4. Correct and incorrect numbers of ground truth pixels for 2023

LULC Class	Built-up	Vegetation	Waterbody	Bareland	Total
Built-up	5900	1	40	7	5948
Vegetation	0	282	0	3	285
Water bodies	0	0	321	0	321
Bareland	22	15	2	2063	2102
Total	5922	298	363	2073	8656

The various accuracy assessments can be calculated using the following formulas:

$$\text{Consumer Accuracy} \ \frac{\text{Number of correctly classified training samples in each class}}{\text{Number of training samples classified to that class}} \qquad 1$$

$$\text{Producer Accuracy} \ \frac{\text{Number of correctly classified training samples in each class}}{\text{Number of training samples in each class}} \qquad 2$$

$$\text{Overall Accuracy} = \frac{\text{Number of correctly trained samples}}{\text{Number of total samples}} \qquad 3$$

$$\text{Koppa coefficient} = \frac{\textit{Overall Accuracy} - \text{Estimated chance agreement}}{1 - \text{Estimated chance of agreement}} \qquad 4$$

(Nasiri et al., 2022; Kadri et al., 2023, Okoduwa & Amaechi, 2024)

3. Results

3.1 Accuracy Assessment

Table 5 presents the classification accuracy for 1984, 1998, and 2023. The overall accuracies for the three years (1984, 1998, and 2023) were 99.59%, 94, and 98.96%, respectively. The kappa coefficients were 0.99, 0.92, and 0.98, respectively, which are considered acceptable (Tadese et al., 2020; Koko et al., 2022; Amaechi et al., 2024).

Table 5. Accuracy assessment results for 1984, 1991, and 2023

Class	1984		1991		2023	
	PA	UA	PA	UA	PA	UA
Build-up	99.72	98.88	0.96	0.88	99.63	99.19
Vegetation	97.95	97.28	100	0.88	94.63	98.95
Water bodies	82.20	98.98	100	100	88.43	100
Bareland	99.92	99.83	0.83	100	99.52	98.14
Overall Accuracy	**99.59**		**94**		**98.96**	
Koppa Coefficient	**0.99**		**0.92**		**0.98**	

3.2 Spatial distribution of LULC

The findings of the geospatial evaluation for the year 1984 (Figure 4) demonstrate a landscape that has yet to experience significant change from anthropogenic activities, as evidenced by the quantity of vegetation in the Fagge local government area. The built-up class was concentrated in Nassarawa and the southern part of Ungogo. Tarauni, Kano, Gwale, Dala, and Kumbotso were covered with bare land. The assessment results for the year 1998 (Figure 5) show that built-up area is gradually increasing, and bare land and water bodies are being lost within Fagge, Ungogo, and Nassarawa. Increased patches of vegetation were found in Tarauni.

The assessment results for the year 2023 (Figure 6) show that vegetation and bare land are gradually being lost over time and replaced with built-up areas within Fagge, Tarauni, Ungogo, Kano, Gwale, Dala, and Kumbotso. Some patches of vegetation were also found across the eight local government areas (LGAs). The projected year (Figure 7) reveals a massive built-up area within all the respective local government areas of the Kano metropolis. Some patches of vegetation are still projected to occur within the six LGAs. By 2050, the built-up area is expected to increase by approximately 82.89 km², representing a 16% growth from 2023 levels. This continued urban expansion suggests that previously undeveloped land will be converted to residential, commercial, and industrial uses, reflecting population growth and economic development pressures. Expanding urban areas could have profound implications for environmental sustainability, including increased land surface temperature, heightened pollution levels, and greater demand for infrastructure and public services.

Vegetation cover, on the other hand, is projected to decline by 4.7 km² (1%), indicating the ongoing loss of green spaces due to urban encroachment. This reduction in vegetation could lead to adverse ecological consequences, such as decreased air quality, disruption of local climate regulation, and the exacerbation of the urban heat island effect. Similarly, bare land is expected to decrease by 78.13 km² (16%) as more open spaces are converted to built-up areas. The rapid decline in bare land signifies the increasing pressure on available land resources, necessitating effective land-use policies to balance development with environmental conservation. In contrast, water bodies are projected to remain relatively stable, with a minimal decrease of 0.06 km². While this suggests that urban expansion may have a limited direct impact on water bodies, indirect effects such as pollution and increased water demand could pose challenges for water resource management in the long term.

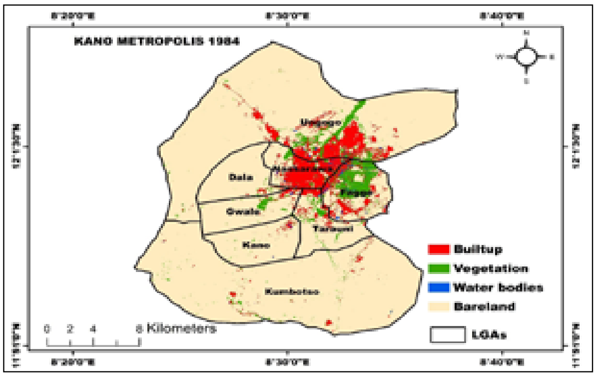

Figure 4. LULC map of 1984

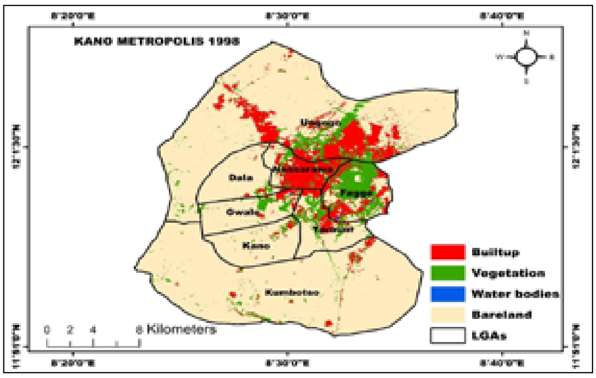

Figure 5. LULC map of 1998

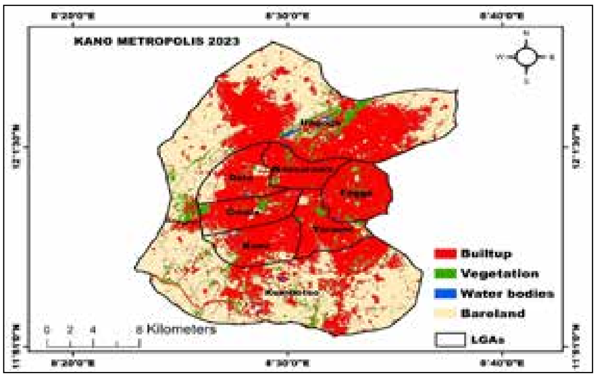

Figure 6. LULC map of 2023

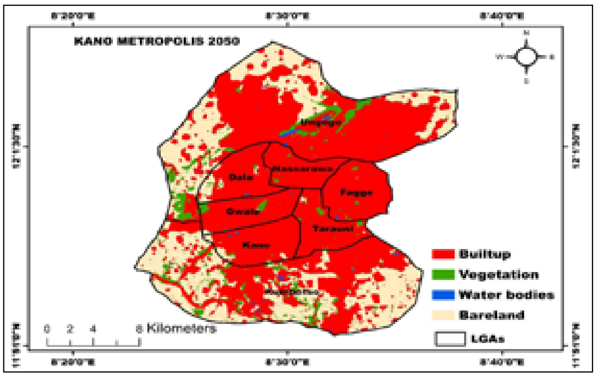

Figure 7. LULC map of 2050

3.3 LULC statistics

In 1984, the study area comprised 25.43 km^2 (7.2%) of built-up land, 20.46 km^2 (4%) of vegetation, 1.81 km^2 (0.4%) of water bodies, and 435.81 km^2 (88%) of bare land. By 1998, built-up land had increased to 53 km^2 (10.7%), vegetation expanded to 40 km^2 (8.1%), while water bodies and bare land covered 0.35 km^2 (0.1%) and 400 km^2 (81.1%), respectively. By 2023, the built-up area had significantly expanded to 240.06 km^2 (49%), while vegetation decreased to 29.01 km^2 (6%). Water bodies remained relatively stable at 0.94 km^2 (0.4%), whereas bare land declined to 222.46 km^2 (45%) (Table 6).

Using classified LULC maps of the Kano metropolis from 1984 to 2023, the city's land use was projected for 2050. According to the projections, by 2050, Kano's built-up areas are expected to cover approximately 322.95 km^2, representing 65% of the city's total landmass. Vegetation areas are projected to cover approximately 24.31 km^2, accounting for 5% of the city's total landmass. Water bodies are projected to cover approximately 1.88 km^2, making up 0.4% of the city's total landmass. Finally, bare land areas are projected to cover approximately 144.33 km^2, representing 29% of the city's total landmass. (Table 6).

Table 6. LULC statistics for 1984, 1998, 2023, and 2050

LULC Class	1984		1998		2023		2050	
	Area (Km^2)	Area (%)	Area (Km^2)	Area (%)	Area (Km^2)	Area (%)	Area (Km^2)	Area (%)
Built-up	35.43	7.2	53	10.7	240.06	49	322.95	65
Vegetation	20.46	4	40	8.1	29.01	6	24.31	5
Water bodies	1.81	0.4	0.35	0.1	1.94	0.4	1.88	0.4
Bareland	435.81	88	400	81.1	222.46	45	144.33	29
TOTAL	493.5	100	493.5	100	493.5	100	493.5	100

3.4 LULC Net change

Table 7 presents comprehensive LULC change statistics from 1984 - 2023 and projections from 2023-2050. The results indicate that between 1984 and 2023, the built-up area increased by 204.63 km^2 (41.8%). Vegetation expanded by 8.55 km^2 (2%). Water bodies experienced a slight decrease of 0.12 km^2 (0%), while bare land decreased by 43%. For the period from 2023 to 2050, the built-up area is projected to increase by 82.89 km^2 (16%), the vegetation area is projected to decrease by 4.7 km^2 (1%), the water body area is projected to decrease by 0.06 km^2 (0%), and the bare land area is projected to decrease by 78.13 km^2 (16%).

Figures 8 and 9 depict the change dynamics of various LULC classes over different periods. For 1984-2023, the LULC classes that increased included built-up areas (BU) and vegetation (V). From 2023-2050, BU will continue to increase, while bare land (BL), water bodies (WB), and vegetation (V) will decrease.

Table 7. LULC net change statistics

LULC Class	1984 - 2023		2023 - 2050	
	Area (Km^2)	Area (%)	Area (Km^2)	Area (%)
Built-up	204.63	41.8	82.89	16
Vegetation	8.55	2	-4.7	-1
Water bodies	0.13	0	-0.06	0
Bareland	-213.35	-43	-78.13	-16

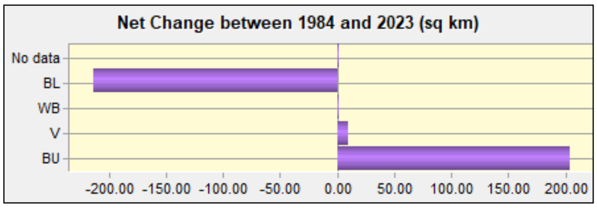

Figure 8. Net change from 1984 – 2023

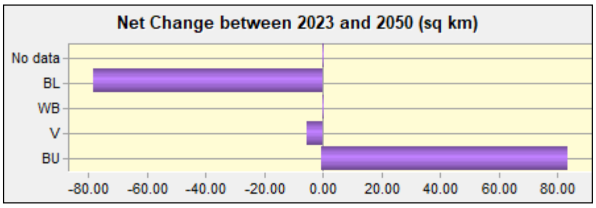

Figure 9. Net change from 2023 - 2050

3.5 Transition Probability Matrix

The transition probability matrix (Table 8) illustrates the probability of a specific LULC class transitioning into another land use class. The analysis highlights the built-up areas of the Kano metropolis as the most stable land cover class, with transition probabilities of approximately 0.98. This finding suggests a minimal likelihood of the city's built-up areas transitioning into other LULC categories. Vegetation showed a transition probability of approximately 0.52 for transforming into built-up areas, while water bodies and bare land had transition probabilities of roughly 0.32 for transforming into built-up areas. The analysis (Figure 10) identified bare land and vegetation as the primary LULC classes contributing to the expansion of built-up areas.

Table 8. Transition Probability Matrix (1984 – 2023)

	Built-up	Vegetation	Water bodies	Bareland
Built-up	0.9825	0.0058	0.0052	0.0065
Vegetation	0.5213	0.4336	0.0017	0.0434
Water bodies	0.3199	0.0373	0.3017	0.0188
Bareland	0.3199	0.0459	0.0027	0.6316

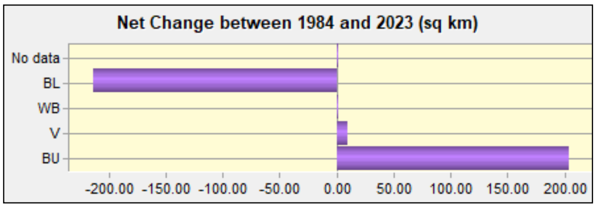

Figure 10. LULC classes contributing to changes in built-up areas.

4. Discussion

This research reveals that the built-up area will continue to increase at the expense of bare land and vegetation. This finding aligns with the work of Koko et al. (2022), who reported urban growth in the Kano metropolis from 1991 to 2020 at the expense of bare land and vegetation. The rapid urban development of Kano could be attributed to the continuous in-migration of a large population to the city due to various pull factors, including but not limited to suitable farmlands, better business and job opportunities, better urban infrastructure, and healthcare facilities (Koko et al., 2023). Population growth contributes significantly to urban congestion and transforms other land classes into built-up areas (Hussain et al., 2022). The transformation of bare land to built-up areas in the Kano metropolis aligns with a recent study in Delhi that indicated a rapid increase in built-up areas at the expense of bare land (Chaudhuri et al., 2022). A study conducted by Koko et al. (2020) in Zaria and Amaechi et al. (2023) in Abuja, Nigeria, showed that as a result of urbanization and deforestation, these patterns of barren land and vegetation cover turning into built-up areas will persist until 2050. Another study conducted in Bathinda by Rani et al. (2023) suggested that barren land is anticipated to decrease by 2050.

From 1984 to 2023, there was an increase in vegetation cover within the study area. This increase in vegetation could be linked to various Fadama programs (Sulaiman et al., 2021) and government efforts to achieve all-season farming (Koko et al., 2023). A similar increase in vegetation from 1990–2020 was observed in the Zaria metropolis and Abuja Municipal Area Council from 1987–2023 due to afforestation schemes (Koko et al., 2020; Okoduwa et al., 2023). However, the projected results indicate that vegetation will decrease from 2023 to 2050. This decrease in vegetation can be attributed to continuous urbanization and infrastructure development (Amaechi et al., 2023).

Increasing built-up areas at the expense of vegetation cover could jeopardize ecosystem health, human well-being, and food security (Rahman, 2016; Khanal et al., 2019). Gogoi et al. (2019) reported that an increased population could result in increased pollution, leading to detrimental consequences, including urban heat waves and health problems (Hansen et al., 2013; Wang et al., 2021). Okoduwa et al. (2023) confirmed that the increase or decrease in temperature changes was linked to the amount of vegetation cover in cities. It is generally proven that the loss of forest and vegetative cover degrades ecosystem services by reducing water retention, drying up water sources, decreasing biodiversity, reducing the sequestration rate of carbon dioxide (CO_2), and enhancing the magnitude and frequency of disasters such as flooding (Bradshaw et al., 2007), which are vital for human well-being (Bewket, 2002).

Urbanization poses challenges to environmental sustainability (Keshtkar et al., 2017; Rijal et al., 2018), as urban expansion often comes at the expense of biodiversity and ecosystem services (Poppenborg and Koellner, 2013; Tao et al., 2015). With urban development, there is a high demand for natural resources (Balatsky et al., 2015), food, and fibre production (Tilman et al., 2011). Consequently, ecosystems face unprecedented pressure, potentially leading to degradation and conversion, thereby affecting the provisioning of ecosystem services for both current and future generations (Rimal et al., 2019). The increase in built-up areas due to urbanization can exacerbate runoff by limiting the areas where floodwaters can flow, as a large part of urban environments are covered with tarred roads and pavement (Mukhtar et al., 2022).

A balance between urban development and the conservation of natural resources is crucial for sustainable urban development (Koko et al., 2022). Implementing strategies such as open green spaces, green infrastructure, water conservation techniques, and various afforestation initiatives is essential for promoting public health and environmental sustainability in urban areas (Okoduwa et al., 2023). These interventions play a critical role in mitigating soil erosion, preventing land degradation, minimizing environmental pollution, and regulating surface temperatures (Tsegaye, 2019; Asuquo et al., 2022). Another way to promote urban sustainability is through developing and implementing a land-use plan (Qingsong He, 2023) that prioritizes sustainable development and protects ecologically valuable areas such as green spaces to mitigate urban heat islands and floods.

5. Conclusions and recommendations

To design future policies and plans for healthy urban development, it is vital to understand how LULC has evolved in the past, present, and future. The findings of this study will help policymakers, environmental managers, and individuals improve environmental management methods in the Kano metropolis. To protect vegetation, this study advises the development and implementation of ecosystem-based adaptation strategies and other legal frameworks. Such initiatives should concentrate on planting trees in urban areas such as parking lots, between buildings, in backyards, and along roadways. These steps will considerably protect soil from erosion, support biodiversity, and manage temperature and pollution. To prevent any irreparable effects that changes in LULC may have on the environment in the near future, we urge environmental managers to make use of the conclusions and suggestions of this study.

References

Alqahtany, A., Rezgui, Y., Lic, H. (2013). A proposed model for sustainable urban planning development for environmentally friendly communities. Architectural Engineering and Design Management 9 (3): 176-194.

Amaechi, C.F., Ugwu, V.C., Okoduwa, A.K. (2024). Geospatial Assessment of Land Use/Land Cover of the Federal Capital Territory: A Case Study For The Year 2050. Ethiopian Journal of Environmental Studies & Management 17 (1): 95 – 109.

Balatsky, A. V., Balatsky, G. I., Borysov, S. S. (2015). Resource demand growth and sustainability due to increased world consumption. Sustainability 7 (3): 3430-3440.

Barau, A. S., Maconachie, R., Ludin, A. N. M., Abdulhamid, A. (2015). Urban morphology dynamics and environmental change in Kano, Nigeria. Land Use Policy 42: 307-317.

Bewket, W. (2002). Land cover dynamics since the 1950s in Chemoga watershed, Blue Nile basin, Ethiopia. Mountain research and development 22 (3): 263-269.

Bradshaw, C. J., Sodhi, N. S., Peh, K. S. H., Brook, B. W. (2007). Global evidence that deforestation amplifies flood risk and severity in the developing world. Global change biology 13(11): 2379-2395.

Bren d'Amour, C., Reitsma, F., Baiocchi, G., Barthel, S., Güneralp, B., Erb, K. H., Seto, K. C. (2017). Future urban land expansion and implications for global croplands. Proceedings of the National Academy of Sciences 114(34): 8939-8944.

Chaudhuri, G., Mainali, K. P., Mishra, N. B. (2022). Analysing the dynamics of urbanization in Delhi National Capital Region in India using satellite image time-series analysis. Environment and Planning B: Urban Analytics and City Science 49 (1): 368-384.

Chotchaiwong, P., and Wijitkosum, S. (2019). Predicting urban expansion and urban land use changes in Nakhon Ratchasima City using a CA-Markov model under two different scenarios. Land 8(9): 140.

Dankani, I. M. (2013). Constraints to sustainable physical planning in Metropolitan Kano. International Journal of Management and Social Sciences Research.

Enoh, M. A., Njoku, R. E., Okeke, U. C. (2023). Modelling and mapping the spatial–temporal changes in land use and land cover in Lagos: A dynamics for building a sustainable urban city. Advances in Space Research 72(3): 694-710.

Fabolude, G., and Aighewi, I.T. (2022). Evaluation of the Extent of Land Use-Land Cover Changes of Benin City, Edo State, Nigeria from 1987-2019. Journal of Applied Science and Environmental Management 26 (8): 1443 - 1450.

Ghalehteimouri, K. J., Shamsoddini, A., Mousavi, M. N., Ros, F. B. C., Khedmatzadeh, A. (2022). Predicting spatial and decadal of land use and land cover change using integrated cellular automata Markov chain model based scenarios (2019–2049) Zarriné-Rūd River Basin in Iran. Environmental Challenges 6: 100399.

Gogoi, P. P., Vinoj, V., Swain, D., Roberts, G., Dash, J., Tripathy, S. (2019). Land use and land cover change effect on surface temperature over Eastern India. ScientificRreports 9(1): 8859.

Guan, D., Gao, W., Watari, K.; Fukahori, H. (2008). Land use change of Kitakyushu based on landscape ecology and Markov model. Journal of Geographical Sciences 18 (4): 455-468.

Han, H., Yang, C., Song, J. (2015). Scenario simulation and the prediction of land use and land cover change in Beijing, China. Sustainability 7(4): 4260-4279.

Hansen, M. C., Potapov, P. V., Moore, R., Hancher, M., Turubanova, S. A., Tyukavina, A., Townshend, J. R. (2013). High-resolution global maps of 21st-century forest cover change. Science 342(6160): 850-853.

He, C., Shi, P., Chen, J., Li, X., Pan, Y., Li, J., Li, J. (2005). Developing land use scenario dynamics model by the integration of system dynamics model and cellular automata model. Science in China Series D: Earth Sciences 48: 1979-1989.

He, Q. (2023). Urban Planning and Sustainable Land Use. Sustainability 15(12): 9524.

Huang, Q., Huang, J., & Yang, X. (2019). Quantifying the seasonal contribution of coupling urban land use types on Urban Heat Island using Land Contribution Index: A case study in Wuhan, China. Sustainable Cities and Society 44: 666-675.

Hussain, S., Mubeen, M., Karuppannan, S. (2022). Land use and land cover (LULC) change analysis using TM, ETM+ and OLI Landsat images in district of Okara, Punjab, Pakistan. Physics and Chemistry of the Earth, Parts a/b/c 126: 103117.

Jiansheng, W., Zhe, F.E.N.G., Yang, G.A.O., Xiulan, H.U.A.N.G., Hongmeng, L.I.U., Li, H.U.A.N.G. (2012). Recent progress on the application and improvement of the CLUE-S model. Progress in Geography 1: 3-10.

Kadri, N., Jebari, S., Augusseau, X., Mahdhi, N., Lestrelin, G., Berndtsson, R. (2023). Analysis of four decades of land use and land cover change in semiarid Tunisia using Google Earth Engine. Remote Sensing 15 (13): 3257.

Keshtkar, H., Voigt, W., Alizadeh, E. (2017). Land-cover classification and analysis of change using machine-learning classifiers and multitemporal remote sensing imagery. Arabian Journal of Geosciences 10: 1-15.

Khanal, N., Uddin, K., Matin, M. A., Tenneson, K. (2019). Automatic detection of spatiotemporal urban expansion patterns by fusing OSM and Landsat data in Kathmandu. Remote Sensing 11(19): 2296.

Khawaldah, H.A. (2016). A prediction of future land use/land cover in Amman area using GIS-based Markov Model and remote sensing. International Journal of Geographical Information Science 8(03): 412-427.

Koko, A. F., Bello, M., Sadiq, M. A. (2023). Understanding the Challenges of 21st Century Urbanization in Northern 'Nigeria's Largest City, Kano.

Koko, A. F., Han, Z., Wu, Y., Abubakar, G. A., Bello, M. (2022). Spatiotemporal land use/land cover mapping and prediction based on hybrid modeling approach: a case study of Kano Metropolis, Nigeria (2020–2050). Remote Sensing 14 (23): 6083.

Koko, A. F., Yue, W., Abubakar, G. A., Hamed, R., Alabsi, A. A. N. (2020). Monitoring and predicting spatiotemporal land use/land cover changes in Zaria City, Nigeria, through an integrated cellular automata and markov chain model (CA-Markov). Sustainability 12 (24): 10452.

Li, G., Zhang, X., Mirzaei, P., Zhang, J., Zhao, Z. (2018). Urban heat island effect of a typical valley city in China: Responds to global warming and rapid urbanization. Sustainable Cities and Society 8: 736–745.

Li, J., Li, C., Zhu , F., Song, C., Wu, J. (2013). Spatiotemporal pattern of urbanization in Shanghai, China between 1989 and 2005. Landscape Ecology 28: 1545–1565.

Lia, J., Oyanaa, T., Mukwayac, P. (2016). An examination of historical and future land use changes in Uganda using change detection methods and agent-based modeling. African Geographical Review 35(3): 247–271.

Liang, X., Zeng, G., Yujie, Y. (2019). The effects of interaction between climate change and landuse/cover change on biodiversity-related ecosystem services. Global Challenges 3: 1-8.

Liping, C., Yujun, S., Saeed, S. (2018). Monitoring and predicting land use and land cover changes using remote sensing and GIS techniques—A case study of a hilly area, Jiangle, China. PloS one 13 (7): e0200493.

Mohamed, M. A., Anders, J., Schneider, C. (2020). Monitoring of changes in land use/land cover in Syria from 2010 to 2018 using multitemporal Landsat imagery and GIS. Land 9 (7): 226.

Mohammed, M. U., Musa, I. J., Jeb, D. N. (2014). GIS-based analysis of the location of filling stations in metropolitan Kano against the physical planning standards. American Journal of Engineering Research 3 (9): 147-158.

Mukhtar, I., Iguisi, E. O., Shehu, A. U., Dabo, Y., Abubakar, M., Zubairu, S. M., Balarabe, A. (2020). Effects of Landuse and Landcover Change on Flooding in Kano Metropolis, Kano State, Nigeria. Fudma Journal of Sciences 4 (3): 505-512.

Nabegu, A. B. (2014). Analysis of vulnerability to flood disaster in Kano State, Nigeria. Greener journal of physical sciences 4 (2): 22-29.

Nasiri, V., Deljouei, A., Moradi, F., Sadeghi, S.M.M., Borz, S.A. (2022). Land use and land cover mapping using Sentinel-2, Landsat-8 Satellite Images, and Google Earth Engine: A comparison of two composition methods. Remote Sensing 14 (9): 1977.

Nourqolipour, R., Mohamed Shariff , A. B., Balasundram, S., Ahmad , N., Sood , A., Buyong, T. (2016). Predicting the effects of urban development on land transition and spatial patterns of land use in Western Peninsular Malaysia. Applied Spatial Analysis and Policy 9 (1), 1-19.

Nwagbara, M. O. (2015). Case study: Emerging advantages of climate change for agriculture in Kano State, northwestern Nigeria. American Journal of Climate Change 4 (3): 263-268.

Okoduwa, A., and Amaechi, C. F. (2024). Exploring Google Earth Engine, Machine Learning, and GIS for Land Use Land Cover Change Detection in the Federal Capital Territory, Abuja, between 2014 and 2023. Applied Environmental Research 46 (2).

Okoduwa, K. A., Amaechi, C.F., Enuneku, A. A. (2024) Soil Adjusted Vegetation Index, Normalized Difference Buildup Index, and Land Surface Temperature between 1987 and 2023 in Abuja Municipal Area Council, Nigeria. Journal of Applied Science and Environmental Management 28 (3): 665-674.

Okopi, M. (2021). Urbanization and sustainable growth of urban Kano, Nigeria. In IOP Conference Series: Earth and Environmental Science. IOP Publishing, 1(665):012063

Osman, T., Shawb, D., Kenawy, E. (2018). An integrated land use change model to simulate and predict the future of greater Cairo metropolitan region. Journal of Land Use Science 13(6): 565– 584.

Rahman, M. T. (2016). Detection of land use/land cover changes and urban sprawl in Al-Khobar, Saudi Arabia: An analysis of multitemporal remote sensing data. ISPRS International Journal of Geo-Information 5 (2): 15.

Rahnama, M. R. (2021). Forecasting land-use changes in Mashhad Metropolitan area using Cellular Automata and Markov chain model for 2016-2030. Sustainable Cities and Society 64: 102548.

Rani, A., Gupta, S. K., Singh, S. K., Meraj, G., Kumar, P., Kanga, S., Dogančić, D. (2023). Predicting future land use utilizing economic and land surface parameters with ANN and Markov chain models. Earth 4(3): 728-751.

Rigden, A., and Li, D. (2017). Attribution of surface temperature anomalies induced by land use and land cover changes. Geosphacial Research Letters, 44(13): 6814-6822.

Rimal, B., Sharma, R., Kunwar, R., Keshtkar, H., Stork, N. E., Rijal, S., Baral, H. (2019). Effects of land use and land cover change on ecosystem services in the Koshi River Basin, Eastern Nepal. Ecosystem services 38: 100963.

Rimal, B., Zhang, L., Keshtkar, H., Sun, X., Rijal, S. (2018). Quantifying the spatiotemporal pattern of urban expansion and hazard and risk area identification in the Kaski District of Nepal. Land 7(1): 37.

Samat, N., Mahamud, M. A., Tan, M. L., Maghsoodi Tilaki, M. J., Tew, Y. L. (2020). Modeling land cover changes in peri-urban areas: A case study of George Town conurbation, Malaysia. Land 9(10): 373.

Simwanda, M., and Murayama, Y. (2018). Spatiotemporal patterns of urban land use change in the rapidly growing city of Lusaka, Zambia: Implications for sustainable urban development. Sustainable Cities and Society 39: 262–274.

Singh, P., Kikon, N., VermaAmity, P. (2017). Impact of land use change and urbanization on urban heat island in Lucknow city, Central India. A remote sensing based estimate. Sustainable Cities and Society 32: 100-114.

Sulaiman, S. M., Yahaya, A., Muhammad, M. A., Muhammad, A. D. (2021). Evaluating Fadama III Development Project in Kano State, Nigeria: Using Difference in Difference Estimation with Propensity Score Matching Approach. International Journal of Economics, Management and Accounting 499-517.

Sun, X., Crittenden, J. C., Li, F., Lu, Z., Dou, X. (2018). Urban expansion simulation and the spatiotemporal changes of ecosystem services, a case study in Atlanta Metropolitan area, USA. Science of the Total Environment 622, 974-987.

Tilman, D., Balzer, C., Hill, J., Befort, B. L. (2011). Global food demand and the sustainable intensification of agriculture. Proceedings of the national academy of sciences 108(50): 20260-20264.

Tobore, A., Senjobi, B., Oyerinde, G. (2021). Spatio Temporal Analysis and Simulation Pattern of Land Use and Land Cover Change in Odeda Peri-urban of Ogun State, Nigeria. Jordan Journal of Earth & Environmental Sciences 12(4).

Tsegaye, B. (2019). Effect of land use and land cover changes on soil erosion in Ethiopia. International Journal of Agricultural Science and Food Technology 5(1): 26-34.

United Nations Department of Economic and Social Affairs. World Urbanization Prospects: The 2018 Revision. Available online: https://population.un.org/wup/Country-Profiles/ (accessed on 15 June 2020).

Verburg, P. H., and Overmars, K. P. (2007). Dynamic simulation of land-use change trajectories with the CLUE-s model. Modelling land-use change: Progress and applications 321-337.

Wang, K., Zhang, J., Huang, H. (2019, June). Impact of Land Use/cover Changes on Carbon Storage in Chinese Resource-Based City. In Abstract Proceedings of 2019 International Conference on Resource Sustainability-Cities (icRS Cities).

Wang, R., Hou, H., Murayama, Y. (2018). Scenario-based simulation of Tianjin City using a cellular automata–Markov model. Sustainability 10 (8): 2633.

Wang, S. W., Munkhnasan, L., Lee, W. K. (2021). Land use and land cover change detection and prediction in Bhutan's high altitude city of Thimphu, using cellular automata and Markov chain. Environmental Challenges 2: 100017.

Wang, S., and Zheng, X. (2023). Dominant transition probability: Combining CA-Markov model to simulate land use change. Environment, Development and Sustainability 25(7): 6829-6847.

Xu, C., Liu, M., Hong, C., Chi, T. (2012). Temporal variation of characteristic scales in urban landscapes: an insight into the evolving internal structures of 'China's two largest cities. Landscape Ecology 27: 1063–1074.

Yuan, T., Yiping, X., Lei, Z., Danqing, L. (2015). Land use and cover change simulation and prediction in Hangzhou city based on CA-Markov model. International Proceedings of Chemical. Journal of Biological and Environmental Engineering 90: 108-113.

Zhu, X., Zhang, P., Wei, Y., Li, Y., Zhao, H. (2019). Measuring the efficiency and driving factors of urban land use based on the DEA method and the PLS-SEM—A case study of 35 large andmedium-sized cities in China. Sustainable Cities and Society 50:101646.

JJEES

JJEES (2025) 16 (3): 276-283
ISSN 1995-6681

Jordan Journal of Earth and Environmental Sciences

Analysis of the Extremely Heavy Rainfall over Uttar Pradesh (India) during September 2022

Ruma[1], Shashi Kant[2*], Deepak Kumar[1]

[1] *Department of Applied Sciences, School of Engineering and Technology, Manav Rachna International Institute of Research and Studies, Faridabad, India*
[2] *India Meteorological Department, Ministry of Earth Sciences, New Delhi, India*

Received on December 7, 2024, Accepted on March 3, 2025

Abstract

Extremely heavy rainfall (>20cm/day) activities were recorded over some stations in different parts of India during the southwest monsoon (June to September) 2022. Furthermore, the persistence of extremely heavy rainfall events is unusual, particularly over Uttar Pradesh, where only one or two events occurred during the monsoon season. One extremely heavy rainfall episode was recorded over Uttar Pradesh from 15-17 September 2022. This paper analyzes the associated meteorological conditions.

The enhanced rainfall activity can be attributed to several key atmospheric processes working together over a geographical area. In this case, the synoptic analysis reveals that an active monsoon low-pressure area over the region provided favorable atmospheric conditions at the synoptic scale. Moisture transport from the Arabian Sea played a crucial role in fueling precipitation, with strong southwesterly winds bringing large amounts of moisture into the study area across central India. At lower tropospheric levels, the presence of a trough in the atmosphere contributes to the development of favorable conditions for rainfall. Positive relative vorticity was another key factor. Upper-level divergence supports the upward motion of air, aiding in removing air from the upper levels of the atmosphere. This divergence at higher altitudes allows more air from below to rise, creating a more favorable environment for convection and precipitation. In addition, high relative humidity at lower tropospheric levels of the atmosphere ensures that the air contains a significant amount of moisture. Lower-level convergence occurs when winds at the surface converge and force air upwards, further contributing to upward motion and cloud formation. In this case, the overall dynamics support upward air motion, amplifying rainfall activity. Together, these processes create an environment where rainfall is not only sustained but also intensified.

Keywords: *Southwest Monsoon; Heavy rainfall; Meteorological Analysis; Uttar Pradesh (India)*

1. Introduction

It is well known that the southwest monsoon (SWM) during June to September is the primary rainy season in India. Heavy rainfall occurrences are not a uncommon during the SWM; however, each heavy rainfall spell usually brings new experiences for operational forecasters, numerical weather prediction (NWP) modelers, disaster managers, decision-makers, and other stakeholders, including the public. For a summary of Monsoon 2022, readers can refer to salient features of Monsoon-22 issued by India Meteorological Department (IMD). The extremely heavy rainfall (>20cm/day) over a station in Uttar Pradesh for two or more days consecutively is a rare phenomenon and occurs only one or two such cases in the whole SWM season (June to September). The documentation of such cases is essential to understand the mechanism for further improvement in its management and their early warning for the safety of the public and livestock. Scientific experiences, the accuracy of early warnings, lead period and field experiences to reduce the impact of such events may be documented and published in the form of reports and articles.

Some studies have been reported in the scientific literature on heavy rainfall in various regions of India. Rao et al. (2021) investigated heavy rainfall events over Haryana in July 2016. Authors discussed observational aspects from different sources, synoptic conditions associated with the heavy rainfall, and thermo-dynamical situations for this severe weather event. Their analysis found that during Haryana's extreme rainfall episodes, an interaction between a trough in mid-tropospheric levels westerlies and strong monsoonal winds created a strong convergence zone. Kumar et al. (2017) studied the meteorological features associated with the unprecedented precipitation that occurred in different parts of the country in March 2015. The authors also discussed synoptic systems in this study. Viswanadhapalli et al. (2019) conducted a diagnostic analysis of extreme heavy rainfall over Kerala in August 2018. Kant (2023) examined synoptic systems associated with extreme heavy rainfall in July 2022. In this paper, synoptic systems were documented for extremely heavy rainfall. Nandargi & Dhar (2011) documented extreme heavy rainfall over the Himalayas between 1871 and 2007. Mehfoozali et al. (2013) discussed synoptic systems for heavy rainfall over the Lower Yamuna Catchment for the period 1998-2010. Several case studies of extremely heavy rainfall, mainly from Madhya Pradesh and

---

* Corresponding author e-mail: onlineskmishra@gmail.com

East Rajasthan, were discussed in terms of synoptic systems.

Gond et al. (2025) analyzed dry–wet events and their transitions using 48 years of data (1971–2018) from 18 synoptic locations in the state of Uttar Pradesh. Ankit et al. (2024) conducted a statistical analysis of extreme rainfall over the eastern parts of Uttar Pradesh, mainly in Ambedkar District, using data from 1985 to 2019 to investigate the trends in the region. Saha et al. (2020) discussed the spatial distribution of extreme rainfall events over India during the monsoon period from 2016 to 2018. They used the Global Forecast System (GFS) and National Centre for Medium-Range Weather Forecasting (NCMRWF) Unified Model (NCUM) models for verification. In these studies, no rigorous synoptic discussions were conducted.

Latheef and Mohamed (2023) investigated rainfall patterns across three agro-ecological regions of Sri Lanka using data from the period 1961–2005 and applying different statistical methods. Their study showed that climate change had impacted rainfall trends, although they were statistically insignificant. Dzarma et al. (2020) studied the trends, rainfall variability, and discharge in the River Kilange catchment in Adamawa State, Nigeria, using time-series data from 1987 to 2013 and Pearson's Product-Moment Correlation. They concluded that mean monthly rainfall and discharge were moderately and positively correlated and provided some recommendations. Mohammed et al. (2015) proposed an aridity classification based on rainfall data for the period 1961–2012 from 22 weather stations in Jordan.

The documentation and analysis of extreme or unprecedented heavy rainfall events are indeed crucial for scientific understanding and improving preparedness and response strategies. In general, some important points in connection with such weather events need rigorous scientific discussion. Hence, in general, the following points may be relevant in the studies of extremely heavy rainfall:

i. **Timing and duration of weather event:** Start and end timings of intense spells are important for the detection of persistence. The impact varies with the time of occurrence. For instance, during daytime, it may have a direct impact on day-to-day economic activities.

ii. **Spatial distribution of heavy rainfall:** During summer monsoon, rainfall is received in active and break spells. Active spells are usually related to some heavy rainfall events. These spells are not uniformly distributed, and more specifically, extremely heavy rainfall is usually not reported in wider areas. Hence, the investigation of extremely heavy rainfall regions that were most affected and whether these weather events were localized or had widespread impacts.

iii. **Intensity & comparison to Climatology:** As mentioned in point (i) above, it is a matter of concern to identify the peak rainfall recorded during the weather event and how this rainfall compares to climatological records.

iv. **Accumulated rainfall:** As per meteorological convention, 24-hour accumulated rainfall is classified into different intensities. IMD follows the well-specified classification of rainfall (See Table 1).

Table 1. Classification of the intensity of Rainfall (Source: IMD)

Category	24 hours cumulative rainfall (mm)
No Rain/dry	0.0
Very light Rain	0.1-2.4
Light Rain	2.5 - 15.5
Moderate Rain	15.6 - 64.4
Heavy Rain	64.5 – 115.5
Very Heavy Rain	115.6 – 204.4
Extremely Heavy Rain	>204.4

v. **Meteorological conditions and temporal evolution:** Scientific discussion is required on synoptic, dynamic, mesoscale & thermodynamic features during the event (e.g., Low Pressure Area (LPA), convergence zones, moisture influx, instability, etc.). How did the synoptic systems evolve leading up to and during the heavy rainfall event? Were there any significant changes in meteorological parameters before and after the event?

vi. **Impacts:** What were the impacts of the heavy rainfall event on infrastructure, agriculture, transportation, and communities? Were there any casualties or significant damage reported?

The literature review highlights several studies on heavy rainfall from different regions of India and other countries; some of them are highlighted here. However, very few, if any, specific case studies have been reported that focus on the synoptic analysis of heavy rainfall, particularly over Uttar Pradesh. Accordingly, the main objective of this study is to understand the major synoptic systems associated with heavy rainfall in Uttar Pradesh. The primary reason for selecting this case study is the occurrence of extremely heavy rainfall episodes in regions typically categorized as having deficient rainfall, particularly in the state of Uttar Pradesh. One such example is the persistent extreme heavy rainfall episode that occurred from 15–17 September 2022 over Uttar Pradesh, which is considered in this study.

2. Study area, the climatology, and observational aspects of weather events

The study area in this paper is the state of Uttar Pradesh in India. This state is surrounded by Uttarakhand in the northwest, Madhya Pradesh, Rajasthan in the south & southeast, Haryana in the west, Bihar in the east, and Nepal in the north. IMD issues the weather forecast and warnings for 36 meteorological subdivisions of India, including two meteorological subdivisions (West & East) of Uttar Pradesh. For districts and other details, refer to the official web page of Uttar Pradesh: https://up.gov.in/en.

The following generic questions are also selected for the sake of understanding the observational aspect of this weather event.

- Whether the heavy rainfall has occurred in particular districts/places of the state, or is it distributed in the whole state? This distribution will ensure the nonuniform distribution and discontinuous nature of rainfall occurrences.
- What was the actual amount of extreme rainfall, district-wise/station-wise ,in each day? This amount will confirm the intensity of rainfall and the spatial impact of the weather event.
- Whether such amount of rainfall per day occurred during the last 20 to 30 years? What is the actual rainfall map along with the anomaly for the study area, and what is the anomaly for climatological rainfall values during this period?

Therefore, before delving into the details of the case, it is important to understand the climatology (Hazard Atlas IMD Pune). The maximum probable frequency of very heavy rainfall and extremely heavy rainfall events (for September) for the period 1901-2019 is studied. It included the maximum probable frequency in the category more (>3-4 days) over Uttar Pradesh. Data showed that the regions of northwest Uttar Pradesh, southeast & southwest Uttar Pradesh (Bundelkhnad region) had the highest probable frequency (5-8) in the class of very heavy rainfall & extremely heavy rainfall. The districts of Bareilly, Barabanki, Lalitpur, Muzaffarnagar, Pilibhit, Saharanpur, Shahjahanpur, Sitapur, Varanasi, and Hamirpur were in the same frequency with the highest frequency of 8 in Muzafarnagar. The month-wise rainfall progress during monsoon 2022 showed that Uttar Pradesh reported deficient rainfall from June to August (specific figures are not attached). September was the only month when the state reported normal to above-normal rainfall (Figure 1).

The persistent very heavy to extremely heavy rainfall episodes during the period of 15-17 September contributed to above-normal rainfall. On the 15th of September, heavy rainfall activity commenced, and large excess rainfall was reported over the stations of east and adjoining west & northwest Uttar Pradesh (Figure 1a). On the 16th, the peak activity was reported with excess/large excess rainfall over most parts of Uttar Pradesh (Figure 1b). On the 17th of September, activity concentrated mainly over north Uttar Pradesh(Figure 1c).

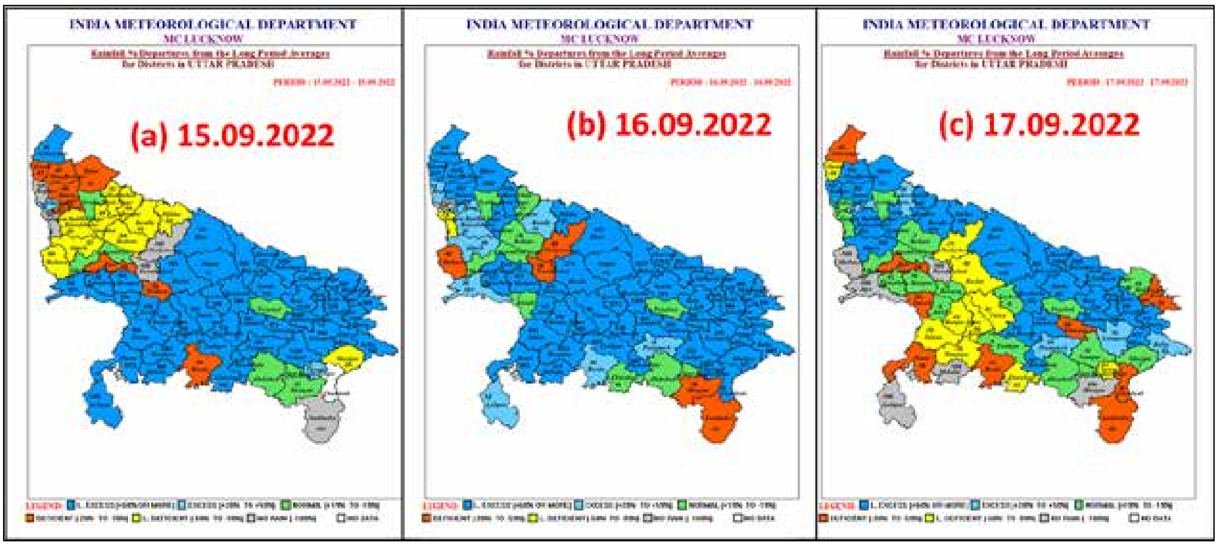

Figure 1. Rainfall percentage departure from the long period average over UP during 15-17 September 2022 (Source: IMD).

In this study, we collected rainfall data from 190 stations in east Uttar Pradesh and 135 stations in west Uttar Pradesh. The cumulative 24-hour rainfall (RR24) data from recording stations shows that East Uttar Pradesh reported very heavy rainfall (RR24 > 12cm) to extremely heavy rainfall (RR24>20cm) each day (Figure 2). The highest number of stations with heavy rainfall was recorded over East Uttar Pradesh on the 15th of September and West Uttar Pradesh on the 16th of September. East Uttar Pradesh reported the highest number of instances of extremely heavy rainfall on 16th September, followed by the 17th September, and isolated on the 15th of September. The very heavy rainfall was observed in West Uttar Pradesh on 15th with no instances of extremely heavy rainfall (Figure 2). On 15th September, Jaunpur; on 16th September, Barabanki and Kheri; and on the 17th of September, Gorakhpur and Kheri reported extremely heavy rainfall.

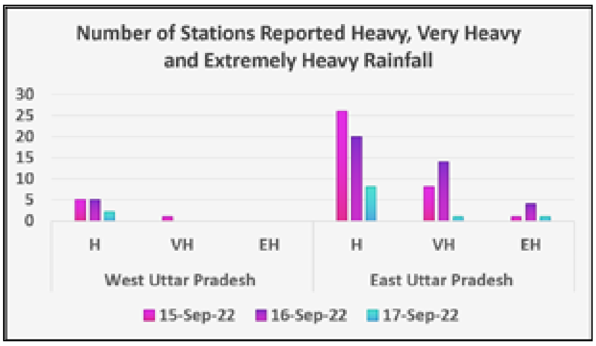

Figure 2. The number of stations reported heavy, very heavy, and extremely heavy rainfall during 15-17 September 2022 over Uttar Pradesh. H-Heavy Rainfall; VH-Very Heavy Rainfall; EH-Extremely Heavy Rainfall (Source: IMD)

3. Results and Discussion

Daily Rainfall data is collected from IMD. IMD-GFS model analysis charts are collected from the Numerical Weather Prediction (NWP) division of IMD, and synoptic charts are collected from IMD Pune. Additionally, for synoptic systems, all India weather bulletins from IMD have been collected; dynamical parameters from Cooperative Institute for Meteorological Satellite Studies (CIMSS) / University of Wisconsin-Madison (https://tropic.ssec.wisc.edu/) and upper air temperature, Relative humidity (RH) and Omega from Physical Science Laboratory, National Centers for Environmental Prediction (NCEP) and the National Center for Atmospheric Research (NCAR) reanalysis page https://psl.noaa.gov/data/composites/day/ (Kalnay, E. and Coauthors, 1996). Otherwise, the sources of most of the images are mentioned at the bottom of the respective images. Mathematical formulation of dynamical variables and units of different quantities are listed in Appendix I. The methodology is summarized in Figure 3.

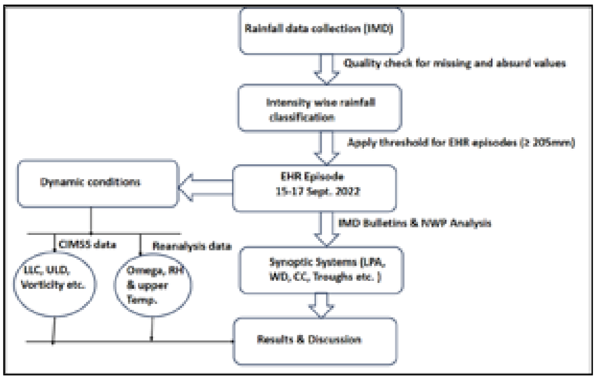

Figure 3. Data and methodology

Synoptic conditions and other meteorological analyses are discussed at four tropospheric levels:

i. **Surface Analysis**. For surface analysis, operational weather forecasting is mainly done using isobaric and wind analysis. During SWM (June to September), surface analysis is most important to identify the monsoon trough, heat low, and other synoptic systems. It is important to mention that in the Indian region, 10 m winds are considered surface winds, and an analysis of the same has been done to identify the LPA/Well Marked LPA or Cyclonic Circulation at the surface.

ii. **Lower tropospheric levels**. The tropospheric levels up to 600 hPa (4.5 km above mean sea level) are usually considered in the lower levels. In this paper, the analysis at the three standard levels of 925, 850, and 700 hPa is done. Wind analysis, upper Air Temperature & Omega at 850 hPa (NCEP re-analysis), relative vorticity at 850 & 700 hPa (from CIMSS), and RH (from NCEP re-analysis) will be discussed.

iii. **Middle tropospheric levels**. For this wind analysis from the NWP model (IMD-GFS), Air Temperature & Omega Analysis at 500 hPa (from NCEP re-analysis) and relative vorticity at 500 hPa (from CIMSS) will be discussed.

iv. **Upper tropospheric Levels.** Analysis at 200 hPa will be discussed for Jet streams. Additionally, air temperature analysis (from NCEP re-analysis) and upper-level divergence (from CIMSS) will be considered.

3.1 Synoptic Analysis

3.1.1 Surface Analysis:

In this sub-section, Mean Sea Level Pressure (MSLP) analysis (mainly isobaric) and wind (10 m) analysis are adopted to identify synoptic systems like LPA [or cyclonic circulation at the surface] during the period of study. MSLP analysis showed a well-marked LPA over northwest Madhya Pradesh & adjoining Uttar Pradesh, and the associated cyclonic circulation was visible in 10 m winds. It lay over central parts of Uttar Pradesh on the 16th of September, and the well-marked LPA weakened on the 17th of September. However, a remnant cyclonic circulation was seen over north Uttar Pradesh.

Additionally, an important feature of 10 m winds was observed on the 15th of September. Strong southwesterly/ southerly winds (20-25 knots) have prevailed from the northwest & central Arabian Sea to LPA. Accordingly, the moisture supply was seen. Similar meteorological conditions prevailed on the 16th of September, and the intensity of winds reduced on the 17th of September and accordingly rainfall intensity over Uttar Pradesh reduced on 17th September.

3.1.2 analysis in lower tropospheric levels

The following synoptic systems on the 15th of September were identified;

i. The associated cyclonic circulation with the LPA over northwest Madhya Pradesh,

ii. A trough from the northwest & central Arabian Sea to Uttar Pradesh across Madhya Pradesh.

iii. The strong southwesterly winds over Arabian Sea, Central India, and Uttar Pradesh (20-30 kt) with isolated patches of 30-40 kt.

Two systems listed at (ii) & (iii) created a favorable channel for moisture transport from the Arabian Sea to Uttar Pradesh. This channel induced the LPA/Well Marked LPA to generate intense spells over Uttar Pradesh on the 15thof September. The moisture incursion from either the Arabian Sea or the Bay of Bengal remained favourable. The weather systems persisted on 16th September except for the associated cyclonic circulation with the LPA, which lay over central parts of Uttar Pradesh. LPA/Well Marked LPA continued to generate intense spells of rainfall over Uttar Pradesh. The weakening of the wind intensity was seen on the 17th of September with the cyclonic circulation over northern Uttar Pradesh. The trough also got weakened on the 17th of September. This was an indication of a reduction in rainfall from the 17th of September.

This paper also analyzes Air temperature composite anomaly & mean temperature at 850 hPa. A positive anomaly was reported over northwest India, including parts of Uttar Pradesh. An increase was reported on the 16th of September, and the same persisted on the 17th of September. The peak positive anomaly was reported on 16th September. Relative

Humidity (RH) analysis at 700 hPa showed that it was more than 80% on the 15th & 16th of September over Uttar Pradesh, over east & adjoining west Uttar Pradesh, and northeast Uttar Pradesh, with a reduction on 17th September. A significant reduction over many parts of Uttar Pradesh was seen on the 17th of September, a clear indication of the reduction in the intensity of rainfall over Uttar Pradesh. Accordingly, RH was consistent with the rainfall pattern.

The vertical velocity (often referred to as Omega,) in meteorology. It is used to describe the upward or downward motion of air. In the context of heavy rainfall, vertical velocity plays a key role in developing thunderstorms and heavy precipitation. It typically represents the rate at which air is rising or sinking in the atmosphere. A negative omega ($\omega<0$) represents upward motion in the atmosphere. This is the condition conducive to heavy rainfall because it signifies rising air, which is a key component in the development of clouds and precipitation. A positive omega ($\omega>0$) represents downward motion or subsidence, which is typically associated with dry, clear conditions rather than rain. Accordingly, the negative vertical velocity (Omega) is favorable for heavy rainfall. The negative Omega at 850 hPa was concentrated over northwest Madhya Pradesh & adjoining Uttar Pradesh (-0.4 Pa/s) on the 15th of September, over central parts of Uttar Pradesh on the 16th of September, and over extreme northeast Uttar Pradesh on the 17th of September. Hence, Omega was favourable.

Another important dynamic parameter is the relative vvorticity at different tropospheric levels. Mathematically, vorticity (ξ) is defined as (**Annexure I**):

$$\xi = \vec{\nabla} \times \vec{V}, \eta = \frac{\partial v}{\partial x} - \frac{\partial u}{\partial y}. \tag{1}$$

In operational weather forecasting, we monitor the vorticity profile mainly from two sources, namely CIMSS and Satellite products from INSAT 3D/R https://satmet.imd.gov.in/. The Vorticity profile is received from the CIMSS webpage (https://tropic.ssec.wisc.edu/archive/). The relative vorticity at 850 hPa (> 100 $\times10^{-6}$ Sec^{-1}) was reported on the 15th & 16th of September with a reduction on 17th September. Therefore, the relative Vorticity profile at lower tropospheric levels was favorable for rainfall.

Mathematically, convergence (in two-dimensional cases) is written as,

$$Conv.\ \vec{F} = -\left(\frac{\partial u}{\partial x} + \frac{\partial v}{\partial y}\right). \tag{2}$$

For more details, refer to Annexure I. At 00 UTC (the 15th of September), lower level convergence was positive over south Uttar Pradesh, and it was over east Uttar Pradesh & Madhya Pradesh at 12 UTC. At 00 UTC (16th September), lower level convergence was positive over east Uttar Pradesh, and it was over east Uttar Pradesh and adjoining Bihar, and at 12 UTC, the same conditions prevailed. At 00& 12 UTC (the 17th of September), weakening of lower level convergence was seen only 5×10^{-6} Sec^{-1} over Bihar. Therefore, the lower level convergence was favourable for the weather and also suggest the reduction in rainfall from 17th September.

3.1.3Analysis at Middle Tropospheric Levels

Wind analysis at 500 hPa on the 15th of September showed a cyclonic circulation CC over northwest Madhya Pradesh associated with LPA. Also, westerly winds from the Arabian Sea prevailed and supported the moisture incursion over Uttar Pradesh. A similar wind pattern prevailed on the 16th, and cyclonic circulation was relocated to the central parts of Uttar Pradesh. The pattern of winds changed on the 17th of September; cyclonic circulation became less marked. This change indicated the reduction in the intensity of rainfall from the 17th of September.

Air Temperature (K) composite Anomaly (Climatology 1991-2020) at 500 hPa and composite mean are analyzed. On the 15th of September, positive anomalies (1.5-2.5K) were seen over most parts of northwest & west India. On the same day, warm core with the center of peak (the highest temperature) was seen over northwest India. The second layer (271-272K) of this warm core extended up to Uttar Pradesh. A shift in the direction of the northeast of warm core temperature and anomaly was observed on the16th of September and seen over Nepal with the second and third layers over September. A further shift was observed on the 17th of September and was seen over Nepal; however, a positive anomaly was seen over North Uttar Pradesh and the second layer over eastern parts of Uttar Pradesh. This feature was in agreement with the heavy rainfall.

Analysis of Omega showed that on 15th September, the major zone of negative Omega was over Nepal and Uttar Pradesh, with the maxima over Nepal (<-0.3 Pa/s). The second layer was seen over Uttar Pradesh (around -0.25 Pa/s). On the 16th of September, the major shifted towards Nepal with the maxima (<-0.3 Pa/s). The second and third layers were seen over Uttar Pradesh (around -0.25 Pa/s). This zone remained favourable for heavy rainfall. On the 17th of September, Omega increased, and only negative Omega (-0.1 Pa/s) was seen over Uttar Pradesh. Thus, the Omega was consistent with the heavy rainfall.

The maxima of vorticity at 500 hPa (> 50 $\times10^{-6}$ Sec^{-1}) over Uttar Pradesh on 00 & 12 UTC of 15th September. The maxima are seen over central Uttar Pradesh at 00 UTC on 16th September. The vorticity started decreasing from 12 UTC, indicating the weakening of the LPA. Patches of yellow color were seen till 00 UTC on 17th September. Further reduced at 12 UTC. Thus, the vorticity pattern at 500 hPa was consistent with the heavy rainfall.

3.1.4 Analysis at upper tropospheric levels

Referring to 200 hPa winds, no Jet winds prevailed over any parts of the country. Winds <40 kts prevailed over most parts of the country, including Uttar Pradesh from 15-17 September.

At the same time, air temperature analysis at 200 hPa showed the presence of the warm core over west Uttar Pradesh on the 15th & 16th of September, and temperature decreased on 17th September. This was consistent with the rainfall episode. Regarding anomaly, it was reported positive all three days and highest on the 15th& 16th of September. This showed that in the absence of any active Jet core at 200 hPa during monsoon season, very heavy/extremely heavy rainfall over Uttar Pradesh is possible.

The relative Vorticity profiles at 200 hPa remained negative over Uttar Pradesh on most days except isolated patches of the order of 0×10^{-6} Sec^{-1} on 16th September. This shows that during the monsoon period, even in the negative relative Vorticity profile at 200 hPa, an intense spell of rainfall over Uttar Pradesh is possible.

Mathematically, divergence in two-dimensional case is written as, the negative of convergence as shown in Equation (2),

$$Div.\vec{F} = \left(\frac{\partial u}{\partial x} + \frac{\partial v}{\partial y}\right). \tag{3}$$

For more details, refer to Annexure I. The patches of positive upper-level divergence remained favourable over Uttar Pradesh during the period till 12 UTC on 17th September. On 15th September, upper level divergence was reported of the order of 10×10^{-6} Sec^{-1}. It increased to 20-30 $\times10^{-6}$ Sec^{-1} on 16th September, reduced on 17th September, and moved east-northeast wards. This increase was an indication of a reduction in intensity of rainfall from 17th September.

4. Conclusion

- Before closing the discussion, the following meteorological conditions are highlighted;
- A Well Marked Low-Pressure Area lay over northwest Madhya Pradesh & neighbourhood on 15th September; it lay over central parts of Uttar Pradesh on 16th September; it weakened into an LPA over the same region in the early morning hours of 17th September before getting less marked in the morning of that day; its remnant cyclonic circulation lay over north Uttar Pradesh on 17th September.
- A trough in the lower tropospheric levels extends from Northwest / westcentral Arabian Sea to the cyclonic circulation associated with the above-mentioned Well Marked Low-Pressure Area. This helped transport the moisture from the Arabian Sea to Uttar Pradesh.
- Relative Vorticity remained favourable in lower and middle tropospheric levels. We observed that Relative Vorticity was positive up to the level of 500 hPa. The presence of positive vorticity at these levels also suggested that the weather systems were dynamically supportive of convection over several days, contributing to the intensity and persistence of the rainfall, especially on the 15th and 16th of September. Positive vorticity supported the favorable conditions for heavy rainfall by maintaining a cyclonic system that encouraged continuous rising motion and moisture transport. This likely contributed significantly to the rainfall observed over Uttar Pradesh, especially during the event's peak.
- Upper-level Divergence remained consistent with the rainfall episode. This showed the good weather activity on 15th & 16th September and a reduction from 17th September. Evolution of Upper-level Divergence was in good agreement for the weather event. On 15th September, it was relatively low but still supported some divergence aloft. This divergence likely helped to initiate upward motion at lower levels, facilitating cloud formation and the start of the rainfall event. On 16th September, it increased to 20-30 $\times 10^{-6}$ s^{-1}, which was a significant increase that indicated a stronger divergence aloft on the 16th September. This enhanced upward motion at lower levels, leading to more intense convection and, therefore, heavier rainfall. The increase in divergence was in line with the peak intensity of the rainfall on that day. On 17th September, it further decreased, suggesting that the divergence aloft had weakened. This would lead to less upward motion and a reduction in the conditions favorable for sustained heavy rainfall. As a result, the intensity of the rainfall started to decrease, aligning with the end of the heavy rainfall episode.
- RH profile, lower level convergence, and vertical velocity (Omega) showed consistency with the heavy rainfall episode. RH at 700 hPa was more than 80% on the 15th & 16th over Uttar Pradesh and reduced onthe 17th of September. High relative humidity at 700 hPa (approximately 3 km above sea level) indicated a substantial amount of moisture in the lower to mid-layers of the atmosphere. When RH was above 80%, it suggested conditions conducive for rainfall, as the air is saturated and can support cloud formation and precipitation. A drop in RH on the 17th of September suggested that moisture in the atmosphere decreased, possibly indicating that the rainfall event was ending or transitioning into a drier period.
- Discussion showed that during the monsoon period, even in the absence of any active Jet core at 200 hPa, extremely heavy rainfall may occur over Uttar Pradesh. The jet stream at 200 hPa (upper-tropospheric winds) plays a significant role in large-scale atmospheric circulation. An active jet core can enhance divergence aloft, promoting upward motion and creating favorable conditions for convection and rainfall. However, even in the absence of a strong or active jet core, extremely heavy rainfall can still occur, particularly over Uttar Pradesh. This suggested that other meteorological factors are at play in driving rainfall during the monsoon season.
- In addition to Cyclonic Circulation/LPA, the moisture supply from the Arabian Sea, with the help of westerly/southwesterly winds, was an important mechanism for the occurrence of rainfall episodes.

We understand that each heavy rainfall episode provides valuable lessons and helps to enhance the experience during its monitoring, evaluation, and dissemination of its forecast to different users. This case study serves this purpose. It may be useful for policymakers, disaster managers, and those involved in disaster response and mitigation. Early warning is one of the most important pillars in the disaster management of natural extreme weather events. There are very few case studies addressing the synoptic aspects of heavy rainfall over Uttar Pradesh. During short to medium-range weather forecasting (3-10 days lead period), even in active monsoon conditions, synoptic-scale systems are a significant tool for issuing heavy rainfall warnings. This case study suggests that whenever a low-pressure system is located over northwest Madhya Pradesh or its vicinity, a heavy rainfall warning may be issued for Uttar Pradesh, keeping in mind the climatology of a particular district. Accordingly, this case study serves as a precedent for early warnings of heavy rainfall in the state of Uttar Pradesh. Future work will include the climatology of synoptic systems that induce heavy rainfall events over the state.

Acknowledgment

The authors are thankful to the Director General, IMD, for all their support and providing the rainfall data. The authors are thankful to CIMSS (https://tropic.ssec.wisc.edu/) for dynamical parameters, NOAA/ESRL Physical Sciences Laboratory, from their Web site at http://psl.noaa.gov/" for re-analysis data.

Disclaimer

The contents and views expressed in this study are the views of the authors and do not necessarily reflect the views of the organizations they belong to.

References

Ankit et al. (2024). Analyzing the patterns of extreme rainfall in the eastern Uttar Pradesh. International Journal of Statistics and Applied Mathematics SP-9(2), 101-107.

Dzarma Sayd, Ezekiel Yonnana, Aishatu Mubi (2020). An Analysis of Rainfall and Discharge Relationship at the River Kilange Catchment, Adamawa State, Nigeria. Jordan J. Earth and Environ. Sci. (JJEES) 11 (4), 248-252.

Gond, S., Agnihotri, A.K., Gupta, N. and Dikshit, P.K.S. (2025). Comprehensive analysis of characteristics of dry–wet events and their transitions in Uttar Pradesh, India. Water Science and Engineering 18(1), 59-68. https://doi.org/10.1016/j.wse.2024.06.003

Hazard Atlas IMD Pune https://imdpune.gov.in/hazardatlas/index.html (Accessed on 30th October 2022)

Kalnay, E. and Coauthors (1996). The NCEP/NCAR Re-analysis 40-year Project. Bull. Amer. Meteor. Soc. 77, 437-471. http://psl.noaa.gov/ (Accessed on 29th October 2022)

Kant, S. (2023). Meteorological conditions associated with extremely heavy rainfall over some Indian states in July 2022. Current Science 125 (10), 1068-1077. https://doi.org/10.18520/cs/v125/i10/1068-1077

Kumar, N., Mohapatra, M. & Jaswal, A.K. (2017). Meteorological features associated with unprecedented precipitation over India during 1st week of March 2015. J Earth Syst Sci 126, 62. https://doi.org/10.1007/s12040-017-0842-y

Latheef Fathima Zisath Shama and Mohamed M. M. Najim (2023). Analysis of Rainfall Trends in Three Selected Rain Gauging Stations from WL3, IL1a, and DL1f Agroecological Regions in Srilanka. Jordan J. Earth and Environ. Sci. (JJEES) 14 (3), 175-181.

Mohammed A. Salahat, Mohammed I. Al-Qinna (2015). Rainfall Fluctuation for Exploring Desertificationand Climate Change: New Aridity Classification. Jordan J. Earth and Environ. Sci. (JJEES), 7(1), 27-35.

Mehfoozali, M. A., Singh, U., Joardar, D. and Nizamuddin, N. (2013). Synoptic study of extremely heavy rainfall events over lower Yamuna catchment : Some cases. Mausam 64 (2), 265–280.

Rao, Narasimha, N., Paul, S., Skekhar, M. S., Singh, G. P., Mitra, A. K., & Bhan, S. C. (2021). Unprecedented heavy rainfall event over Yamunanagar, India during 14th July 2016: An observational and modelling study. Meteorological Applications 28(6), e2039. https://doi.org/10.1002/met.2039

Salient Features of Monsoon-22 https://internal.imd.gov.in/press_release/20221001_pr_1849.pdf

Saha, U., Singh, T., Sharma, P., Gupta, M.D. and Prasad, V.S. (2020). Deciphering the extreme rainfall scenario over Indian landmass using satellite observations, re-analysis and model forecast: Case studies. Atmospheric Research 240, p.104943. https://doi.org/10.1016/j.atmosres.2020.104943

Nandargi and Dhar O. N. (2011). Extreme rainfall events over the Himalayas between 1871 and 2007. Hydrological Sciences Journal 56(6), 930-945. https://doi.org/10.1080/02626667.2011.595373

Viswanadhapalli, Y, Srinivas, CV, Basha, G, et al. (2019). A diagnostic study of extreme precipitation over Kerala during August 2018. Atmos Sci Lett. 20:e941. https://doi.org/10.1002/asl.941

Annexure I. (Mathematical Formulation & units)

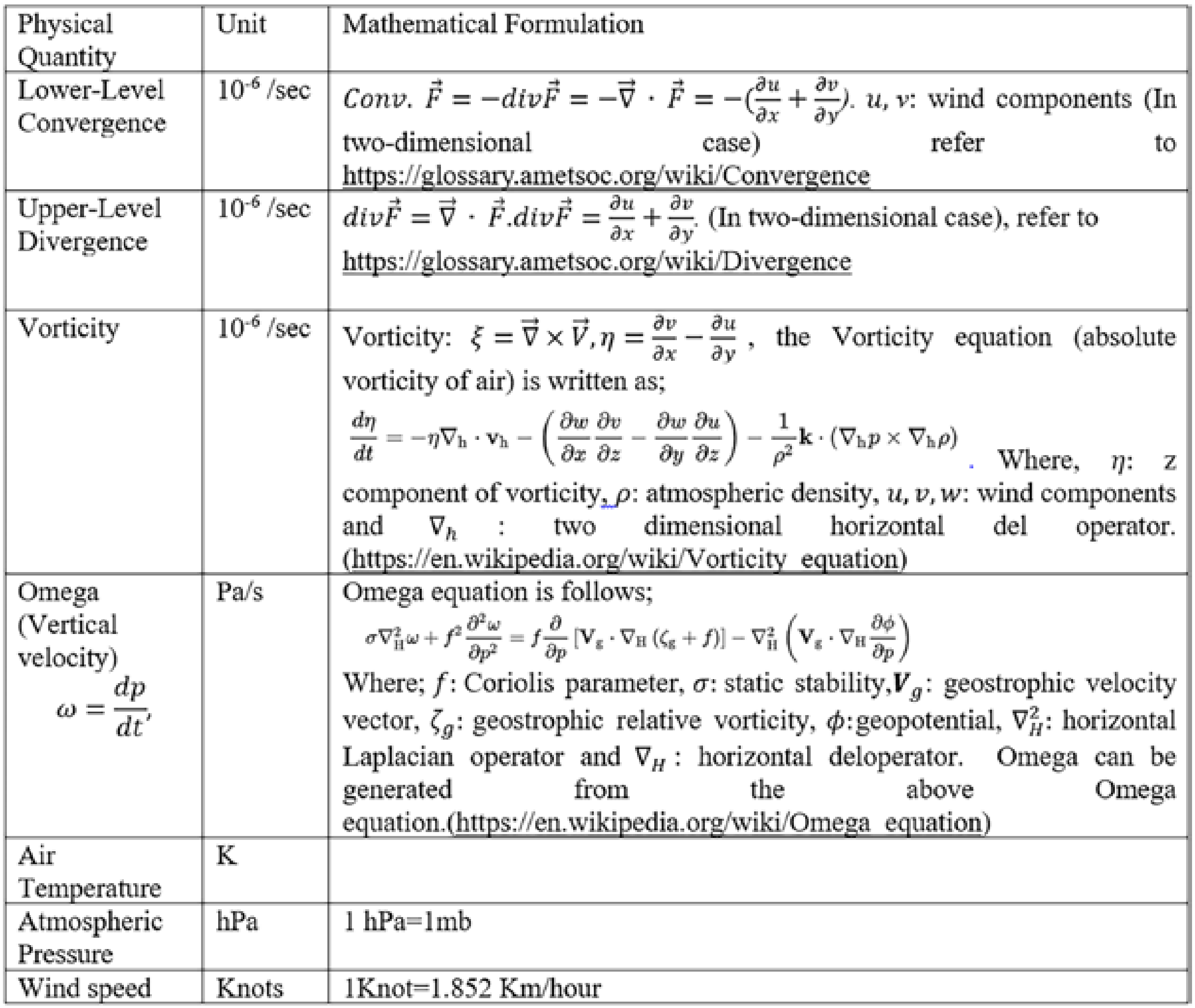

Physical Quantity	Unit	Mathematical Formulation
Lower-Level Convergence	10^{-6} /sec	$Conv.\ \vec{F} = -div\vec{F} = -\vec{\nabla} \cdot \vec{F} = -(\frac{\partial u}{\partial x} + \frac{\partial v}{\partial y})$. u, v: wind components (In two-dimensional case) refer to https://glossary.ametsoc.org/wiki/Convergence
Upper-Level Divergence	10^{-6} /sec	$div\vec{F} = \vec{\nabla} \cdot \vec{F}. div\vec{F} = \frac{\partial u}{\partial x} + \frac{\partial v}{\partial y}$. (In two-dimensional case), refer to https://glossary.ametsoc.org/wiki/Divergence
Vorticity	10^{-6} /sec	Vorticity: $\xi = \vec{\nabla} \times \vec{V}, \eta = \frac{\partial v}{\partial x} - \frac{\partial u}{\partial y}$, the Vorticity equation (absolute vorticity of air) is written as; $\frac{d\eta}{dt} = -\eta \nabla_{\mathrm{h}} \cdot \mathbf{v}_{\mathrm{h}} - \left(\frac{\partial w}{\partial x} \frac{\partial v}{\partial z} - \frac{\partial w}{\partial y} \frac{\partial u}{\partial z} \right) - \frac{1}{\rho^2} \mathbf{k} \cdot (\nabla_{\mathrm{h}} p \times \nabla_{\mathrm{h}} \rho)$. Where, η: z component of vorticity, ρ: atmospheric density, u, v, w: wind components and ∇_h : two dimensional horizontal del operator. (https://en.wikipedia.org/wiki/Vorticity_equation)
Omega (Vertical velocity) $\omega = \frac{dp}{dt}$,	Pa/s	Omega equation is follows; $\sigma \nabla_{\mathrm{H}}^2 \omega + f^2 \frac{\partial^2 \omega}{\partial p^2} = f \frac{\partial}{\partial p} [\mathbf{V}_{\mathrm{g}} \cdot \nabla_{\mathrm{H}} (\zeta_{\mathrm{g}} + f)] - \nabla_{\mathrm{H}}^2 \left(\mathbf{V}_{\mathrm{g}} \cdot \nabla_{\mathrm{H}} \frac{\partial \phi}{\partial p} \right)$ Where; f: Coriolis parameter, σ: static stability, $\boldsymbol{V}_g$: geostrophic velocity vector, ζ_g: geostrophic relative vorticity, ϕ: geopotential, ∇_H^2: horizontal Laplacian operator and ∇_H : horizontal deloperator. Omega can be generated from the above Omega equation.(https://en.wikipedia.org/wiki/Omega_equation)
Air Temperature	K	
Atmospheric Pressure	hPa	1 hPa=1mb
Wind speed	Knots	1Knot=1.852 Km/hour

JJEES

JJEES (2025) 16 (3): 284-288
ISSN 1995-6681

Jordan Journal of Earth and Environmental Sciences

Evaluation of Petrophysical Properties and Oil Content of Hartha Formation in Qayyarah Oil Field, Northern Iraq

Bashar A. Al-Juraisy [1*] and Maan H. Abdullah Al-Majid [2]

[1] *Department of Geology - College of Science, University of Mosul, Mosul-Iraq*
[2] *Department of Petroleum Reservoir Engineering- College of Petroleum and Mining Engineering, University of Mosul, Mosul-Iraq*

Received on February 13, 2025, Accepted on March 3, 2025

Abstract

Among the many oil fields in Iraq, the Qayyarah oil field is considered one of the most important fields in producing heavy oil. Oil is produced in this field from more than one formation, and the Hartha Formation is considered one of the important formations produced in this field, as well as in many producing fields in Iraq because of its good reservoir properties.

In the current study, data from three wells (A-1, A-2, and A-3) were used and analyzed to identify some petrophysical properties and oil content of the rocks of the Hartha Formation.

Analysis and interpretation were made using the Didger program to convert analoque data into digital data and the IP3.5 program to analyze and interpret digital data.

The study results showed that the rocks of the Hartha Formation have relatively good porosity. Also, with regard to the oil content, most parts of the formation contain a relatively good percentage of oil, and the formation can also be divided based on the oil content into three regions (A, B, and C). The first zone (A) contains the largest percentages of oil saturation, while the third zone (C) does not contain oil.

Keywords: *Petrophysical, Properties; Oil, Content, Hartha, Qayyarah*

1. Introduction

Qayyarah oil field can be considered one of the important oil fields in northern Iraq. Its dimensions are about 16 kilometers long and 5-kilometer wide, and structurally, it is an asymmetrical anticline. According to some publications, its field's oil reserves are estimated is about 800 million barrels of crude oil (API gravity 15°). One of most important reservoir formations in this oil field is Hartha Formation (Upper Campanian-Lower Maastrichtian) which consists mainly of limestone (detrital & glauconitic), and it's dolomitized in some places with layers of shale and chalk (Jassim and Goff, 2006).

The importance of the Hartha formation lies in the fact that it is one of the reservoirs and produces oil in many oil fields in Iraq; therefore has aroused the interest of many researchers like (Homadi and Al-Zaidy, 2020; Al-Badrani et al.,2021; Al-Hadidy et al., 2022; Abed and Al-Jaberi, 2023; Albarzanji and Alhamdani, 2024).

Geophysical well logs are one of the most widely used scientific tools in subsurface investigation, especially in the mining and oil industry. It is usually used the open (non-cased) wells for determination of the petrophysical and reservoir properties (Serra,1988; Al-Juraisy, and Al-Majid, 2021; Al-Majid, 2021; Abuseda and Sayed, 2022; Al-Mawla et al., 2023; Umoren et al., 2023) in addition to determining the formation lithology and shale distribution.

The aim of the current study is to evaluate some petrophysical characteristics, the most important one being the oil content in the Hartha Formation. Through this, the quantities of oil reserves and the economic feasibility of extraction can be estimated.

2. Site Description:

The study area (Qayyarah oil field) is situated on the western side of the Tigris River, approximately 55 km southwest of Mosul city. It is located within a low folded zone according to the tectonic division of Iraq (Dunnington, 2005). One of the region's most important general features is the presence of linear structures in a northwest-southeast direction, such as the Najma, Jewan, and Qayyarah anticline (Figure 1).

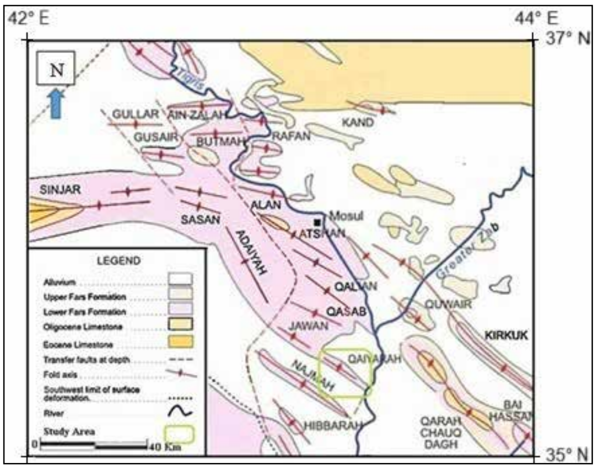

Figure 1. Geological map of the study area (modified from Aqrawi et al., 2010)

---

* Corresponding author e-mail: basharaziz@uomosul.edu.iq

The varying thickness of Hartha Formation in the Qayyarah field was attributed by some researchers to ground movements in the Late Cretaceous, which affected the study area, represented by many complex faults and narrow grabens (Ditmar et al., 1971; Murrise, 1980).

Petrographically Hartha Formation in the study area consists of organic, clastic, and dolomitized limestone. It is affected by several types of diagenetic processes, the most important of which are dolomitization, compaction, cementation, silicification, and neomorphism. Several porosity types, including interparticle, vuggy, moldic, fractures, and channel, have been found in the formation rocks, as shown in the figure (Younis et al., 2015).

According to wells information in the study area, the thickness of the formation varies between 61-187 m. This variation in thickness may be due to various depositional basin shapes (Jassim and Buday 2006). Figure 2 shows the petrographic section of the Hartha Formation in one of the study wells (A-1).

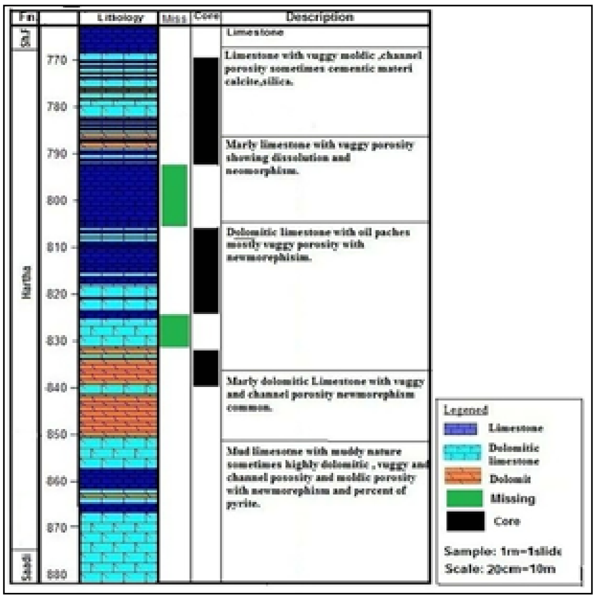

Figure 2. Petrographic section of well A-1 (Younis et al., 2015)

3. Materials and methods

This study used analogue data for three wells from the Qayyarah oil field (A-1, A-2, and A-3) after converting them to the digital format using the Didger software and IP3.5 software to analyze and represent the data. These data were are: Caliper (Cal.), Gamma-ray (GR), Density (RHOB), Neutron (NPHI), Sonic (DT), and three types of Resistivity logs (LLD, LLS, and MSFL).

The work can be summarized in five main stages:

Evaluate the shale percentage using the non-linear gamma ray Larionov equations for tertiary age (Eq.1)

$$Vsh = 0.083 * \left[2^{(3.7\times IGR)} - 1\right] \quad (1)$$

Where: IGR represent gamma ray coefficient =

$$\frac{GRlog-GRmin}{GRmax-GRmin}$$

GRlog, GRmax, and Grmin represent gamma log value, maximum, and minimum reading of gamma log respectively

Determine the formation's lithology and mineralogy using NPHI/Density and N/M cross-plots, whereas:

$$N = \frac{(NPHIf - NPHIlog)}{(\rho b - \rho f)} \quad (2)$$

$$M = \frac{(\Delta tf - \Delta tlog)}{(\rho b - \rho f)} * 0.01 \quad (3)$$

NPHIf: Neutron porosity for drilling fluid =1; NPHIlog Neutron porosity reading; ρb: Density log reading; ρf: Density of the drilling fluid (1 g/cm3 of fresh water); Δtf: The time difference of the sound wave traveling through the drilling fluid =189 m.sec./ft for fresh clay (it's used) ; Δtlog: Sonic log reading.

Evaluate Total porosity (PHIT) and Effective porosity (PHIE) (which represents the most important porosity in oil extraction) from Neutron, Density, and Sonic log according to the following equations:

$$PHIT = \frac{PHIN + PHID}{2} \quad (4)$$

$$PHIE = PHIT * (1 - Vsh) \quad (5)$$

Finally, evaluate the total oil saturation (So) and water saturation (Sw) in Hartha Formation rocks whereas:

$$Sw = \left(\frac{aRw}{Rt * PHI^m}\right)^{1/n} \quad (6)$$

$$Sw = \left(\frac{Ro}{Rt}\right)^{1/n} \quad (7)$$

$$So = 1 - Sw \quad (8)$$

4. Results

4.1 Shale percentage evaluation

By calculating the percentage of shale, we can notice that the formation in the study area contains a relatively small percentage of shale, with a close average percentage in the three wells, as shown in Table 1.

Table 1. Shale ratios in the three studied wells

Well	Shale percentage (%.)		
	Minimum	Maximum	Average
A-1	1.2	97.8*	14.3
A-2	0.2	38.5	15.2
A-3	1.1	31.1	13

**In very limited places*

4.2 Lithology and Mineralogy Determination

According to the results of the neutron porosity/Density cross-plots (Figure 3), it is clear that the lithology of the Hartha Formation in the area consists mainly of limestone with a percentage of dolomitic limestone. The percentage of dolomitic limestone increases at well A-1, where a percentage of points are located below the limestone line towards the dolomite (Figure 3a).

On the other hand, to estimate the mineralogy of formation rocks, M-N plots (Boddy and Smith, 2009) were used,

M-N plots (Figure 4) showed that the main component of the formation rocks in the area is calcite (the main component of limestone rocks) and that some points trend towards the dolomite mineral. These points increase in number at well A-1, which supports the results of the previous cross-plots (Figure 4a).

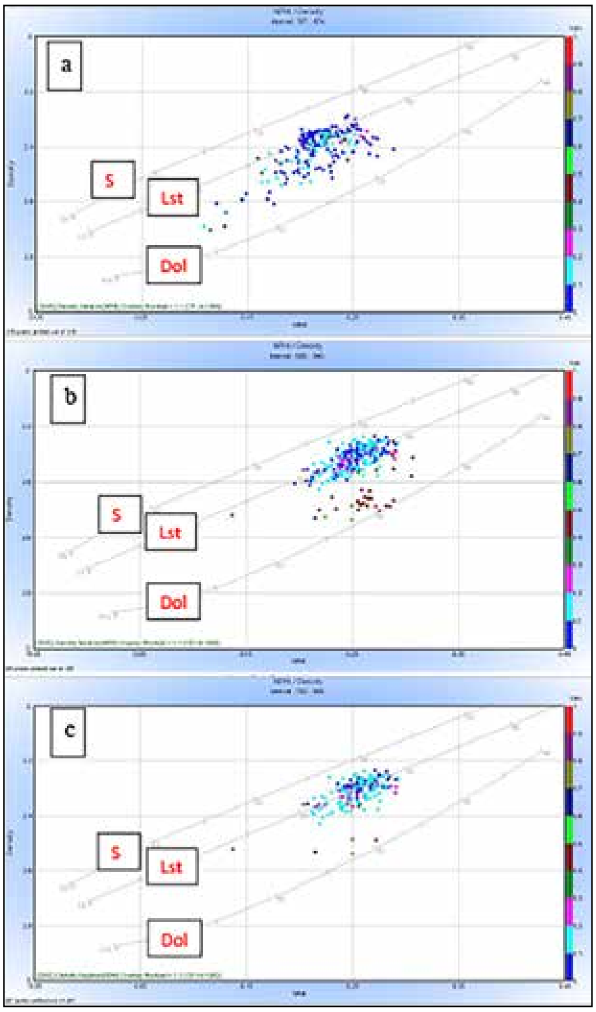

Figure 3. porosity/Density cross-plots for studied wells a: A-1, b: A-2, c: A-3

4.3 Evaluation of porosity types

Two main types of porosity were estimated from porosity logs data (Neutron" PHIN", Density" PHID, and Sonic" PHIS") after making corrections to the shale percentage (PHINc, PHIDc, and PHISc). These two main types are 1-Total porosity (PHIT) and 2-Effective porosity" PHIE") as shown in the figures 4, 5, and 6. From these figures, it can be seen that a large match between the total and effective porosity in most parts of the formation and for the three wells is due to the relatively low percentage of shale in the formation rocks. It is also some porosity details shown in the Table 2:

Table 2. The total and effective porosity values for the three wells.

Well	Depth of Hartha Formation (m.)	Porosity (%)					
		Total			Effective		
		Min.	Max.	Average	Min.	Max.	Average
A-1	767-874	8.2	24.1	19.3	0.1*	23.2	17.8
A-2	688-840	6.7*	24	19.6	7.2*	22.5	17.2
A-3	704-790	12.2	27.3	24.2	5.6*	25.4	21.3

**In very limited places*

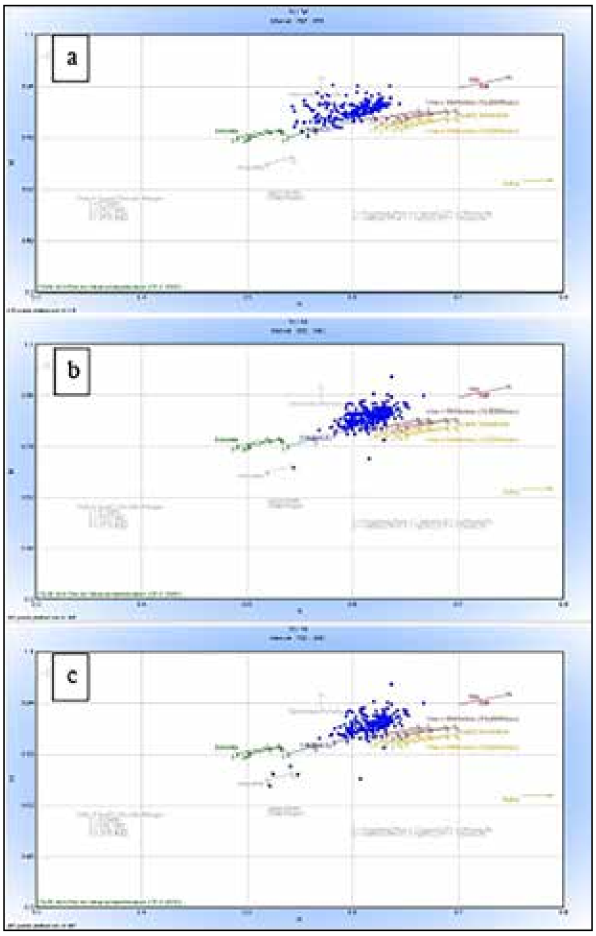

Figure 4. N/M cross-plots for studied wells a: A-1, b: A-2, c: A-3

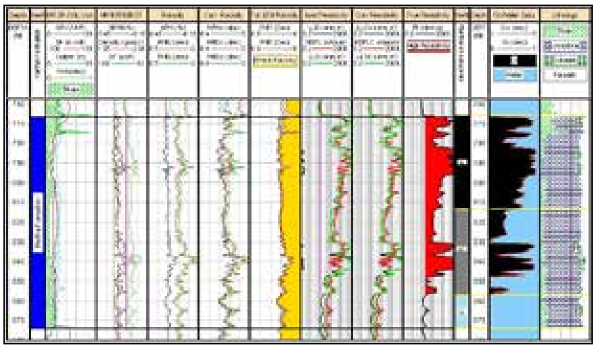

Figure 5. Interpretation results of A-1 well log data

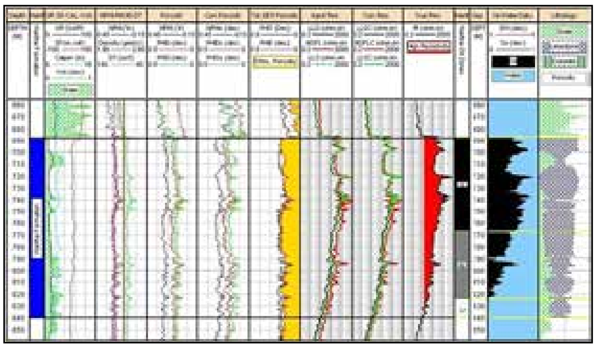

Figure 6. Interpretation results of A-2 well log data

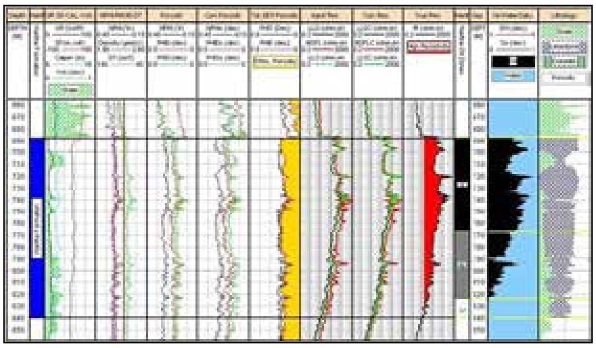

Figure 7. Interpretation results of A-3 well log data

From Figures 5 and 6, we can notice that the Hartha Formation can be divided into three zones in each well based on the oil saturation: The first(A) contains a high percentage of saturation, the second(B) contains a lower percentage of oil saturation. At the same time, the third zone(C) is almost devoid of oil content and contains only water. Table 3 shows some characteristics of the three zones along with the percentage of oil saturation for the three zones in the study wells.

Table 3. Average porosity and oil saturation of wells zones

Well	Depth of Hartha Formation (m.)	Zone	Depth of zone (m.)	Average value 0f porosity (%)		Average oil saturation from the total solution (%)
				Total porosity	Effective porosity	
A-1	767-874	A	767-812.5	20.3	18.5	69.3
		B	812.5-856.5	17.9	16.8	35.9
		C	856.5-874	18.5	17.2	0.0
A-2	688-840	A	688-767.3	19.1	17.4	57.1
		B	767.3-823.2	19.9	17.1	26.9
		C	823.2-840	20.4	16.5	0.0
A-3	704-767	A	704-741.8	24.3	21.3	27.2
		B	741.8-771.1	23.6	20.6	1.0
		C	771.1-790	22.6	18.8	0.0

5. Discussion

The position of the solutions contained in the rocks follows the gravitational differential, as water occupies the lower part of the rock formations due to its high density compared to oil, which is usually located above the water, and this was clearly observed through the results of interpreting the borehole data (Figures 5, 6, and 7).

By observing the interpretation of the results of the well data, it is clear that the three wells vary between the wells, as well as the value of one well. It may be related to the subsurface structural situation, like the effect of subsurface faults or the variance of the number of internal fractures. The distribution of oil over the three zones within each well may be related to the gravitational differential of the oil. It also depended on the effective porosity values for each area, and this indicates that effective porosity has an important role in oil content. It can be clearly observed from the values of effective porosity and saturation percentage in table 3, where the oil saturation percentage increases in each well with increasing effective porosity.

6. Conclusion

From the results of the current study, the following can be concluded:

- The average total porosity of the Hartha Formation ranged between 19.3-24.2 for the three wells, while the average effective porosity ranged between 17.2-21.3.
- Oil saturation varies from each well to another in the Qayyarah field, where its average from zero to approximately 69.3%.
- The Haritha formation in the Qayyarah field was divided into three zones depending on the percentage of its saturation with oil (A, B, C), the highest of which is in the upper zone (A). In contrast, the lower zone does not contain oil.
- The percentage of oil saturation inside each well depended on the percentage of effective porosity inside the well, as the percentage of oil saturation increases with the increase in effective porosity, considering the gravitational differentiation of solutions inside the rocks.

References

Abed, S. R. and Al-Jaberi, M. H. (2023). The Diagenesis Processes of the Hartha Formation in Majnoon Oil Field, Southern Iraq. Iraqi Geological Journal. 56(1E): 84-96 https://doi.org/10.46717/igj.56.1E.7ms-2023-5-17

Abuseda, H. and El_Sayed, A.M. (2022). Petrographical and Petrophysical Studies of Some Upper Cretaceous Rocks, Western Desert, Egypt. Jordan Journal of Earth and Environmental Sciences, 13 (1): 37-47

Al-Badrani, O.A., Hassan, F.N., and Al-Hadeedy, M.A. (2021). Calcareous Nannofossil Biostratigraphy and Ostracoda Paleoecology of Hartha Formation from Balad (1) well, Central Iraq. Iraqi Journal of Science, 62(11): 3962-3972. DOI: 10.24996/ijs.2021.62.11.17

Albarzanji, P. K. and Alhamdani, S. A. (2024). The Consequences of Petrophysical Effects on Reservoir Properties of Hartha Formation at Balad Oil Field, Central Iraq. Journal of Petroleum Research and Studies. 14 (1): 1-17. DOI: https://doi.org/10.52716/jprs.v14i1.776

Al-Hadidy, A.H., Nasser, M. E., Nooralddin, A.K., and Qadhi, A. (2022). Evaluation of oil reservoir of Hartha Formation in Y and J field, North Iraq, Journal of petroleum research and studies. 12 (1): .70-84, DOI: https://doi.org/10.52716/jprs.v12i1.591.

Al-Juraisy, B.A. and Al-Majid, M.H.A. (2021). Importance of velocity deviation technique and negative secondary porosity in detection of hydrocarbon zones in Khasib formation, east Baghdad oil field. The Iraqi geological journal, 54(2E): 86-103. DOI: org/10.46717/igj.54.2E.6Ms-2021-11-2

Al-Majid, M.H.A. (2021). Petrophysical properties estimation of euphrates reservoir in qayyarah oil field using core and well log data. Iraqi geological journal. 54(2e):186–197. DOI:org/10.46717/igj.54.2E.13Ms-2021-11-29

Al-Mawla, F.M., Al-Juraisy, B.A., Al-Hamidi, R.I., and Hussain Q.M. (2023). The Use of Geophysical Well Logs in Determining the Some Petrophysical Properties of the Bajawan Formation in Selected Wells from the Kirkuk Field, Northern Iraq. Iraqi National Journal of Earth Science. 23 (2): 168 - 188, DOI: 10.33899/earth.2023.141399.1105.

Boddy, R. and Samith, G. (2009). Statistical methods in practice, for scientists and technologists, Wiley, U.K. 248p.

Ditmar, V. and Iraqi-Soviet Team (1971). Geological conditions and hydrocarbon prospects of the Republic of Iraq (Northern and Central parts). Manuscript report, INOC Library, Unpublished report, Iraq Notional Oil Company, Baghdad.

Homadi B. J. and Al-Zaidy A. A.H. (2020) Analysis and Basin Development of Hartha Formation in East Baghdad Oil field, Central Iraq, Iraqi journal of science. 61 (11): 2978-2989 https://doi.org/10.24996/ijs.2020.61.11.19

Jassim S.Z., Buday T. (2006). Tectonic framework. In: Jassim SZ, Goff JC (eds) Geology of Iraq. Dolin, Prague and Moravian Museum, Brno, pp 141–154

Jassim, S.Z. and Goff, J.C. (2006). Geology of Iraq. 1st Edition, published by Dolin, Prague and Moravian Museum, Brno, Printed in the Czech Republic.

Murris, R. J. (1980). Middle East: stratigraphic evolution and oil habitat: AAPG Bull., 64: 597-618.

Serra.O., (1988). Fundamentals of well-logging interpretation, Elsevier science publishers B.V, 3rd Ed., 423p.

Umoren, E. B., Atat, J. G., Akankpo, A. O., and Usen, I. C. (2023). Porosity estimation using RHG apperoach and well log data from southern Niger delta, Nigeria, World Journal of Applied Science and Technology. 15 (2): 207 – 212, https://dx.doi.org/10.4314/wojast.v15i2.8

Younis, W.A., Kadhim, L.S., and Omar, F.M. (2015) Sedimentological study of the Hartha & Saadi Formations from selected wells in Qayara oil field Northern Iraq, Kirkuk University Journal /Scientific Studies (KUJSS). 10 (4): 393-414.

JJEES

JJEES (2025) 16 (3): 289-297
ISSN 1995-6681

Jordan Journal of Earth and Environmental Sciences

A Statistical Survey for Drilling Problems at North Rumaila Field, Southern Iraq. A Review enhanced with Well Logs Analyses

Ahmed N. Al-Dujaili[1*], Sundos Hameed Mousa[2] , Nurbol Tileuberdi[3]

1 Petroleum Engineering Department / Amirkabir University of Technology, Tehran, Iran.
2 faculty of Administration and Economics/ Department of Financial and Banking Sciences / University of Kufa, Najaf, Iraq.
3 Laboratory of Engineering Profile, Satbayev University, Satbayev St. 22a, Almaty 050013, Kazakhstan.

Received on October 29, 2024, Accepted on March 3, 2025

Abstract

This study was accomplished to review the drilling problems in the North Rumaila Field, Southern Iraq. A statistical analysis for each formation reflecting the effect of drilling problems with overall analysis for the selected part of the field. The recorded mud logs will be used to confirm the results. The results show that losses should be expected at the base of the Dammam Formation and Hartha, Mishrif, and Zubair Formations. A significant washout in the Tanuma Formation occurred. The injector(s) should remain shut in until the Mishrif Formation case is off to prevent the potential for flow. The variability of Mishrif reservoir architecture and rock types might lead to irregular sweep and water breakthrough if higher permeability layers are present. Sloughing formations represent Tanuma, Nahr Umr, and Upper Shale. Generally, the potential for stuck pipes will be evident in the Mishrif, Nahr Umr, and Zubair Formations. Bit damage occurs through drilling entire anhydrite layers in L. Fars and Rus Formations. The high-effect problem (36.41%) was the loss of mud circulation, while slide drilling (0.54%) represented the lesser effect. Dammam is the most formation that faced drilling problems according to the percentage of all wells drilled (56.4% for each caving and mud loss), while no significant problems occurred in Dibdibba, Khasib, Rumaila, Ahmedi, Mauddud, and Shuaiba Formations. In general, the Middle South part of the field shows fewer drilling problems than the edge of the Field with South Rumaila Field, especially in the productive Formations (Mishrif, Mauddud, and Zubair).

Keywords: *Statistical Analysis; Drilling Problems; North Rumaila Field; Mud log; Mud Loose*

1. Introduction

Drilling and completion of the wells represent over 40% of all assets in the oil and gas industry. Decreasing losses in drilling time to eliminate difficulties facing drilling and their results is one of the prospects for increasing the effective drilling time (Kiran et al., 2024). The main complications include drill string sticking due to talus and unstable rock collapses, wellbore narrowing from crumbling rocks, absorption of drilling mud, and occurrences of gas-oil-water and brine showings (Al-Dujaili et al., 2025). All drill cuttings must be removed from the well during drilling in a process known as hole cleaning (Nazari et al., 2010). Residual material often remains in the well, causing issues such as pipe sticking, premature bit wear, slow drilling, formation damage (fracturing), excessive torque and drag, and difficulties in logging and cementing (Borozdin et al., 2020; Orun et al., 2023).

Drilling fluid loss is a familiar concern in the oil and gas industry (Zhuang et al., 2024). Loss of mud completely or partially within a formation during the drilling operation or the recovery mud from the well does not match the mud injected into the well, is known as drilling fluid loss or retrieval loss (Salih and Hussein, 2022). Circulation loss normally occurs in highly permeable, depleted reservoirs, natural cracks,cavernous and fracture formations, as shown in Figure 1 (Miranda et al., 2017). Many techniques are utilized to control the loss of circulation (Kang et al., 2023). The first method to address lost circulation is by reducing the density of the drilling mud (Caughron et al., 2022). The second method involves adding lost circulation materials (LCM) to plug and seal off loss zones (Toreifi et al., 2014). Several factors can influence the loss of drilling fluid, including the petrophysical properties (such as porosity and permeability), the characteristics of the drilling mud itself (like mud weight, equivalent circulating density, yield point, and plastic viscosity), as well as the drilling parameters (such as rate of penetration, weight on bit, revolutions per minute, strokes per minute, standpipe pressure, and total flow area). Factors like pore pressure gradient and fracture pressure can also play a significant role (Yang et al., 2023). An analysis revealed that 54% of stuck pipe incidents occurred during tripping and back-reaming operations (Yarim et al., 2007). Growth in the risk stuck pipe was marked due to a current expansion in drilling activities, drilling in depleted and higher-risk reservoirs (Muqeem et al., 2012). Several studies suggest the statistical method to be utilized for predicting stuck pipes (Shadizadeh et al., 2010; Salminen et al., 2017; Elahifar and Hosseini, 2022]. The formations of southern

---

* Corresponding author e-mail: ahmed.noori203@aut.ac.ir

Iraqi oilfields were studied clearly, and a full description approach was achieved for the upper Faris to Mishrif formations (Simmons et al., 2025). The power and stringency of the problem were defined in each formation by offering the causes of the problem/s in the wells or what might ensue (Saleh et al., 2018).

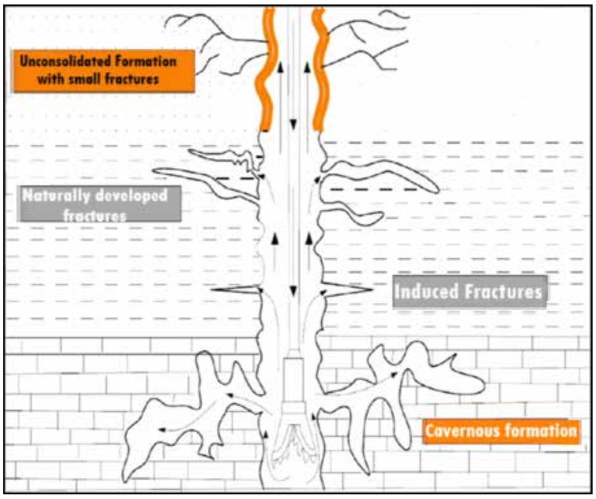

Figure 1. Various types of lost circulation of drilling fluid (Miranda et al., 2017)

2. Geological setting

North Rumaila is a supergiant oilfield situated 50 km to the west of Basrah city in the south of Iraq (Salih et al., 2016). It has piled up in multiple Clastic and Carbonate reservoirs. North Rumaila field was explored in 1953 and represents 33% of Iraq's total oil production (Figure 2) (Almalikee and Al-Najm, 2019). Rumaila structure represents a mild tilting longitudinal anticline that extends approximately longitudinally 83 km and 12 km wide. The North Rumaila structure is approximately 11 to 42 km in width and slopes southwards to form a saddle that separates it from the southern part (Handhal et al., 2022; Al-Dujaili, 2023). Two faults have been found, the northeast to southwest, Takadid-Qurna and Al-Batin. Faults are reactivated Precambrian transverse faults that define the Zubair fault block within the Mesopotamian basin (Al-Dujaili, 2024a). The stratigraphic column from the Rumaila field represents sedimentary rocks, ranging in age from Late Jurassic to recent (Chafeet and Handhal, 2024). It mainly comprises clastic, carbonate, and evaporitic rock cycles (Shehab et al., 2023). This stratigraphic column's most prominent hydrocarbon system is the Early Cretaceous to Miocene (Al-Dujaili, 2024b). In this petroleum system, the Sulaiy and Yamama formations represent source rocks; the Tanuma, Shranish, and Rus formations form the sealing rocks; and the Yamama, Zubair, Nahr Umr, and Mishrif formations represent the reservoir rocks (Figure 3). (Al-Ameri et al., 2011; Al-Dujaili et al., 2023; Lazim et al., 2024). The drilling issues in the Rumaila oilfield have been addressed in various studies where key drilling parameters were identified to mitigate mud losses in the Dammam Formation of the South Rumaila Field (Al-Mimar et al., 2018; Khashman et al., 2025), and the requirements solutions for their previous study were suggested (Al-Hameedi et al., 2017), and machine learning was used to predict lost circulation in the Rumaila Field (Al-Hameedi et al., 2018). The Hartha and Mishrif formations behave similarly to the Dammam formations, causing the loss of cement and drilling mud circulation (Al-Dujaili et al., 2024).

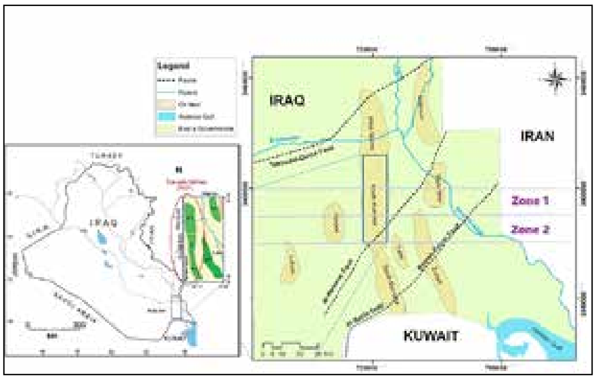

Figure 2. Location of North Rumaila oilfield

3. Data and methods

3.1 Data and Methods

The data were obtained from 80 drilled wells in the North Rumaila oilfield, southern Iraq, between latitude lines (3360000 to 3400000 N).

The wells, drilled between 1977 and 2014, were divided into two categories:

1. Zone 1: includes the wells drilled in the field (41 wells) between latitude lines (3370000 to 3385000 N).
2. Zone 2: includes the wells drilled in the field (39 wells) between latitude lines (3385000 to 3400000 N) (Figure 1).

The data also include mud logs, which were used to determine lithology descriptions in addition to core data and to identify drilling problems with the support of field outlook. (Figure 4).

The wells under study were drilled across 19 formations in the North Rumaila field with different reservoir targets. Geomechanical analyses were made for all formations. The statistical methods were utilized to survey all drilling problems in many categories:

1. Identifying drilling problems for each formation and calculating the percentage of each problem relative to the total number of identified drilling problems in the selected formations.
2. Determining the percentage of drilling problems concerning the total number of wells for the southern part of the field (Zone 1) and the northern part (Zone 2).
3. Calculating the percentage of each drilling issue relative to the total.
4. Evaluating the likelihood of various drilling problems occurring in the North Rumaila field based on all formations drilled and the projected formations.
5. Assessing the likelihood of drilling issues in the North Rumaila field by considering the drilling processes of all formations and comparing this to the possibility in formations where they have occurred.

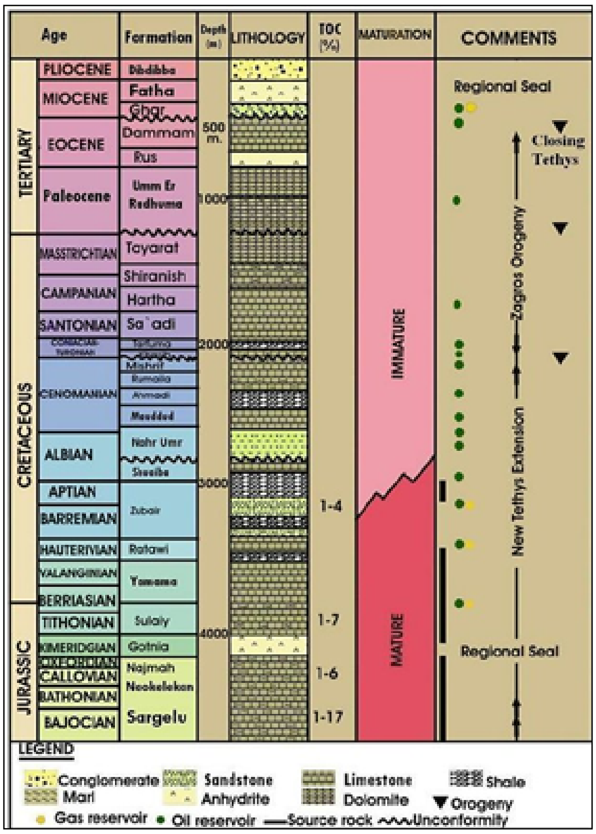

Figure 3. Stratigraphic column of North Rumaila oilfield [28]

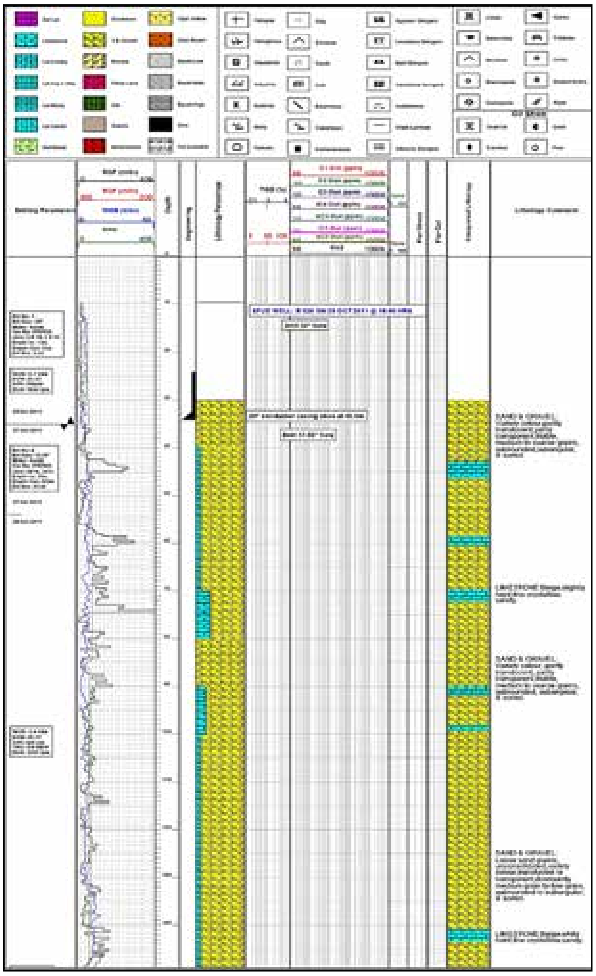

Figure 4. Mud log from Well R-XX6

4. Results

4.1 Mud Weight Window

Figure 5 shows the results of geomechanical analyses conducted on the formations from Dibdiba to Zubair. Initial studies do not indicate any significant pressure ramps or regions of overpressure within the horizons likely to be encountered, except an implied minor pressure ramp in the Shiranish. The appropriate pressure/depth summary should be examined and incorporated into the detailed well planning.

4.2 Percentage of each drilling problem to the total problems in the specified formation

The percentage of each drilling problem in the selected formations (from the Dibdibba to Hartha Formations) was summarized in Figure 6.

The percentage of each drilling problem in the selected formations (from the Sadi to Zubair Formations) was summarized in Figure 7.

4.3 Percentage of each drilling problem to the total number of wells for Zones 1 and 2

The percentage of drilling problems related to the total number of wells for the Southern part of the field (Zone 1) and Northern part (Zone 2) was summarized in Figures 8 and 9.

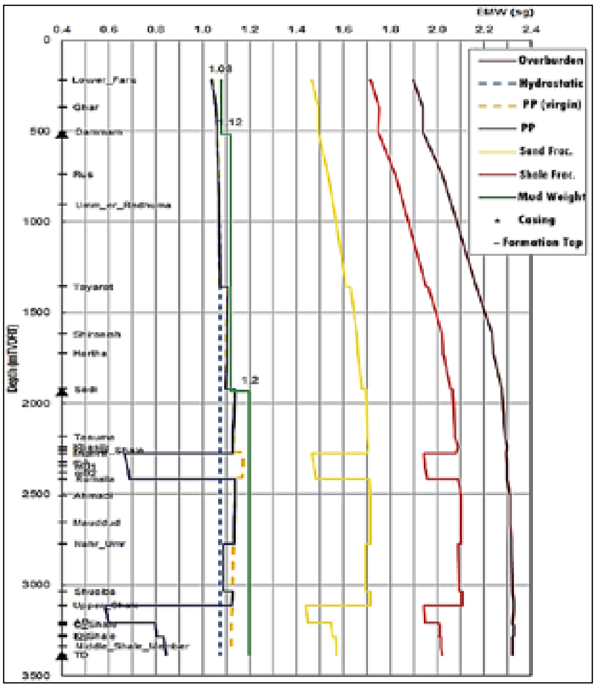

Figure 5. Geomechanical analyses for Rumaila field

Figure 6. Percentage of drilling problems in Dibdibba, L. Fars, Rus, Ghar, Dammam, Um E Radhuma, Tayarat, Shiranish and Hartha Formations

Figure 7. Percentage of drilling problems in Sadi, Tanuma, Khasib, Mishrif, Rumaila, Ahmedi, Mauddud, Nahr Umr, Shuaiba, and Zubair Formations

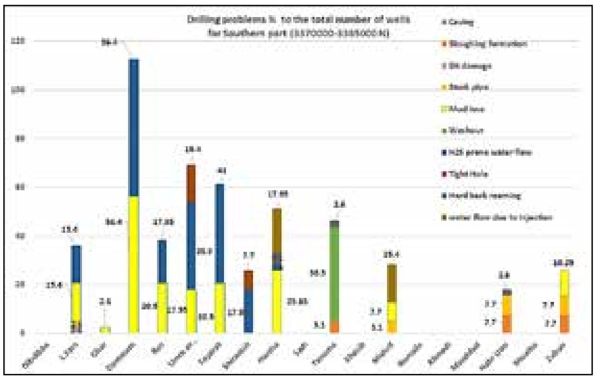

Figure 8. Drilling problems percentage to the total number of wells for zone 2

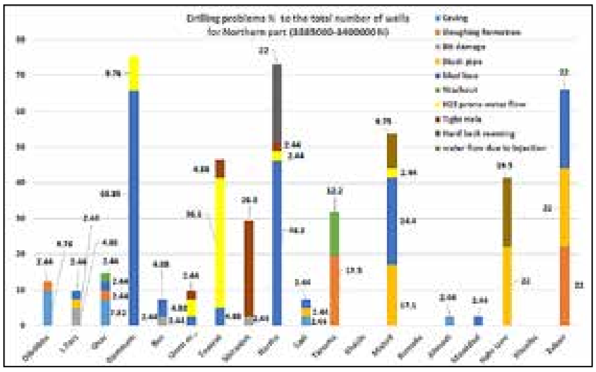

Figure 8. Drilling problems percentage to the total number of wells for zone 1

4.4 Percentage of each drilling problem to the total number of problems

The Possibility percentage for the drilling problem in the North Rumaila field according to all formations drilled was summarized in Figure 10.

4.5 Percentage of the drilling problems according to all drilling processes

The Possible percentage for the drilling problem in the North Rumaila field according to all formations drilled and the formations in which the problems are expected was summarized in Figure 11-A.

4.6 Percentage of the drilling problems according to all drilling processes

The possible percentage for the drilling problems in the North Rumaila field according to all drilling processes in all formations is also the same. Still, the formations in which the problems are expected are only shown in Figure 11-B.

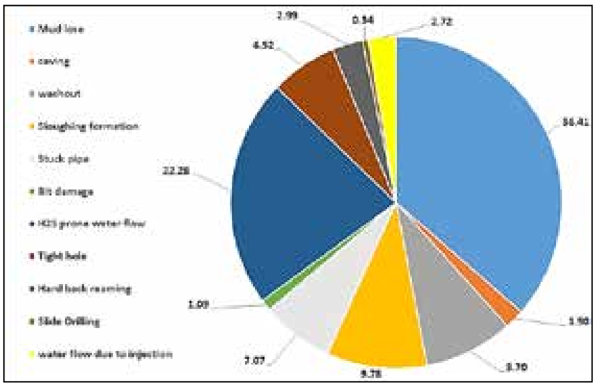

Figure 10. Percentage of each drilling problem according to the total problems that occurred

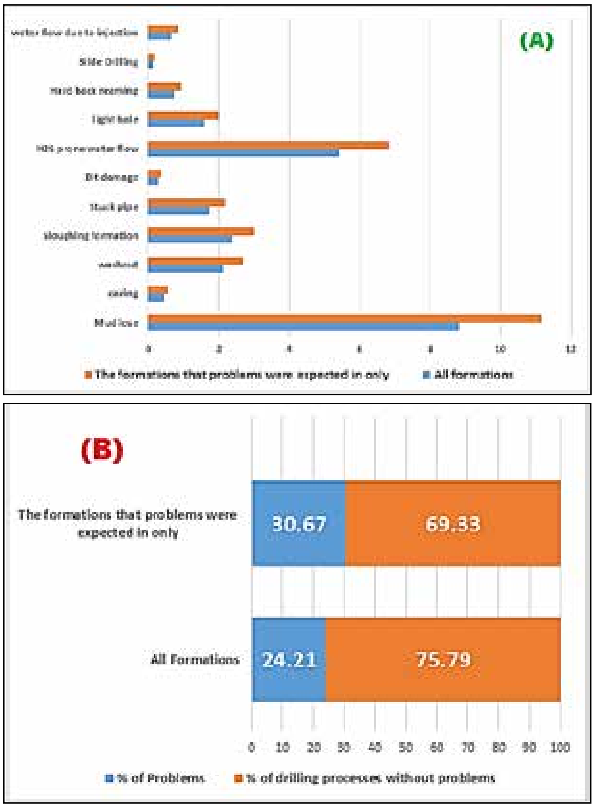

Figure 11. A- % of each problem to (All formations and formations that the problems are expected in)

B- % of all to (All formations problems and to formations that the problems are expected in)

4.7 Analysis of the Drilling Problems

Analysis of drilling problems was based on Table 1, which classified the problem due to its effect on the drilling process into eight groups.

The results of this analysis are shown in Figure 12.

Table 1. Classification of drilling problems due to the percentage of iteration in each formation

Legend	% of Problems	Analysis
	Zero	Excellent
🟩	1-10%	Very Good
🟨	11-20%	Good
🟨	21-30%	Acceptable
🟨	31-40%	Medium
🟫	41-50%	Noteworthy
🟧	51-60%	High
🟥	over 60%	Severe

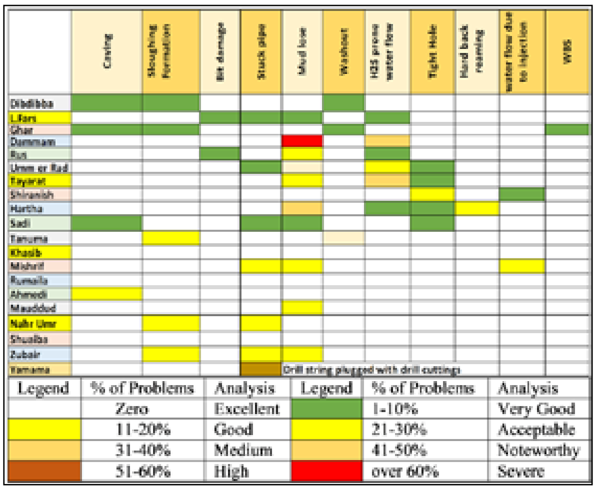

	Caving	Sloughing Formation	Bit damage	Stuck pipe	Mud lose	Washout	H2S prone water flow	Tight Hole	Hard back reaming	water flow due to injection	WBS
Dibdibba	🟩	🟩				🟩					
L.Fars			🟩	🟩	🟩		🟩				
Ghar	🟩	🟩				🟩					🟩
Dammam					🟥		🟧				
Rus			🟩		🟨		🟩				
Umm er Rad				🟩			🟨	🟩			
Tayarat					🟨		🟧	🟩			
Shiranish								🟨		🟩	
Hartha					🟧		🟩	🟩	🟨		
Sadi	🟩			🟩	🟩			🟩			
Tanuma		🟨									
Khasib											
Mishrif				🟨	🟨					🟨	
Rumaila											
Ahmedi	🟨										
Mauddud					🟨						
Nahr Umr		🟨		🟨							
Shuaiba											
Zubair		🟨		🟨	🟨						
Yamama				🟫	Drill string plugged with drill cuttings						

Legend	% of Problems	Analysis	Legend	% of Problems	Analysis
	Zero	Excellent	🟩	1-10%	Very Good
🟨	11-20%	Good	🟨	21-30%	Acceptable
🟧	31-40%	Medium	🟧	41-50%	Noteworthy
🟫	51-60%	High	🟥	over 60%	Severe

Figure 12. Analysis of the drilling problems problem for each formation due to its effect on the drilling process

5. Discussion

The most common hazard is the potential for severe losses in the Dammam formation. Current understanding suggests that no losses can be expected whilst drilling the first 50-100m of the formation in North Rumaila Field. The probability of incurring significant or even total losses increases from the depth onwards. This increase has led to Non-Productive Time (NPT). Also, it is called (dead time)—over 10 days from the total time for the well. Another potential hazard is water ingress while drilling across the formation. This water flow could occur because the field has water disposed in Dammam. Surge and swab in Dammam, Rus, or UER Formations must be avoided. They might fracture formation and cause excessive losses. H2S exists in the vuggy porosity of the Dammam Formation (Figure 13).

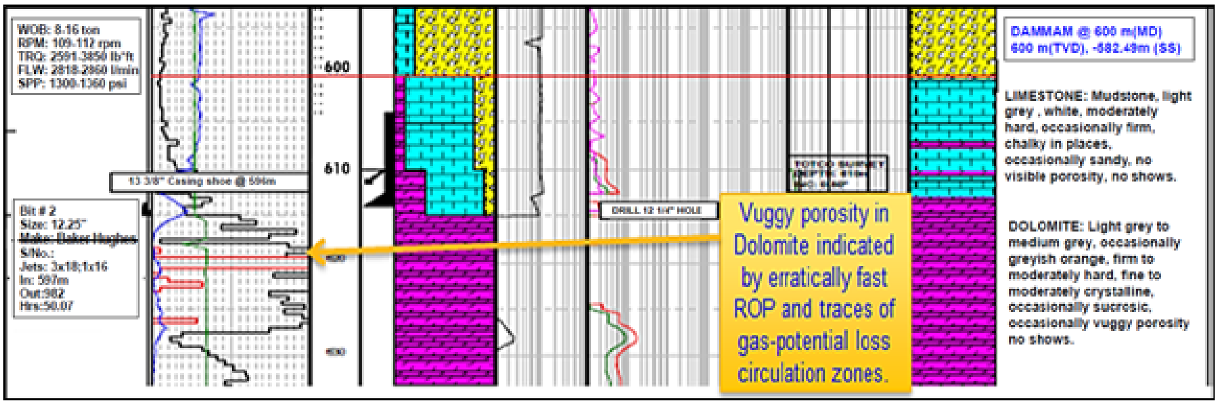

Figure 13. Master log of Dammam Formation in Well RN-X31

Several historical wells were experienced, and loss events, more commonly called sulfurous water gains, were found while drilling through Tayarat Formation. This has been seen in wells with static mud weights of up to 1.18 sg. Increasing the mud weight up to 1.19 sg should kill any ingress.

Shale at the top of the Tayarat Formation then became massive hard, crystalline dolomite was noted with tight porosity and very low gas values throughout this formation (Figure 14).

Drilling in the Shiranish carbonate formation expects the unexpected; pits trend and mud losses must be watched closely. The formation consists of Marly Limestone, poorly visible porosity, uniform ROP, low background gas (Figure 15).

Mud Loss has occurred in the Hartha Formation (Figure 16).

Tanuma Formation is a massive fissile Shale with sloughing and water flows. Note that gas peaks just above Tanuma top, as well as increasing background gas, indicate porosity and path for fluid flow (Figure 17).

Mishrif limestone zones show several layers of differing porosity. Gas leaks and oil show throughout the formation, indicating good porosity development.

Potential for flow in the Mishrif Formation due to active injection operations. The adjacent injector(s) should be shut in while the Mishrif Formation is being drilled to prevent flow into the Mishrif Formation (Figure 18).

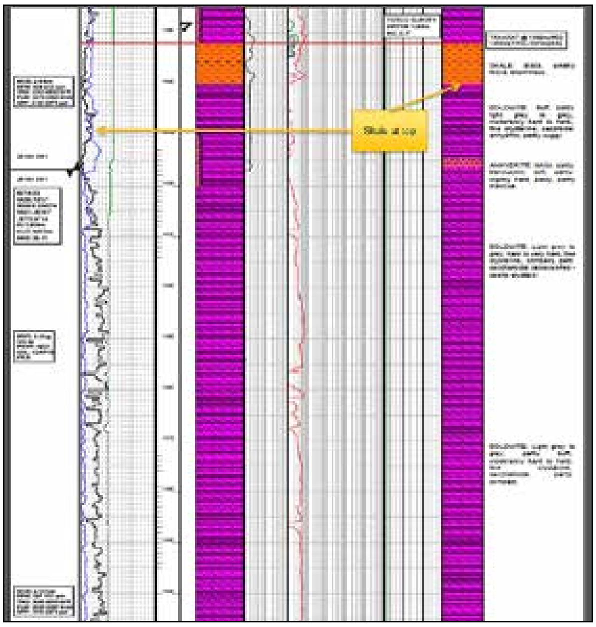

Figure 14. Master log of Tayarat Formation in Well RN-X26

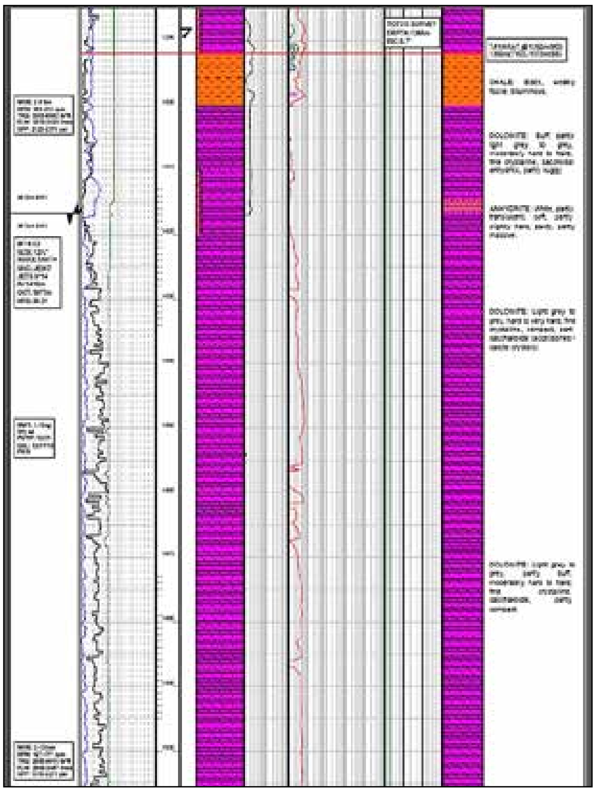

Figure 15. Master log of Tayarat Formation in Well RN-X31

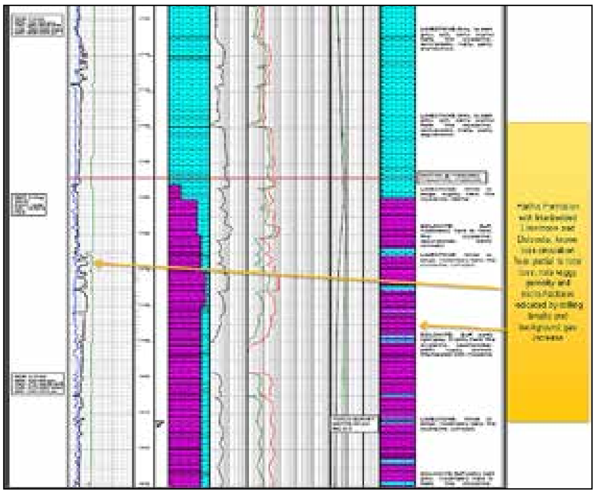

Figure 16. Lost circulation from partial to total in Hartha Formation (Well RN-X41)

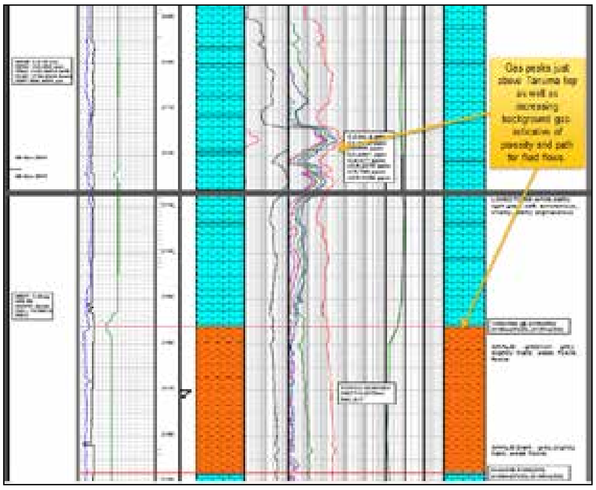

Figure 17. Tanuma Formation (Well RN-X31)

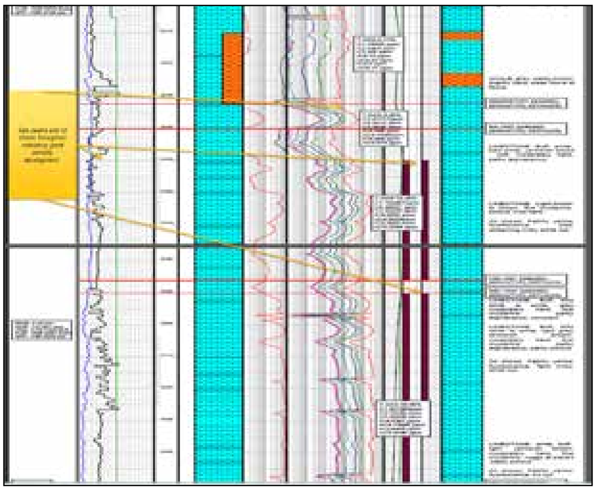

Figure 18. Mishrif Formation (Well RN-X40)

According to Figure 19 and Table 2, the percentage of drilling problems that face the drilling operations in the Rumaila Field will increase at Zone (1) by about 66% for the sandstone Formations and 46% for dolomite and dolomitic limestone Formations. In comparison, it will decrease for the anhydrate Formations to 8.5%. In Zone (2), the percentage will increase for dolomite and anhydrate Formations to 63.6% and 35.9%, respectively, while it decreases to 6.85%, 16%, and 26.65% for limestone, shale, and sandstone formations.

Table 2. Problems percentages according to the type of Formations in the Zones 1 and 2

Formation Lithology	% of problems	
	zone 1	zone 2
Sand/ Gravel Intercalation	26.80%	2.60%
Anhydrite (L. Fars and Rus)	8.5%	35.90%
Dolomite and Dolomitic Limestone	46.80%	63.60%
Limestone (Mishrif, Mauddud, and Shuaiba)	26%	6.85%
Shale (Tanuma, Ahmedi, and Nahr Umr)	19.00%	16.00%
Sandstone (Zubair)	65.85%	26.65%

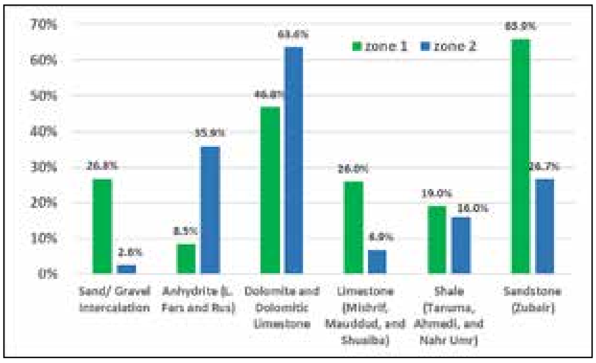

Figure 19. Problems percentages according to the Formations in the Zones 1 and 2

6. Validation of results

The stability validation was carried out with WellCheck™. In this case, it was found that the case where σV =σHmax is similar to the strictly strike-slip case (σHmax=1.05*σV), so there is sufficient confidence in the results, providing the chosen stresses are appropriate. The figure contains the estimated trends of the magnitudes of the pore pressure (Pp) in blue, the least stress (σHmin) for the shaly materials in brown, and the minimum mud weight for drilling a breakout-free hole in red. Also included are the casing points as designed and the various formations likely to be penetrated (Figure 20).

The pale green shade defines the mud-weight windows for drilling breakout-free holes at any depth. The darker green shade defines the available mud weight window for drilling a hole section based on a single minimum mud weight per section. The simulation suggests that the minimum mud weights for drilling the three well sections are 1.06SG, 1.07SG, and 1.26SG, respectively, with corresponding upper mud weight limits of 1.75SG, 1.79SG, and 2.06SG, respectively. However, in the past, we have restricted the mud weight for drilling the lowest section to 1.24SG because of potential damage to the reservoir. Although the mud weight of 1.24SG has not been sufficient to allow breakout-free drilling in the Tanuma, it has adequately facilitated running casing. Therefore, we recommend maintaining an initial mud weight of 1.24SG for the 8-1/2" section with the proviso that mud weight can be raised in steps of 0.02SG immediately 10%-plus cavings have been detected or observed during the operation. When mud weight is raised by 0.02SG (e.g., from 1.24 to 1.26SG), the adjustment must be allowed to work through the fluid system before further step increases of 0.02SG can be applied, as necessary.

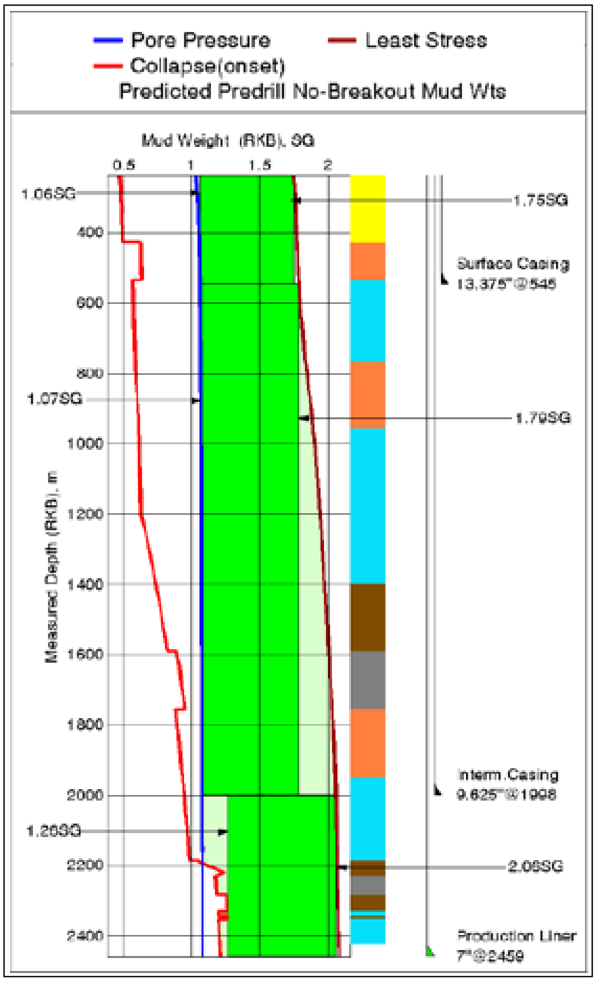

Figure 20. Predrill Mud Weight Validation

The recommended starting mud weights are summarized in Table 3.

Table 3. Recommended Predrill Mud Weights according to drilling problems and validation

Hole Section (inches)	Mud Weight (SG)	Comments
17-1/2	1.06	
12-14	1.07	
8-1/2	1.24	Observe and react to cavings by raising mud weight in steps of 0.02SG (as necessary) in the section.

7. Conclusions

1. Loses should be expected at the base of the Dammam Formation, and lost circulation plans should be ready to execute while drilling this section. In this way, a good casing seat can be achieved before drilling the vuggy/karstic sequence beneath, in which total losses are represented. Water ingress while drilling across the Dammam Formation occurs, so Dammam injectors, which are located within 1.5 km of the wellbore should be shut from 50m above the top of Dammam to the entire formation to be cased off and cemented.
2. Losses occurred in the Hartha Formation. The plans for mitigating lost circulation should be ready to be executed while drilling this section.
3. There was a significant washout in the Tanuma Formation. A program must be adopted to deal with the problem through changes in drilling practices and revisions to the drilling fluid recipe.
4. The injector(s) should remain shut in until the Mishrif formation is cased off to prevent the potential for flow in the Mishrif Formation.
5. The variability of Mishrif reservoir architecture and rock types might lead to irregular sweep and water breakthrough if higher permeability layers are present.
6. Sloughing formations are represented in Tanuma, Nahr Umr, and Upper Shale. Losses occur in Mishrif and Zubair Formations, and potential Stuck Pipes in Mishrif, Nahr Umr, and Zubair Formations.
7. Bit damage through drilling entire anhydrite layers in L. Fars and Rus Formations was the problem with lower effect in the drilling program, so the Tri-cone bit drill must be changed to a PDC bit.
8. In general, Zone 2 shows fewer drilling problems than Zone 1, especially in the productive Formations (Mishrif, Mauddud, and Zubair), which may be due to the differences between Zones 1 and 2 in the sequence of stratigraphy, depositional environment, and the effect of the Al-Hammar Fault on Zone 1.

Nomenclature

ECD	Equivalent Circulating Density
EMW	Equivalent Mud Weight
LCM	Lost Circulation Materials
MW	Mud Weight
NPT	Non Productive Time
NR	North Rumaila oilfield
PDC	polycrystalline diamond compacts
PP	Pore Pressure
PV	Pore Volume
R	North Rumaila oilfield
ROP	Rate of Penetration
RPM	Round per Minute
SPM	Strokes per Minute
SSP	Site Safety Plan
TFA	Total Flow Area
WOB	Weight on Bit
YP	Yield Point

Declaration of Interest

Title of Paper: A Statistical Survey for Drilling Problems at North Rumaila Field, Southern Iraq. A Review enhanced with Well Logs Analyses by the authors declare that they have no known competing financial interests or personal relationships that could have appeared to influence the work reported in this paper.

Funding

The authors did not receive support from any organization for the submitted work.

References

Al-Ameri, T. K., Jafar, M. S., & Pitman, J. (2011). Hydrocarbon generation modeling of the Basrah oil fields, Southern Iraq. In AAPG Annual Convention and Exhibition, Houston, Texas. Vol. 20116, p. 2011.

Al-Dujaili, A. N. (2023). Reservoir rock typing and storage capacity of Mishrif Carbonate Formation in West Qurna/1 Oil Field, Iraq. Carbonates & Evaporites, 38(4). https://doi.org/10.1007/s13146-023-00908-3

Al-Dujaili, A. N. (2024a). Reservoir and rock characterization for Mishrif Formation/Zubair Field (Rafdiya and Safwan Domes) by nuclear magnetic resonance and cores analysis. Iraqi Journal of Chemical and Petroleum Engineering, 25(3), 1-14. https://doi.org/10.31699/IJCPE.2024.3.1

Al-Dujaili, A. N. (2024b). New advances in drilling operations in sandstone, shale, and carbonate formations: A case study of five giant fields in the Mesopotamia Basin, Iraq. Mining Science and Technology (Russia), 9(4), 308-327. https://doi.org/10.17073/2500-0632-2023-08-146

Al-Dujaili, A. N., Asad, M. S., Saeed, N., & Tileuberdi, N. (2025). Optimizing polycrystalline diamond compact bit selection and drilling parameters for deviated wells in the Majnoon Field, Iraq. Scientific Reports, 15(1), 3178. https://doi.org/10.1038/s41598-025-87484-9

Al-Dujaili, A. N., Shabani, M., & Al-Jawad, M. S. (2024). The efficient and economical application of a cement slurry programme for sandstone and carbonate reservoirs. A case study of the Zubair, Mauddud, and Mishrif formations in a supergiant oilfield, in southern Iraq. Bulletin of Geophysics & Oceanography (BGO), 65(3). https://bgo.ogs.it/issues/2024-vol-65-3/efficient-and-economical-application-cement-slurry-programme-sandstone-and

Al-Dujaili, A. N., Shabani, M., and Al-Jawad M. S. (2023). Effect of heterogeneity on recovery factor for carbonate reservoirs. A case study for mishrif formation in West Qurna Oilfield, southern Iraq. Iraqi Journal of Chemical and Petroleum Engineering, vol. 24, no. 3, pp. 103–111. https://doi.org/10.31699/IJCPE.2023.3.10

Al-Hameedi, A. T., Alkinani, H. H., Dunn-Norman, S., Flori, R. E., Hilgedick, S. A., Amer, A. S., & Alsaba, M. T. (2018, October). Using machine learning to predict lost circulation in the Rumaila field, Iraq. In SPE Asia Pacific Oil and Gas Conference and Exhibition. OnePetro. https://doi.org/10.2118/191933-MS

Al-Hameedi, A. T., Dunn-Norman, S., Alkinani, H. H., Flori, R. E., Torgashov, E. V., Hilgedick, S. A., & Almohammedawi, M. M. (2017, October). Preventing, Mitigating, or Stopping Lost Circulation in Dammam Formation, South Rumaila Field, Iraq; Requires Engineering Solutions, the Best Treatments Strategies, and Economic Evaluation Analysis. In SPE/IATMI Asia Pacific Oil & Gas Conference and Exhibition. OnePetro. https://doi.org/10.2118/186180-MS

Almalikee, H. S., & Al-Najm, F. M. (2019). Wellbore stability analysis and application to optimize high-angle wells design in Rumaila oil field, Iraq. Modeling Earth Systems and Environment, 5(3), 1059-1069. https://doi.org/10.1007/s40808-019-00591-1

Al-Mimar, H.S., Awadh, S.M., Al-Yaseri, A.A. et al. (2018) Sedimentary units-layering system and depositional model of the carbonate Mishrif reservoir in Rumaila oilfield, Southern Iraq. Model. Earth Syst. Environ. 4, 1449–1465. https://doi.org/10.1007/s40808-018-0510-5

Borozdin, S., Dmitrievsky, A., Eremin, N., Arkhipov, A., Sboev, A., Chashchina-Semenova, O., ... & Safarova, E. (2020, October). Drilling problems forecast system based on neural network. In SPE annual Caspian technical conference (p. D023S013R008). SPE. https://doi.org/10.2118/202546-MS

Caughron, D. E., Renfrow, D. K., Bruton, J. R., Ivan, C. D., Broussard, P. N., Bratton, T. R., & Standifird, W. B. (2002, February). Unique crosslinking pill in tandem with fracture prediction model cures circulation losses in deepwater Gulf of Mexico. In IADC/SPE drilling conference. OnePetro. https://doi.org/10.2118/74518-MS

Chafeet, H. A., & Handhal, A. M. (2024). Evaluating the Zubair reservoir (Main Pay) in selected wells of the Rumaila Oilfield, southern Iraq, using nuclear magnetic resonance logging and petrophysical analysis data. Carbonates and Evaporites, 39(3), 65. https://doi.org/10.1007/s13146-024-00977-y

Elahifar, B., & Hosseini, E. (2022). Machine learning algorithm for prediction of stuck pipe incidents using statistical data: case study in middle east oil fields. Journal of Petroleum Exploration and Production Technology, 12(7), 2019-2045. https://doi.org/10.1007/s13202-021-01436-3

Handhal, A. M., Ettensohn, F. R., Al-Abadi, A. M., & Ismail, M. J. (2022). Spatial assessment of gross vertical reservoir heterogeneity using geostatistics and GIS-based machine-learning classifiers: A case study from the Zubair Formation, Rumaila oil field, southern Iraq. Journal of Petroleum Science and Engineering, 208, 109482. https://doi.org/10.1016/j.petrol.2021.109482

https://doi.org/10.2118/109914-MS

Kang, Y., Ma, C., Xu, C., You, L., & You, Z. (2023). Prediction of drilling fluid lost-circulation zone based on deep learning. Energy, 276, 127495. https://doi.org/10.1016/j.

energy.2023.127495

Khashman, M.A., Shirazi, H. & Al-Dujaili, A.N. (2025). Comparative evaluation of productivity indicators in carbonate reservoir modeling by a case study for the Mishrif Formation in the Iraqi Buzurgan Oilfield. Discov Geosci 3, 17. https://doi.org/10.1007/s44288-025-00118-5

Kiran, R., Wood, D. A., & Salehi, S. (2024). Innovations in drilling and well construction technologies in natural gas reservoir drilling. In Sustainable Natural Gas Drilling (pp. 475-503). Elsevier. https://doi.org/10.1016/B978-0-443-13422-7.00016-7

Lazim, A. A., Ismail, M. J., & Mahdi, M. M. (2024). High resolution sequence stratigraphy of the Mishrif Formation (cenomanian-early turonian) at Zubair oilfield (al-rafdhiah dome), southern Iraq. Petroleum Research, 9(1), 61-71. https://doi.org/10.1016/j.ptlrs.2023.08.002

Miranda, C. R., Oliveira, J. L., Cavalcante, G. M., d'Almeida, A. R., Pereira, R. F., Santos, R. L., & Surmas, R. (2017, May). Materials for controlling severe lost circulation-laboratory evaluation. In SPE Latin America and Caribbean Petroleum Engineering Conference. OnePetro. https://doi.org/10.2118/185582-MS

Muqeem, M. A., Weekse, A. E., & Al-Hajji, A. A. (2012, April). Stuck Pipe Best Practices–A Challenging Approach to Reducing Stuck Pipe Costs. In SPE Saudi Arabia Section Technical Symposium and Exhibition. OnePetro. https://doi.org/10.2118/160845-MS

Nazari, T., Hareland, G., & Azar, J. J. (2010, May). Review of cuttings transport in directional well drilling: systematic approach. In SPE western regional meeting. OnePetro. https://doi.org/10.2118/132372-MS

Orun, C. B., Akpabio, J. U., & Agwu, O. E. (2023). Drilling fluid design for depleted zone drilling: An integrated review of laboratory, field, modelling and cost studies. Geoenergy Science and Engineering, 211706. https://doi.org/10.1016/j.geoen.2023.211706

Saleh, I. A. S., Khalaf, A. H., & Al-Jawad, M. S. (2018, March). Southern Iraqi Oil Fields Drilling Problems Identification, Analysis, and Treatment. In Offshore Technology Conference Asia. OnePetro. https://doi.org/10.4043/28597-MS

Salih, A., & Hussein, H. A. A. (2022). Artificial Intelligent Models for Detection and Prediction of Lost Circulation Events: A Review. Iraqi Journal of Chemical and Petroleum Engineering, 23(4), 81-90. https://doi.org/10.31699/IJCPE.2022.4.10

Salih, T.A., Sahi, S.H., AL-Dujaili, A.N. (2016). Using Different Surfactants to Increase Oil Recovery of Rumaila Field (Experimental Work). Iraqi Journal of Chemical and Petroleum Engineering, 17(3), 11-31. https://doi.org/10.31699/IJCPE.2016.3.2

Salminen, K., Cheatham, C., Smith, M., & Valiullin, K. (2017). Stuck-pipe prediction by use of automated real-time modeling and data analysis. SPE Drilling & Completion, 32(03), 184-193. https://doi.org/10.2118/178888-PA

Shadizadeh, S. R., Karimi, F., & Zoveidavianpoor, M. (2010). Drilling stuck pipe prediction in iranian oil fields: An artificial neural network approach. Iranian Journal of Chemical Engineering, 7(4), 29-41.

Shehab, M. N., Al-Najm, F. M., & Al-Kaabi, M. H. (2023). Image log facies and lost circulation of the Dammam Formation in Rumaila Oil Field, Southern Iraq. The Iraqi Geological Journal, 150-168. https://doi.org/10.46717/igj.56.1C.10ms-2023-3-21

Simmons, M. D., Bidgood, M. D., Davies, R. B., Droste, H., Levell, B., Razin, P., & van Buchem, F. S. (2025). Intra-Turonian stratigraphic reorganization on the Arabian Plate. Geological Society, London, Special Publications, 545(1), SP545-2023. https://doi.org/10.1144/SP545-2023-207

Toreifi, H., Rostami, H. & manshad, A.K. (2014) New method for prediction and solving the problem of drilling fluid loss using modular neural network and particle swarm optimization algorithm. J Petrol Explor Prod Technol 4, 371–379. https://doi.org/10.1007/s13202-014-0102-5

Yang, J., Bai, Y., Sun, J., Lv, K., & Lang, Y. (2023). Recent advances of thermosetting resin and its application prospect in oil and gas drilling and production engineering. Geoenergy Science and Engineering, 212222. https://doi.org/10.1016/j.geoen.2023.212222

Yarim, G., Uchytil, R., May, R., Trejo, A., & Church, P. (2007, November). Stuck pipe prevention—A proactive solution to an old problem. In SPE Annual Technical Conference and Exhibition. OnePetro. https://doi.org/10.2118/109914-MS

Zhuang, G., Li, Q., Bergaya, F., & Yuan, P. (2024). The significance of clay minerals in drilling and drilling fluids. In Clay Science in Drilling and Drilling Fluids (pp. 1-19). Elsevier. https://doi.org/10.1016/B978-0-443-15598-7.00003-1

JJEES

JJEES (2025) 16 (3): 298-305
ISSN 1995-6681

Jordan Journal of Earth and Environmental Sciences

Magnetic Anomaly Analysis Reveals Mineral Potential in the Udi Region of south-eastern Nigeria

Ema Abraham*, Ayatu Usman, Iheanyi Ikeazota

Department of Geology/Geophysics, Alex Ekwueme Federal University, Ndufu-Alike Ikwo, P.M.B. 1010 Abakaliki, Ebonyi, Nigeria.

Received on September 3, 2024 Accepted on March 28, 2025

Abstract

Geophysical data processing techniques were employed to investigate the mineral potential of the Udi region in south-eastern Nigeria. High-resolution aeromagnetic data were analyzed using multiple methods, including magnetic anomaly mapping, source edge detection (SED), analytic signal (AS), source parameter imaging (SPI), and 3D inversion. Significant magnetic anomalies, ranging from -28.1 to 135 nT, correlate with known mineral deposits, including limestone, iron ore, lead-zinc (Pb-Zn) sulfides, and coal. Depth estimates for potential mineral sources range from 280 to 3600 m. Linear trends in Euler solutions suggest the presence of faults and fractures, which are likely to influence mineral emplacement. 3D inversion models corroborated these findings, revealing subsurface structures with contrasting magnetic susceptibilities. This study confirms known mineralization and identifies new prospective areas for future exploration.

Keywords: *Aeromagnetic analysis, structural interpretation, mineral prospectivity, subsurface modeling, geophysical inversion, depth estimation*

1. Introduction

The Udi region in south-eastern Nigeria is of significant geological interest due to its complex subsurface structures and rich mineral resources. The region has been identified as a potential hotspot for mineral exploration (Abraham et al., 2024a; Onwuka et al., 2010), but detailed subsurface evaluations of these deposits are limited. Surficial assessments indicate the presence of mineral-bearing rocks such as limestone, iron ore, clay, lead-zinc (galena and sphalerite), glass sand, gypsum, and coal. However, the extent and depth of these deposits have not been thoroughly investigated. This study focuses on the application of magnetic data to explore and map the geological structures hosting these mineral resources.

Magnetic surveys have proven effective in mineral exploration, particularly in areas abundant in magnetite and other magnetic minerals (El-Kelani, 2020). These surveys provide valuable insights into the structure of these magnetic bodies and often offer information about the structural system of mineralization (Abraham et al., 2024a, 2024b; Couto et al., 2017; Leão-Santos et al., 2015; Obaje, 2009; Büyüksaraç et al., 1998). The method has also provided valuable insights into the subsurface by detecting variations in the Earth's magnetic field caused by the presence of ferromagnetic minerals (Usman et al., 2024a, 2024b; Abraham et al., 2022; Reeves, 2005). Magnetic surveys are particularly effective in regions with complex geology, where traditional methods may fall short. The application of the magnetic method in south-eastern Nigeria has shown promise in identifying and characterizing mineral deposits, offering a non-invasive and cost-efficient alternative for identifying mineral deposits (Ugodulunwa et al., 2021; Abraham et al., 2022).

The study area covers geographic latitudes 6°00′ and 6°30′ N and geographic longitudes 7°00′ and 7°30′ E within the sedimentary terrain of south-eastern Nigeria (Figure 1). It covers an area of about 3025 km^2 and consists of many major settlements that are engaged in various forms of farming and localized mining activities.

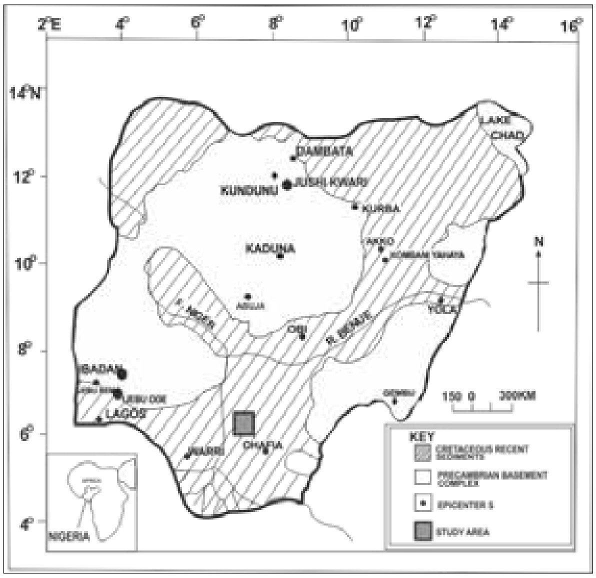

Figure 1. Map of Nigeria showing the study area (modified from Abraham et al., 2018)

In Udi, coal mining dates back to 1916, when it was exploited by the Nigerian Coal Corporation (NCC) at Onyema coalfield, which was later industrialized in October 1977 (Onwukeme, 1995). Although both local and industrial coal mining activities have stopped in the area for some time due to the alternative discovery and industrial exploitation

---

* Corresponding author e-mail: ema.abraham@funai.edu.ng

of fossil fuel in the nation, there are no formal evaluations of their subsurface host structures, neither has the location, geometry, and estimate of other possible deposits been sufficiently assessed.

Some geophysical studies conducted within the region have investigated the groundwater potentials (Onwe et al., 2022; Ekwe et al., 2020; Onwe et al., 2019), with a few highlighting the diverse mineralization potentials (Ugodulunwa et al., 2021; Abraham et al., 2022), particularly in areas like the Udi region, which is known for its rich deposits of coal, limestone, and other economically significant minerals (Obaje, 2009). The geophysical characterization of these resources has been relatively limited, emphasizing the need for comprehensive studies that leverage advanced geophysical techniques. Therefore, this study aims to analyze the subsurface structures in the Udi region using aeromagnetic data to determine their mineralization potential. Specifically, we propose to map structural trends, estimate depths of key geologic features, and evaluate their significance in guiding mineral exploration efforts. We hope to provide insights into the structural controls on mineral deposition, which would be essential for resource evaluation and sustainable extraction planning.

1.1 Geological Setting

The study area lies within the Southern Benue Trough of the Anambra Basin, South-eastern Nigeria. The Early Cretaceous witnessed the separation of the South American and African continents, forming the Benue Trough Sedimentary basin. According to Murat (1972), three major tectonic cycles were identified within the South-eastern Nigeria. During the Aptian-Early Campanian period, the initial phase of the tectonic setting was marked by the onset of rifting and the opening of the Benue Trough. Subsequently, in the Santonian-Early Campanian period, compression tectonics led to the folding and uplift of the Abakaliki Anticlinorium, the formation of the Anambra Basin, and the development of the complementary Afikpo Syncline (Figure 2).

Figure 2. Geologic map of the study area (modified from Abraham et al., 2018)

During the Late Campanian to Eocene, the third phase of the tectonic setting led to alternating periods of rapid uplift and subsidence, followed by the progradation of a delta and the subsequent deposition of sedimentary infill in the Anambra Basin. The Cretaceous depocenter of Anambra Basin received sedimentary fill during the Campanian-Tertiary age. The sedimentary formation of the Anambra Basin is abridged in (Nwajide, 2013). Freshwater sandstones were deposited till the north and west onto the Precambrian Basement. Sedimentation was entirely nonmarine until the deposition of the Nsukka Formation, in which marine intercalations indicate a gradual encroachment of the sea and mark the end of deposition in the Anambra Basin. The Udi region is characterized by the Nsukka Formation, the Bende Ameki group, the Imo clay-shale group, and part of the Mamu Formation (Figure 2).

1.2 Mineral Resources Map of the Study Area

The Udi region's mineral resources map (Figure 3) was extracted from the Mineral Resources Map of Nigeria as published by the Geological Survey of Nigeria Agency (GSNA) in 2004. Figure 3 reveals a mineral-rich region within the Cretaceous sedimentary basin of south-eastern Nigeria. The mineral emplacements also hint at the possible presence of associated mineral deposits that may not have been identified at the time.

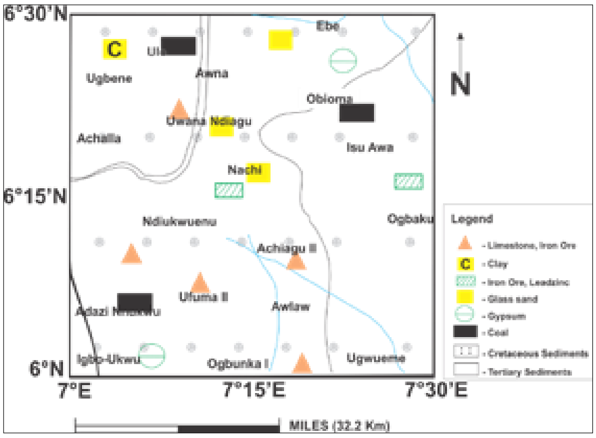

Figure 3. Mineral map of the study area (Extracted from Nigeria Geological Survey Agency (NGSA): Mineral Resources map of Nigeria, 2004)

Notable minerals in the region include the calcite and aragonites domiciled in the vast accumulation of limestone in the southern and northwestern (NW) regions. Other minerals include dolomite, siderite, and lead-zinc (galena and sphalerite) in the central and eastern regions. Gypsum dominates the NE and SE regions, and the earlier coal deposits were discovered in the NW, NE, and SE regions. Some significant clay and glass sand depositions have also been recorded in the northern region of the study area.

2. Methodology

A high-resolution aeromagnetic data was used for this study. The data was acquired from the Nigerian Geological Survey Agency (NGSA), which had acquired the digital data for the entire country between years 2005 and 2009. The airborne survey was conducted by Fugro Airways Services. The surveys were flown at 500m line spacing with an average flight elevation of 80 m along NW – SE directions, and data published in the form of grids of by map sheets. The regional field and diurnal magnetic effects were eliminated from the data. We then applied the Reduction to Equator (RTE) correction, following the methodology outlined by Abraham et al. (2024a), Ganguli et al. (2021), Abraham et al.

(2018), Jain (1988), and Leu (1981). This correction assumed a magnetic declination of -2.15° and an inclination of -13.91° for the study area, utilizing the fast Fourier transform operator. Figure 4 displays the resulting aeromagnetic map of the Udi region.

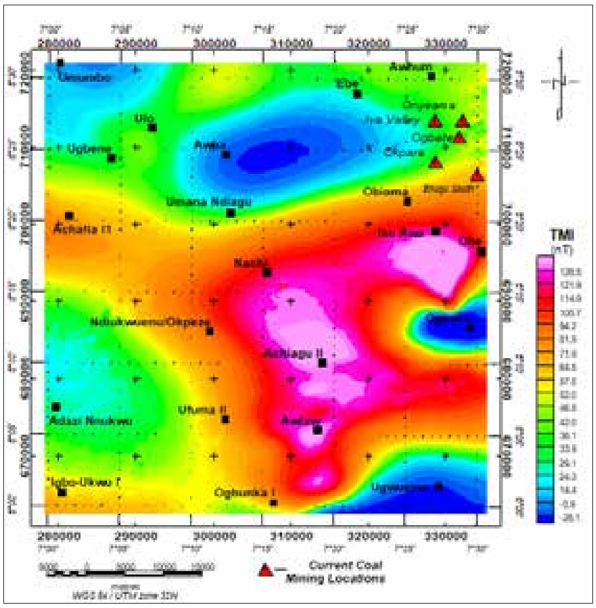

Figure 4. Residual Magnetic Anomaly Map of Udi.

The map revealed significant fluctuations in magnetic strengths, indicating diverse magnetic characteristics. At Awlaw, Achiagu II, Nachi, Isu Awa, Oba, and certain areas of the Ndiukwuenu – Achalla regions, there are noticeable positive irregularities with values ranging from 71 to 140 nT. These irregularities indicate the possible presence of high magnetic minerals within the subsurface at these locations. The mixture of positive (38 – 57 nT) and negative (-25 – 29 nT) magnetic anomalies at Onyeama and Iva Valley, Ulo, and Adazi locations could be signals from the coal deposits embedded in the region. The magnetic susceptibility of coal is a mixture of diamagnetic, paramagnetic, and ferromagnetic (Seferinoglu and Duzenlf, 2022).

2.1 Source Edge Detection (SED)

The Source Edge Detection (SED) technique would be used to locate edges (i.e., geological contacts) or peaks from magnetic field data by analyzing the local gradients. The SED function estimates the location of abrupt lateral changes in magnetization or mass density of upper crustal rocks following the procedure of identifying maxima on a grid of horizontal gradient magnitudes. Using the technique of Cordell and Grauch (1982), a database of source edge locations was derived from the grid of the total magnetic field. A map is produced with ˧ symbols representing locations and gradient directions of magnetic field anomalies (Figure 5).

2.2 Analytic signal (AS)

The AS processing technique was used to enhance the resolution and interpretability of magnetic data anomalies. With the AS computations, information on the amplitude and phase of anomalies were extracted to aid in identifying subtle magnetic anomalies associated with geological boundaries and lithological variations. The analysis of magnetic anomalies presents unique challenges due to the phenomenon of spatial offset between the observed anomalies and their underlying sources. This displacement, often called skewness and the non-vertical nature of the Earth's magnetic field and the induced magnetization within geological bodies. In this context, the Analytic Signal (AS) function emerges as a particularly valuable tool for interpretation despite not being a directly measurable parameter. Its key advantage lies in its independence from both the magnetization direction and the orientation of the inducing field. This property ensures that geological bodies with identical geometries produce identical analytic signals, regardless of their magnetic characteristics or geographical location. Another notable feature of the AS function is the symmetry of its peaks. These peaks align precisely with the edges of broad geological structures and centrally over narrow features. This predictable behavior significantly enhances the accuracy of source localization and geometric interpretation in magnetic surveys. By leveraging these properties, the AS function overcomes many ambiguities associated with traditional magnetic anomaly interpretation, offering a more direct and reliable method for delineating subsurface structures and geological boundaries (Abraham et al., 2024a).

The Analytic Signal is given by Equation (1):

$$A(x,y) = \sqrt{\left(\frac{\partial T}{\partial x}\right)^2 + \left(\frac{\partial T}{\partial y}\right)^2 + \left(\frac{\partial T}{\partial z}\right)^2} \tag{1}$$

where T is the observed field at x and y.

The Analytic Signal (AS) method offers a practical approach to estimating the depth of magnetic sources, particularly when assuming these sources are vertical contacts. This technique employs a straightforward amplitude half-width rule, which typically yields depth estimations with an accuracy of around 70%. A significant advantage of the AS method is its ability to circumvent the challenges often encountered in traditional reduction-to-pole processes. These conventional methods can be problematic when the effects of natural remanent magnetization on the source's overall magnetization are not well understood or quantified. Figure 6 provides a visual display of the AS results. This approach proves especially valuable in situations where the magnetic properties of subsurface structures are complex or poorly constrained. By focusing on the geometry of the anomaly rather than its absolute magnetic properties, the AS method provides a more robust and versatile tool for magnetic data interpretation.

2.3 Source Parameter Imaging (SPI)

The Source Parameter Imaging (SPI) technique is an automated method for determining the depths of magnetic sources from gridded magnetic data. A key advantage of this approach is its independence from magnetic inclination and declination, eliminating the need for pole-reduced input grids in the analysis process. Empirical studies involving real-world datasets with drillhole verification have demonstrated the reliability of SPI, with depth estimates typically falling within a ±20% margin of error. This level of accuracy is comparable to that achieved by Euler deconvolution, another widely used technique in magnetic data interpretation. However, SPI offers distinct benefits over Euler deconvolution. Notably, it generates a more comprehensive and coherent set of solution points, providing a fuller picture of the subsurface structure.

SPI assumes a step-type source model (Thurston and Smith, 1997; Blakely and Simpson, 1986).). For a step, the following formula holds:

$$\mathrm{Depth} = 1/\mathrm{K}_{\mathrm{max}}, \tag{2}$$

where is the peak value of the local wavenumber K over the step source.

$$\mathrm{K} = \sqrt{\left(\frac{\mathrm{dA}}{\mathrm{dx}}\right)^2 + \left(\frac{\mathrm{dA}}{\mathrm{dy}}\right)^2}, \tag{3}$$

where

$$\text{Tilt derivative A} = \tan^{-1}\left\{[\mathrm{dM/dz}]/\left(\sqrt{\left(\frac{\mathrm{dA}}{\mathrm{dx}}\right)^2 + \left(\frac{\mathrm{dA}}{\mathrm{dy}}\right)^2}\right)\right\}, \tag{4}$$

and, M = the total magnetic field anomaly grid.

The result of the SPI computations for this study area is presented in Figure 7.

2.4 Euler Deconvolution

Euler deconvolution was applied to the residual magnetic data to estimate the depth and location of magnetic sources contributing to observed anomalies. By analyzing the second vertical derivative of the magnetic field, this method facilitated the identification and delineation of isolated magnetic sources, including faults, dykes, and mineralized zones.

The Standard 3D form of Euler's equation can be defined (Reid et al., 1990) as:

$$x\frac{\partial T}{\partial x} + y\frac{\partial T}{\partial y} + z\frac{\partial T}{\partial z} + \eta T = x_o\frac{\partial T}{\partial x} + y_o\frac{\partial T}{\partial y} + z_o\frac{\partial T}{\partial z} + \eta b \tag{5}$$

Where x, y, and z are the coordinates of a measuring point, x_o, y_o, z_o and are the coordinates of the source location whose total field is detected at x, y, and z, b is a base level, and η is a structural index (SI). The SI represents an exponential factor that correlates with the field decay rate over distance for a source with a specific geometry. The value of the SI is contingent upon the type of source body under investigation (Whitehead and Musselman, 2005). For instance, $\eta = 0$ denotes a contact, $\eta = 1$ signifies the top of a vertical dyke or the edge of a sill, $\eta = 2$ corresponds to the center of a horizontal or vertical cylinder, and $\eta = 3$ represents the center of a magnetic sphere or dipole (Thompson, 1982; Reid et al., 1990). The implementation of Euler deconvolution is depicted in Figure 8 (a and b) for structural indexes of 0 and 1.

2.5 3D Modeling of Susceptibility Contrast

The processed magnetic data were integrated into three-dimensional (3D) geological models to visualize and interpret subsurface geological structures of mineralized interests. Incorporating information on magnetic susceptibility contrast, these models enabled the quantification of magnetic properties and characterization of geological features in three dimensions, facilitating the identification of potential mineralization targets and the assessment of structural extents. The 3D modeling results are displayed in Figure 9.

Pilkington (2009) applied the Cauchy norm described by Sacchi and Ulrych (1995) to address the 3D magnetic inverse problem. This approach aimed to generate sparse models, characterized by minimizing the number of non-zero values that adequately fit the observed data. The resulting inversion technique is classified as geologically unconstrained (Abraham et al., 2024a). This classification distinguishes it from constrained inversion methods incorporating specific geological information. Constrained inversions typically integrate hard geological data, such as information from drill hole intersections, to guide the inversion process. By contrast, the unconstrained approach developed by Pilkington relies solely on magnetic data and mathematical principles to produce a solution. This method offers flexibility in scenarios where detailed geological constraints are unavailable or when an unbiased interpretation of the magnetic data is desired. However, the lack of geological constraints may result in solutions that, while mathematically sound, might not fully align with known geological structures or properties in some cases.

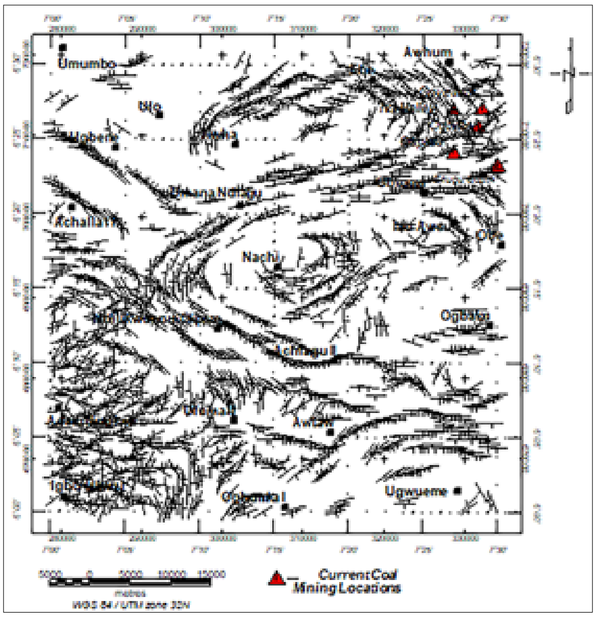

Figure 5. Source Edge Detection in 2 peak directions showing location and gradient direction of potential field anomalies.

The choice of methods, particularly SPI and Euler Deconvolution, was based on the specific requirements of this study and the nature of the geological formations in the Udi region. SPI was selected for its ability to provide depth estimates without requiring detailed prior geological constraints. This is particularly important in underexplored areas where detailed geological mapping is scarce. SPI has been successfully applied in similar sedimentary environments (Büyüksaraç et al., 1998; Abraham et al., 2024a, 2024b), where it has proven effective in estimating the depth to magnetic sources, particularly in regions with complex magnetic anomalies. On the other hand, Euler Deconvolution was chosen for its ability to identify subsurface structural lineaments such as faults and fractures. Given the presence of known mineral deposits associated with fault systems in the Udi region, Euler Deconvolution was particularly useful in identifying these structural features and estimating their depths. Compared to alternative methods, such as spectral analysis or tilt-depth methods, Euler Deconvolution provides a more direct approach to delineating vertical and horizontal discontinuities in the magnetic data (Abraham et al., 2024b; Abraham and Alile, 2019). Combining these methods enhances this study's robustness by providing complementary information on the depth and structural characteristics of the mineralized zones.

3. Results and Discussion

The magnetic anomalies in the Udi region exhibit significant highs (29–135 nT) and lows (-28.1 to -0.9 nT) (Figure 4). High anomalies are concentrated in regions with recorded mineral signatures, particularly at Achiagu II (limestone and iron ore), Nachi (Pb-Zn and glass sand), Uwana Ndiagu (limestone and iron ore), and the Isu Awa–Obe axis (Pb-Zn and iron ore). In contrast, the magnetic lows show no direct correlation with surface mineral occurrences, except in Umumbo, where documented clay deposits are present. This investigation suggests that anomalous subsurface structures may be mineralized but remain unexposed at the surface.

The observed anomaly values (-28.1 to 135 nT) align with previously reported values in south-eastern Nigeria (Nwankwo and Ene, 2020; Abraham et al., 2022, 2024a; Ugodulunwa et al., 2021). Similar anomaly ranges (-30 to 120 nT) were noted in the Enugu coal basin and Ajao area (Nwankwo et al., 2020; Ugodulunwa et al., 2021), supporting our interpretation that the Udi region is highly prospective for mineralization. The stronger magnetic responses at Achiagu II and Isu Awa (up to 135 nT) suggest higher concentrations of ferromagnetic minerals such as iron ores and Pb-Zn sulfides. Additionally, the negative anomalies associated with coal deposits at Ulo and Adazi Nnukwu are consistent with Usman et al. (2024a), further validating this methodology.

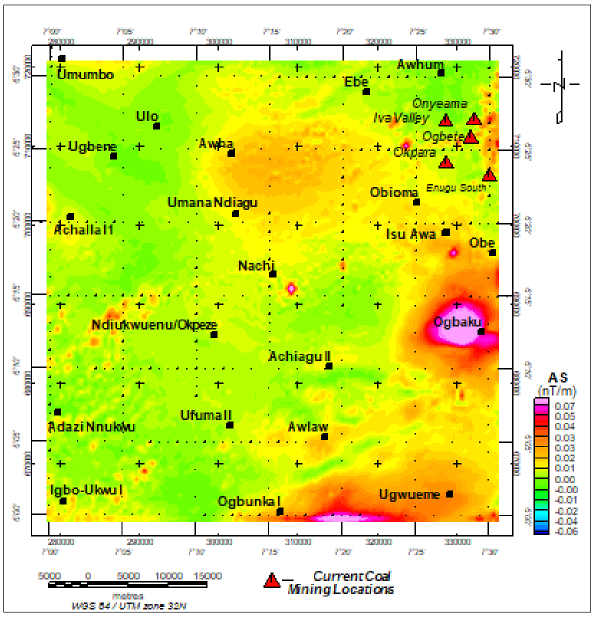

Figure 6. Result of Analytic Signal computations on the magnetic anomalies. Some isolated anomalous structures could be identified from the map.

The source edge detection (SED) analysis (Figure 5) highlights steep magnetic gradient changes at Obioma, Ndiukwuenu, and Adazi Nnukwu. These correspond to sharp anomaly variations and may indicate shifts in the magnetic mineral properties of the underlying formations. The gradient changes at Nachi, Isu Awa, and Awlaw coincide with magnetic highs, suggesting variations in the distribution of magnetized subsurface structures. These results reinforce the role of fault and fracture systems in controlling mineral emplacement.

The analytic signal (AS) response (Figure 6) reveals maxima over magnetization contrasts, particularly at Ndiukwu, Nachi, Ogbaku, Ogbunka-I, Awna, and Obe. These maxima indicate significant subsurface sources corroborated by other geophysical analyses. The AS amplitudes suggest proximity to mineralized structures, such as Pb-Zn mineralization at Ogbaku–Isu Awa and limestone and iron ore deposits at Uwana Ndiagu, Ndiukwuenu, and Ogbunka-I. A comparison of this method with results from Abraham et al. (2024b) confirms the effectiveness of the AS method in delineating Pb-Zn mineralization structures.

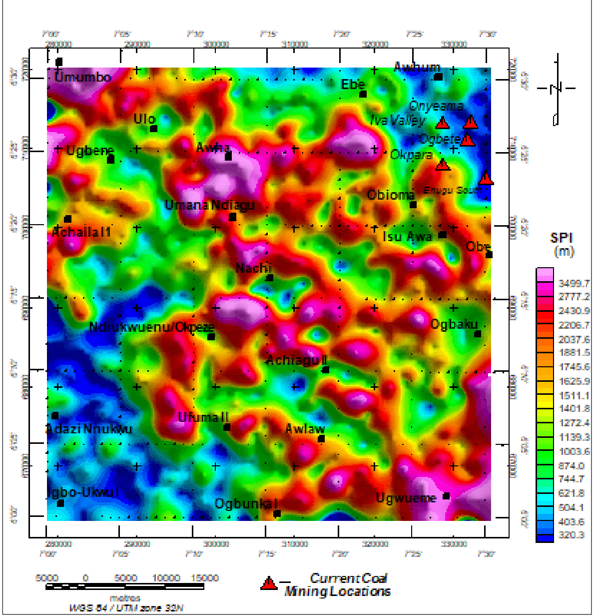

Figure 7. Depths result from SPI computations on the magnetic data.

The SPI method (Figure 7) estimates magnetic source depths ranging from 280 to 3600 m, with deeper anomalies observed in the central study area and shallower sources in the NE and SW. The revealed depths align with known mineralized zones (Figure 3), providing depth estimates for target structures. For instance, the Pb-Zn and iron ore deposits at Nachi are inferred to be within 600–1000 m, while the Isu Awa–Ogbaku mineralization extends to depths of 1200–1500 m. Similarly, limestone and iron ore formations at Ufuma-II, Ogbunka-I, Achiagu-II, and Uwana are estimated at 700–2100 m depths.

Euler deconvolution (Figure 8) further corroborates these depth estimates and identifies subsurface faults trending EW and NW-SE with depths of 10–2300 m. These fault systems likely facilitated the emplacement of Pb-Zn sulfides at Ogbaku and influenced coal deposition at Ulo through sedimentary basin subsidence. Nwankwo and Ene (2020) had achieved similar deductions in the region using gravity and Landsat datasets. Additionally, clusters of Euler solutions indicate possible dykes and sills at depths of 300–3400 m. These intrusive structures may have contributed to metasomatism, influencing Pb-Zn formation at IsuAwa–Ogbaku and Nachi. Intrusive heat sources around Ebe and Igbo-Ukwu may have driven gypsum precipitation in the Cretaceous basin. Similar observations and conclusions have been drawn by Abubakar et al. (2023) on the ability of magnetic data to map subsurface geological structures in southwestern Nigeria. Table 1 summarizes the key mineralized zones identified in this study, highlighting their corresponding magnetic anomaly ranges, depth estimates, associated minerals, and structural controls. The observed variations in magnetic signatures reinforce the influence of fault and fracture systems on mineralization. For instance, the higher magnetic anomalies at Achiagu II and Isu Awa–Obe align with known iron ore and Pb-Zn deposits. In contrast, the negative anomalies at Onyeama and Adazi Nnukwu correspond to coal-rich zones. These findings provide further validation of the geophysical methods used in this study.

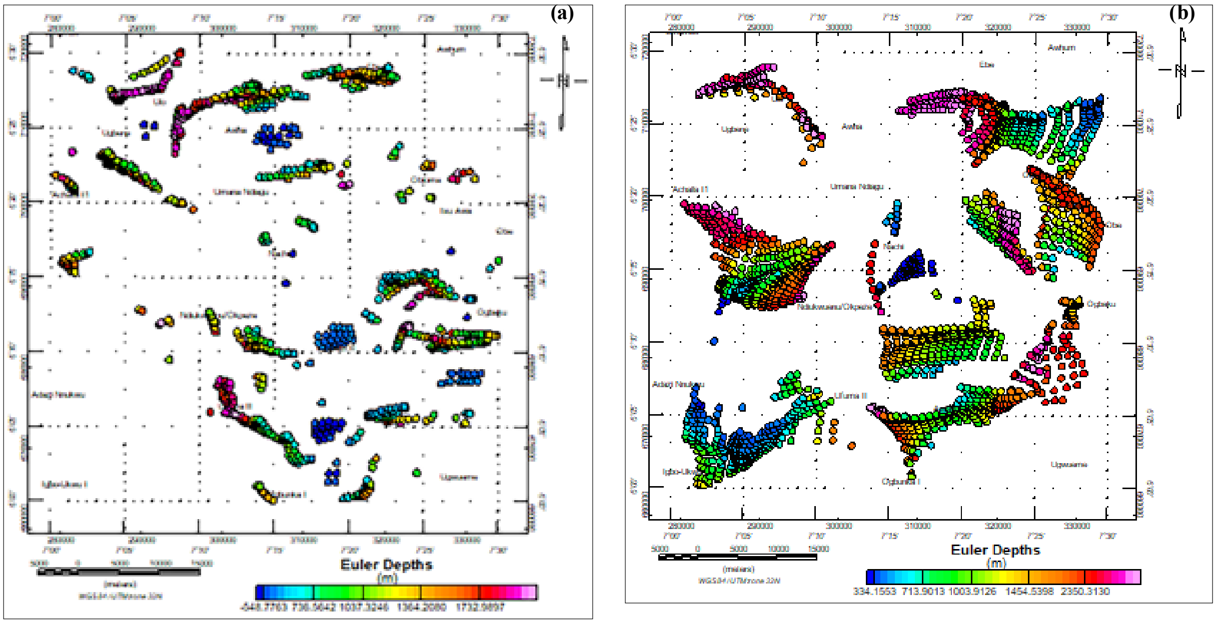

Figure 8. Euler depth solutions map. **(a)** SI=0 for geologic contacts. **(b)** SI=1 for the top of a vertical dyke or the edge of a sill identification in the region.

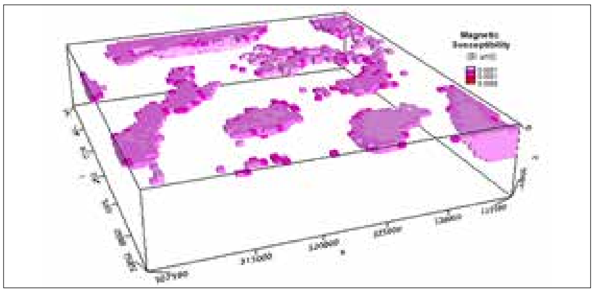

Figure 9. 3D inversion result for the study region obtained from clipping susceptibilities lower than 0.0001 SI.

The 3D magnetic inversion results (Figure 9) delineate subsurface structures with varying magnetic susceptibilities, supporting the presence of mineralized bodies. The successful mapping of known coal deposits in the NE confirms the reliability of this approach and suggests that other identified anomalies are likely indicative of mineralized zones.

Table 1. Summarizes the key mineralized zones and their respective magnetic properties.

Mineralized Zone	Magnetic Anomaly Range (nT)	Depth Range (m)	Associated Minerals	Structural Control
Achiagu II	71 to 140	700 – 2100	Limestone, Iron ore	Fault-controlled
Nachi	71 to 140	600 – 1000	Pb-Zn (Galena, Sphalerite), Glass Sand	Fault zone
Isu Awa – Obe	71 to 135	1200 – 1500	Pb-Zn, Iron ore	Fracture zone
Uwana Ndiagu, Ndiukwuenu	71 to 120	700 – 2100	Limestone, Iron ore	Structural zones
Onyeama, Ogbete	38 to 57	< 300	Coal	Basin margin structures
Adazi Nnukwu	-25 to -29	< 300	Coal	Fault-controlled

4. Conclusion

This comprehensive magnetic study of the Udi region in southeast Nigeria has yielded valuable insights into the region's mineral potential and subsurface structures. The integration of multiple magnetic data analysis techniques, including magnetic anomaly mapping, source edge detection (SED), analytic signal (AS), source parameter imaging (SPI), Euler deconvolution, and 3D inversion, has proven highly effective in characterizing the region's geology and mineralization.

Key findings of this study include:

- Significant magnetic anomalies (ranging from -28.1 to 135 nT) correlate well with known mineral deposits, including limestone, iron ore, lead-zinc (Pb-Zn) sulfides, and coal.
- Depth estimates of potential mineral sources ranging from 280 to 3600 m provide crucial information for future exploration efforts.
- Identification of linear trends suggests faults and fractures, which likely played a vital role in mineral emplacement and formation.
- Successful mapping of subsurface structures with contrasting magnetic susceptibilities through 3D inversion modelscorroborates other analytical results.
- Confirmation of known mineralization sites and identification of new prospective areas for further investigation.

The study demonstrates the power of integrating multiple magnetic data analysis techniques in mineral exploration, particularly in sedimentary basin environments. The results validate this approach's effectiveness and provide a solid foundation for future targeted exploration efforts in the Udi region. This research contributes significantly to understanding of the area's geological structures and mineral potential, offering valuable guidance for resource development in Nigeria. Further work, including ground-based geophysical surveys and drilling programs, is recommended to expand upon these findings. This study is a model for similar investigations in other sedimentary basins with potential mineral resources.

Acknowledgment

We are grateful to the anonymous reviewers and the Editor for their useful comments. We are also grateful to the Geophysical Research Group of AE-FUNAI for their support throughout this study.

References

Abraham, E. M., Alile, O. M. (2019). Modelling Subsurface Geologic Structures at Ikogosi Geothermal Field, Southwestern Nigeria, using Gravity, Magnetics, and Seismic Interferometry Techniques (2019). Journal of Geophysics and Engineering (2019) 16, 729–741. https://academic.oup.com/jge/advance-article-abstract/doi/10.1093/jge/gxz034/5531815

Abraham, E. M., Onwe, M. R., Usman, A. O., Gwazah, C. A., Uchenna, M. E. (2022). Mapping of mineral deposits within granitic rocks by aeromagnetic data-a case study from Northern Nigeria. Arabian Journal of Geosciences, 15:1656 https://doi.org/10.1007/s12517-022-10947-0.

Abraham, E. M., Uwaezuoke, A. E., Usman, A. (2024b). Geophysical investigation of subsurface mineral potentials in North-Central Nigeria: implications for sustainable mining and development. Geomechanics and Geophysics for Geo-Energy and Geo-Resources 10(1). https://doi.org/10.1007/s40948-024-00913-3

Abraham, E., Itumoh, O., Chukwu, C., Onwe R. (2018). Geothermal Energy Reconnaissance of South-eastern Nigeria from Analysis of Aeromagnetic and Gravity Data. Pure and Applied Geophysics, 176: 22 – 36. https://doi.org/10.1007/s00024-018-2028-1

Abraham, E., Usman, A., Chıma, K., Azuoko, G.-B., Ikeazota, I. (2024a). Magnetic inversion modeling of subsurface geologic structures for mineral deposits mapping in south-eastern Nigeria. Bulletin of the Mineral Research and Exploration, 173: 85-105. https://doi.org/10.19111/bulletinofmre.1267876

Abubakar, H. O., Ige, O. O., Olatunji, S. (2023). Remote Sensing and Aeromagnetic Study in Part of Sheet 244 Ado Ekiti Northeast for Groundwater Development, Nigeria. Jordan Journal of Earth and Environmental Sciences, 14 (4): 280-286.

Blakely, R. J., Simpson, R.W. (1986). Approximating edges of source bodies from magnetic or gravity anomalies, Geophysics, v. 51, 1494-1498.

Büyüksaraç, A., Jordanova, D., Ates¸ A., Karloukovski, V., (2005). Interpretation of the Gravity and Magnetic Anomalies of the Cappadocia Region, Central Turkey. Pure appl. geophys. 162 (2005) 2197–2213. DOI 10.1007/s00024-005-2712-9

Cordell, L., Grauch, V. J. S. (1982). Mapping Basement Magnetization Zones from Aeromagnetic Data in the San Juan Basin, New Mexico. SEG Technical Program Expanded Abstracts, 246-247. https://doi.org/10.1190/1.1826915

Couto, M.A., Aisengart, T., Barbosa, D., Ferreira, R.C.R., Baltazar, O.F., Marinho, M., Cavalcanti, A.D., Araujo, J.C.S., (2017). Magnetization-Vector Inversion, Application in quadrilatero Ferrifero region, MG, Brazil. 15th International Congress of the Brazil Geophysical Society, Rio de Janeiro, Brazil 31 July to 3 August 2017.

Ekwe, A. C., Opara, A. I., Okeugo, C. G., Azuoko, G., Nkitnam, E. E., Abraham, E. M., Chukwu, C. G., Mbaeyi, G. (2020). Determination of aquifer parameters from geosounding data in parts of Afikpo Sub-basin, south-eastern Nigeria. Arabian Journal of Geosciences volume 13(4): 189. https://doi:10.1007/s12517-020-5137-y

El-Kelani, R. (2020). A Review of Gravity and Magnetic Studies in the Jordan Dead. Jordan Journal of Earth and Environmental Sciences, 11 (1): 49-61. https://staff.najah.edu/media/published_research/2020/06/04/JJEES_Vol_11_No_1_P6_2.pdf

Ganguli, S. S., Pal, S. K., Kumar, S. K. P. (2021). Insights into the crustal architecture from the analysis of gravity and magnetic data across Salem-Attur Shear Zone (SASZ), Southern Granulite Terrane(SGT), India: an evidence of accretional tectonics. Episodes 44(4) 419 – 422.

Jain, S. (1988). Total magnetic field reduction—The Pole or Equator? A model study. Canadian Journal of Exploration Geophysics 24 (2) 185–192

Leâo-Santos, M., Li, Y., Moraes, R. (2015). Application of 3D-magnetic amplitude inversion, to iron oxide-copper-gold deposits, at low magnetic latitudes: A case-study from Carajas Mineral Province, Brazil. Geophysics 80(2): B13 – B22.

Leu, L. K. (1981). Use of reduction-to-the-equator process for magnetic data interpretation. Geophysics 47, 445.

Mohammed, I., Taufiq, S. (2022). Geoelectrical Study of Groundwater Potential at Waziri Umaru Federal ' 'Polytechnic's Gesse Campus BirninKebbi, Kebbi State, Nigeria. Jordan Journal of Earth and Environmental Sciences, 13 (2): 82-88. https://jjees.hu.edu.jo/files/Vol13No2/JJEES_Vol_13_No_2_P2.pdf

Murat, K. C. (1972) Stratigraphy and Paleogeography of the Cretaceous and Lower Tertiary in Southern Nigeria. In: Dessauvagie, T.F.J. and Whiteman, A.J., Eds., African Geology, University of Ibadan, 251-266.

Nwajide, C.S. (2013) Geology of ' 'Nigeria's Sedimentary Basins. CSS Bookshop Ltd., Lagos, 1-565.

Nwankwo, C. N., Ene, E. C. (2020). Structural Investigation of Udi LGA of Enugu State, South Eastern Nigeria Using High

Resolution Bouguer Gravity and Landsat Data. Asian Journal of Research and Reviews in Physics, 3(1): 17-32

Obaje N. G. (2009). The Benue Trough". Geology and Mineral Resources of Nigeria. Springer. 57. SBN 3-540-92684-4.

Onwe, M. R., Abraham, E. M., Ambrose, N. T., Osike, O. K. (2022). An evaluation of the hydrogeology potential of Nsukka, Southern Nigeria, using geographic information system. Applied Water Science 12:54, https://doi.org/10.1007/s13201-022-01579-6

Onwe, R. M., Ifedilichukwu, N. G., Ahiarakwem C. A, Abraham, E. M., Emberga T. T. (2019). Assessment of Geospatial Capability Index for Siting Waste Dump/Landfill to Control Groundwater Geopollution Using Geographic Information System (GIS) Approach: case study of Abakaliki area and Environs Southern Nigeria. Applied Water Science, (2020) 10:12. https://doi.org/10.1007/s13201-019-1087-5

Onwuka, S. O., Ezeh, C. S., Ekwe, A. C. (2010). Application of Chemometric Technique in the Assessment of Groundwater Quality in Udi and its Environs, South-eastern Nigeria. Jordan Journal of Earth and Environmental Sciences, 3(2), 63- 78.

Onwukeme, E. N. (1995). The crust in the Nigeria Mining Geoscience Society. Newsmag Preconf (ed). 92:2 – 5.

Pilkington, M. (2009). 3D magnetic data-space inversion with sparseness constraints. Geophysics 74 (1) P.L7-L15.

Reeves, C. (2005). Aeromagnetic Surveys: Principles, Practice & Interpretation. GEOSOFT.

Reid, A. B., Allsop, J. M., Grauser, H., Millet, A. J., Somerton, I. N. (1990). Magnetic interpretation in 3D using Euler-Deconvolution. Geophysics 55, pp. 80-91

Riedel, S. (2008). Airborne-Based geophysical investigation in Dronning Maud land Antarctica. Dissertation, Christian Albrechts Universitat Zu Kiel, Kiel.

Sacchi, M. D., Ulrych, T. J. (1995). High-resolution velocity gathers and offset space reconstruction: Geophysics 60, 1169–1177.

Seferinoglu, M., Duzenlf, D. (2022). Mineral and chemical characterization of magnetic and non-magnetic products obtained from dry magnetic enrichment of the lignite coals. GU J. Sci. 35(4): 1280 – 1295. DOI: 10.35378/gujs.939443

Thompson, D. T. (1982). Euldph: A new technique, for making computer-assisted, depth- estimates, from magnetic data, Geophysics 47. pp. 31-37

Thurston, J. B., Smith, R. S. (1997). Automatic conversion of magnetic data to depth, dip and susceptibility contrast using the SPITM method, Geophysics, v. 62, p. 807-813.

Ugodulunwa, F. X. O., Ekwe, A. C., Abraham, E. M., Chukwu, C. G., Onwe, R. M. (2021). Determination of depths to magnetic sources within Abakaliki–Afikpo area and environs, South-eastern Nigeria: implications for mineral and hydrocarbon prospectivity. Exploration Geophysics, https://doi.org/10.1080/08123985.2021.1982646

Usman, A. O., Abraham, E. M., Chris, E., Azuoko, G-B., Chinwuko, A. I., Chizoba, C. J., Akakuru, O. C. (2024a). Structural modelling of subsurface geologic structures in Anambra and adjoining Bida Basins using aeromagnetic data: Implications for mineral explorations. Kuwait Journal of Science, 52, 100307. https://doi.org/10.1016/j.kjs.2024.100307.

Usman, A. O., Abraham, E. M., Okonkwo, C. C., Augustine, I. C., Azuoko, G-B. (2024b). Geothermal energy appraisal and subsurface structural mapping of the Rafin Rewa Warm Spring region, Precambrian Basement Complex of Nigeria. Scientific Reports, 14, 17368. https://doi.org/10.1038/s41598-024-66927-9

Whitehead, N., Musselman, C. (2005). Montaj Gravity/Magnetic interpretation: Processing, analysis, and visualization system, for 3-D inversion of potential field data, for Oasis montaj v6.1. Geosoft Inc. ON, Canada

المملكة الأردنية الهاشمية
صندوق دعم البحث العلمي
الجامعة الهاشمية

المجلة الأردنية
لعلوم الأرض والبيئة

JJEES

مجلة علمية عالمية محكمة

المجلد (١٦) العدد (٣)

http:// jjees.hu.edu.jo/

ISSN 1995-6681

المجلة الأردنية لعلوم الأرض والبيئة

مجلة علمية عالمية محكمة

المجلة الأردنية لعلوم الأرض والبيئة: مجلة علمية عالمية محكمة ومفهرسة ومصنفة، تصدر عن عمادة البحث العلمي في الجامعة الهاشمية وبدعم من صندوق البحث العلمي - وزارة التعليم العالي والبحث العلمي، الأردن.

ترسل البحوث إلكترونيا إلى البريد الإلكتروني التالي:

رئيس تحرير المجلة الأردنية لعلوم الأرض والبيئة

jjees@hu.edu.jo

لمزيد من المعلومات والأعداد السابقة يرجى زيارة موقع المجلة على شبكة الانترنت على الرابط التالي:

www.jjees.hu.edu.jo

المملكة الأردنية الهاشمية صندوق دعم البحث العلمي الجامعة الهاشمية

JJEES

المجلة الأردنية لعلوم الأرض والبيئة

المجلد (16) العدد (3)

مجلة علمية عالمية محكمة تصدر بدعم من صندوق دعم البحث العلمي

ISSN 1995-6681

jjees.hu.edu.jo

أيلول 2025